# THE TECTONOMETAMORPHIC EVOLUTION OF THE GREATER HIMALAYAN SEQUENCE AS EXPOSED IN CENTRAL NEPAL AND ADJACENT SOUTH-CENTRAL TIBET

by

Kyle P. Larson

A thesis submitted to the Department of Geological Sciences and Geological Engineering

In conformity with the requirements for

the degree of Doctor of Philosophy

Queen's University

Kingston, Ontario, Canada

(March, 2009)

Copyright © Kyle P. Larson, 2009

View across the Kali Gandaki valley from Poon Hill towards the east face of Dhaulagiri (left centre), Tukuche Peak (right centre) and Dhampus Peak (right). The South Tibetan detachment system crops out at the base of the Dhaulagiri massif and dips shallowly towards the north (right). It separates rocks of the Tethyan Sedimentary sequence above from rocks of the Greater Himalayan sequence below.

# Abstract

Understanding the development of the Himalaya is critical to elucidating continental collisional processes. The Greater Himalayan sequence (GHS), the exhumed mid-crust of the Himalayan orogen, records the diachronous tectonometamorphic evolution of the Himalaya from its deep hinterland to its foreland. The GHS in central Nepal and adjacent Tibet is deformed pervasively; quartz *c*-axis orientation fabrics from across the GHS indicate that the entire package was deformed at high temperatures (~550-650˚C). The asymmetries of these quartz *c*-axis orientation fabrics confirm field observations that define a reversal in shear sense from top-south shear near the bottom and middle of the GHS to top-north shear near the top of the package proximal to the South Tibetan detachment system (STDS). Estimates of mean kinematic vorticity from across the GHS indicate a pure shear contribution between 33% and 67%.

U-Pb geochronologic data from the upper GHS exposed in the Changgo culmination in south Tibet indicate that melt crystallization and metamorphism related to crustal thickening occurred at *ca*. 35 Ma and was succeeded by a second metamorphic episode and syn-kinematic voluminous anatexis at *ca*. 22 Ma. The upper GHS was thinned vertically by 50% and extended horizontally during and immediately after the second metamorphic event, in a manner typical of the deep hinterland regions of orogens.

In central Nepal, the ductile lateral extrusion of the upper GHS between the Main Central thrust (MCT) below and STDS above ceased by ~19 Ma. The cessation of lateral extrusion followed the collapse of the orogenic wedge and a reduction in the gravitational potential necessary to drive the propagation of deformation southwards towards the foreland. To restore the geometry of the wedge, deformation stepped out-of-sequence into southern Tibet, with the exhumation of the Changgo culmination and the North Himalayan antiform, before migrating incrementally back toward the foreland. Subsequently, the MCT migrated downward structurally adding material to the lower GHS as thrust slices, characteristic of foreland-style deformation. Thus, the transition between the upper and lower GHS in central Nepal records the transition from hinterland-style deformation to foreland-style deformation.

## Statement of Co-Authorship

This thesis and the manuscripts presented herein are my own work. My supervisor, L. Godin, is a co-author on chapters 2-4 for which he provided scientific direction, rigourous discussion, and editorial guidance. Chapter 3 is co-authored by W.J. Davis and D.W. Davis who contributed to the study through laboratory expertise, scientific method accounts, and editorial direction. Chapter 4 is co-authored with R.A. Price who provided conceptual discussion and editorial assistance.

# Acknowledgements

It is with great pleasure that I am able to acknowledge the people who have contributed so profoundly to my life over the past number of years. Firstly, I would like to thank Dr. Laurent Godin for the opportunity to work on the project that has evolved into this dissertation. His insight, challenges, patience, and friendship are greatly appreciated. I am also indebted to Dr. Ray Price for the chance to come to Queen's and for the mentoring role he continues to occupy for my scientific career. He has provided me with copious books to read and things to think about. My development as a structural geologist owes much to Dr. Stephen Johnston and my understanding of the Himalaya has benefited through discussion and interaction with Drs. Rick Law and Mike Searle. The U-Pb geochronology presented in this dissertation is the result of collaboration with Dr. Bill Davis and his co-workers at the SHRIMP II laboratory at the Geological Survey of Canada and Dr. Don Davis and the staff of the Jack Satterly Geochronology laboratory at the University of Toronto. Thermochronologic analyses, conducted in the Queen's University $^{40}Ar/^{39}Ar$ laboratory, reflect the tutelage of Dr. Doug Archibald. Peter Jones provided electron microprobe support at Carleton University.

Financial support for this thesis has been gratefully received through a Natural Sciences and Engineering Research Council (NSERC) Discovery Grant to L. Godin, an NSERC PhD Canada Graduate Scholarship, a Geological Society of America Student Research Grant, and Queen's University Doctoral Travel Grant.

My time in the Department of Geological Sciences and Geological Engineering at Queen's University has been marked by a number of friends to whom I remain beholden for discussions on everything from science to fine scotch. While many are worthy of thanks, the most influential of those folks remain John Rivers, Dawn Kellett, and Drew Brenders. I would be remiss to forget to mention my family, both immediate and gained through law, who have all been exceedingly supportive and accommodating.

Finally, I would like to thank my wife Alicia whose patience with an often absent (and certainly absent minded) husband has made this thesis possible.

## Table of Contents

# List of Figures

# List of Tables

# Chapter 1

# The Himalaya-Karakoram-Tibet orogen

## 1.1 Background

The Himalaya-Karakoram mountain chain and adjacent Tibetan plateau are the physiographic expressions (Figure 1.1A) of the continued convergence between India and Asia, which began between 55-50 million years ago (Figure 1.2A, B; e.g. Green et al., 2008). The bulk of the Himalaya and adjacent southern Tibet comprises variably metamorphosed and deformed sedimentary rocks that were deposited as part of a southward tapering supracrustal sedimentary wedge on the northern paleo-passive margin of India (Figures 1.1B, 1.2A; Searle et al., 1987). Those rocks were deformed and detached from the Indian craton during collision with Asia and now comprise three distinct tectonostratigraphic domains that can be followed along the entire >2000 km length of the Himalayan arc (Figure 1.1B). From north to south at the longitude of central Nepal (~84˚E; Figure 1.1B), these domains include: (1) the Tethyan sedimentary sequence, a Cambrian to Cretaceous succession of unmetamorphosed sedimentary rocks, (2) the Greater Himalayan sequence, the exhumed mid-crustal infrastructure of the orogen, which comprises a gently north-dipping homoclinal slab bounded on top and below by opposite-sense shear zones, the top-to-the-north sense South Tibetan detachment system and the top-to-the-south sense Main Central thrust, respectively (Burchfiel and Royden, 1985; Burchfiel et al., 1992; Hodges, 2000; Figure 1.1B), and (3) the Lesser Himalayan sequence, which consists of low-metamorphic grade Proterozoic sedimentary rocks.

The Himalaya records evidence of at least two distinct metamorphic events since the onset of continent-continent collision. The oldest phase, dubbed Eohimalayan (Vannay and Hodges, 1996) is associated with crustal thickening (Figure 1.2C) and is characterized by high pressure and moderate temperature metamorphic conditions. The vertical thickening of the crust

**Figure 1.1**
A) Shaded relief map of the Himalaya-Karakoram-Tibet orogen. Black rectangle outlines the region shown in B. B) Simplified geologic map of the Himalayan-Karakoram arc and adjacent Tibet. Field areas investigated as part of this thesis include the Dhaulagiri, Manaslu, and Changgo regions. Black rectangle outlines the region shown in C. C) Geologic map of the study area for this thesis. Figures are modified from Searle et al., 2008.

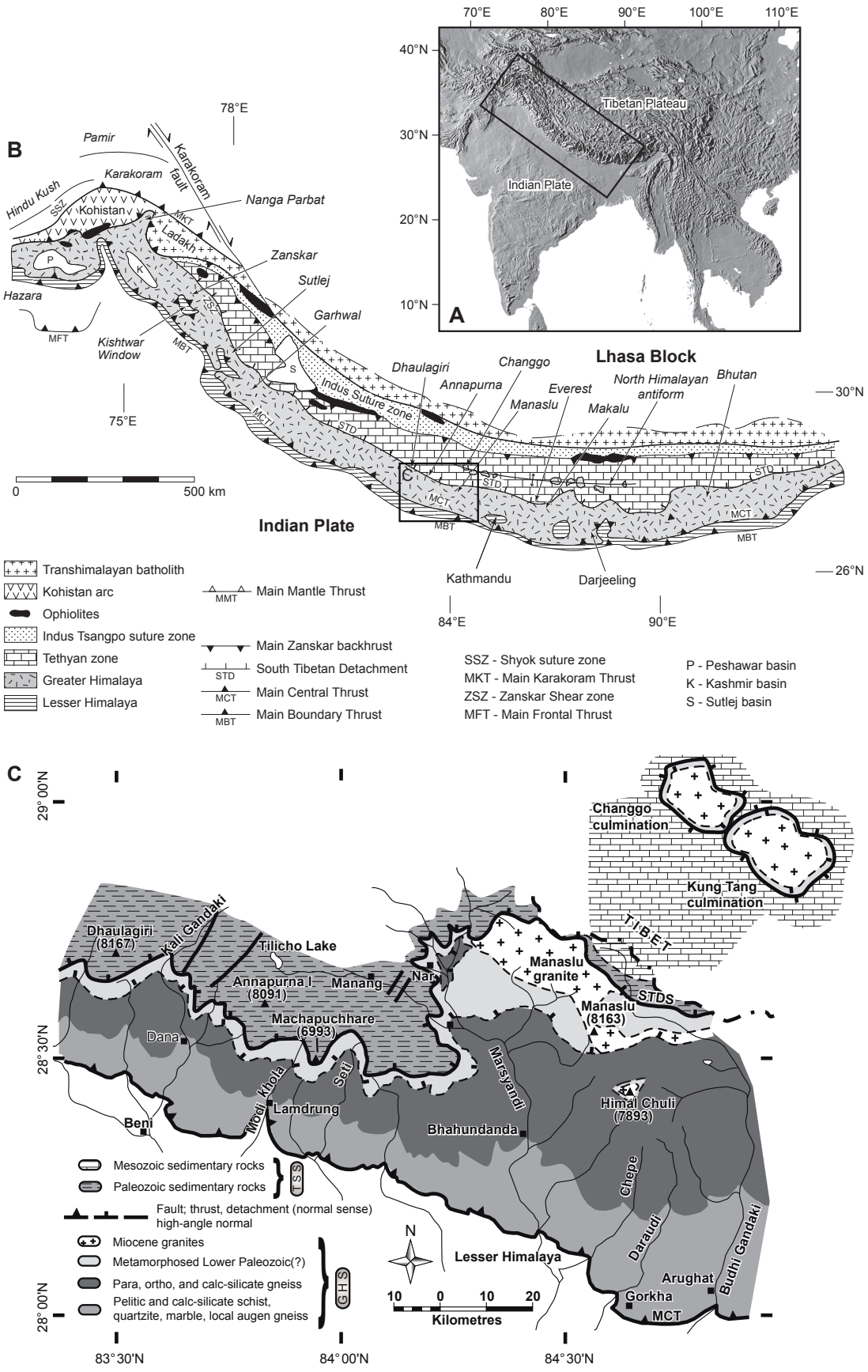
A
B
C
70°E
80°E
90°E
100°E
110°E
40°N
30°N
20°N
10°N
Tibetan Plateau
Indian Plate
78°E
75°E
Pamir
Karakoram
Karakoram fault
Hindu Kush
SSZ
Kohistan
MKT
Ladakh
Nanga Parbat
Zanskar
Sutlej
Garhwal
Hazara
MFT
Kishtwar Window
MBT
ZSZ
S
Indus Suture zone
MCT
STD
Lhasa Block
Dhaulagiri
Annapurna
Changgo
Manaslu
Everest
Makalu
North Himalayan antiform
Bhutan
30°N
26°N
0
500 km
Indian Plate
Kathmandu
Darjeeling
84°E
90°E
Transhimalayan batholith
Kohistan arc
Ophiolites
Indus Tsangpo suture zone
Tethyan zone
Greater Himalaya
Lesser Himalaya
MMT
Main Mantle Thrust
Main Zanskar backhrust
South Tibetan Detachment
Main Central Thrust
Main Boundary Thrust
SSZ - Shyok suture zone
MKT - Main Karakoram Thrust
ZSZ - Zanskar Shear zone
MFT - Main Frontal Thrust
P - Peshawar basin
K - Kashmir basin
S - Sutlej basin
29° 00'N
28° 30'N
28° 00'N
83° 30'N
84° 00'N
84° 30'N
Changgo culmination
Kung Tang culmination
TIBET
Dhaulagiri (8167)
Kali Gandaki
Tilicho Lake
Annapurna I (8091)
Manang
Nar
Manaslu granite
STDS
Manaslu (8163)
Machapuchhare (6993)
Dana
Marsyandi
Seti
Modi Khola
Lamdrung
Beni
Bhahundanda
Himal Chuli (7893)
Chepe
Daraudi
Budhi Gandaki
Arughat
Gorkha
MCT
Lesser Himalaya
N
10 0 10 20
Kilometres
Mesozoic sedimentary rocks
Paleozoic sedimentary rocks
TSS
Fault; thrust, detachment (normal sense) high-angle normal
Miocene granites
Metamorphosed Lower Paleozoic(?)
Para, ortho, and calc-silicate gneiss
Pelitic and calc-silicate schist, quartzite, marble, local augen gneiss
GHS

at this time is recorded as cylindrical folding within the Tethyan sedimentary sequence with a steeply north-dipping, but locally south-dipping, axial planar cleavage (Godin et al., 2001; Kellett and Godin, 2009). U-Pb monazite and zircon ages from kyanite-bearing leucosomes in the Greater Himalayan sequence, which are interpreted to have formed as a consequence of Eohimalayan crustal thickening (Figure 1.2C), indicate that the melt crystallized at ~35 Ma (Godin et al., 2001). Eohimalayan-age leucosomes are also observed within tectonic windows along the North Himalayan antiform (Figure 1.1B) in Tibet (Lee and Whitehouse, 2007; Chapter 3 of this thesis). Interpretations of regional seismic reflection data connect the Greater Himalayan sequence through the subsurface with the granite and/or gneiss-cored culminations that crop-out along the North Himalayan antiform (Hauck et al. 1998). These interpretations are supported by geochemical data that also indicate a link between rocks exhumed within the North Himalayan antiform and those which comprise the Greater Himalayan sequence in the frontal Himalaya (Zhang et al., 2004). Lee and Whitehouse (2007) interpreted the 35.0 ± 0.8 Ma U-Pb date for anatectite they collected from the Mabja Dome in southern Tibet to record the onset of southward ductile lateral flow of the mid-crust. Implicit in their interpretation is that the crust must be over-thickened by this time.

The exhumed Himalayan mid-crust also records isothermal decompression during the Miocene; the Neohimalayan event (Vannay and Hodges, 1996). It has been suggested that the decompression of the mid-crust was associated with the production of anatectite within paragneiss and orthogneiss of the Greater Himalayan sequence (Harris and Massey, 1994; Harris et al., 2004), which coalesced locally along the Himalayan arc to form large leucogranite plutons (e.g. Manaslu pluton; Searle and Godin, 2003). U-Pb zircon and monazite crystallization ages of

---

**Figure 1.2**
Diagrammatic illustration of the Indian-Asian collision. A) Northward movement of India relative to Asia facilitated by the subduction of oceanic crust beneath Asia resulting in the formation of the Transhimalayan batholith complex. B) The closing of the Tethys ocean and the onset of continent-continent collision preceded by ophiolite obduction; waning stages of volcanism related to subduction. C) Initial deformation of Indian plate rocks. This corresponds to the Eohimalayan event and is characterized by fold thickening of the former Indian passive margin succession and the local development of kyanite-grade granitic melt (dark, feathered ellipse). D) The Neohimlayan event, which is marked by contemporaneous movement on the South Tibetan detachment system and Main Central thrust and voluminous decompressional leucogranite melt production (shown as dark grey material between the Main Central thrust, MCT, and South Tibetan detachment system, STDS).

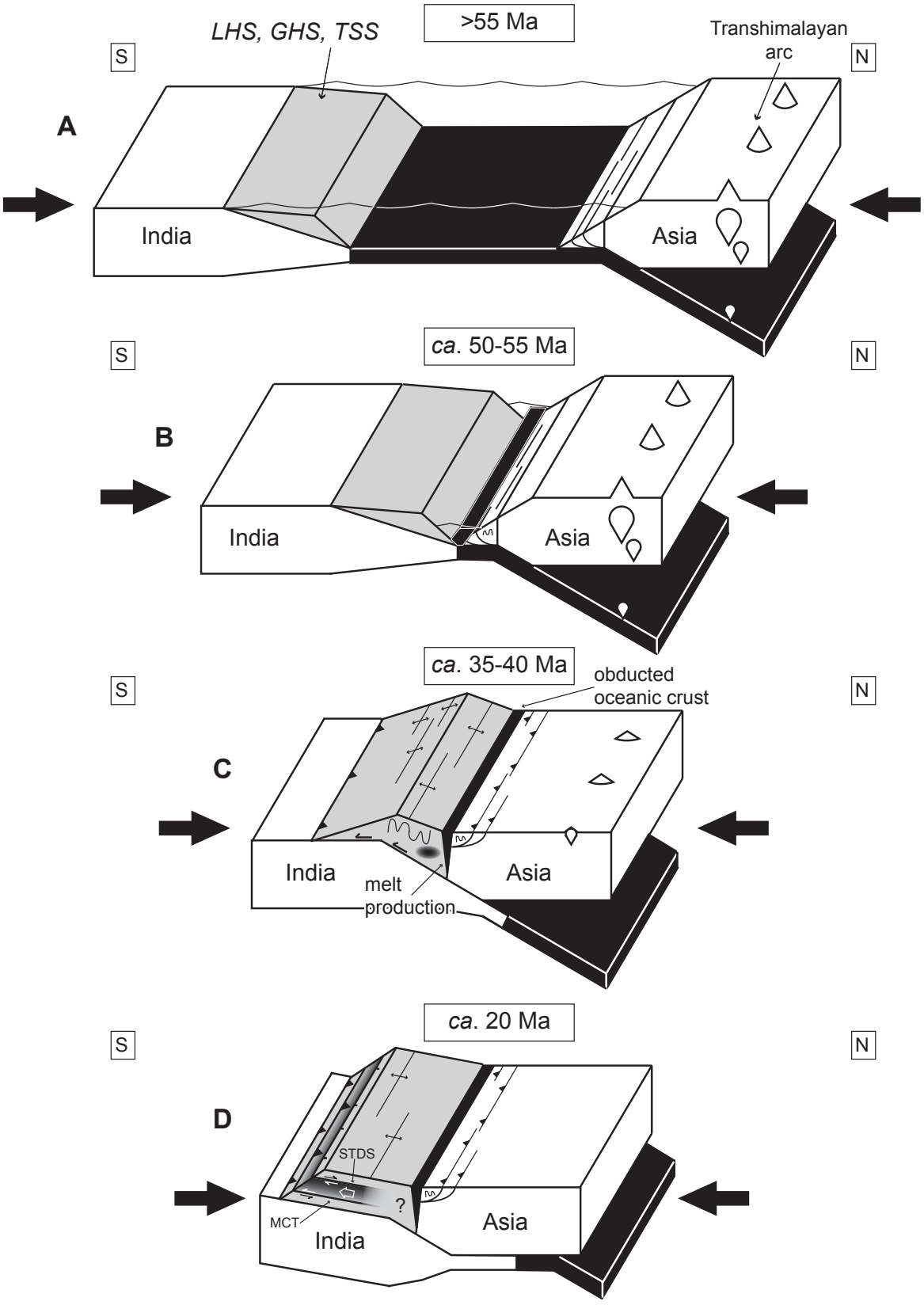
A
>55 Ma
LHS, GHS, TSS
Transhimalayan
arc
S
N
India
Asia
B
ca. 50-55 Ma
S
N
India
Asia
C
ca. 35-40 Ma
obducted
oceanic crust
S
N
India
melt
production
Asia
D
ca. 20 Ma
S
N
STDS
MCT
?
India
Asia

leucosomes that are interpreted to have formed during the Neohimalayan event are generally early Miocene in age *(ca*. 19-24 Ma; Godin et al., 2006a). The decompression of the mid-crust at this time may be associated with a change from subduction of the Indian lithosphere beneath Asia to under-plating of Indian crust beneath Asia (Figure 1.2D; Hetényi, 2007). The Neohimalayan event is contemporaneous with coupled, but opposite shear sense, displacement across the Main Central thrust and South Tibetan detachment system that effectively extruded the Greater Himalayan sequence laterally over India from beneath Tibet.

The processes that facilitated the southward lateral translation of the Greater Himalayan sequence is one of the most contentious issues in Himalayan geology and presently in tectonics in general (e.g. Law et al., 2006). Current prevailing end-member theories include: (1) channel flow, in which the mid-crust (i.e. the Greater Himalayan sequence) is significantly less viscous than both the upper and lower crust that bounds it. In this model the mid-crust flows laterally, in response to the lithostatic pressure gradient between the over-thickened crust beneath Tibet and thinner crust beneath India, toward a rapidly eroding southern boundary (Figure 1.3A: Bird, 1991; Grujic et al., 1996; Beaumont et al., 2001; 2004; 2006), or (2) critical taper wedge, in which the Greater Himalayan sequence was translated and strained in the hanging wall of a thrust fault that propagated as part of foreland-style thrust and fold belt governed by critical taper theory (Figure 1.3B; DeCelles et al., 2001; Robinson et al., 2003; Pearson and DeCelles, 2005; Kohn 2008; McQuarrie et al. 2008; Robinson, 2008).

A contributing factor to the disagreement surrounding the evolution of the Greater Himalayan sequence has been a lack of consensus of the nature, position, and characteristics of the Main Central thrust (Figure 1.1B). The Main Central thrust was originally defined by Heim & Gansser (1939) and Gansser (1964) as the thrust fault that places high-grade metamorphic rocks of the Greater Himalayan sequence southward over low-grade rocks of the Lesser Himalayan sequence. The terms Greater Himalayan sequence and Lesser Himalayan sequence, however, are structural terms that refer to fault-bounded tectonostratigraphic domains, not to lithostratigraphic domains (Searle et al., 2008). If a fault that bounds a domains cuts up or down section along or across strike it will juxtapose different rocks on either side and, as such, may make the structure difficult to correlate along the orogen. As noted by Searle et al., (2008):

Previous attempts to map the Main Central thrust have used

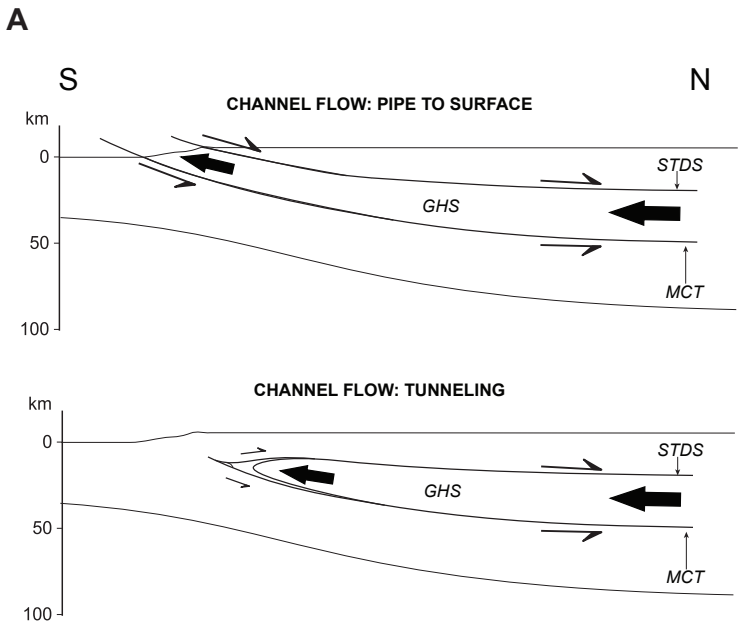


***Channel flow*** - Contemporaneous motion along the Main Central thrust and South Tibetan detachment system extrudes the mid-crust southwards. In the typical channel flow model focused erosion exhumes the mid-crust to the surface as it is extruded creating a 'pipe to the surface' from the mid-crust (Beaumont et al., 2001). If the extruded mid-crust remains below the surface, however, it is considered tunneling (Beaumont et al., 2004).

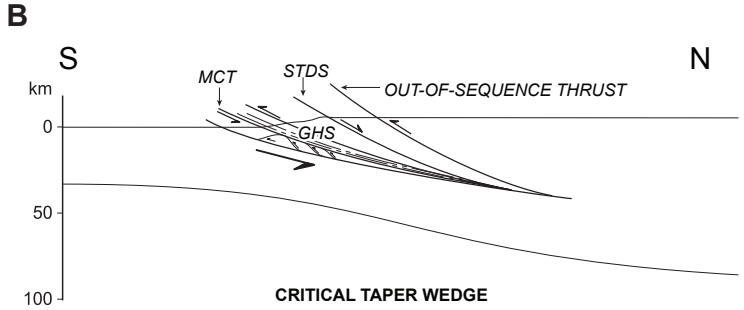


***Critical taper wedge*** - Gravitational spreading of the orogenic wedge governed by the strength of the basal detachment and the wedge material, and the focus and intensity of erosion. The wedge spreads laterally through thrust propagation. The STDS may form as result of collapse near the back of the wedge (Robinson, 2008) or it may represent a roof thrust (Webb et al., 2007).

**Figure 1.3**
The two end-member models for the evolution of the Himalaya. A) Channel flow; B) Critical taper wedge. See text for discussion. STDS, South Tibetan detachment system; MCT, Main Central thrust.

indirect methods such as: (1) a lithological contrast following a distinctive quartzite unit beneath an orthogneiss unit (e.g. Gansser 1983; Daniel et al., 2003); (2) following the kyanite isograd (e.g. Bordet, 1961; LeFort, 1975; Colchen et al., 1986); (3) differences in U-Pb detrital zircon ages (e.g. Parrish and Hodges, 1996; Ahmad et al., 2000; DeCelles et al., 2000); (4) differences in Nd isotope compositions (e.g. Robinson et al., 2001; Martin et al., 2005; Richards et al., 2005, 2006); (5) location of young U-Pb and Th-Pb monazite ages (e.g. Harrison et al., 1997; Catlos et al., 2001, 2002). None of these methods in themselves can be used independently to define a thrust fault. Lithology, detrital zircon ages and Nd isotopes give information on stratigraphy, not structural relationships. Isograds and monazite ages give information on metamorphic reactions, fluids, and timing of mineral growth, not structure.

Because of the confusion surrounding the location of the Main Central thrust there is uncertainty with respect to whether rocks are part of the Lesser Himalayan sequence or Greater Himalayan sequence along the Himalaya (i.e. whether they are in the hanging wall or footwall of the fault; e.g. Parrish and Hodges, 1996; Martin et al., 2005; Chambers et al., 2007; Caddick et al., 2007). The interpretations and implications of published data from various rock specimens thought to be from the Lesser Himalayan sequence change significantly if those specimens are actually from the hanging wall of the Main Central thrust and part of the Greater Himalayan sequence. Data that may have been incompatible with a specific model as part of the footwall of the Main Central thrust may be entirely compatible with it as part of the hanging wall. As such, elucidating the location and characteristics of the Main Central thrust, and therefore the transition between the Lesser Himalayan sequence and Greater Himalayan sequence, is critical to constrain the evolution of the Himalayan-Tibetan orogen.

## 1.2 This Study

The ultimate goal of this project is to contribute scientifically to our understanding of how mountain belts form. More specifically this study aims to elucidate the complex processes that have created the Himalaya by addressing the questions: 1) What are the kinematic characteristics (i.e. structural framework, deformation history) of the Greater Himalayan sequence? and 2) By what process(es) has the Greater Himalayan sequence been exhumed from mid-crustal depths and translated laterally from beneath the Tibetan plateau?

The answers to those questions have been formulated (as described in Chapters 2, 3, and 4) through detailed mapping of lithology and geologic structures in the Kali Gandaki valley in the Dhaulagiri-Annapurna Himalaya, the Budhi Gandaki and Daraudi valleys in the Manaslu-Himal Chuli Himalaya in Nepal, and in the Changgo culmination in the Gyrong region of south-central Tibet (Figure 1.1C). The resultant detailed geological maps serve as the framework around which interpretations of both new and previously published analytical data can be based. Fieldwork was carried out over six months during four field seasons, two conducted in Nepal and two carried out in Tibet, between Fall 2004 and Spring 2006. Specimens were collected during mapping to both construct a representative suite of rocks for each map-area and to conduct subsequent laboratory analyses. The analyses carried out as part of this study included microstructural investigation of mean kinematic vorticity (in porphyroclast-bearing ductilely deformed rocks) and lattice preferred orientation in quartz (in quartzite and/or quartz-rich schist, gneiss, or granitic rocks), U-Pb geochronology via isotope-dilution thermal ionization mass spectroscopy (ID-TIMS) and sensitive high-resolution ion microprobe (SHRIMP) techniques (on zircon and monazite separates from igneous intrusive rocks), laser step-heating $^{40}Ar/^{39}Ar$ thermochronology (on muscovite and/or biotite separates from mica-bearing rocks), and paleogeothermobarometric estimates based on chemical data from electron microprobe spot analyses (in garnet-biotite-plagioclase±alumniosilicate rocks). The results and interpretation of these analyses have not only contributed significantly to the quantitative geologic database of the central Himalaya and provided important constraints on the evolution of central Nepal and adjacent Tibet, but also have orogen-wide implications as outlined in chapters 2, 3 and 4.

The results of my research are presented as three stand-alone manuscripts, which comprise chapters 2, 3, and 4. Chapter 2, which has been published in the ***Journal of the Geological Society, London*** (Larson and Godin, 2009), describes the geology and kinematics of the Greater Himalayan sequence in the Dhaulagiri Himalaya as exposed along the Kali Gandaki river valley, central Nepal. Chapter 3 presents the results of geologic mapping, U-Pb geochronology, $^{40}Ar/^{39}Ar$ thermochronology, and kinematic analysis of the Greater Himalayan sequence, the South Tibetan detachment system, and Tethyan sedimentary sequence rocks that crop out in the Changgo culmination, south-central Tibet and discusses the orogen-wide implications of these data. Chapter 3 has been submitted to ***Tectonics*** for peer-review. Chapter 4

outlines the geology of the Budhi Gandaki and Dauradi river valleys in the Manaslu-Himal Chuli Himalaya as mapped during this study. Chapter 4 also presents new paleogeothermobarometric estimates, kinematic analyses, and $^{40}Ar/^{39}Ar$ thermochronology for Greater Himalayan sequence rock specimens collected during mapping. The implications of the new geologic map and analytical data are discussed and later incorporated with data from chapters 2 and 3 to form the basis for a new conceptual model for the evolution of the Himalayan-Tibetan orogen. Chapter 4 has been submitted to the ***Geological Society of America Bulletin*** for peer review and publication.

# Chapter 2

# Kinematics of the Greater Himalayan sequence, Dhaulagiri Himal: implications for the structural framework of central Nepal

## 2.1 Abstract

In the Dhaulagiri region of central Nepal quartz-rich specimens collected from the Greater Himalayan sequence yield well-defined quartz *c*-axis fabrics with a dominant top-to-the-southwest sense of shear. These fabrics reflect pervasive crystal-plastic deformation extending more than 8 km structurally below previously mapped locations of the Main Central thrust fault. Quartz *c*-axis fabric opening angles suggest deformation temperatures of c.500 ± 50 °C within the lower portion of the Greater Himalayan sequence and up to c.670 ± 50°C within the migmatitic upper portion. These temperatures generally plot within error of garnet-biotite temperature estimates for metamorphic assemblages and are interpreted to reflect Cenozoic deformation during extrusion of the mid-crust. The quartz *c*-axis data, and a new detailed tectonostratigraphic map, constrain the position of the Ramgarh thrust in the Dhaulagiri region to be coincident with the Main Central thrust at the base of the pervasively deformed exhumed mid-crustal core. Mean kinematic vorticity numbers ($W_m$) measured in specimens collected from the lower portion of the Greater Himalayan sequence range between 0.49 and 0.80 (*c*.66-41% pure shear) with an average value of 0.67 (*c*.53% pure shear). These data indicate that extrusion of the mid-crust was facilitated by a significant component of pure shear strain.

## 2.2 Introduction

Recently proposed hypotheses of gravitationally-driven mid-crustal lateral flow have influenced the direction of research on orogens (e.g., Grujic et al., 1996, 2002; Beaumont et al., 2001, 2004; Jamieson et al., 2004; White et al., 2004; Searle and Szulc, 2005; Williams and Jiang, 2005; Law et al., 2006 [and references therein]; Lee and Whitehouse, 2007). In the Himalaya, where the concept of mid-crustal flow has largely been developed (Nelson et al., 1996; Grujic et al., 1996; Beaumont et al., 2001), the exhumed migmatitic mid-crustal rocks of the Greater Himalayan sequence have been interpreted to represent a formerly-ductile mid-crustal layer

that was extruded laterally from beneath the Tibetan plateau above the Main Central thrust fault (MCT) and below the South Tibetan detachment system (STDS).

The Greater Himalayan sequence is characterized by greenschist to granulite-grade metamorphism and associated anatectic melt. It is separated from the structurally-overlying unmetamorphosed Tethyan sedimentary sequence by the South Tibetan detachment system, a network of top-to-the-north-sense faults that is mapped along the length of the orogen (Figure 2.1A; Burchfiel et al., 1992). Along its base, the Greater Himalayan sequence is thrust over unmetamorphosed to low grade metamorphic rocks of the Lesser Himalayan sequence across the top-to-the-south-sense MCT (Figure 2.1B). Contemporaneous Miocene displacement along the top-to-the-north sense STDS and the top-to-the-south sense MCT (see review of age constraints in Godin et al., 2006a) extruded the Greater Himalayan sequence from beneath the Tibetan plateau and facilitated its intrusion into the rapidly eroding Himalaya during the Miocene. While the general concept of this extrusive mid-crustal flow has been applied to various orogens (e.g., Law et al., 2006), the processes involved have been the subject of numerous orogen-scale thermal-mechanical, numerical, and structural models (Burchfiel et al., 1992; Grujic et al., 1996, 2002; Grasemann et al., 1999; Vannay and Grasemann, 2001; Beaumont et al., 2001, 2004; Robinson et al., 2003; Bollinger et al., 2006; Kohn, 2008).

Recent research on kinematics in the Himalaya has focused on analysis near the top of the Greater Himalayan sequence and within the STDS (Law et al., 2004, Jessup et al., 2006), near the centre of the Greater Himalayan sequence (see following discussion on the position of the MCT; Grasemann et al., 1999; Martin et al., 2005; Carosi et al., 2006), and near its base (Jessup et al., 2006; Carosi et al., 2007; Figure 2.1A). These studies provide critically important empirical data that describe the kinematics of extrusive flow within the orogen and provide constraints within which more refined models can be developed.

One of the most fundamental challenges for the interpretation of kinematics within the Greater Himalayan sequence is identifying and locating the bounding shear zones. Whether a specimen is collected from the base of the mid-crustal slab or the middle depends upon where these shear zones are mapped. For example, the nature and location of the MCT is the subject of considerable debate (e.g., Searle et al., 2008), one that has been complicated in central Nepal by recent studies of the Ramgarh thrust (Figure 2.1B; Pearson and DeCelles, 2005; Robinson et al.,

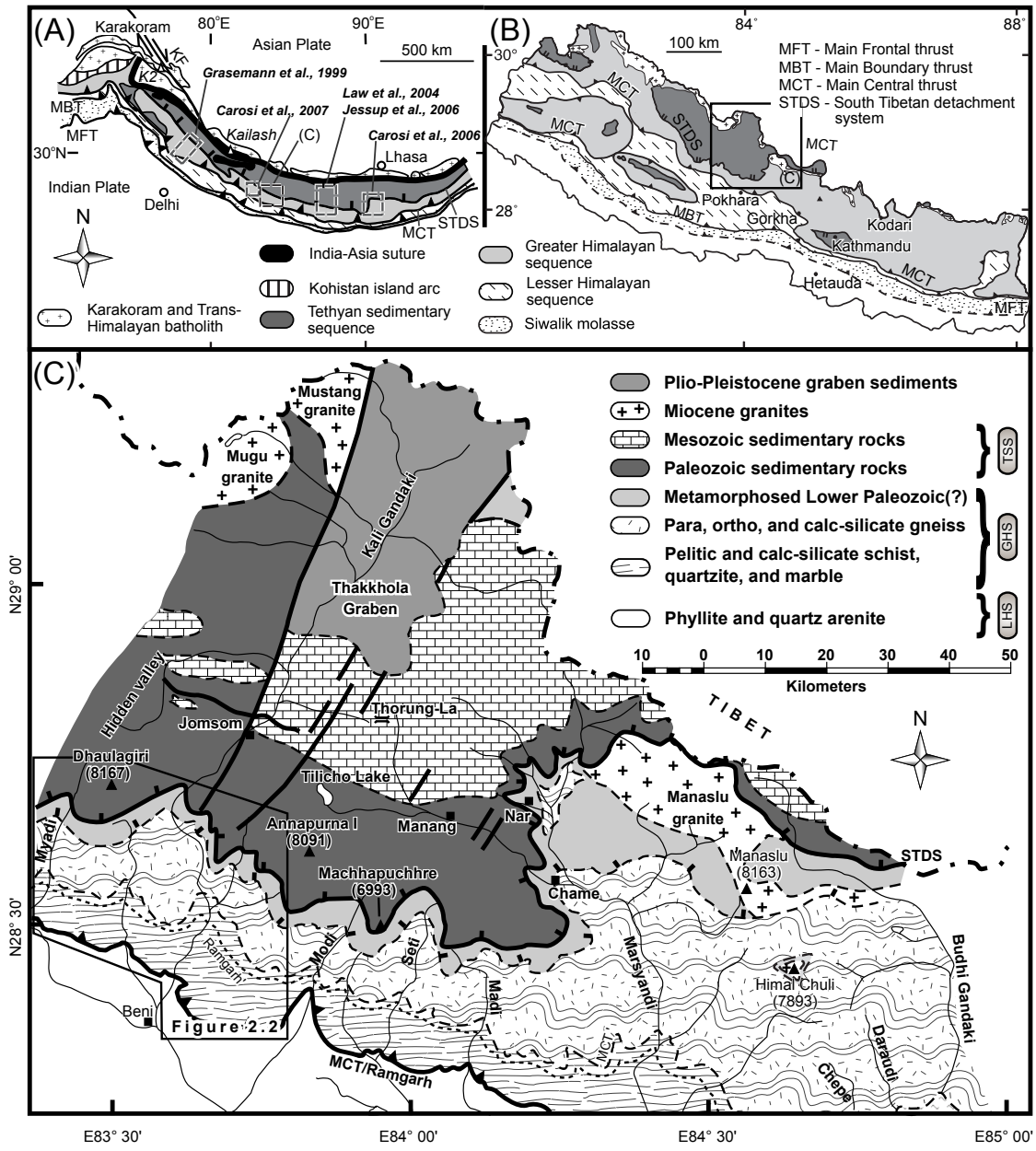


**Figure 2.1**
(A) Simplified tectonostratigraphic map of Himalaya-Karakoram system and adjacent Tibet (Modified after Searle et al., 1987). Principle faults include the South Tibetan detachment system (STDS), the Main Central thrust zone (MCT), Main Boundary thrust (MBT), Main Frontal thrust (MFT), and the Karakoram fault (KF). (B) Regional geologic map of Nepal (modified after Robinson et al., 2001 and Pearson and DeCelles 2005). Note the mapped trace of the Ramgarh thrust is coincident with the MCT. (C) Geological map of central Nepal (modified from Colchen et al., (1986) and Searle and Godin 2003) portraying the location of the study area as shown in Figure 2.2. The previously mapped positions of both the Ramgarh thrust and MCT are shown by labeled dashed lines. TSS, Tethyan sedimentary sequence; GHS, Greater Himalayan sequence; LHS, Lesser Himalayan sequence. For the location of C, see A and B.

2006). Locating and structurally documenting the position of the MCT and the Ramgarh thrust is critical in providing constraints on lower boundary conditions and kinematics during the extrusion and southward transport of the Greater Himalayan sequence. Consistency with respect to how key tectonic boundaries, such as the MCT, are recognized is essential for comparing data from different studies along the Himalaya.

In this paper we present the results of geologic mapping transects that extend across the Greater Himalayan sequence in the Kali Gandaki and Myadi valleys of central Nepal (Figure 2.1C). Field observations are augmented by microstructural analyses of oriented specimens, which provide new insight on strain, temperature of deformation, and vorticity. These data help constrain the kinematics of the Greater Himalayan sequence and its lower bounding shear zone in central Nepal and add significantly to the kinematic database on extruded mid-crustal material. Furthermore, this study, which reinterprets the position of both the Ramgarh thrust fault and the MCT, has direct implication for the structural framework of the orogen.

## 2.3 The Main Central thrust

The contact between the Lesser Himalayan sequence and the Greater Himalayan sequence is one of the most controversial tectonic features in the Himalayan-Tibetan orogen. In this study we follow the Searle et al., (2008) definition (after Gansser, 1964) of the Greater Himalayan sequence as comprising all material above the MCT. A discontinuity, subsequently interpreted to be between the Greater Himalayan sequence and the Lesser Himalayan sequence, was recognized by Heim and Gansser (1939) during reconnaissance fieldwork in northwestern India. In their report, they describe a change from an upper greenschist-grade meta-limestone and minor phyllitic schist to a gently north-dipping amphibolite-grade paragneiss and surmised that this juxtaposition was the result of a north-dipping, top-to-the-south sense thrust fault (Heim and Gansser, 1939). This inferred fault later became known as the MCT, a shear zone that has been drawn along the entire >2500 km east-west length of the orogen (Le Fort, 1975). Exactly how the MCT is identified in different localities, however, varies considerably. Some researchers have adhered to the original definition and mapped the MCT based on the juxtaposition of different rock types (e.g., Colchen et al., 1986; Vannay and Hodges, 1996; Kohn et al., 2001; Pearson and DeCelles, 2005; Robinson et al., 2006), which commonly coincides with the kyanite isograd in the

exhumed mid-crustal core (e.g., Bordet, 1961; Colchen et al., 1986). In other studies, however, the MCT has been described as a zone of penetrative deformation bounded by interpreted upper and lower limits (e.g., Arita, 1983; Pêcher, 1989; Grasemann et al., 1999; Bhattacharya and Weber, 2004; Martin et al., 2005). The upper boundary of the shear zone is commonly coincident with the Heim and Gansser (1939) defined MCT, while the lower boundary is placed at the interpreted lower or southern limit of MCT-related strain (Arita, 1983; Searle and Godin, 2003; Bhattacharya and Weber, 2004).

In a recent re-examination of the MCT fault conundrum, Searle et al., (2008) recognize a thick zone of penetrative south-verging deformation extending below the migmatitic portion of the high-grade slab, and map the MCT at the base of this shear zone. Rocks above their interpreted MCT are defined as part of the Greater Himalayan sequence and are characterized by an inverted Cenozoic greenschist-to upper amphibolite-grade metamorphic field gradient and pervasively developed, south-verging ductile deformation (Searle et al., 2008). This contrasts with rocks below the MCT, which are by definition part of the Lesser Himalayan sequence, and preserve sedimentary structures such as cross-bedding and ripples, contain abundant detrital clasts, and are characterized by large-scale south-verging folding, brittle faulting, and multiple cleavages. This interpretation of the MCT satisfies metamorphic temperature and pressure data that show little-to-no break across the original Heim and Gansser (1939) discontinuity (e.g., Hubbard, 1989; Macfarlane, 1995; Vannay and Hodges, 1996; Fraser et al., 2000; Kohn et al., 2001) and agrees with studies that have interpreted the contact between the previously defined Greater Himalayan sequence and Lesser Himalayan sequence as an unconformity (Goscombe et al., 2006; Searle et al., 2006) characterized by an isotopically-defined change in lithology (e.g., Martin et al., 2005).

## 2.4 Geology of the Dhaulagiri Himalaya

The Dhaulagiri Himalaya and its environs have long been the subject of geologic research. Early stratigraphic work by Fuchs (1964), Bordet et al., (1971), and Bodenhausen and Egeler (1971) was built upon by subsequent metamorphic, structural, and geochronologic studies (e.g., Pêcher, 1978, 1989; Colchen et al., 1986; LeFort et al., 1986; Brown and Nazarchuk, 1993; Vannay and Hodges, 1996; Godin et al., 1999a, 1999b, 2001; Godin, 2003; Godin et al., 2007).

The wealth of data resulting from the preceding studies provides a detailed geologic background within which to place the current study.

The southern Dhaulagiri Himalaya is broadly divisible into three tectonostratigraphic units (Figures 2.1B, 2.1C, 2.2). From north to south these include: 1) the unmetamorphosed Tethyan sedimentary sequence, 2) the structurally underlying greenschist-to amphibolite-grade Greater Himalayan sequence, which is separated from the Tethyan sedimentary sequence by the STDS, and 3) the unmetamorphosed to low-metamorphic grade rocks of the Lesser Himalayan sequence, which are overthrust by the Greater Himalayan sequence across the MCT.

### 2.4.1 Tethyan Sedimentary sequence

The Tethyan sedimentary sequence consists of a southward-tapering wedge of supracrustal passive margin sedimentary strata scraped off the under-riding northern margin of the Indian craton during its collision with Asia (Searle et al., 1987). In the Dhaulagiri Himalaya, the Tethyan sedimentary sequence consists of unmetamorphosed-to-low-grade limestone, marly limestone, quartz arenite, lithic sandstone, shale, and calcareous psammite that range in age from Cambro-Ordovician to Cretaceous (Fuchs, 1967; Bordet et al., 1971; Godin, 2003; Kellett and Godin, 2009). The structure of the Tethyan sedimentary sequence is dominated by large, north-verging folds with associated south-dipping cleavage that are interpreted to have formed either during Eohimalayan deformation and initial imbrication of the supracrustal northern margin of India (Godin, et al., 1999a), as a result of shear related to top-to-the-north sense Neohimalayan displacement across the STDS (Burchfiel et al., 1992), or due to reorientation during partial coupling with a southward extruding viscous mid-crust (Kellett and Godin, 2009). These folds are transposed at lower structural levels by a moderately north-dipping pervasive foliation related to motion along the STDS (Godin et al., 1999b).

### 2.4.2 South Tibetan detachment system

The STDS, locally comprising the Annapurna detachment (Kali Gandaki valley; Brown

---

**Figure 2.2**
Geologic map of the southern Dhaulagiri Himalaya, central Nepal. Geologic data is predominantly from this study, but is augmented by data from the South Tibetan detachment zone published in Godin et al., (2001). The rectangle outlined by the dashed lines is the location of the detailed map of Figure 2.5. LHS, Lesser Himalayan sequence.

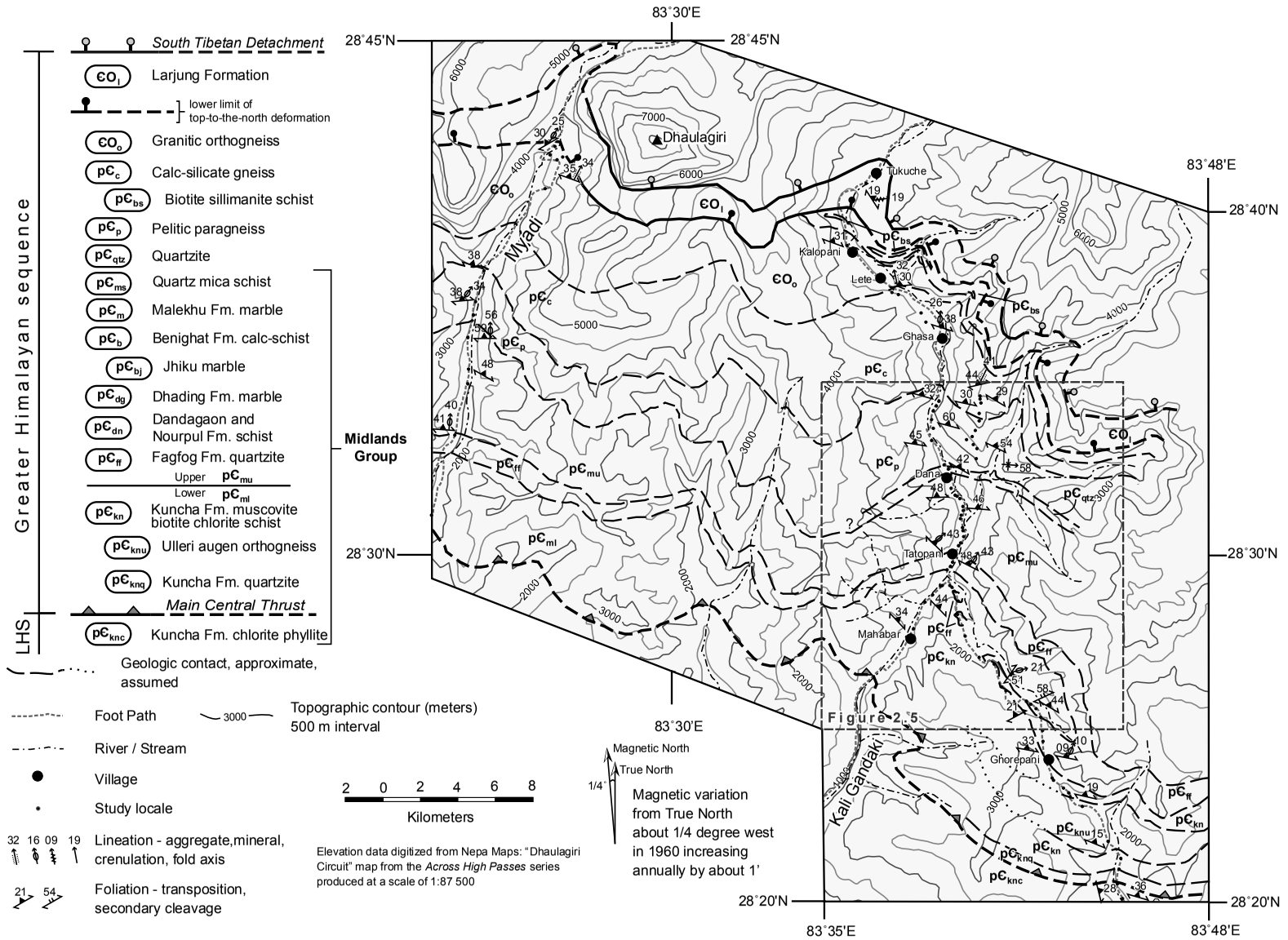
Greater Himalayan sequence
LHS
South Tibetan Detachment
Larjung Formation
lower limit of top-to-the-north deformation
Granitic orthogneiss
Calc-silicate gneiss
Biotite sillimanite schist
Pelitic paragneiss
Quartzite
Quartz mica schist
Malekhu Fm. marble
Benighat Fm. calc-schist
Jhiku marble
Dhading Fm. marble
Dandagaon and Nourpul Fm. schist
Fagfog Fm. quartzite
Upper
Lower
Kuncha Fm. muscovite biotite chlorite schist
Ulleri augen orthogneiss
Kuncha Fm. quartzite
Main Central Thrust
Kuncha Fm. chlorite phyllite
Midlands Group
Geologic contact, approximate, assumed
Foot Path
River / Stream
Village
Study locale
Lineation - aggregate,mineral, crenulation, fold axis
Foliation - transposition, secondary cleavage
Topographic contour (meters) 500 m interval
2 0 2 4 6 8
Kilometers
Elevation data digitized from Nepa Maps: "Dhaulagiri Circuit" map from the Across High Passes series produced at a scale of 1:87 500
Magnetic North
True North
1/4°
Magnetic variation from True North about 1/4 degree west in 1960 increasing annually by about 1'
83°30'E
28°45'N
83°48'E
28°40'N
28°30'N
28°20'N
83°35'E
Dhaulagiri
Tukuche
Kalopani
Lete
Ghasa
Dana
Tatopani
Mahabar
Ghorepani
Myadi
Kali Gandaki
Figure 2.5

and Nazarchuk, 1993; Godin et al., 1999a), the Deurali and Macchapuchhare detachments (Modi valley; Hodges et al., 1996;), and the Chame and Phu detachments (Nar valley; Coleman, 1996; Searle and Godin, 2003; Gleeson and Godin, 2006; Godin et al., 2006b) in central Nepal, crops out in the Daulagiri Himal as a plastic-brittle normal-sense fault that juxtaposes the Tethyan sedimentary sequence in its hanging wall against the Greater Himalayan sequence in its footwall (Brown and Nazarchuk, 1993; Godin et al., 1999b). The STDS is a 1500 m thick high-strain zone that predominantly affects the upper greenschist facies Larjung Formation (Figure 2.2), but also extends structurally downwards in the Greater Himalayan sequence and structurally upwards into the lowermost Tethyan rocks (Godin et al., 1999b; Godin, 2003). The lower boundary of the STDS, comprising the Chame, Annapura, Deurali detachments, was active in central Nepal prior to ~22 Ma (Guillot et al., 1994; Harrison et al., 1995; Hodges et al., 1996; Godin et al., 2001), coincident with motion along the MCT (Godin et al., 2006a). Displacement across the upper boundary of the STDS, the Macchapuchhare and Phu detachments, ceased in central Nepal by ~16 Ma (Godin et al., 2006b).

### 2.4.3 Greater Himalayan sequence

In the southern Dhaulagiri Himalaya, the Greater Himalayan sequence consists of greenschist-to upper amphibolite-grade paragneiss, calc-silicate gneiss, and orthogneiss in which all planar and linear fabric elements are transposed into the penetrative foliation. The Greater Himalayan sequence comprises metamorphosed rocks from Proterozoic and Cambrian supracrustal protoliths that were deposited on the northern Indian passive margin between Mesoproterozoic and lower Paleozoic times (Brookfield, 1993; Parrish and Hodges, 1996). The greenschist-to upper amphibolite-grade Greater Himalayan sequence records a multi-stage, post-initial collision metamorphic history including late-Eocene-to-Oligocene crustal thickening and Barrovian-type metamorphism (Eohimalayan deformation and metamorphism; Hodges et al., 1988; Pêcher, 1989; Godin et al., 2001) followed by higher temperature, but lower pressure, Miocene metamorphism (Neohimalayan deformation and metamorphism; Hodges et al., 1988; Pêcher, 1989) related to lateral extrusion of the mid-crust facilitated by channel flow (Hodges 2006; Searle et al., 2006), tectonic wedging (Webb et al., 2007), or critical taper adjustment (Kohn, 2008). The Lesser Himalayan sequence crops out structurally below the

Greater Himalayan sequence where it comprises little-to-unmetamorphosed sedimentary rocks characterized by macro-scale folding.

Within and subjacent to the STDS, the Greater Himalayan sequence comprises marble and calc-silicate gneiss (Figure 2.2). The calc-silicate gneiss locally contains thin lenses of rusty yellow weathering biotite sillimanite schist (Figure 2.2; Godin et al., 2001). Anatectite-bearing orthogneiss, locally containing feldspar augen, crops out below the calc-silicate. The orthogneiss consists of the assemblage: quartz, K-feldspar, and biotite whereas the anatectite component comprises quartz, k-feldspar, muscovite, garnet, and tourmaline (Figure 2.3A). This unit has been dated as Ordovician in age (Parrish and Hodges 1996; DeCelles et al., 2000; Godin et al., 2001; Gehrels et al., 2003), which is younger than the interpreted Neoproterozoic protolith age of both the paragneiss and calc-silicate gneiss (Parrish and Hodges 1996; DeCelles et al., 2001). The orthogneiss is interpreted to have been intruded during Paleozoic orogenesis on the northern Indian margin (Gehrels et al., 2003) coeval with an Ordovician metamorphic signature preserved locally in nearby pelitic schist (Godin et al., 2001).

Structurally below the orthogneiss is a ~2500 m thick unit of calc-silicate gneiss (Figure 2.2). It is typified by the mineral assemblage: calcite, muscovite, biotite, hornblende, diopside, scapolite, and epidote (Figure 2.3B) and locally contains up to 20% (by volume) leucogranitic anatectite (Figure 2.3C). The base of the calc-silicate gneiss is is characterized by an interleaving with the structurally underlying paragneiss.

Below the calc-silicate gneiss, is a ~1500 m thick unit (Figure 2.2) of quartz, feldspar, muscovite, biotite, garnet, kyanite paragneiss (Figure 2.3D) that includes up to 20% (by volume) leucogranitic anatectite (Figure 2.3E). Analyses of prograde mineral assemblages preserved locally in these rocks suggest they reached 610 ˚C and were metamorphosed at a depth of 35 km as a result of crustal thickening during Eohimalayan deformation (Vannay and Hodges, 1996). The subsequent Neohimalayan metamorphic event, associated with extrusion and decompressional melting of the Greater Himalayan sequence, is preserved as metamorphic mineral assemblages that yield a mean temperature 540 ˚C and equilibrated at a depth of 24 km (Vannay and Hodges, 1996).

The base of the pelitic gneiss is marked by a light grey on weathered and fresh surfaces, 40-50 m thick quartzite unit (Figure 2.2). At the scale of a hand specimen, this quartzite consists

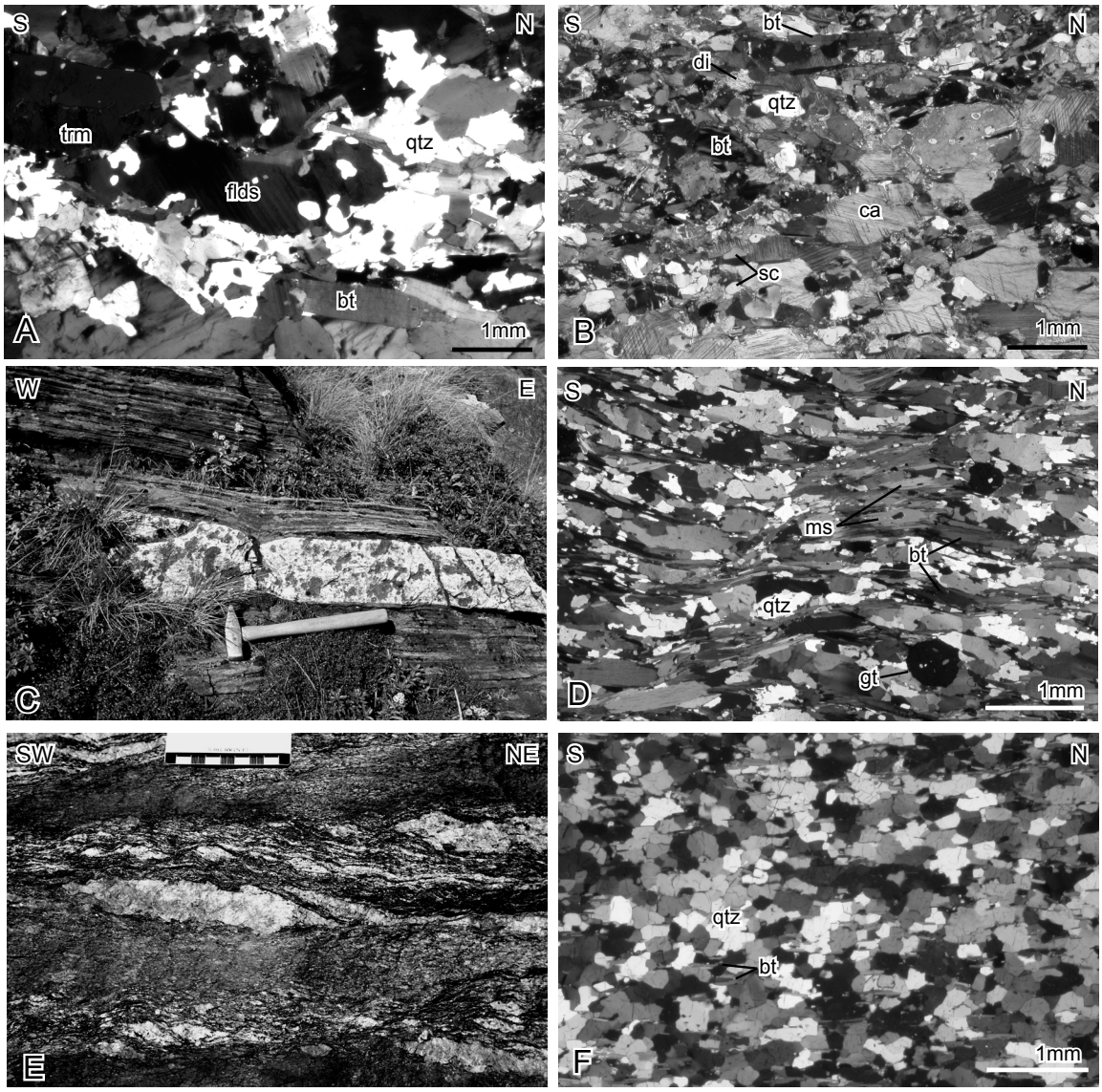


**Figure 2.3**
Greater Himalayan sequence rocks exposed in the Kali Gandaki and Myadi valleys. (A) Photomicrograph of deformed and recrystallized orthogneiss. (B) Photomicrograph of a specimen of calc-silicate gneiss pictured in 3C. (C) View to the north of calc-silicate gneiss with a leucogranitic sill (hammer is approximately 35 cm long). (D) Photomicrograph from the paragneiss in 3B with prominent shear bands indicating top-to-the-south shear. (E) Deformed leucogranite-bearing kyanite paragneiss (scale bar is in cm). (F) Photomicrograph of specimen 015 illustrating its recrystallization texture. Abbreviations are a follows: bt, biotite; ca, calcite; di, diopside; flds, feldspar; gt, garnet; ms, muscovite; qtz, quartz; sc, scapolite; trm, tourmaline.

of ribbon-like lenses of quartz, and it parts along thin biotite-rich layers spaced approximately 4-8 cm apart. In thin section, the quartz displays a polygonal texture and minor subgrains (Figure 2.3F), suggesting it has been entirely recrystallized through a combination of subgrain rotation, grain boundary migration, and grain boundary area reduction. The recrystalized quartz grains have a conspicuous preferred orientation making them suitable for crystallographic preferred orientation analysis (discussed in a following section below).

In this study we follow the Searle et al., (2008) definition of the Greater Himalayan sequence, which includes all rocks in the hanging wall of the MCT. Thus because of our mapped position of the MCT, which is discussed in a later section, units formerly described as part of the informal Lesser Himalayan sequence 'Midlands group' in central Nepal are here reinterpreted to be part of the Greater Himalayan sequence (Figure 2.4A). Equivalents of the Midlands group crop out along the entire length of the Himalayan orogen and different researchers (e.g., Heim and Gansser, 1939; Hashimoto, 1973; Stöcklin, 1980; Srivastava and Mitra, 1996; Paudel and Arita, 2000; Ahmad et al., 2000; DeCelles et al., 2001; DeCelles et al., 2002; Robinson et al., 2006) have applied a variety of different names to laterally-equivalent units. As summarized in Figure 2.4B, correlations made during previous studies (Upreti 1996; DeCelles et al., 2001; Pearson and DeCelles, 2005; Martin et al., 2005) have helped clarify the nomenclature in Nepal. In this paper, we use the unit names originally assigned in central Nepal (Figure 2.4B) and discuss them as part of the informal "Midlands group". Rocks of the Midlands group (Figure 2.4: Bordet et al., 1964; Hashimoto, 1973; Bordet, 1977; Colchen et al., 1986; Hodges et al., 1996; Vannay and Hodges, 1996) have traditionally been separated into upper and lower divisions. Note that in the present study area all of the Midlands group rocks mapped above the MCT are part of the Greater Himalayan sequence and have reached at least greenschist-grade metamorphism. However, for simplicity and continuity with previous studies we will continue to refer to the metamorphic units with their original formation names.

The top of the Midlands group observed in the Kali Gandaki valley comprises a non-calcareous quartz, muscovite, biotite schist that structurally overlies the Malekhu Formation (Figure 2.5), a conspicuous limestone unit characterized by a light yellowish brown weathering surface and a light grey fresh surface. It crops out as well-defined layers locally with thin micaceous partings.

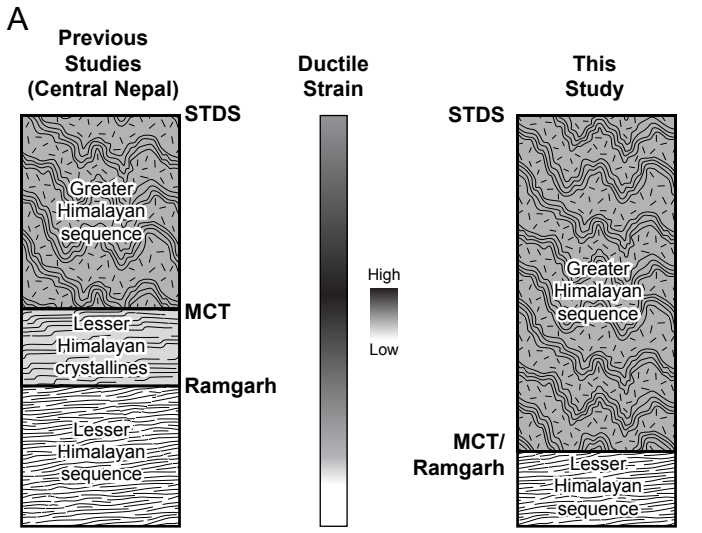


B

| Age | Western & Eastern Nepal[1] | | | Central Nepal[2] | |
|---|---|---|---|---|---|
| Miocene | Dumri Fm. | | | Dumri Fm. | |
| Eocene | Bhainskati Fm. | | | Bhainskati Fm. | |
| Permian-Paleocene | Gondwanas | | | Gondwanas | |
| Middle Proterozoic | Nawakot unit (West Nepal) | Lakarpata Gr. | Tumlingtar Group (East Nepal) | Midlands group | Robang Fm.<br>Malekhu Fm.<br>Benighat Fm.<br>Dhading Fm. |
| | | Syangia Fm. | | | Nourpul Fm. |
| | | Galyang Fm. | | | Dandagaon Fm. |
| | | Sangram Fm. | | | Fagfog Fm. |
| Early Proterozoic | | Ranimata Fm. (and Ulleri Gneiss) | | | Kuncha Fm. (and Ulleri Gneiss) |
| | | Kushma Fm. | | | |

[1] Schelling 1992; DeCelles et al. 2001; Pearson and DeCelles 2005; Robinson et al. 2006

[2] Hashimoto 1973; Bordet 1977; Stöcklin 1980; Colchen et al. 1986; Upreti 1996

**Figure 2.4**
(A) A comparison of the nomenclature used in previous studies in central Nepal against that used in this study and qualitative estimate of ductile strain across the Greater Himalayan sequence in the Kali Gandaki valley. MCT, Main Central thrust; STDS, South Tibetan detachment system (B) Correlation diagram of different stratigraphic units proposed for the Lesser Himalaya sequence in Nepal. This study uses the Midlands group nomenclature originally proposed for central Nepal. Modified after Pearson and DeCelles (2005).

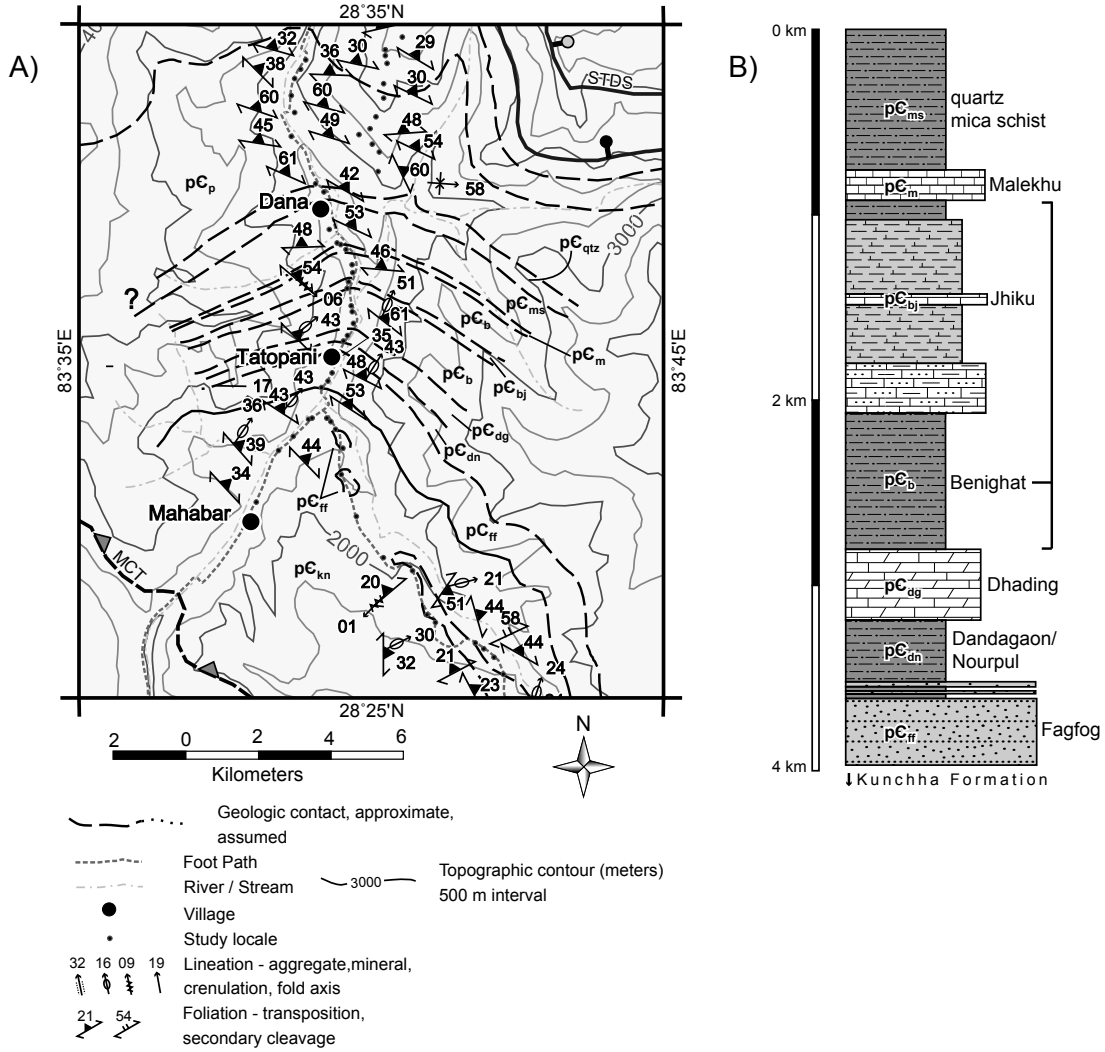


**Figure 2.5**
Detailed geologic map (A) and lithologic section (B) depicting the lithologic succession of the upper Midlands formations as exposed in the Kali Gandaki and Ghar valleys. See Figure 2.1 for location see Figure 2.2 for abbreviations used. See text for unit descriptions. MCT, Main Central thrust; STDS, South Tibetan detachment system.

The Malekhu Formation overlies the Benighat Formation (Figure 2.5), which consists of dark weathering phyllitic schist and calc-schist (Figure 2.6A) with thin intercalations of limestone near the upper part. In the map-area the thickest of these Jhiku carbonate beds (Stöcklin, 1980) are decimetre-scale dark grey to black weathering, white crystalline marble layers separated by thin, millimetre-scale, partings of dark grey to black phyllitic material. The dark weathering of the limestone may reflect a relatively high graphite content in the carbonate or the surrounding schist.

The Dhading Formation crops out below the Benighat Formation and consists of light grey-to-tan weathering meta-dolostone and meta-limestone that is isoclinally folded locally (Figure 2.6B). In the Kali Gandaki valley, it crops out just north of the village of Tatopani and is up to ca. 375 m thick (Figure 2.2). While the Dhading Formation is reportedly fossiliferous in the Kathmandu area (Stöcklin, 1980) no fossils were observed in the Kali Gandaki or Myadi valleys. The Dandagaon Formation, which is observed below the Dhading Formation (Figure 2.5) is not distinguishable from the overlying Nourpul Formation in the Kali Gandaki valley; together, the Nourpul and Dandagaon formations comprise a ca. 400 m thick sequence of interbedded carbonate rocks, phyllitic carbonate rocks, limey phyllitic schist and phyllitic schist, intercalated dark grey weathering quartz, biotite, muscovite schist, and thin layers of light tan weathering quartzite and, locally, more immature sandstone.

The base of the upper Midlands group is marked by a ~500 m thick medium-grained tan-to-light yellow weathering quartzite unit termed the Fagfog Formation (Figures 2.2 and 2.5; also referred to locally as the Ghandrung quartzite). It is characterized by 10 to 50 centimeter-scale bedding defined by thin muscovite-rich partings; deformed cross-bedding appears to be preserved locally (Figure 2.6C). The Fagfog Formation is distinguishable from the structurally higher quartzite at the base of the pelitic gneiss by its tan-coloured weathered surface and its lack of biotite on parting surfaces.

In the Kali Gandaki valley the lower Midlands group is ~ 5000 m thick and consists primarily of a succession of phyllitic schist and minor meta-sandstone comprising part of the Kunchha Formation (Bordet et al., 1964). The base of the Kunchha Formation is marked by a 50-100 m thick, medium-to-coarse-grained, light tan weathering quartzite unit that is equivalent to the Kushma Formation mapped in western Nepal (DeCelles et al., 2001; Robinson et al., 2006).

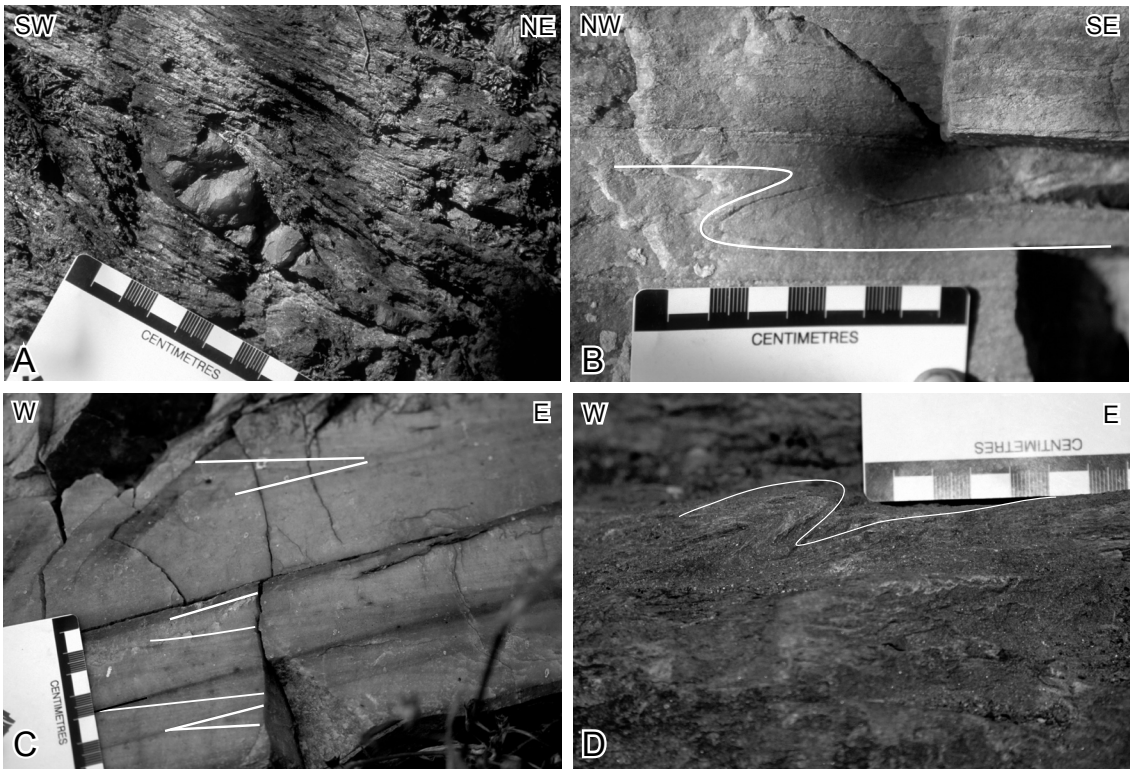


**Figure 2.6**
Lower Greater Himalayan sequence rocks exposed in the Kali Gandaki and Myadi valleys. (A) View to the northwest of a deformed quartz vein within the quartz muscovite biotite schist at the top of the Midlands group. (B) Centimeter-scale isoclinal folding within the Dhading Formation. The fold is highlighted with a white line; view is to the northeast. (C) View to the north of strained cross-bedding(?) within Fagfog Formation quartzite. Cross beds(?) are highlighted by white lines. (D) View to the north of isoclinal folding within the Kunchha Formation. The fold is outlined by a white line.

This basal meta-sandstone is structurally-overlain by muscovite, biotite, quartz, chlorite phyllitic schist (Figure 2.6D) that is intercalated with lesser amounts of medium-grained, immature meta-sandstone, and mafic meta-volcanic sills or dykes. The meta-pelitic assemblage is interpreted to be equivalent to the Ranimata Formation of western Nepal (as in Martin et al., 2005; Pearson and DeCelles, 2005; Figure 2.4).

The lower Midlands group also includes the Ulleri gneiss, a 2 km thick band of mylonitized orthogneiss with large (up to 5 cm long) potassium feldspar augen. The Ulleri gneiss is laterally discontinuous and crops out in kilometer-scale lenses along the length of the orogen (Colchen et al., 1986). It is everywhere contained within the Kunchha Formation (and its equivalents) and has been interpreted as a syn-depositional intrusion (Pêcher and LeFort, 1977). This interpretation is supported by preliminary early Proterozoic zircon ages for the Ulleri augen orthogneiss of ca. 1831 Ma (DeCelles et al., 2000).

Cenozoic leucosome is present throughout the upper portion of the Greater Himalayan sequence in the Dhaulagiri Himalaya, and reflects at least two episodes of melt generation. Kyanite-grade anatectite from near the STDS at the top of the Greater Himalayan sequence has yielded Eohimalayan ages (35-32 Ma) from U-Pb analyses of zircon (Godin et al., 1999a; 2001). This leucosome is thought to have formed in response to initial tectonic descent of the Indian plate beneath Asia (Godin et al., 1999a, 2001). In the middle portion of the Greater Himalayan sequence in the Kali Gandaki valley, a slightly deformed leucogranitic dyke has been dated by U-Pb zircon analyses as ~22 Ma (Nazarchuk, 1993). This is Neohimalayan in age, and the dyke may have formed as a result of decompressional melting during extrusion of the Greater Himalayan sequence from mid-crustal levels (Vannay and Hodges, 1996; Godin et al., 2001). The spatial distribution and relative extent of each generation of anatectite within both the Dhaulagiri Himal and the Himalayan orogen in general is not known; however, ages from similar rocks in parallel transects across the Himalaya are predominantly Miocene (Godin et al., 2006a).

The total amount of Cenozoic anatectite within the Greater Himalayan sequence in the Kali Gandki valley is significantly less than in other portions of the orogen such as the Manaslu (Pêcher, 1989) and Khumbu regions (Bordet, 1979). The variation in along-strike anatectite volume may reflect a difference in the positions of the exposures measured parallel to the transport direction (Pêcher, 1989). Regions with abundant Cenozoic anatectite may reflect a more

hinterland transect of the Greater Himalayan sequence.

### 2.4.4 Main Central thrust

In this study we follow Searle et al., (2008) and map the MCT below the transposed planar features and pervasive top-to-the south ductile deformation that characterizes the Greater Himalayan sequence. In the Dhaulagiri Himal the MCT separates unmetamorphosed-to low metamorphic grade sedimentary rocks, in which features such as ripple marks and trough crossbeds are preserved, from pervasively deformed rocks above in which all primary features have been transposed into parallelism.

### 2.4.5 Lesser Himalayan sequence

The rocks below the MCT in the Dhaulagiri Himal consist of chloritic phyllite and intercalated quartz arenite of the Kunchha Formation. The phyllitic rocks are characterized by fold-related cleavages while the sandstones preserve sedimentary cross-bedding and oscillation ripples (Hodges et al., 1996). The preservation of pristine sedimentary structures and the lack of transposition of planar and linear features suggest that the amount of ductile strain in these rocks is significantly less than those above the MCT.

## 2.5 Microstructures and quartz *c*-axis fabrics

Quartz *c*-axis fabrics have been used to characterize the strain and kinematic behaviour of parts of the Greater Himalayan sequence in various localities along the orogen including the STDS in the Everest region (Law et al., 2004), the exhumed migmatitic high-grade metamorphic core in Bhutan (Grujic et al., 1996), and the deformed extruded Greater Himalayan sequence of northwestern India (Grasemann et al., 1999; Bhattacharya and Weber, 2004). In central Nepal quartz *c*-axis fabrics from the Greater Himalayan sequence in the Modi, Madi, Chepe, Daraudi, and Budhi Gandaki valleys (Figure 2.1C), were first reported by Bouchez and Pêcher (1976) and subsequently revisited by Bouchez (1978), and Bouchez and Pêcher (1981). Within these studies, Bouchez and Pêcher (1981) describe a broad zone of penetrative deformation, which they interpreted as extending more than 10 km south of (structurally below) the previously interpreted MCT (Figure 2.1c). They conclude that no large post-metamorphic strain affects their data and that the quartz *c*-axis fabrics measured reflect the kinematics of flow during the main deformation

episode.

The present study builds upon the earlier work of Bouchez and Pêcher (1976), Bouchez (1978), and Bouchez and Pêcher (1981), extending that work farther west to the Kali Gandaki valley (Figures 2.1c and 2.2). Oriented specimens of quartz-rich mylonitic paragneiss, orthoquartzite, orthogneiss, calc-silicate gneiss, and pelitic schist from across the Greater Himalayan sequence were collected for quartz *c*-axis orientation analyses. The collection locations are identified in Figure 2.7. Quartz *c*-axis orientations were measured optically, in thin sections cut parallel to lineation and perpendicular to foliation, using a universal stage mounted on a petrographic microscope. Orientation data from all specimens are presented in equal area lower hemisphere projections with the plane of projection perpendicular to the foliation and parallel to the lineation. The sense of shear motion along the foliation is indicated by half-arrows (Figure 2.8). Preferred crystallographic alignment of quartz was not observed in all specimens. Specimens from the middle and upper portion of the Greater Himalayan sequence (hollow circles in Figure 2.7) did not yield discernible *c*-axis patterns. This may reflect partitioning of strain into mineral phases other than quartz, such as calcite in calc-silicate gneiss and/or post-kinematic re-crystallization of quartz grains. In the following section, we describe the mineral assemblages, microstructures, and quartz *c*-axis fabrics from collected specimens beginning with those from highest structural positions, progressing to those collected at lower structural positions.

### 2.5.1 Results of quartz petrofabric analysis

Specimen 018 (Figure 2.8) is the structurally highest specimen that yielded a well-defined *c*-axis fabric (Figure 2.7). It is an amphibolite-grade paragneiss consisting of the assemblage of quartz, plagioclase, muscovite, biotite, garnet, ± kyanite. The foliation has an average strike of 266˚ and dips at 48˚ to the NNW and is defined by aligned muscovite and biotite grains and elongate, plastically deformed quartz grains. A mineral shape lineation, defined by quartz, is visible on some foliation surfaces with an enigmatic orientation that plunges at 8˚ towards 286˚. This west-northwest plunge direction contrasts with a prevailing northeast-trending lineation from across the Greater Himalayan sequence. It is possible that specimen 018 represents a local perturbation in flow, or perhaps that the specimen was collected from a block that was slumped and rotated. The quartz in specimen 018 exhibits abundant pinning structures, subgrain

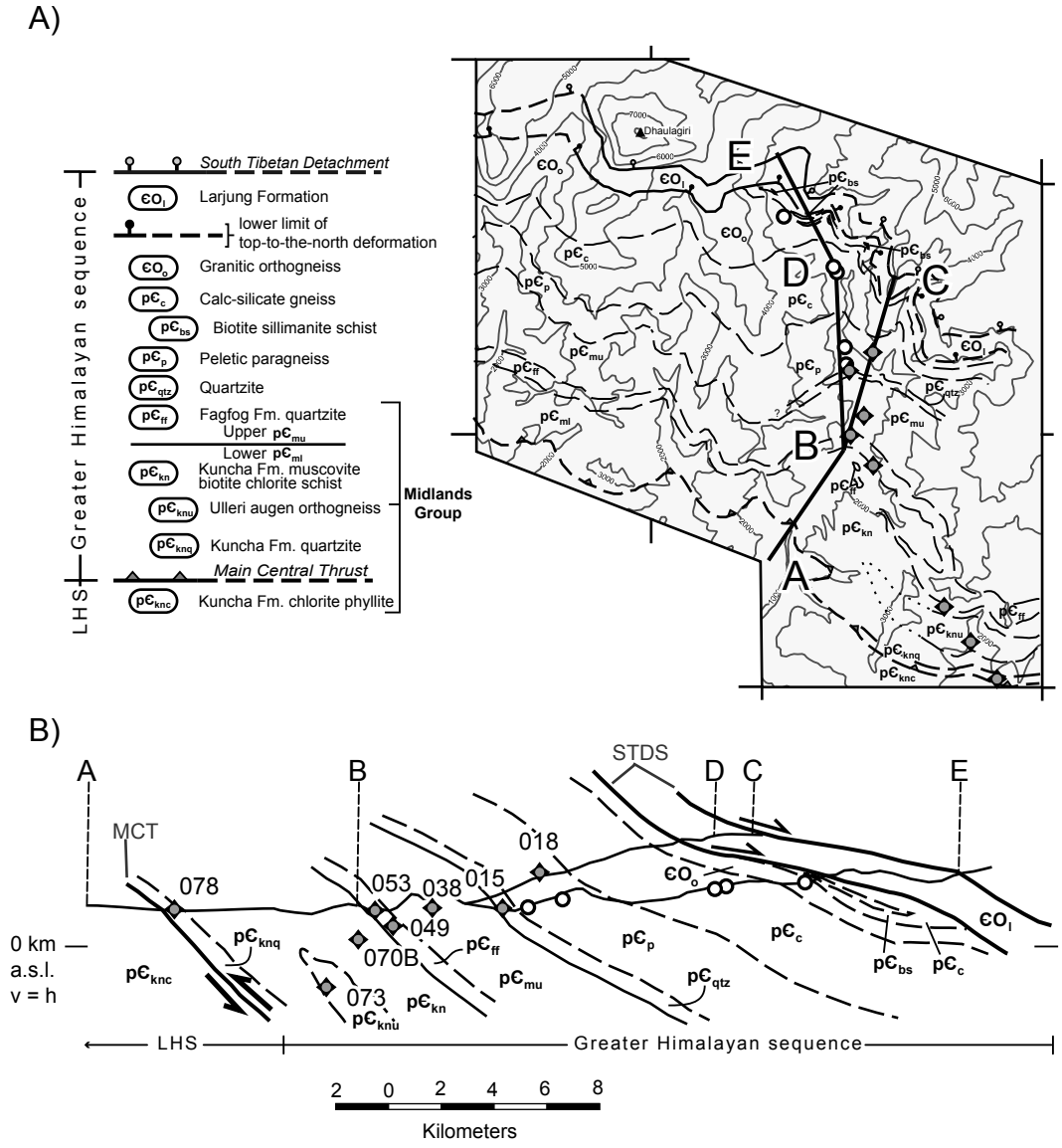


**Figure 2.7**
Cross-section through the southern Dhaulagiri Himalaya near the Kali Gandaki river. (A) Location of section shown within outline of map-area. Note that two different lines are drawn after point B, one roughly along the river (B-D-E) and the other along the Thulo Bugin ridge (B-C). (B) Structural cross-section through the study area. The collection locations of specimens used for quartz petrofabric analyses are shown in both A and B. Sample locations are projected horizontally to the profile plane. Open circles indicate specimens that did not yield an organized quartz *c*-axis pattern. LHS, Lesser Himalayan sequence; MCT, Main Central thrust; STDS, South Tibetan detachment system.

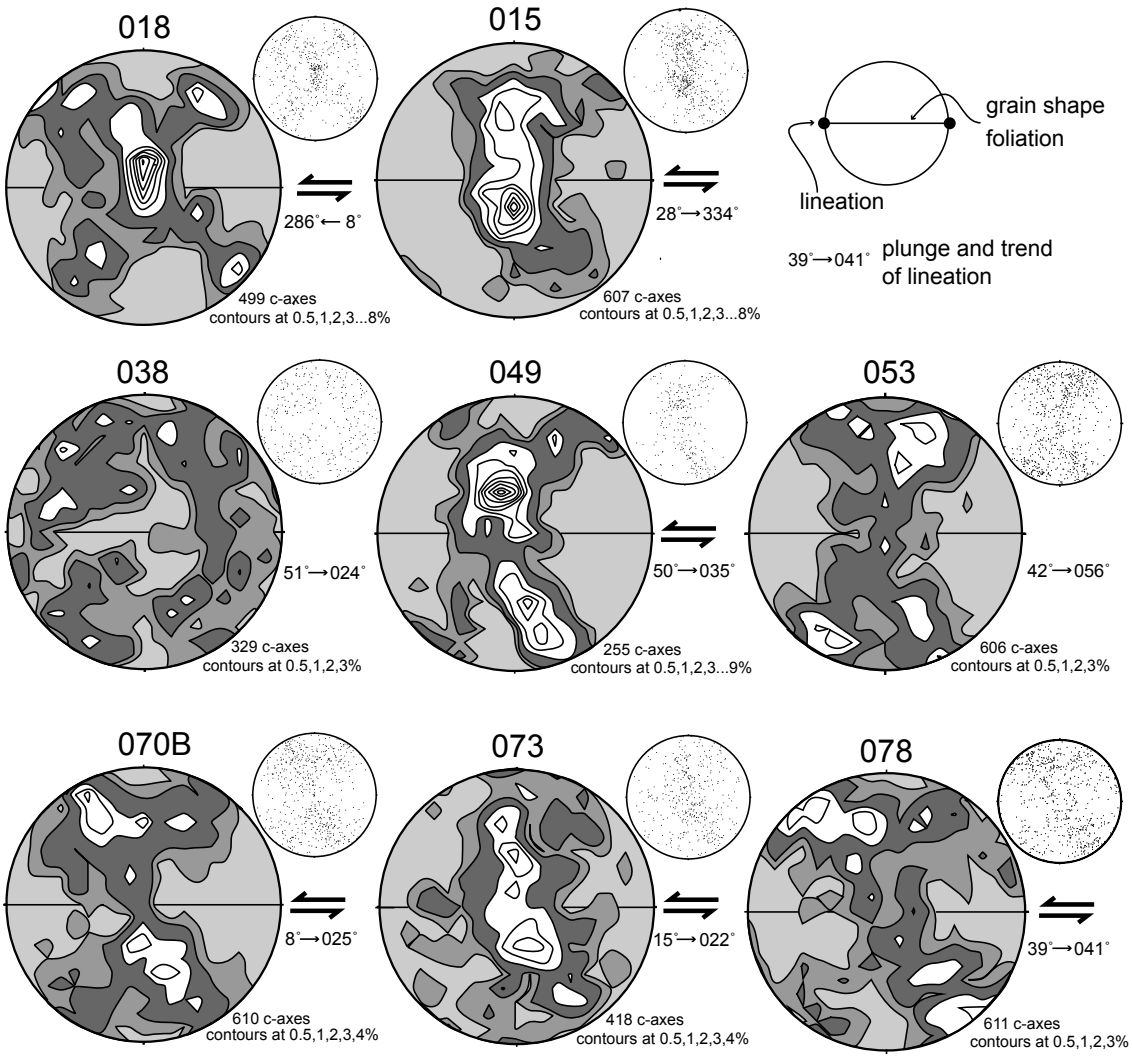


**Figure 2.8**
Quartz *c*-axis fabrics measured in quartz-rich specimens from the Greater Himalayan sequence. Collection locations are shown in Figure 2.7. The fabric data are shown on equal area lower hemisphere stereographic projects; plane of projection is perpendicular to foliation and parallel to lineation. Shear sense is indicated by the half-arrows. The quartz *c*-axis fabrics are contoured at 0.5, 1, 2…% area intervals using version 6.3.3 of Stereonet developed by R.D. Allmendinger. See appendix for photographs of specimen thin sections.

extinction, and a moderate foam texture (indicating Regime 3 recrystallization conditions of Hirth and Tullis (1992)) and is interpreted to have recrystallized by both subgrain rotation and grain boundary migration. Quartz *c*-axes define a moderately well-developed, slightly asymmetric, type-II cross-girdle pattern characterized by predominant prism <a> slip (Figure 2.8). The asymmetric distribution of *c*-axes suggests a top-to-the-west-northwest sense of shear.

Specimen 015 (Figure 2.8) was collected from the quartzite unit at the base of the pelitic gneiss (Figure 2.7) near the contact mapped as the MCT by Colchen et al., (1986). It is a mylonitic orthoquartzite with a macroscopic foliation defined by aligned biotite mica that strikes 300˚ and dips 42˚ to the NE. The lineation present in the specimen is defined by aligned biotite grains and plunges 28˚ towards 344˚. Quartz in specimen 015 is dominantly recrystallized through grain boundary migration resulting in a well-developed foam texture (Figure 2.3F; Regime 3 of Hirth and Tullis, 1992). Quartz *c*-axis orientations yield a well-defined, type-I cross-girdle pattern with a slight top-to-the-southeast shear sense (Figure 2.8). The crystallographic preferred orientation pattern of *c*-axes in this specimen reflects dominant prism <a> slip.

Specimen 038 was collected from a chlorite quartz schist. Chlorite comprises 65-70 % of the rock and defines the foliation, which strikes 309˚ and dips 56˚ to NE, and the lineation, which plunges 51˚ towards 024˚. Quartz and a minor opaque phase make up the other 30-35%. Quartz in the specimen exhibits a moderate foam texture, indicative of grain boundary migration, and minor undulose extinction. The size of the quartz crystals is everywhere constrained by the distance between chlorite partings, which also suggests recrystallization through grain boundary migration. Specimen 038 does not yield an organized *c*-axis pattern and instead is characterized by a random scattering of quartz *c*-axis (Figure 2.8). The lack of a preserved quartz *c*-axis pattern may be the result of significant post-kinematic recrystallization, however, rocks both structurally above and below specimen 038 are characterized by well-developed quartz crystal lattice-preferred orientations. Alternatively, strain may have been preferentially partitioned into the thick chlorite layers present in the rock such that the quartz crystals were not subject to enough strain to cause alignment of their *c*-axis. Similar results have been observed in calc-silicate gneiss specimens (Figure 2.7) where strain may have been preferentially accommodated by calcite.

Specimens 049, 053, 070B, and 78 were collected from outcrops of mylonitic quartzite. In these specimens (Figures 2.7 and 2.8) the lineation is defined by the alignment of muscovite

aggregates on foliation surfaces that are defined by quartz grain-shape fabrics and thin muscovite partings. Locally, muscovite also lies along and defines weakly-developed extensional shear bands and S-planes with a top-to-the-southwest shear sense. Quartz grains exhibit subgrain formation, bulging and minor foam textures indicative of subgrain rotation and grain boundary migration that is transitional between recrystallization regimes 2 and 3 of Hirth and Tullis (1992). Specimens 049, which contains a foliation that strikes 315˚ and dips 54˚ to the NE and a lineation that plunges 50˚ towards 035˚, and 053, which contains a foliation that strikes 325˚ and dips 45˚ to the NE and a lineation that plunges 42˚ towards 056˚, were collected from the same structural level at different locations. Specimen 049 yields a well-defined, asymmetric, type-I cross-girdle quartz *c*-axis pattern dominated by rhomb <a> and prism <a> slip with a top-to-the-south shear sense (Figure 2.8). Specimen 053, in contrast appears to define a type-I crossed-girdled pattern with predominant rhomb <a> slip (Figure 2.8); no dominant asymmetry is apparent. Specimen 070B, which contains a foliation that strikes 242˚ and dips 18˚ to the NNW and a lineation that plunges 8˚ towards 025˚, was collected from a lower structural position than 049 and 053. It yields a rhomb-dominated well-defined, asymmetric, type-I cross-girdle quartz *c*-axis pattern with a top-to-the-south shear sense (Figure 2.8).

Specimen 073 (Figure 2.8) was collected from the mylonitic Ulleri augen gneiss (Figures 2.2, 2.7) near the base of the Greater Himalayan sequence. Foliation in the augen gneiss is defined by muscovite and biotite alignment and quartz grain-shape fabrics that strike 292˚ and dip 15˚ to the NNE, and is characterized by strongly developed C/S/C' fabrics with a top-to-the-south shear sense; lineations are defined by quartz rods that plunge 15˚ towards 022˚. Quartz in the specimen is characterized by subgrain boundaries, undulose extinction, and bulging, which are characteristic of subgrain rotation and grain boundary migration, transitional between Regime 2 and 3 of Hirth and Tullis (1992). Quartz *c*-axis orientations define a moderately well-developed, single inclined girdle with a strong asymmetry that suggests a top-to-the-south shear sense. Prism <a> and rhomb <a> slip dominate this fabric.

In the structurally lowest specimen, 078, from the base of the Greater Himalayan sequence (Figure 2.7), quartz *c*-axes define a type-I cross-girdled pattern, dominated by basal <a> slip, with a top-to-the-southwest asymmetry. The *c*-axes also appear to define a weak small circle about the pole to foliation. This may reflect a slight flattening strain (Schmid and Casey, 1986)

possibly due to overthrusting of material above specimen 078.

### 2.5.2 Temperature of deformation

Assuming that critical resolved shear stress values for operative glide systems are primarily controlled by deformation temperature, rather than strain rate or degree of hydrolytic weakening, the opening angle of cross-girdled quartz *c*-axis fabrics can be related to the temperature at which the fabrics were developed (Tullis et al., 1973; Lister and Hobbs, 1980; Lister and Dornsiepen, 1982; Kruhl, 1998; Law et al., 1992; Law et al., 2004). During ductile deformation and dynamic crystallization, increased temperature results in an increased opening angle of quartz *c*-axis fabrics. The relationship between the opening angle of quartz *c*-axis fabrics and deformation temperatures is linear through greenschist to upper amphibolite facies conditions (Kruhl, 1998; Law et al., 2004). However, beyond ~700˚C empirical data indicate that opening angles increase faster than temperature increases (Law et al., 2004). This relationship may reflect the activation of prism <*c*> dominated slip. Kruhl (1998) estimated that temperatures derived from opening angles of quartz *c*-axis fabrics were subject to an uncertainty of ±50˚C. This uncertainty accounts for the range in strain rates and effects of hydrolytic weakening likely to be encountered during deformation (Law et al., 2004).

Quartz *c*-axis fabrics from specimens collected across the lower portion of Greater Himalayan sequence in the Kali Gandaki valley have little systematic variance in opening angle with respect to structural position from its base (Figure 2.9A). However, within the migmatic portion of the Greater Himalayan sequence the opening angle of *c*-axis fabrics increases to a maximum observed angle of 87˚ (Figures 2.8 and 2.9B), which corresponds to a temperature of 670±50˚C (018; Figure 2.9B) using the geothermometer of Kruhl (1998) as modified by Law et al., (2004). Specimens collected from structurally higher positions yielded random quartz *c*-axis fabrics, which precludes deformation temperature estimates in the upper-middle to-top portion of the extruded Himalayan infrastructure. Quartz *c*-axis fabric opening angles for quartzite specimens taken from the lower portion of the Greater Himalayan sequence indicate deformation temperatures of approximately 500˚C (049, 053, 070B, 078; Figure 2.9B).

Published temperature estimates for Neohimalayan equilibrium metamorphic assemblages in the Kali Gandaki valley, interpreted to be coincident with the southward extrusion of the mid-

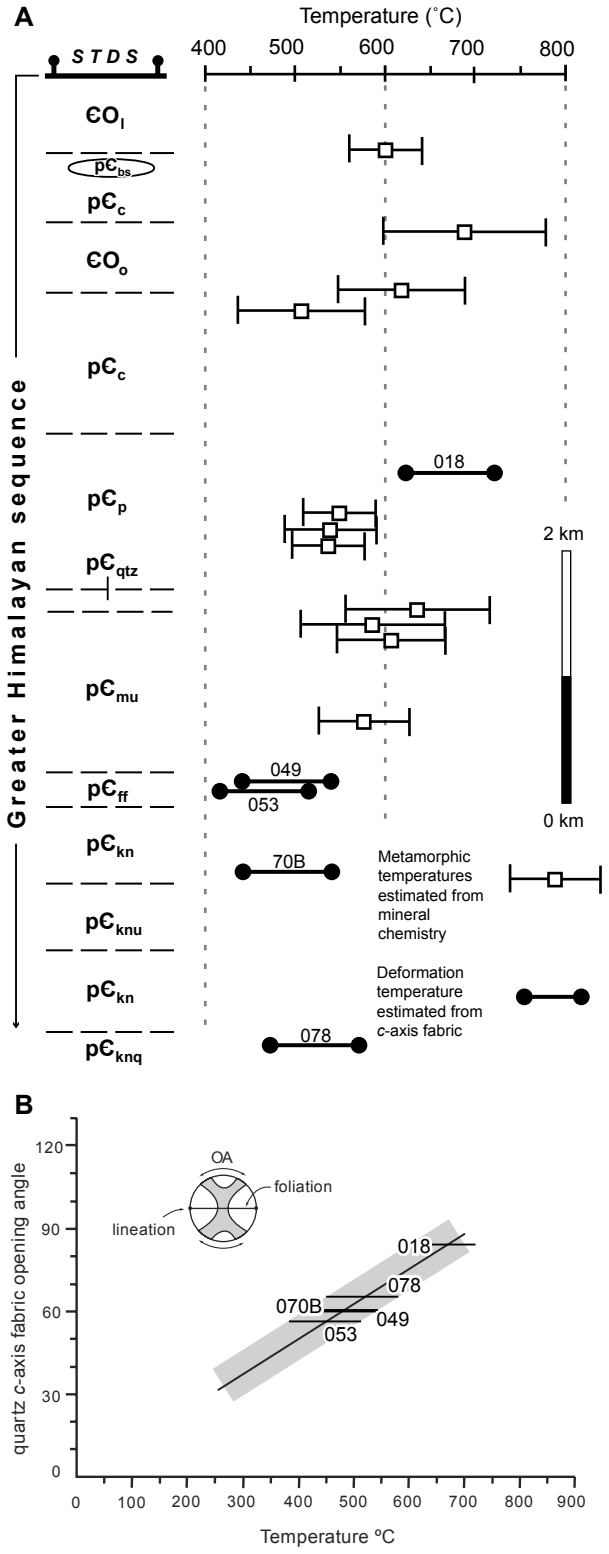


**Figure 2.9**
A) Quartz *c*-axis geothermometry results plotted against structural position within the Greater Himalayan sequence. Equilibrium temperature data from Vannay and Hodges (1996) are also plotted against structural position. See text for discussion. STDS, South Tibetan detachment system. (B) Plot of quartz *c*-axis opening angle against deformation temperature, modified from Law *et al*., (2004). Data from this study are plotted and labeled. See Figure 2.7 for structural position of specimens, Figure 2.8 for the quartz *c*-axis fabrics, and Figure 2.2 for tectonostratigraphic abbreviations.

crust into the Himalaya (Vannay and Hodges, 1996), can be compared with quartz *c*-axis derived temperatures from similar structural positions to determine if quartz *c*-axis fabrics were developed under comparable thermal conditions (Figure 2.9A). The temperatures estimated by each method are similar, thus the quartz *c*-axis fabrics are interpreted to have developed during the same Neohimalayan event as the metamorphic assemblage. The quartz *c*-axis patterns, therefore, reflect strain in the lower half of the Greater Himalayan sequence during Neohimalayan mid-crustal extrusion and not some other deformation event.

Combining the results of quartz *c*-axis and metamorphic assemblage geothermometry results in a more detailed temperature profile across the Greater Himalayan sequence in the Kali Gandaki valley, one which appears to reflect an inverse thermal field gradient (Figure 2.9A). A similar inverse thermal gradient across the exhumed Himalayan metamorphic core has been observed in other transects along the orogen (e.g., Ganser, 1964; Hubbard, 1989; Pêcher, 1989; Searle and Rex, 1989). Perturbations in the temperature profile across the Greater Himalayan sequence rocks exposed in the Kali Gandaki valley may be indicative of post-metamorphic thrusting (e.g., Kalopani shear zone, Vannay and Hodges (1996); Khumbu thrust, Searle (1999)), strain localization and contribution of shear heating, or perhaps diachronous metamorphism and peak temperature that varies with structural position.

## 2.6 Vorticity

Vorticity is defined as the internal rotational component of flow and is equal to the mean angular velocity of material lines with respect to the instantaneous stretching axes (Passchier and Trouw, 2005). Vorticity data are critical to understanding flow kinematics in ductily deformed rocks. In the Himalayan orogen recent vorticity studies have begun to empirically-constrain interpretations of strain within the Greater Himalayan sequence and its bounding shear zones (Grasemann et al., 1999; Law et al., 2004; Jessup et al., 2006; Carosi et al., 2006, 2007).

For plane strain conditions, as indicated by the dominance of type-I cross-girdled quartz *c*-axis fabrics, the relative proportions of pure shear and simple shear can be expressed in terms of the kinematic vorticity number $W_k$, which relates instantaneous rotation to instantaneous stretching at a point (Bailey et al., 2004). For an entirely pure shear system $W_k = 0$, while in simple shear $W_k = 1$. The ratio of pure shear to simple shear is not a linear relationship; equal

contributions of both are made to the instantaneous flow at $W_k = 0.71$ (demonstrated by Law et al., 2004). In natural systems it is rarely possible to quantify rotation rates versus stretch in deformed rocks (Bailey et al., 2004), therefore, vorticity of flow is more appropriately approximated by $W_m$ a mean vorticity number for plane strain deformation.

Vorticity of flow recorded in specimens collected from the lower-middle portion of the Greater Himalayan sequence has been estimated using the Rigid Grain Net (RGN) of Jessup et al., (2007) and the method of Wallis (1992, 1995). Both methods require data collected within the X-Z plane of the strain ellipse; therefore, thin sections were cut perpendicular to foliation and parallel to lineation. Quartz *c*-axis fabrics are interpreted to show that the strain recorded in these rocks is related to the southward transport of the Greater Himalayan sequence. Vorticity analysis of the same rocks, therefore, provides additional kinematic constraints on the same process.

$W_m$ values were estimated using the RGN (Jessup et al., 2007) for three different specimens at various structural positions within the lower portion of the Greater Himalayan sequence (Figure 2.10). This method requires the same assumptions inherent to all vorticity estimates that are based on the orientation of rigid grains. These assumptions include no mechanical interaction between porphyroclasts, a homogenous matrix, high enough strain to allow grains to reach stable sink positions (see Jessup et al., 2007 for explanation), and a wide distribution of aspect ratios amongst the porphyroclasts. In specimen 053, the structurally highest specimen analyzed, 138 amphibole and epidote porphyroclasts that show no internal strain (Figure 2.10A) in a ductily deformed quartz matrix were analyzed and yield $W_m$ values between 0.61 - 0.73, which corresponds to a pure shear component of 48 - 58% (Figure 2.10b). The orientations and aspect ratios of 106 porphyroclasts predominantly of amphibole (Figure 2.10C), also in a ductily deformed quartz matrix, were measured in multiple thin sections of specimen 070B. They yield $W_m$ values between 0.60 and 0.80, which correspond to a pure shear component of 41 - 59% (Figure 2.10d). The structurally lowest specimen analyzed, 073, is from the Ulleri augen orthogneiss (Figures 2.2 and 2.6). Multiple thin sections of this specimen were cut to measure a total of 141 feldspar porphyroclasts. The feldspars are locally brittlely fractured but otherwise show no internal strain (Figure 2.10e). The $W_m$ values estimated for specimen 073 are interpreted to range between 0.69 and 0.71 corresponding to a pure shear component of 50 - 52% (Figure 2.10f).

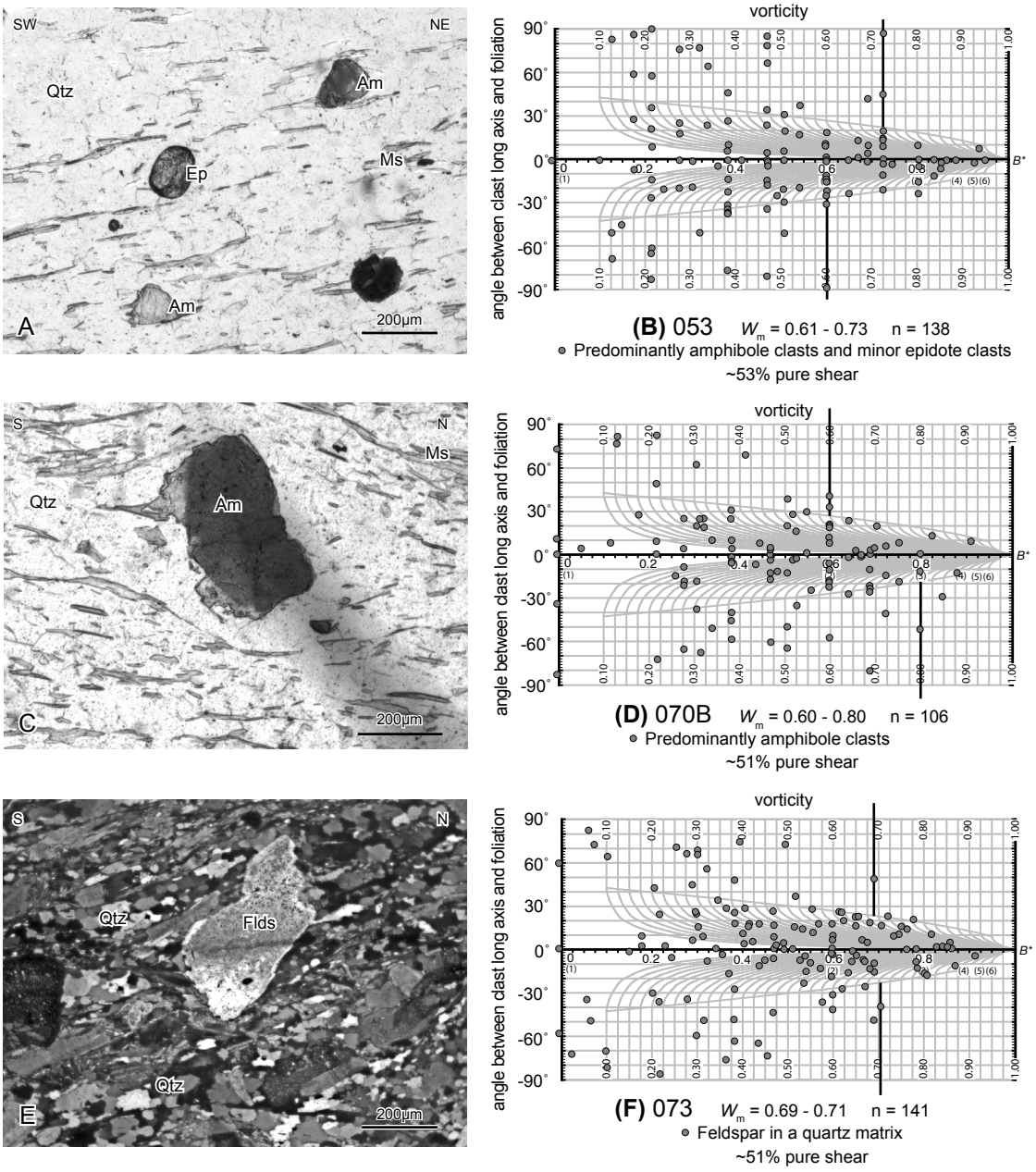


**Figure 2.10**
Vorticity analyses from the lower Greater Himalayan sequence of the Kali Gandaki valley. (A) Plane-polarized light photomicrograph of specimen 053 depicting epidote and amphibole porphyroclasts used for rigid grain analyses. (B) Rigid Grain Net (RGN) plot of specimen 053 yielding $W_m$ between 0.61 - 0.73. (C) Plane-polarized light photomicrograph of specimen 070B showing a large amphibole porphyroclast, within a plastically deformed quartz dominated matrix, used for vorticity analysis. (D) RGN plot of specimen 070B that yields $W_m$ results between 0.60 and 0.80. (E) Cross-polarized light photomicrograph of specimen 073 depicting a typical feldspar porphyroclast used for vorticity analysis in a quartz and mica dominated matrix. (F) RGN plot of specimen 073. $W_m$ values are interpreted to range from 0.69 to 0.71. Am, amphibole; Ep, epidote; Flds, feldspar; Ms, muscovite; Qtz, quartz.

As noted by Law et al., (2004), rigid grain methods may systematically underestimate the vorticity number if clasts of large aspect ratio are not present. Moreover, rigid grain methods may under estimate $W_m$ if strain has not been sufficient to allow clasts to reach a stable sink position. Following Xypolias and Kokkalas (2006), we interpret the rather sharp breaks between clasts in stable sink positions and clasts in freely rotating positions on the RGN (Figures 2.10B, D, F) to reflect that strain was indeed sufficient for stable sinks to be reached. The upper bound of the range of $W_m$ values determined using rigid grain techniques, therefore, might more closely reflect the true value of the kinematic vorticity number (Law et al., 2004).

A second method used in the study for estimating the vorticity of flow incorporates strain ratio data measured in the XZ-plane of finite strain (Rxz) and relates it to the angle between the foliation and the flow plane infered from quartz *c*-axis fabrics. This method was proposed by Wallis (1992, 1995) and has recently been applied to both the top and middle of the Greater Himalayan sequence (Grasemann et al., 1999; Law et al., 2004). Strain ratio data in this study have been derived from deformed relict quartz grains (as in Bailey et al., 2004; Law et al., 2004; Xypolias and Kokkalas, 2006). In specimen 070B the original grain shape aspect ratios have been preserved by muscovite surrounding the original quartz grain, inhibiting grain boundary migration (Figure 2.11A,B). The aspect ratio and orientation with respect to foliation of 38 relict quartz grains were measured in specimen 070B and analyzed using the matrix method of Shimamoto and Ikeda (1976; using the program MacStrain 2.4 written by Kanagawa, 1992) and the Rf/phi/theta curve method of Lisle (1985). The calculated strain ratios for specimen 070B ranged between 2.36 using the matrix method and 2.41, with a chi-squared value of 2.02 (see Lisle [1985] for explanation) using the Rf/phi/theta curve method. These strain ratios can be related to $W_m$, using the angle between the macroscopic foliation and flow plane (Figure 2.11B), through the following equation (Wallis 1992, 1995; Law et al., 2004; Xypolias and Kokkalas, 2006):

$$W_m = \sin\left\{\tan^{-1}\left[\frac{\sin(2\beta)}{\left[\frac{(R_{XZ}+1)}{(R_{XZ}-1)}\right]-\cos(2\beta)}\right]\times\frac{(R_{XZ}+1)}{(R_{XZ}-1)}\right\} \qquad (1)$$

where Rxz, strain ratio in XZ section; β, angle between flow plane and foliation as determined from the quartz *c*-axis fabric.

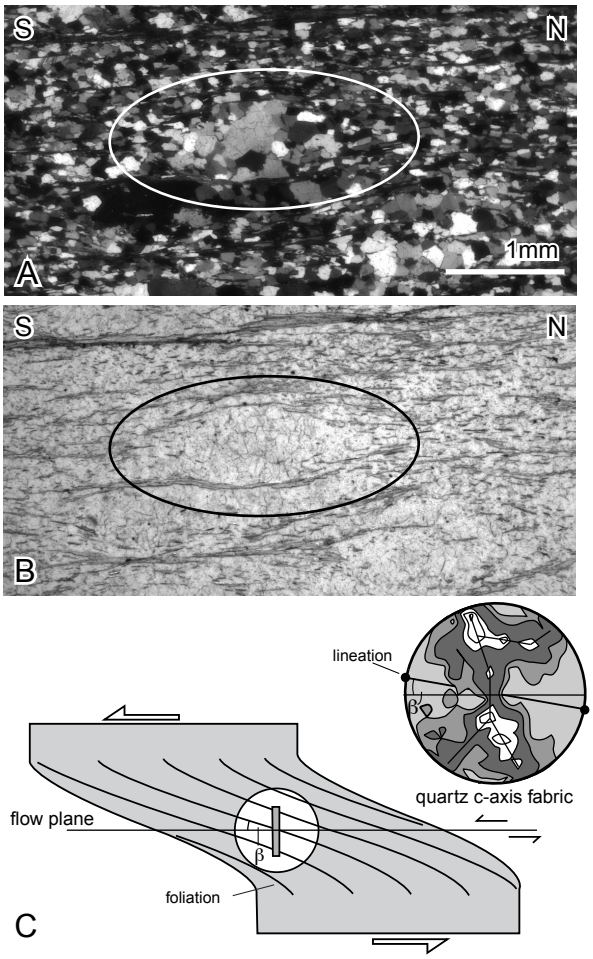


**Figure 2.11**
(A) Photomicrograph of specimen 070B in cross-polarized light showing strained and recrystallized relict quartz grains used for strain analyses. The ellipse encircles a relict quartz grain. (B) Plane polarized light photomicrograph of specimen 070B, same thin section area as in Figure 2.11A. (C) Angular relationship between the flow plane and foliation as represented by a quartz *c*-axis fabric (modified from Wallis, 1995 and Law *et al*., 2004). The β-angle derived from the specimen is used to calculate vorticity.

$W_m$ values for specimen 070B estimated for a β-angle of 12 ± 3˚ (the error in β-angle follows Platt and Behrmann 1986), range from 0.49 to 0.74. The range in values reflects (1) the degree of uncertainty in measuring the angle between foliation and the normal to the leading-edge of the quartz *c*-axis fabric and (2) variation in our estimates of the strain ratio (Law et al., 2004). $W_m$ values of 0.49 and 0.74 correspond to a pure shear component of 47 - 67%. In other studies estimates of vorticity derived by the Wallis (1992, 1995) method are consistently higher than $W_m$ values estimated using rigid grain rotation techniques (Law et al., 2004; Xypolias and Kokkalas, 2006). That same relationship is not observed in this study; the RGN method and the Wallis (1992, 1995) method are indistinguishable (Figure 2.12).

If the boundary between the Greater Himalayan sequence and the subjacent little-metamorphosed Lesser Himalayan sequence is regarded as a shear zone boundary (i.e. parallel to the flow plane) then calculation of the principal stretch magnitudes perpendicular and parallel to this plane may be made through the following equation (Wallis et al., 1993; Law et al., 2004):

$$S = \left\{ \frac{1}{2}\left(1 - W_m^2\right)^{\frac{1}{2}} \left[ \left( R_{XZ} + R_{XZ}^{-1} + 2\frac{\left(1 + W_m^2\right)}{\left(1 - W_m^2\right)} \right)^{\frac{1}{2}} + \left( R_{XZ} + R_{XZ}^{-1} - 2 \right)^{\frac{1}{2}} \right] \right\}^{-1} \quad (2)$$

where S, shortening perpendicular to the flow plane; $S^{-1}$, stretch parallel to flow plane (for plane strain at constant volume),

Data from specimen 070B yield shortening values perpendicular to the flow plane between 25-32%. Furthermore, assuming plane strain deformation, an assumption that is supported by the cross-girdled quartz *c*-axis fabric for specimen 070B and most other specimens analyzed (Figure 2.8), stretch parallel to the flow plane is estimated at between 34-47% parallel to the flow plane. As the neutral vorticity numbers estimated in this study are dependent on the last increment of strain due to dynamic recrystallization (as β values were determined from quartz *c*-axis orientation data) it is likely that the above values underestimate the total stretch and shortening.

All specimens used to estimate vorticity, which were collected ~2 to 6 km above the MCT, are within error of each other and indicate a significant component of pure shear deformation (Figure 2.12). The average vorticity value estimated in this study is 0.67, which implies a pure shear contribution of 53% and a simple shear contribution of 47% in the lower

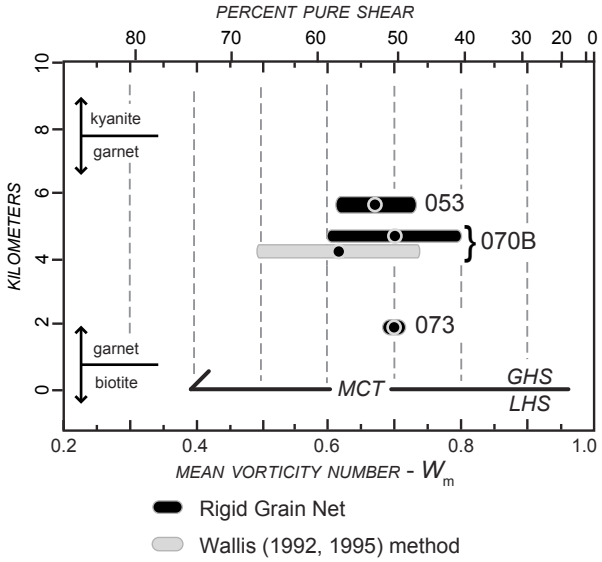


**Figure 2.12**
The results of vorticity analyses from this study. A large uncertainty range in $W_m$ for specimen 070B using the strain ratio method reflects the diffuse nature of the quartz *c*-axis pattern. LHS, Lesser Himalayan sequence; GHS, Greater Himalayan sequence; MCT, Main Central thrust.

portion of the Greater Himalayan sequence exposed in central Nepal.

## 2.7 Discussion

### 2.7.1 Position of the Main Central thrust

Detailed geological mapping and microstructral analyses conducted in this study provide evidence of pervasive top-to-the-south ductile shearing at temperatures of ~500 ˚C through a crustal section that extends for more than 8 km below the previously mapped position of the MCT in the Kali Gandaki valley. We map the MCT at the base of these deformed rocks, where it is manifested as a marked contrast in ductile strain, and juxtaposes the transposed section against rocks that preserve sedimentary structures such as ripple marks and are characterized by macroscopic folding and associated cleavages below. Our interpretation moves the MCT 8 km structurally below the lowest levels of the 'MCT' adopted in previous interpretations (Figures 2.1C, 2.13) by Colchen et al., (1986) and Vannay and Hodges (1996). This is consistent with the MCT as defined by Searle et al., (2008), which separates pervasive top-to-the south deformation and relatively high-grade metamorphism above from relatively low-grade, non-transposed rocks below.

Although the MCT is mapped as a single thrust plane in the Dhaulagiri Himal, we speculate that cumulative displacement between rocks below the MCT and those above it increases progressively upwards to a maximum at the base of the migmatite-bearing assemblages, which likely coincides with the base of the original extruded mid-crustal material (Searle et al., 2008; Figure 2.13). This model of the evolution of the MCT is supported by geochronologic and thermobarometric constraints from the adjacent Marsyandi and proximal Daraudi valleys (Figure 2.1C), which are consistent with a shear zone with upper and lower boundaries that migrate structurally downwards through time and add material to the hanging wall (Catlos et al., 2001). After initial coupling with the STDS in the Miocene to extrude the migmatitic core of the Greater Himalayan sequence (Godin et al., 2006a), the lower boundary of the MCT shear zone propagated down structural section with time and incorporated subjacent material into its hanging wall with increasing net translation across the shear zone relative to a stable India. This model predicts that material in the immediate hanging wall of the MCT would have been subjected to the least

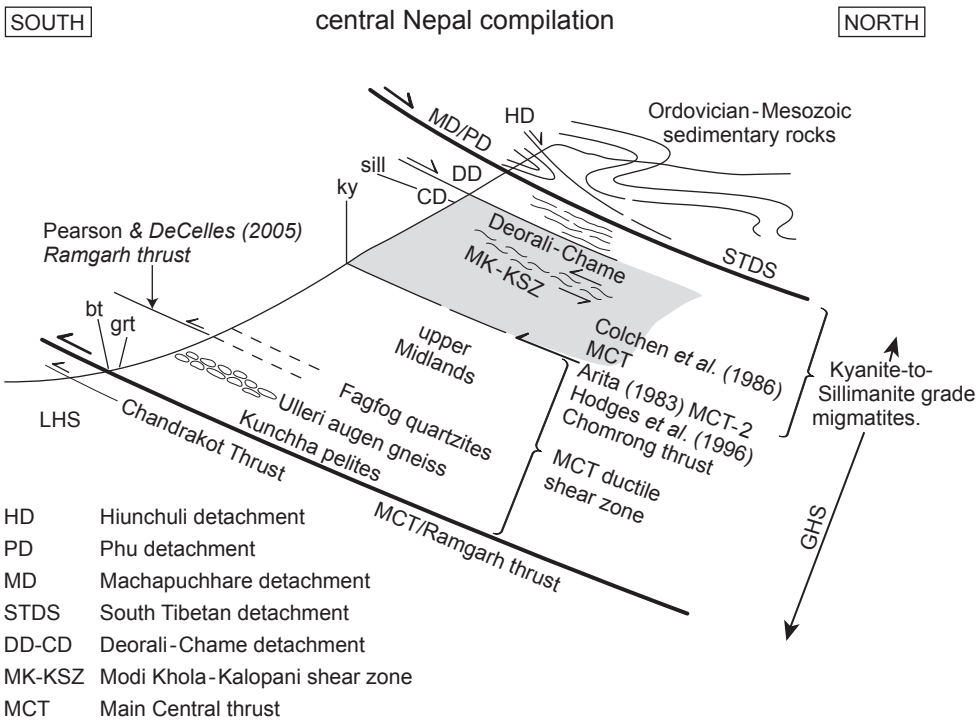


**Figure 2.13**
Simplified, schematic section showing the key features of the structural framework of central Nepal modified from Searle *et al.*, (2008). Previously mapped locations of the Main Central thrust and Ramgarh thrust are depicted. Shaded area represents the migmatitic-bearing mid-crustal material extruded from beneath Tibet during Miocene coupling between the MCT and South Tibetan detachment system. GHS, Greater Himalayan sequence; LHS, Lesser Himalayan sequence, bt, biotite; grt, garnet; ky, kyanite; sill, sillimanite.

amount of translation. In the Kali Gandaki valley the rocks mapped on both sides of the MCT (Figure 2.2) are interpreted to be from the same lithotectonic unit (albeit of different metamorphic grade and structural character). While such a juxtaposition can be achieved even after significant translation along footwall and hanging wall thrust flats if throw along the corresponding ramps does not exceed the thickness of the lithotectonic unit, it may be interpreted as evidence for relatively moderate displacement across the mapped MCT.

Geochronologic constraints are key to elucidating the evolution of the MCT and strain within the Greater Himalayan sequence. $^{208}Pb/^{232}Th$ dating of monazite inclusions in garnet collected from successively lower levels of the Greater Himalayan sequence in other (some adjacent) portions of the Himalaya have been interpreted to record prograde metamorphism related to thrust motion ranging between 3.3 ± 0.1 Ma and 22 Ma (Harrison et al., 1997; Catlos et al., 2001, 2002, 2004; Kohn et al., 2001, 2005). The ages reported generally become younger down structural section, away from the migmatitic core of the Greater Himalayan sequence, and are thus consistent with the model of a downward migrating MCT shear zone boundary. However, Bollinger and Janots (2006) have demonstrated that some young Himalayan monazite is a retrograde product from the breakdown of allanite at low temperatures (<370˚C). Furthermore, Martin et al., (2007) have also questioned the use of monazite to date prograde metamorphism in the Himalaya. Although young Th-Pb monazite ages may only date a low temperature retrograde event and not prograde metamorphism associated with slip along the MCT, these data do not preclude the structural migration of the shear zone through time.

### 2.7.2 Position of the Ramgarh thrust

The Ramgarh thrust (Heim and Gansser, 1939; Pande, 1950; Gansser, 1964; Valdiya, 1980; Shrestha et al., 1987; Srivastava and Mitra, 1994; DeCelles et al., 1998, 2001) and its equivalents, have been interpreted as an orogen-scale thrust, mappable along the entire frontal Himalaya (Figure 2.1b; Shrestha et al., 1987; DeCelles et al., 2001; Pearson and DeCelles, 2005) that, based on balanced cross-sections, has accommodated ca. 120 km of post-initial India-Asia collision shortening (DeCelles et al., 2001; Pearson and DeCelles, 2005; Robinson et al., 2006). The surface trace of the Ramgarh thrust in India and western Nepal has been inferred in numerous studies (e.g., Heim and Gansser, 1939; Pande, 1950; Gansser, 1964; Valdiya, 1980; Shrestha et al.,

1987; Srivastava and Mitra, 1994; DeCelles et al., 1998, 2001; Robinson et al., 2006), however, only in two localities has a fault surface been observed (Pearson and DeCelles, 2005). Martin et al., (2005) and Pearson and DeCelles (2005) inferred the presence of the Ramgarh thrust in central and eastern Nepal on the basis of interpreted stratigraphic repetition.

In the Modi river drainage of central Nepal (Figure 2.1C), the location nearest to the Kali Gandaki valley where the Ramgarh thrust has been mapped, the thrust fault has been interpreted to be at the base of a thick layer of quartzites (Figure 2.13; Martin et al., 2005; Pearson and DeCelles, 2005). These quartzites have been interpreted as being the lower Kunchha Formation and the overlying metapelitic rocks have been interpreted to be part of the upper Kunchha Formation. These interpretations are, however, inconsistent with the rock types described by Hodges et al., (1996) and Pearson and DeCelles (2005) in the Modi river drainage. The Kunchha Formation (Ranimata Formation; Figure 2.4B) is characteristically a chloritic or sericitic phyllite and phyllitic siltite with subordinate amounts of chloritic schist (DeCelles et al., 2001) that is entirely non-calcareous (Stöcklin, 1980). The rocks stratigraphically above the quartzite in the Modi river, however, comprise graphitic phyllite intercalated with thin layers of dolostone and impure marble both near the base and the top of the sequence (Pearson and DeCelles, 2005). There is no evidence for repetition of stratigraphic units. The strata in the Modi valley more closely resemble the lithotectonic sequence observed above the Kunchha Formation and its equivalents in western Nepal and eastern Nepal (Figure 2.4B) and can alternately be interpreted as a succession of the Fagfog, Dandagaon, Nourpul, Dhading, Benighat, and Malekhu formations. A similar lithotectonic succession of units above the Kunchha Formation, has been mapped during this study in the Kali Gandaki valley (Figures 2.2, 2.5). The tectonostratigraphy in the Modi and Kali Gandaki river drainages matches known tectonostratigraphy and does not require repitition across a thrust fault.

In addition to the tectonostratigraphic data, pervasive high-temperature deformation, as documented by the quartz *c*-axis fabrics throughout the lower Greater Himalayan sequence of central Nepal, is also inconsistent with the location of the Ramgarh thrust proposed by Pearson and DeCelles (2005). While high-strain recrystallization of quartz has been recognized along the interpreted Ramgrah thrust in central Nepal (Pearson and DeCelles, 2005), the associated strain is interpreted to be confined to the lower Kunchha (equivalent to the Kushma Formation;

Figure 2.4b) in the proximal hanging wall and immediately adjacent rocks in the footwall of the inferred thrust. In the Kali Gandaki valley, high temperature (~500 ˚C), ductile, top-to-the-south deformation extends downwards more than 8 km below the previously mapped MCT and for more than 6 km farther south of the inferred position of the Ramgarh thrust (Figure 2.1C). Similar deformation profiles across most of central Nepal are apparent from the quartz *c*-axis data of Bouchez and Pêcher (1981). Thus, the Ramgarh thrust, which was originally defined on the basis of intense mylonitization above the fault and a lack of intense shearing below the fault (Pande, 1950; Valdiya, 1980) is here reinterpreted in central Nepal to be the MCT at the base of the Greater Himalayan sequence (Figure 2.13). It separates the transposed Greater Himalayan sequence above from the less-deformed non-transposed Lesser Himalayan sequence below (Figures 2.1C, 2.13).

### 2.7.3 Flow kinematics

Detailed mapping in the Kali Gandaki valley, supplemented by microstructural data, shows that the lower 15 km of the 17 km thick Greater Himalayan sequence is pervasively deformed and exhibits dominant top-to-the-south sense of shear. Comparison of deformation temperatures derived from quartz *c*-axis fabric opening angles to metamorphic equilibrium temperatures from the same structural level suggests that the *c*-axis fabrics reflect Neohimalayan deformational conditions. Thus, the top-to-the-south sense of shear is interpreted to reflect deformation during southward extrusion of the mid-crust.

The vorticity values reported in this study are compatible with structural models of mid-crustal flow and extrusion (e.g., Grasemann et al., 1999; Williams et al., 2006) as well as thermo-mechanical finite-element models (e.g., Beaumont et al., 2001, 2004, 2006; Jamieson et al., 2004, 2006) that predict significant pure shear strain near the base of the mid-crustal rocks. These data are also consistent with deformation in models of critical taper put forth to explain the evolution of the Himalaya (e.g., Bollinger et al., 2006; Kohn, 2008) as significant pure shear is implied within the deforming wedge (e.g., Platt, 1986). Vorticity data from this study complement data from Bhutan (Carosi et al., 2006), the Everest region (Law et al., 2004; Jessup et al., 2006), west-central Nepal (Carosi et al., 2007), and northwestern India (Grasemann et al., 1999) and indicate that pure shear flattening deformation is evident throughout the Greater Himalayan

sequence. Specifically, the range of vorticity values from this study, 0.49 – 0.80 (66 - 41% pure shear) with an average value of 0.67 (53% pure shear) for the lower Greater Himalayan sequence, corroborates other studies that have examined similar structural levels. Data for the adjacent Dolpo region of central Nepal range from 0.66-0.77 (54 – 44% pure shear) with an average vorticity of 0.74 (47% pure shear; Carosi et al., 2007). Data from the lower Greater Himalayan sequence of the Everest region show significant pure shear with $W_m$ values ranging between 0.63 and 0.77 (57 – 44 % pure shear) and an average value of 0.69 or 52% pure shear (Jessup et al., 2006). When the tectonic framework of each study area is reinterpreted to reflect the MCT of Searle et al., (2008), the results of all vorticity studies can be incorporated to provide insight into vorticity variation across the Greater Himalayan sequence (Figure 2.14A). Such a compilation should be viewed with caution, however, as the pressure-temperature-time conditions specific to each specimen used for vorticity analysis is not known and the relative location of the specimens within the Greater Himalayan sequence with respect to the hinterland and foreland changes along the orogen. If the vorticity data are taken at face value, simple shear appears to dominate near the upper boundary of the Greater Himalayan sequence, while almost equal portions of pure shear and simple shear are measured in the interior and lower portions (Figure 2.14B). Increasing pure shear towards the base of the Greater Himalayan sequence may be partially attributable to lithostatic loading. The recognition of significant pure shear implies: (1) thinning and along-dip extension of the Himalayan infrastructure (Law et al., 2004; Jessup et al., 2006); and (2) increased strain rates and extrusion rates relative to that expected in a simple shear system (Law et al., 2004; Jessup et al., 2006).

### 2.7.4 Implications for mid-crustal extrusion processes

The extrusion of the mid-crustal metamorphic core from beneath Tibet has been attributed to contemporaneous movement along the MCT and the STDS during the Miocene (Grujic et al., 1996; Grasemann et al., 1999; Beaumont et al., 2006; Godin et al., 2006a;). During and subsequent to the southward extrusion of the Greater Himalayan sequence from beneath Tibet the décollements at the top and bottom of the panel developed into wide shear zones, the boundaries of which have often been mapped as separate faults with the designations ‘1’ and ‘2’ or ‘lower’ and ‘upper’ (see review by Godin et al., 2006a). These shear zones appear to have evolved

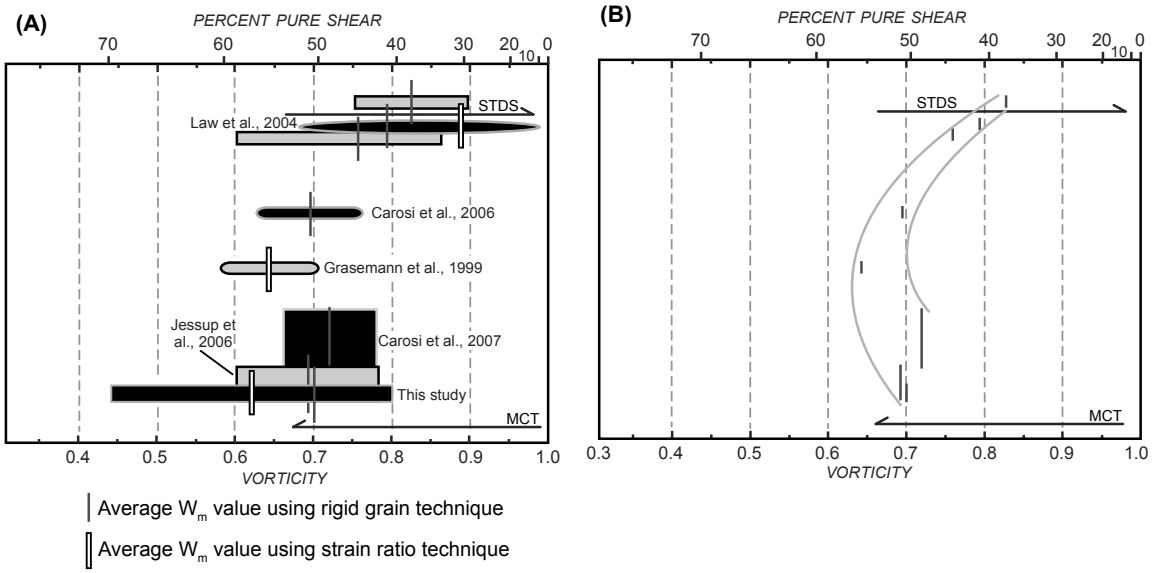


**Figure 2.14**
(A) This diagram is a schematic compilation of vorticity analysis results from across the Himalaya (see Figure 2.1a for location of studies). However, vorticity from different transects across the Himalaya almost certainly reflect different stages of flow and, as such, likely do not indicate a single time profile for flow within the Greater Himalayan sequence, but a mixing of data reflecting flow at different stages of the extrusion process. These data need to be linked with pressure-temperature-time data to ultimately provide a 'snapshot' of strain conditions during extrusion of the Greater Himalayan sequence. Specimens are plotted at the approximate structural position from which they were collected. All data have been plotted with respect to the Main Central thrust (MCT) definition used in this study. The bars and ellipses depict the range of all data from that study; each study is depicted with a unique bar shape/shade combination. The horizontal length of the bar/ellipse represents the range in vorticity data for each study, while the vertical thickness of the bar/ellipse represents a range in the structural position of the specimens. The vertical lines represent the average vorticity value for each study or location. Thin grey lines indicate that a rigid grain technique was used to determine vorticity (e.g., Simpson and De Paor 1993, 1997; Wallis et al., 1993; Jessup et al., 2007). Vertical white bars with a black outline indicate that vorticity was determined through comparison of strain ratio of the specimen to the angle between the strain ellipse and the flow plane (e.g Wallis 1992, 1995). (B) Graphical representation of the change in vorticity across the Greater Himalayan sequence. Vertical dark grey lines represent the approximate structural position of specimens used for vorticity analyses in various studies. The curved light grey lines envelope average vorticity values. STDS, South Tibetan detachment system; MCT, Main Central thrust.

through time with evidence suggesting that the outermost branches, away from the center of the Greater Himalayan sequence, are the youngest (Godin et al., 2006a). The youngest, uppermost branch of the STDS cuts down-section into the ductile shear zone in its footwall, a relationship that is well-documented in the Everest region of Nepal and adjacent Tibet (Searle et al., 2003; Cottle et al., 2007). Because portions of the STDS have been removed, studying the evolution of the shear zone through time, using structural position as a proxy, is difficult. The same problem does not exist along the lower boundary of the Greater Himalayan sequence. Thus, studying different portions of the transposed lower Greater Himalayan sequence, which record the evolution of the high-strain zone associated with the MCT, can provide insight into the kinematics of the shear zone through time.

As discussed previously, vorticity studies carried out along the high Himalaya appear to show a downward increase in pure shear in the Greater Himalayan sequence from the STDS to the base of the migmatitic portion of the exhumed mid-crustal rocks. The results from structurally lower specimens, however, are not significantly different from one another (Figure 2.14). The lack of variation is intriguing, as the structurally lower specimens from the Greater Himalayan sequence, if all deformation is assumed to be contemporaneous, should exhibit a greater amount of pure shear strain simply due to increased lithostatic pressure. The absence of such an increase may reflect continuous unloading by the STDS above and a steady state strain coupling between the two bounding shear zones. Alternatively, and preferred in this study, the vorticity data may reflect extrusion of the Greater Himalayan sequence contemporaneous with its exhumation and a continuous change in the structural level of the active portion of the MCT.

## 2.8 Conclusions

Detailed lithologic mapping, in conjunction with quartz *c*-axis data, has constrained interpretation of the structural position of the Ramgarh thrust and the MCT. Previous studies had placed the Ramgarh thrust within the Greater Himalayan sequence, as defined in this study, in central Nepal. The results of this study are consistent with interpretations that equate the Ramgarh thrust with the MCT at the base of the Greater Himalayan sequence more than 8 km south of the previously mapped locations in the Kali Gandaki valley.

Quartz *c*-axis fabrics and geothermometric data are interpreted to show that the Greater

Himalayan sequence exposed in the Kali Gandaki valley in central Nepal was pervasively deformed during extrusion. This deformation is characterized by a dominant top-to-the-south sense of shear that is observed across the Greater Himalayan sequence from its base up into its migmatitic upper portion. Quartz *c*-axis fabrics were either not preserved or attained in the calc-silicate and orthogneiss dominated parts of the Greater Himalayan sequence.

Estimations of vorticity help quantify the flow kinematics in the Greater Himalayan sequence exposed in central Nepal. Our data add to a limited, but expanding kinematic database from across the orogen that, at a first order, define a general change in vorticity across the Greater Himalayan sequence with structural position. Vorticity values from this study average 0.67, show a significant component of pure shear deformation (53%), and corroborate previous investigations indicating that deformation within the Greater Himalayan sequence is dominantly characterized by a combination of pure shear and simple shear strain (Grasemann et al., 1999; Law et al., 2004; Jessup et al., 2006; Carosi et al., 2006, 2007). While more data are needed to better understand the process of lateral extrusion of the mid-crust, the work currently being done in the Himalaya has direct implications for models of similar processes in other orogens.

## Acknowledgments

This research was supported through a Natural Science and Engineering Research Council of Canada Discovery grant to L. Godin and Canada Graduate Scholarship to K. Larson. Discussion in the field with Dawn Kellett helped elucidate the geologic complexities of the map area. The Late Pasang Tamang, Nurbu Tamang, Pardap Tamang, Lakpa Tamang, Ngima Tamang, and Mangale Sherestsa are thanked for logistic support. S.T. Johnston and R.A. Price helped improve early versions of this paper. Reviews by M.P. Searle, R.D. Law, A.J. Martin, and an anonymous reviewer enhanced the final version of this manuscript. N. Portelance performed copy-editing of the manuscript.

# Chapter 3

# Out-of-sequence deformation and expansion of the Himalayan orogenic wedge: insight from the Changgo culmination, south-central Tibet

## 3.1 Abstract

The Changgo culmination in south-central Tibet is one of a series of tectonic windows through the Tethyan sedimentary sequence along the North Himalayan antiform, in which underlying Greater Himalayan series rocks crop out. The Changgo culmination consists of a multiphase granitic core surrounded by a deformed, predominantly metasedimentary carapace. The carapace comprises two structural domains, a lower domain characterized by recumbent south-verging isoclinal folds and a dominant retrograde metamorphic mineral assemblage, and an upper domain characterized by upright-to-overturned, south-verging open-to-close folds and a dominant prograde metamorphic mineral assemblage. The main intrusive phase within the Changgo culmination, termed the Changgo granite, consists of a well-foliated alkali-feldspar porphyritic granite. Quartz *c*-axis orientations in oriented specimens of the foliated granite show a top-to-the-south shear sense. The quartz *c*-axis fabrics are interpreted to indicate south-verging shearing during deformation of the rocks that are now within the core of the culmination. The contact between the granitic core and the carapace of the Changgo culmination is marked by a top-to-the-north sense shear zone that is interpreted to be the northern continuation of the South Tibetan detachment system. The shear zone, which deforms both the granite and overlying sedimentary carapace, contains large (30 m-scale) lenses of mylonitized leucogranite. Sensitive high-resolution ion microprobe (SHRIMP) dating of zircon from this mylonitized leucogranite yielded a U-Pb age of 35.4 ± 0.3 Ma. This crystallization age is interpreted to reflect Eocene crustal thickening that was coeval in the Changgo area with the shortening event that produced the south-verging folds in the upper domain of the metasedimentary carapace. Zircon from the porphyritic main phase of the Changgo granite yielded a SHRIMP-determined U-Pb age of 23.5 ± 1.0 Ma. Monazite from an undeformed aplite dyke, part of the youngest phase observed in the Changgo granite, was dated by isotope dilution-thermal ionization mass spectrometry U-Pb analyses at 22.08 ± 0.19

Ma. The aplite dyke cross-cuts the fabric associated with south-directed shearing of the Changgo granite; therefore, the south-directed shearing must have ended at this locality between *ca*. 23.5 Ma and 22.08 Ma. The cross-cutting aplite dykes are deformed in the shear zone related to the South Tibetan detachment system. Final ductile displacement along the shear zone must post-date the crystallization of the aplite dykes it deforms. It is interpreted to have ceased prior to 18.4 Ma when muscovite collected from the shear zone became closed to argon diffusion. Zircon from undeformed granitic dykes that cross-cut the South Tibetan detachment system in the adjacent Kung Tang area were dated by SHRIMP U-Pb analyses at *ca*. 16.3 Ma. Displacement along the South Tibetan detachment system must have ended prior to the intrusion of these dykes. The exhumation of the Changgo culmination at *ca*. 18 Ma, as recorded by $^{40}Ar/^{39}Ar$ cooling ages, is interpreted here to be due to tectonically-driven erosion that occurred during crustal thickening that rebuilt the orogenic critical taper wedge in central Nepal. Subsequently, the orogenic critical taper wedge expanded toward the foreland as the main locus of displacement shifted from the Main Central thrust to the Main Boundary thrust.

## 3.2 Introduction and Background

The Greater Himalayan sequence, part of the exhumed mid-crustal metamorphic core of the Himalayan-Tibetan orogen, crops out along the entire length of the high Himalaya at the southern edge of the Tibetan plateau. It is bounded above by the South Tibetan detachment system (STDS; Figures 3.1A,B), an anastomosing network of Miocene-age north-dipping, normal-sense faults (Burchfiel et al., 1992; Hodges et al., 1992) that have been mapped along the length of the orogen. Rocks structurally above the STDS comprise a southward-tapering, supracrustal sedimentary wedge that was deformed as it was scraped off of the under-riding Indian craton by the over-riding Asian crust during the initial stages of the collision (Searle et al., 1987). These rocks, which make up the Tethyan sedimentary sequence (TSS), crop out across the Tibetan plateau northward from the STDS to the Yarlung-Tsangpo ophiolite belt (Figure 3.2), which has been interpreted to mark the suture between India and Asia (see review in Yin and Harrison, 2000). Granitic and metamorphic rocks are exposed in conspicuous ellipsoidal structural culminations between the STDS and the Yarlung-Tsangpo suture (Figure 3.2). These culminations within the TSS outline an east-west trending structure referred to as the North

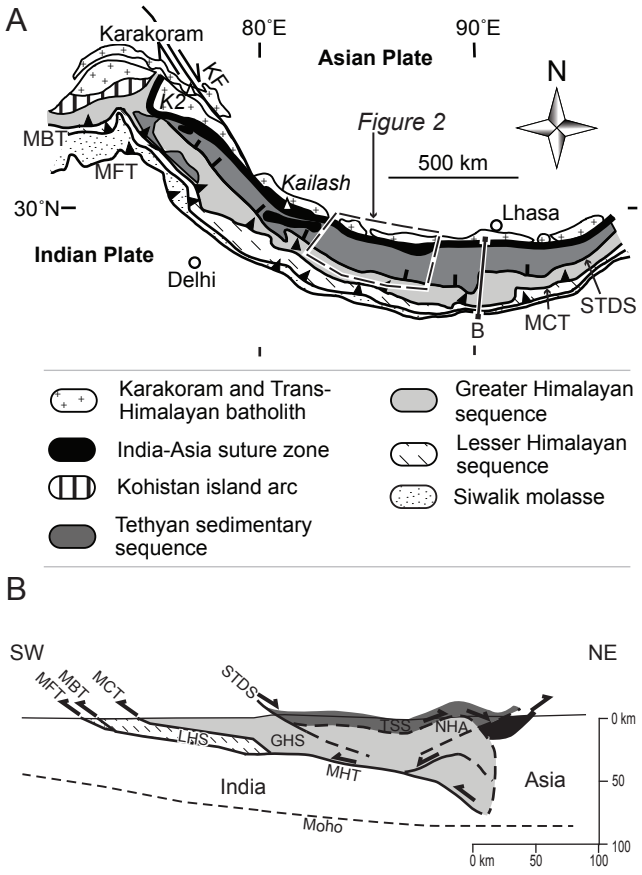


**Figure 3.1**
A) Simplified geologic map of the Himalaya-Karakoram arc and adjacent southern Tibet (Modified after Hauck et al., 1998). Approximate location of Figure 3.2 is outlined by a dashed box. B) Simplified vertical geologic section along the line 'B' as shown in Figure 3.1A (Modified after Hauck et al., 1988). STDS, South Tibetan detachment system; MCT, Main Central thrust; MBT, Main Boundary thrust; MFT, Main Frontal thrust; MHT, Main Himalayan thrust; NHA, North Himalayan antiform; KF, Karakoram fault; GHS, Greater Himalayan sequence; TSS, Tethyan sedimentary sequence.

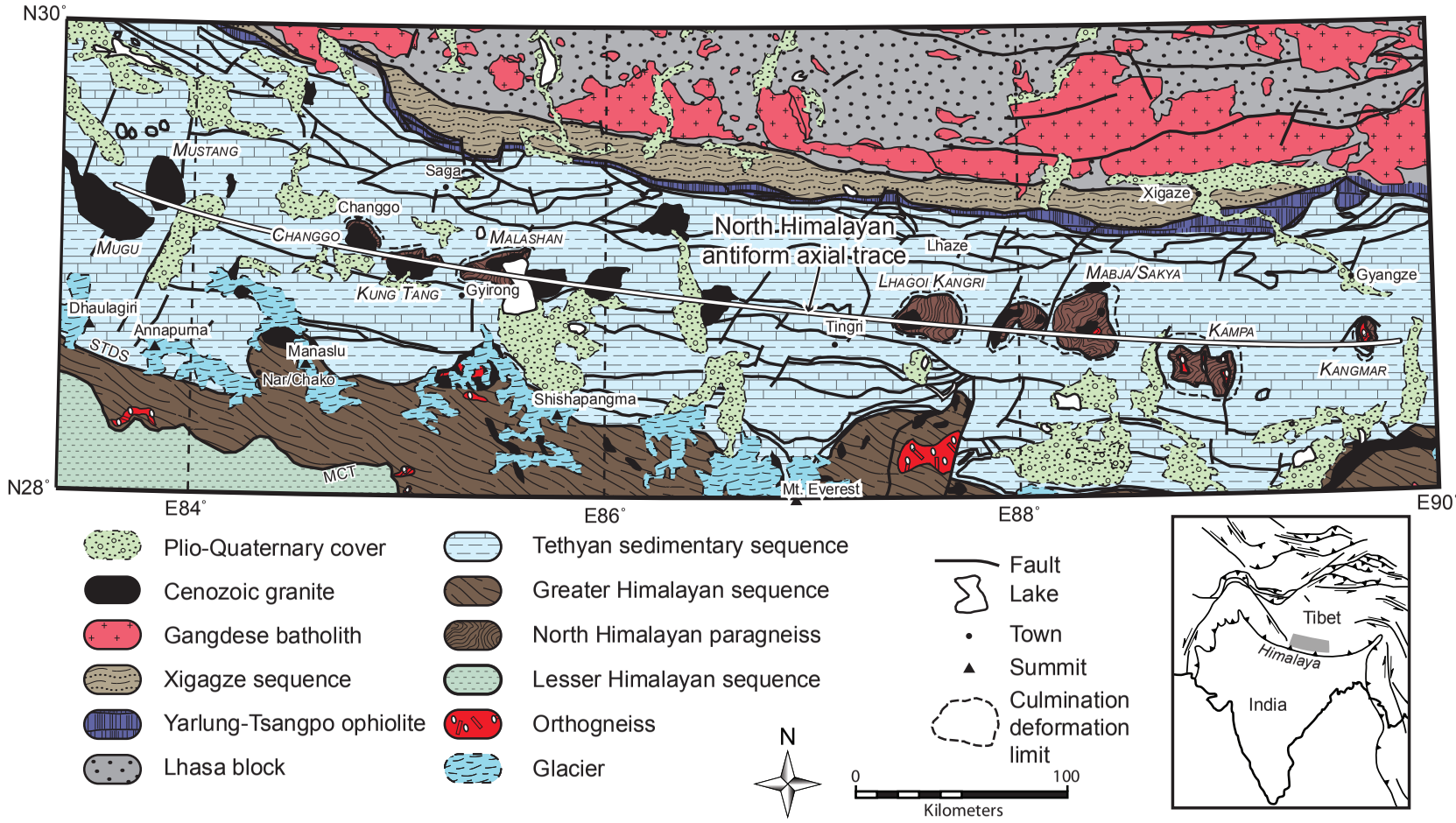


**Figure 3.2**
Simplified geologic map of south-central Tibet and adjacent regions based on data compiled from Schärer et al., (1986), Lee et al., (2000, 2004, 2006), Guitang et al., (2004), Zhang et al., (2004), Aoya et al., (2005, 2006), Watts et al., (2005), Gleeson and Godin (2006), Quigley et al., (2006), Lee and Whitehouse (2007) and this study. Culminations are identified by bold, italicized names in small capital letters; geographic names (towns or summits) are identified by plain text.

Himalayan antiform (Figure 3.2) (Burg and Chen, 1984).

Although syntectonic metamorphism within the North Himalayan antiform was recognized during early regional mapping, the relationship between these metamorphic rocks and the Greater Himalayan sequence rocks that are exposed in the high Himalaya to the south was initially not considered (Burg et al., 1984). Subsequently, crustal-scale seismic reflection data, collected from south of the STDS and extending to the north beyond the Yarlung-Tsangpo suture (Nelson et al., 1996), have been interpreted as indicating that the metamorphic rocks exposed along the North Himalayan antiform are laterally continuous with the exhumed mid-crustal rocks exposed along the high Himalaya (Figure 3.1B; Nelson et al., 1996; Hauck et al., 1998). Furthermore, geochemical comparison of specimens sampled from within the Kangmar and Mabja/Sakya domes, two culminations that are part of the North Himalayan antiform (Figure 3.2), with data from specimens sampled from within the high Himalaya to the south have been interpreted as indicating that the individual culminations are indeed tectonic windows in which the Greater Himalayan sequence is exposed (Zhang et al., 2004).

The culminations that define the North Himalayan antiform share lithochemical and petrologic similarities with metamorphic rocks exposed along the front of the Himalaya, however, these metamorphic and granitic rocks crop out in a peculiar position; *ca*. 100 km north of the surface exposure of the STDS. Recent numerical models of the thermo-mechanical evolution of the Himalayan-Tibetan orogen have shown that a feature like the North Himalayan antiform could have formed during Miocene southward extrusive flow of the mid-crust if the lid to the extruding material was imperfectly decoupled (e.g. Beaumont et al., 2004). Other studies have suggested that the North Himalayan antiform may be the result of out-of-sequence thrusting (Burg et al., 1984), diapirism (Le Fort, 1986; Le Fort et al., 1987), or some combination of the two (Lee et al., 2004, 2006). However, the paucity of geologic data from rocks within the North Himalayan antiform, relative to the better-studied exhumed mid-crustal rocks that crop out along the southern front of the Himalaya, severely limits the amount of data available to verify the predictions of the modeling and thus provide new insight on the evolution of the North Himalayan antiform.

Regional reconnaissance investigations of the geology of southern Tibet (e.g. Schärer et al., 1986; Guitang et al., 2004; Watts et al., 2005) have identified at least twelve culminations along the North Himalayan anticline between E90˚ and E84˚ (Figure 3.2). Only four of these,

the Kangmar dome (Burg et al., 1984; Chen et al., 1990; Lee et al., 2000), the Mabja/Sakja dome (Lee et al., 2004, 2006; Zhang et al., 2004; King et al., 2007; Lee and Whitehouse, 2007), the Kampa dome (Quigley et al., 2006, 2008), and the Malashan dome (Aoya et al., 2005, 2006; Kawakami et al., 2007), have been the subject of detailed and comprehensive geologic investigation. The geologic interpretations resulting from these studies vary considerably. Some workers have interpreted the core of the North Himalayan culminations to be foliated Miocene granite in intrusive contact with its country rocks (Aoya et al., 2005, 2006; Kawakami et al., 2007), while others suggest that the deformed cores comprise Ordovician orthogneiss that underwent metamorphism in the Miocene (Lee et al., 2000, 2004; Quigley et al., 2006). There are also significant differences in interpretation of the nature and significance of the contact between the metamorphic or igneous core and its meta-sedimentary carapace along the North Himalayan antiform. In the Kampa dome (Figure 3.2) a top-to-the-north sense shear zone that marks the interface has been interpreted as the folded continuation of a discrete STDS (Quigley et al., 2006). In the Malashan dome (Figure 3.2) a similarly described shear zone is considered not to be part of the STDS, but instead interpreted as a structurally and stratigraphically higher top-to-the-north sense high-strain zone (Aoya et al., 2006; Kawakami et al., 2007). The contact between the core and the meta-sedimentary carapace in the Kangmar and Mabja domes is interpreted to represent a nonconformity (Lee et al., 2000, 2004) and both domes are thought to have been deformed within a diffuse mid-crustal portion of the STDS (Lee et al., 2000, 2004, 2006).

The differences in data and interpretations reported from various previous studies of the North Himalayan antiform could be a consequence of different fundamental processes controlling the evolution of each dome, but the spatial, temporal, and structural similarities along the North Himalayan antiform suggest that all the domes had a similar history. In this study we have mapped in detail geologic structures in the northern half of the previously unmapped Changgo culmination, southwest of Saga, south-central Tibet (Figure 3.2). We also provide preliminary geochronological data from the nearby Kung Tang culmination. Structural analyses, petrologic investigation, $^{40}Ar/^{39}Ar$ thermochronometry, and U–Pb ID-TIMS and SHRIMP II geochronometry have helped elucidate the tectonic history of this portion of the North Himalayan antiform. The combination of new data from the Changgo area with data from other studies along the North Himalayan antiform provide the basis for a consistent regional tectonic interpretation that explains

both the evolution of the North Himalayan antiform and some of the differences observed along its >500 km length. Our model also incorporates data from the southern front of the Himalaya in Nepal, and provides insight into the evolution of the orogen during the *ca*. 20-12 Ma transfer of slip from the Main Central thrust to more foreland propagating thrust faults such as the Main Boundary thrust.

## 3.3 Geology of Changgo dome

### 3.3.1 Introduction

Based on thermal emissions and reflections from solar radiation intercepted by muscovite within exposed bedrock, detected through ASTER (Advanced Spacebourne Thermal Emission and Reflection Radiometer) imaging, Watts et al., (2005) differentiated between culminations along the the North Himalayan antiform that contain muscovite-poor, Paleozoic orthogneiss and others that contain relatively muscovite-rich Miocene two-mica granite. Comparison of published geologic maps (e.g. Zhang et al., 2004; Lee et al., 2004) with the results of ASTER image analyses by Watts et al., (2005) for the same regions indicates that Watts et al., (2005) were able to successfully distinguish between these two categories of rocks. Applying the same band ratios to ASTER imagery of the Changgo area, Wolters (2006) found that a two-mica muscovite-rich granite body forms the core of the Changgo culmination. This is shown clearly in a processed ASTER image of the Changgo area (Figure 3.3A) where red colours are used to represent the band-ratio values characteristic of muscovite. Subsequent fieldwork has shown that the distribution of red in the image matches closely with the actual distribution of granitic rock (Figure 3.4). ASTER image analysis of the adjacent Kung Tang culmination also indicates that the core is muscovite-rich (Figure 3.3B).

The Changgo dome consists of a granitic core and a surrounding meta-sedimentary carapace that itself is structurally overlain by unmetamorphosed sedimentary rocks (Figure 3.4). U-Pb geochronometry, which will be discussed in a later section of this chapter, shows that the granite core formed in the Miocene. According to the regional compilation map of Guitang et al., (2004) the surrounding cover rocks are Jurassic.

### 3.3.2 Intrusive core

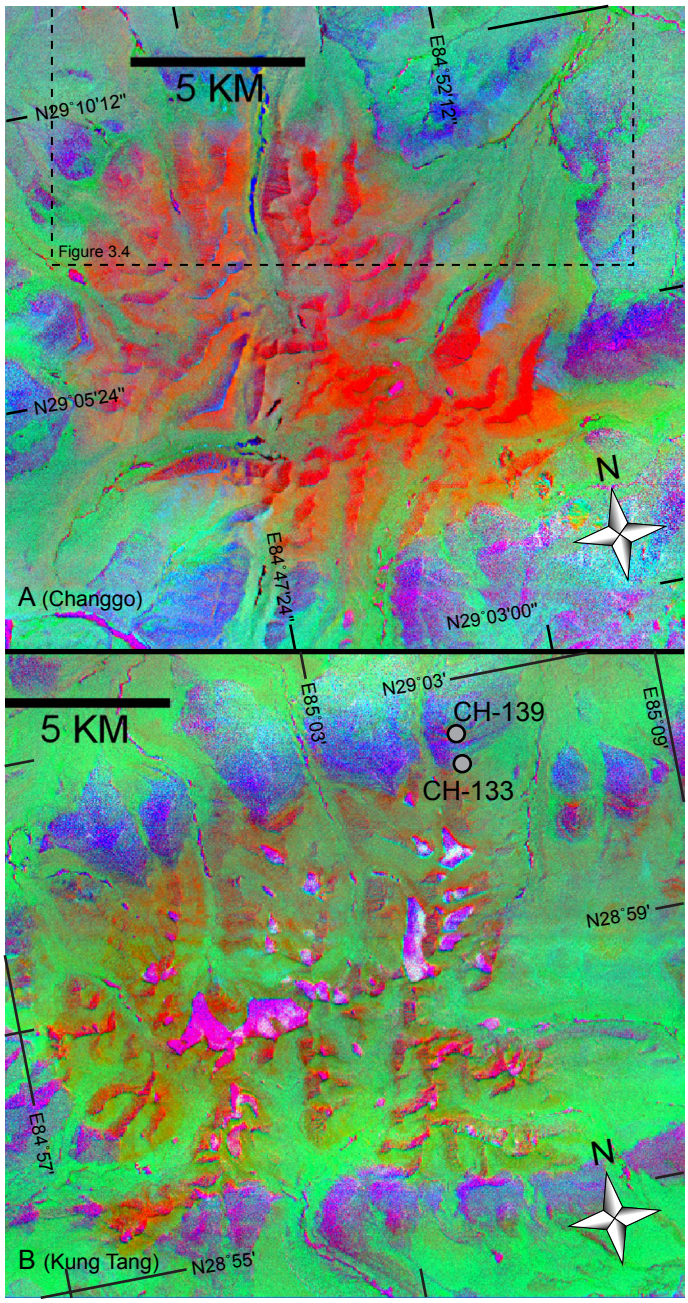


**Figure 3.3**
Processed ASTER (Advanced Spaceborn Thermal Emission and Reflection Radiometer) images of the Changgo culmination (A) and the Kung Tang culmination (B). Red denotes the spectral signature characteristic of muscovite, and therefore, muscovite-rich areas appear red in the image. Muscovite-poor areas appear blue. Geochronologic sample locations in the Kung Tang culmination are indicated by black-outlined grey circles. Modified from Wolters, 2006.

The core of the Changgo dome is a multiphase granitic pluton (Figures 3.4, 3.5A). The oldest and dominant phase, which comprises >90 % of the pluton, is foliated alkali-feldspar porphyritic granite (phase 1 in Figure 3.5B) characterized by feldspar laths up to 5 cm long in a medium-to-coarsely crystalline groundmass of quartz, muscovite, biotite, and minor accessory minerals (Figure 3.5C). The foliation is defined by aligned muscovite and biotite grains and quartz grain-shape fabrics. Quartz grain-shape fabrics also locally define a faint lineation. Where the foliation is strongly developed, the porphyritic granite appears to be similar to descriptions of orthogneiss in the core of the Kangmar dome as described by Lee et al., (2000) and the Kampa dome as described by Quigley et al., (2006). The porphyritic granite is intruded by an intermediate phase of equigranular granite (phase 2 in Figure 3.5B) that comprises less than ca. 10% of the exposed stock and is mineralogically indistinguishable from the older porphyritic phase. The equigranular phase is commonly foliated with a planar fabric defined by mica and quartz grain-shapes. The youngest igneous phase consists of a network of aplitic dykes characterized by a fine-to-medium crystalline alkali-feldspar, quartz, and muscovite dominated assemblage (Figure 3.5D). These dykes cross-cut both of the older foliated phases and are generally undeformed (Figure 3.5B).

### 3.3.3 Core/carapace contact

The aplite dyke phase of the Changgo granite phase appears to be foliated only at the contact between the core and carapace of the culmination. At this contact all planar structures have been transposed parallel to a mylonitic foliation (Figure 3.6A) that defines a > 300 m thick shear zone. The rocks that were deformed in the shear zone commonly have been shattered, detached and displaced by periglacial fracturing to form a felsenmeer that conceals much of the intact bedrock (Figure 3.6B, C; see Figure 3.6E for locations of Figures 3.6B, C). Within the local bedrock exposures in this fault zone most of the porphyroclasts material, predominantly boudinaged quartz veins within a fine-grained mica-rich metapelitic mylonite, exhibit symmetrical pressure shadows. The relative lack of significant asymmetric features may indicate a dominant pure shear strain component in this fault zone. The few porphyroclasts that do record a sense

**Figure 3.4**
Geologic map of the northern half of the Changgo culmination. Line A-A´ denotes the line of section for Figure 3.7.

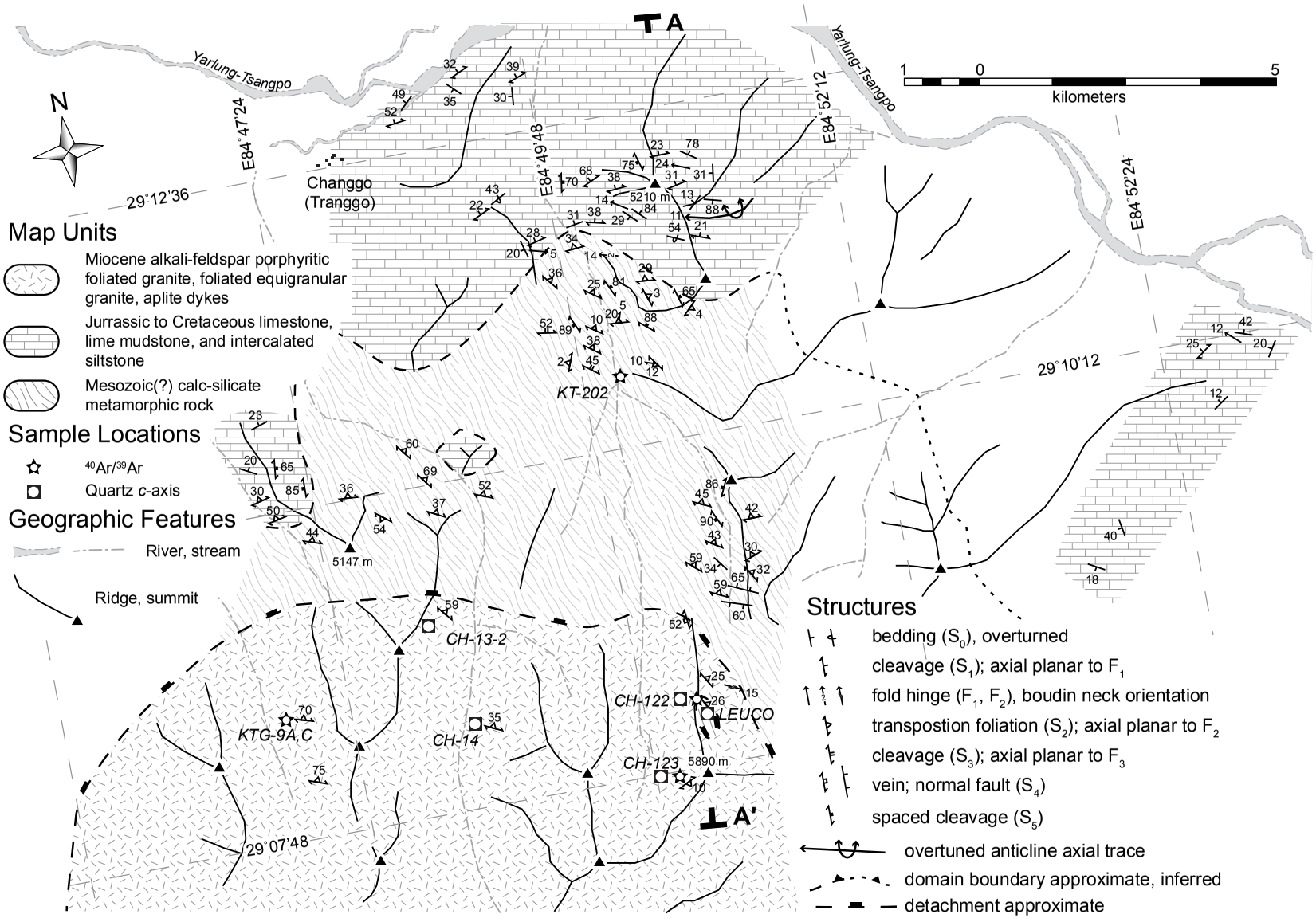
A
A'
Yarlung-Tsangpo
Yarlung-Tsangpo
N
1 0 5
kilometers
E84°47'24
E84°49'48
E84°52'12
E84°52'24
29°12'36
29°10'12
29°07'48
Changgo
(Tranggo)
10 m
5147 m
5890 m
KT-202
CH-13-2
CH-122
LEUCO
CH-14
CH-123
KTG-9A,C
Map Units
Miocene alkali-feldspar porphyritic foliated granite, foliated equigranular granite, aplite dykes
Jurrassic to Cretaceous limestone, lime mudstone, and intercalated siltstone
Mesozoic(?) calc-silicate metamorphic rock
Sample Locations
40Ar/39Ar
Quartz c-axis
Geographic Features
River, stream
Ridge, summit
Structures
bedding (S0), overturned
cleavage (S1); axial planar to F1
fold hinge (F1, F2), boudin neck orientation
transpostion foliation (S2); axial planar to F2
cleavage (S3); axial planar to F3
vein; normal fault (S4)
spaced cleavage (S5)
overtuned anticline axial trace
domain boundary approximate, inferred
detachment approximate

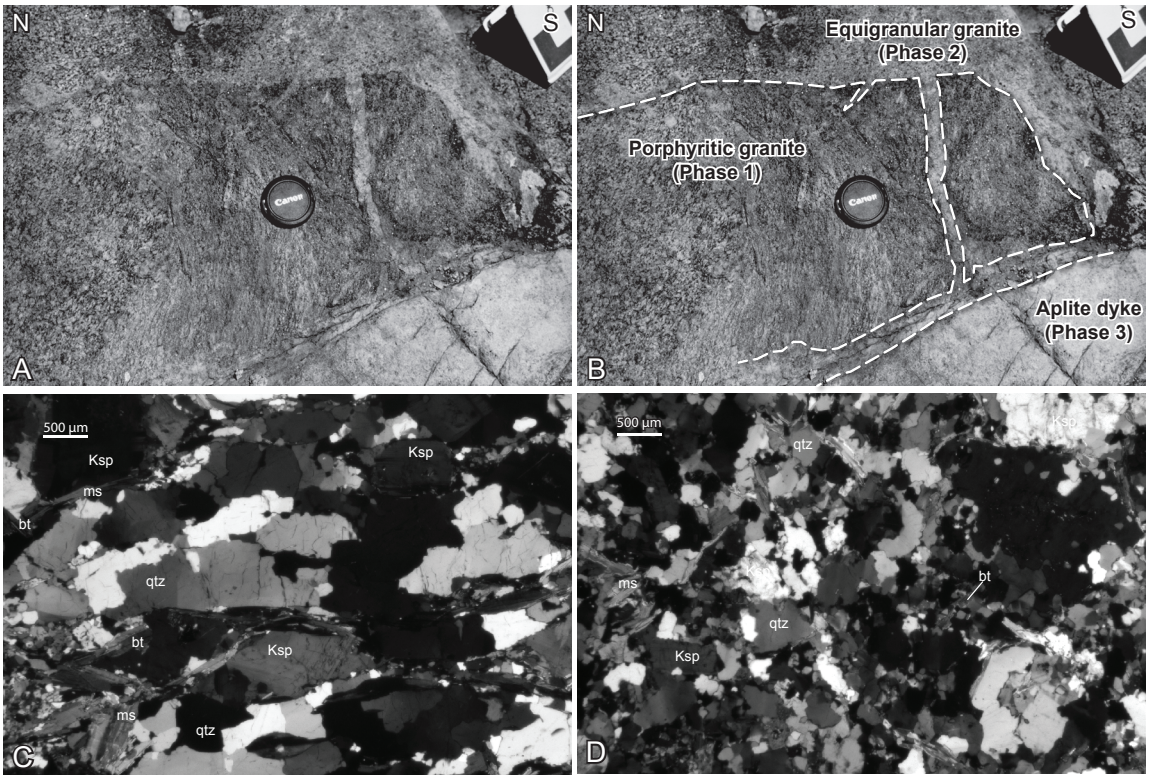


**Figure 3.5**
A) Photograph looking down to the east at the three cross-cutting phases of the Changgo granite. The lens cap is 58 mm in diameter. B) An annotated version of the photograph in A depicting the three main intrusive phases. C) Cross-polarized photomicrograph of the dominant feldspar porphyritic phase of the Changgo granite (phase 1). D) Cross-polarized photomicrograph of the aplite dyke pictured in B (phase 3). Ksp, potassium feldspar; qtz, quartz; bt, biotite; ms, muscovite.

of shear generally suggest top-to-the-north (Figure 3.6D). A top-to-the-north shear sense is also indicated by well-developed extensional shear bands observed in bedrock exposures near the upper boundary of the shear zone (Figure 3.6F). Lenses of medium-to-coarsely crystalline alkali-feldspar + quartz + muscovite + tourmaline leucogranite are found in the shear zone (Figure 3.6B) and are contained entirely within the meta-pelite. The leucogranite, which is in a structural position similar to the Manaslu leucogranite mapped to the south in the high Himalaya (Searle and Godin, 2003), is deformed and is characterized by well-developed quartz ribbons and mylonitic fabrics (Figure 3.6G).

### 3.3.4 Sedimentary and meta-sedimentary cover rocks

The rocks surrounding the core of Changgo culmination comprise two different tectonostratigraphic domains (Figure 3.7). In the lower domain, the protolith was mainly an impure carbonate rock, varying from lime mudstone to medium-grained calcareous sandstone, and shows evidence for at least two episodes of metamorphism. The best-preserved metamorphic episode is characterized by a retrograde assemblage dominated by epidote and calcite overgrowths on severely degraded pyroxene (likely diopside; Figure 3.8A). In some specimens almost no recognizable prograde minerals are preserved. Locally abundant pelitic schist also preserves evidence for retrograde metamorphism (M2) superimposed on earlier prograde metamorphism. In some of these rocks, 0.5-1 mm diameter porphyroblasts of garnet are completely pseudomorphed by fine-grained muscovite (Figure 3.8B). In others, large (up to 2 cm long) randomly oriented andalusite porphyroblasts are pseudomorphed by muscovite and quartz (Figure 3.8C).

**Figure 3.6**
Photographs illustrating the extent and character of the shear zone at the interface between the granite core and the meta-sedimentary cover. A) View to the west at mylonitic meta-pelitic rocks that crop out near the base of the shear zone. The hammer is approximately 35 cm long. B) View south up-ridge at felsenmeer comprising blocks of leucogranite, peltic schist, and granite from the shear zone. All blocks in the field of view comprise rocks that were deformed by movement along the shear zone. Location and view direction of the photo is shown in E. C) View down-ridge to the north at the shear zone. Location and viewing direction of the photo locale is shown in the panorama of the Changgo culmination in E. D) Sigmoidal porphyroclast within a mylonitic meta-pelite within the shear zone. The sense of shear is top-to-the-north; pencil is 19 cm long. E) Panorama of the Changgo culmination showing the approximate location of the contact between the granite and meta-sedimentary carapace. The viewing directions of B and C are depicted. F) Oriented deformed calc-silicate specimen from near the top of the shear zone. Well-defined extensional shear bands indicate top-to-the-north shear. G) Cut-section of mylonitic leucogranite from within the shear zone showing well-developed ribbon quartz. Coin is ~2 cm in diameter.

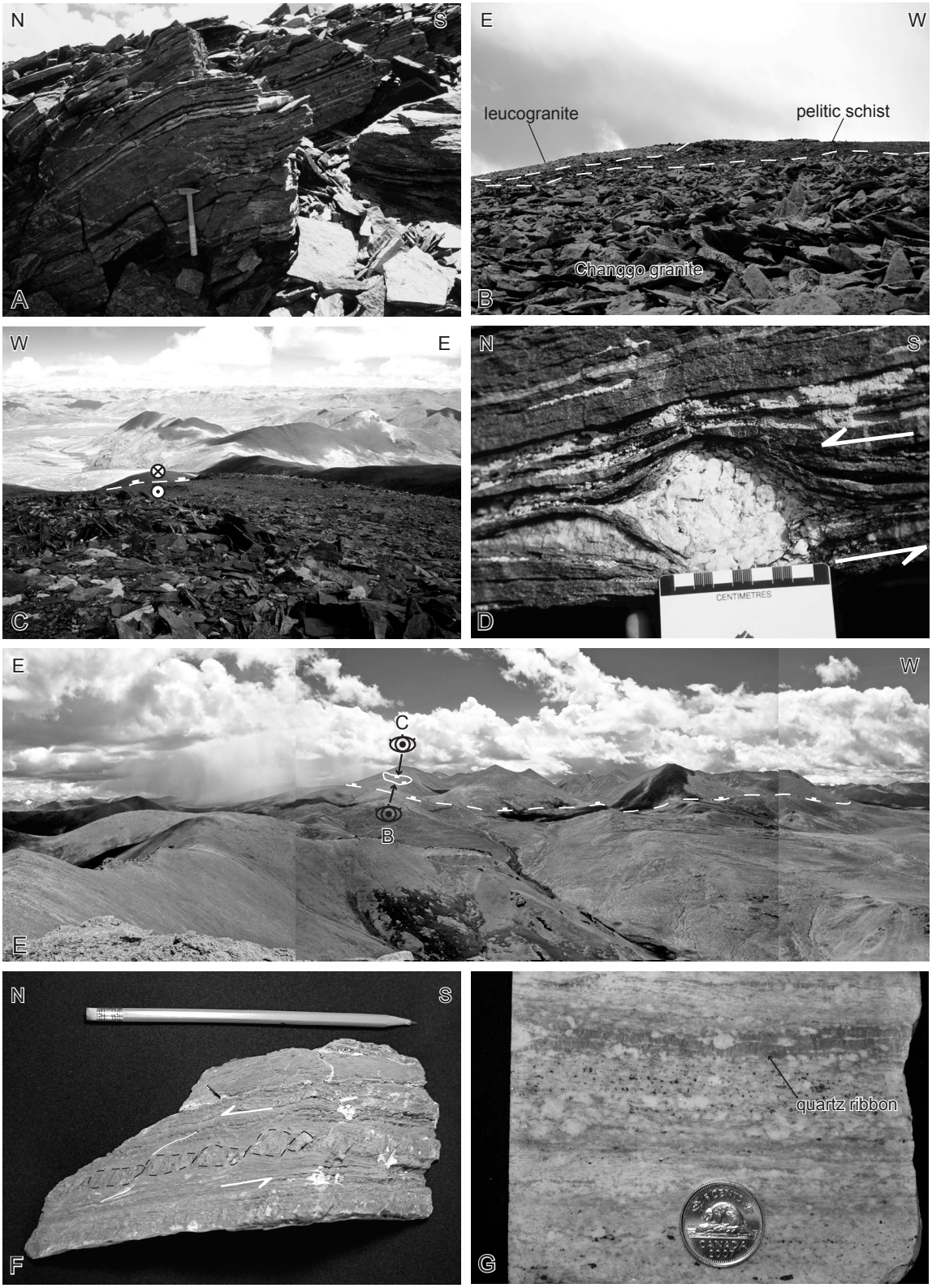
N
S
A
E
W
leucogranite
pelitic schist
Changgo granite
B
W
E
C
N
S
CENTIMETRES
D
E
W
C
B
E
N
S
F
quartz ribbon
G

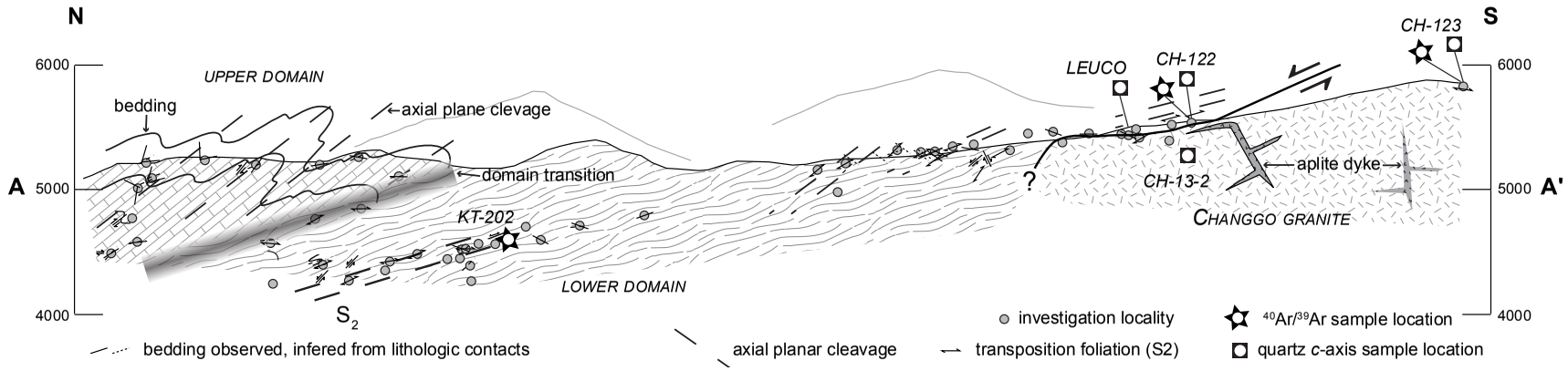


**Figure 3.7**
Vertical geologic section along line A-A´ (see Figure 3.4) through the northern portion of the Changgo culmination (localities depicted are projected horizontally into the vertical section plane). The upper domain is characterized by south-verging overturned folds in Jurassic rocks of the TSS (Tethyan sedimentary sequence), while the lower domain is characterized by large-scale, low-amplitude folding of a transposition foliation. A foliation within the granitic core with the same general orientation is interpreted to be related to this transposition foliation. Late cross-cutting aplitic dyke configurations are portrayed schematically as dark-grey wedge-tipped layers.

Mafic meta-volcanic rocks are intercalated within the calc-silicate dominated assemblage in two localities at similiar tectonostratigraphic levels. At one locality the meta-volcanic rocks form a 1-2 m thick lens of fine-to-medium grained, amphibole porphyroblastic schist (Figure 3.8D) that is cut by aphanitic mafic dykes and sills. Both the schist and the cross-cutting basaltic dykes and sills, which do not appreciably extend into the surrounding meta-sedimentary rock, display the dominant regional foliation. At another location, meta-volcanic rocks comprise a 0.5 m thick reddish-brown weathering, grey-black, foliated aphanitic meta-basalt. The meta-basalt is laterally discontinuous, perhaps because of tectonic boudinage subsequent to its eruption as a flow, or perhaps reflecting its intrusion as a sill. The meta-volcanic rocks, while not voluminous in the Changgo area may reflect rifting that occurred locally within the northern Indian margin contemporaneous with sediment deposition (Liu and Einsele, 1994). Similar volcanic intercalations, although Lower Permian in age, have been described in the nearby Gyirong region (Garzanti et al., 1999), which is located south of the Malashan area (Figure 3.2)

Metamorphism and strain decrease significantly structurally up-section, over a relatively short interval (less than 300 m). This transition marks the boundary between the lower and upper tectonostratigraphic domains (Figure 3.7). The nature of this transition is uncertain; however, it is locally characterized by brittle-ductile top-to-the-south thrust-sense fabrics of an unknown age (Figure 3.8E). The structurally highest domain comprises unmetamophosed-to-low-grade meta-sedimentary rocks. These rocks are dominantly medium grey-to-mottled medium and dark grey

**Figure 3.8**
Photographic depiction of thin-sections and exposures of rocks within the meta-sedimentary carapace of the Changgo culmination. Photomicrographs were taken under plane-polarized light except where noted. A) Calc-silicate specimen from the lower domain exhibiting a transposition schistosity and showing partial regression of diopside (di) to epidote (ep) and calcite (ca). B) Meta-pelitic specimen from the lower domain with a well-established foliation, defined by muscovite (ms) and quartz (qtz), and garnet (gt) porphyroblasts that have been partially pseudomorphed by fine-grained muscovite. C) Andalusite pseudomorphed by muscovite and quartz in a specimen of phyllitic slate from within the lower domain. D) Amphibole, likely actinolite (ac), and calcite in an amphibole schist from the lower structural domain. E) View to the east of south verging c-s fabric within fine-grained calc-silicate phyllite near the upper domain, lower domain boundary. Pencil is 13 cm long. F) View westwards at south-verging folds in low-metamorphic grade limestone within the upper structural domain. Folds, which are defined by thin intercalated silt layers, are outlined by white lines. Lens cap is 58 mm in diameter. G) Photomicrograph of a specimen of phyllitic calc-silicate slate from the lowermost upper domain showing rotated porphyroblasts of talc (tc) and tremolite (tr) with partially developed face-controlled calcite fringes. H) View westwards at isoclinal folding of meta-sandstone within the lower structural domain. Lens cap is 58 mm in diameter; white line outlines a folded bed.

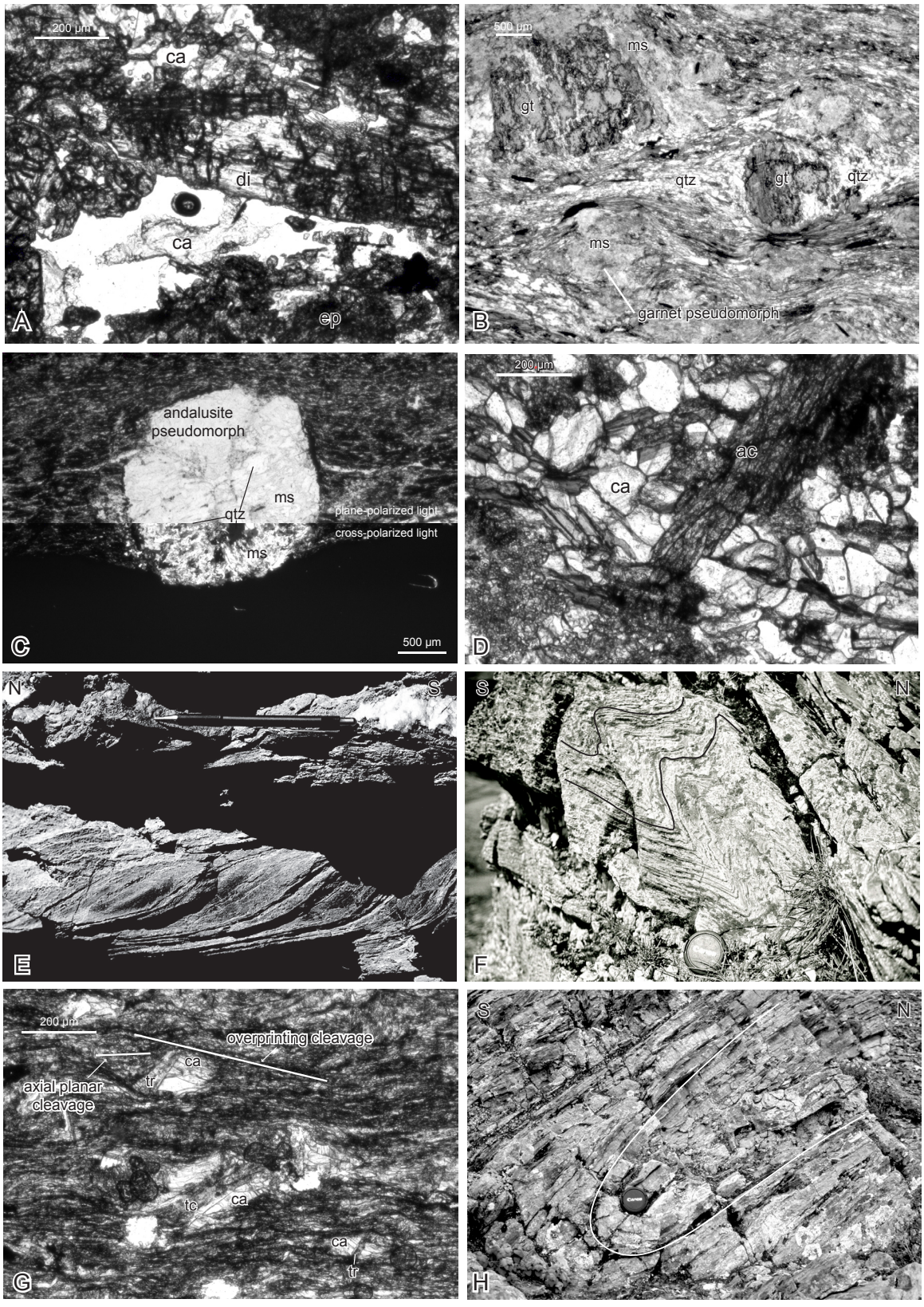
200 µm
ca
di
ca
ep
A
500 µm
ms
gt
qtz
gt
qtz
ms
garnet pseudomorph
B
andalusite
pseudomorph
ms
qtz
plane-polarized light
cross-polarized light
ms
500 µm
C
200 µm
ac
ca
D
N
S
E
S
N
F
200 µm
overprinting cleavage
ca
axial planar
cleavage
tr
tc
ca
ca
tr
G
S
N
H

weathering shaley lime-mudstone, commonly characterized by 2-3 mm thick siltstone interbeds (Figure 3.8F). Locally, more siliciclastic-rich rocks crop out stratigraphically above the shaley lime-mudstones. Such exposures are sparse in the map area, but generally consist of reddish-brown weathering fine-grained sandy-to-silty, lime mudstone. Fossils were not observed in the map area, however Tithonian (Upper Jurassic) ammonite fossils were collected in the nearby Malashan area (Aoya et al., 2006). The Tithonian fossils support the interpretation in a regional compilation map by Guitang et al., (2004), which indicates the sedimentary rocks in the Changgo area are Jurassic. At the lowermost structural levels of the upper domain, strata preserve evidence of metamorphism. The rocks at this level are generally fine grained calcareous phyllite and commonly contain euhedral porphyroblastic talc and tremolite (Figure 3.8G). The significance of these porphyroblasts with respect to structural chronology will be discussed in the following section.

## 3.4 Structural evolution

### 3.4.1 Introduction

Deformational characteristics in the Changgo culmination, summarized in Figure 3.9, change with structural depth both across and locally within structural domains. Description of the structures observed in the Changgo culmination begins with the highest structural domain in the metasedimentary carapace and progresses structurally deeper into the granitic core.

### 3.4.2 Carapace - Upper Domain

Deformation at the highest structural levels in the Changgo area, exposed in the northernmost portions of the map area (Figures 3.4, 3.7), is characterized by tight, inclined-to-overturned, south-verging folding of bedding (Figures 3.7, 3.10A) along west-northwest trending hinge lines (Figure 3.10C). These folds are associated with a moderately north-dipping axial planar cleavage (Figures 3.7, 3.10B) and are recognized at many scales from hand-specimen (Figure 3.8F) to kilometre scale (Figure 3.7). The deformation observed in the highest structural level in the Changgo area resembles features described from similar structural positions in the Malashan, Mabja/Sakya, and Kangmar domes where it is labeled D1 (Lee et al., 2000, 2004, 2006; Aoya et al., 2006; Chen et al., 1990). Based on microstructural observations and

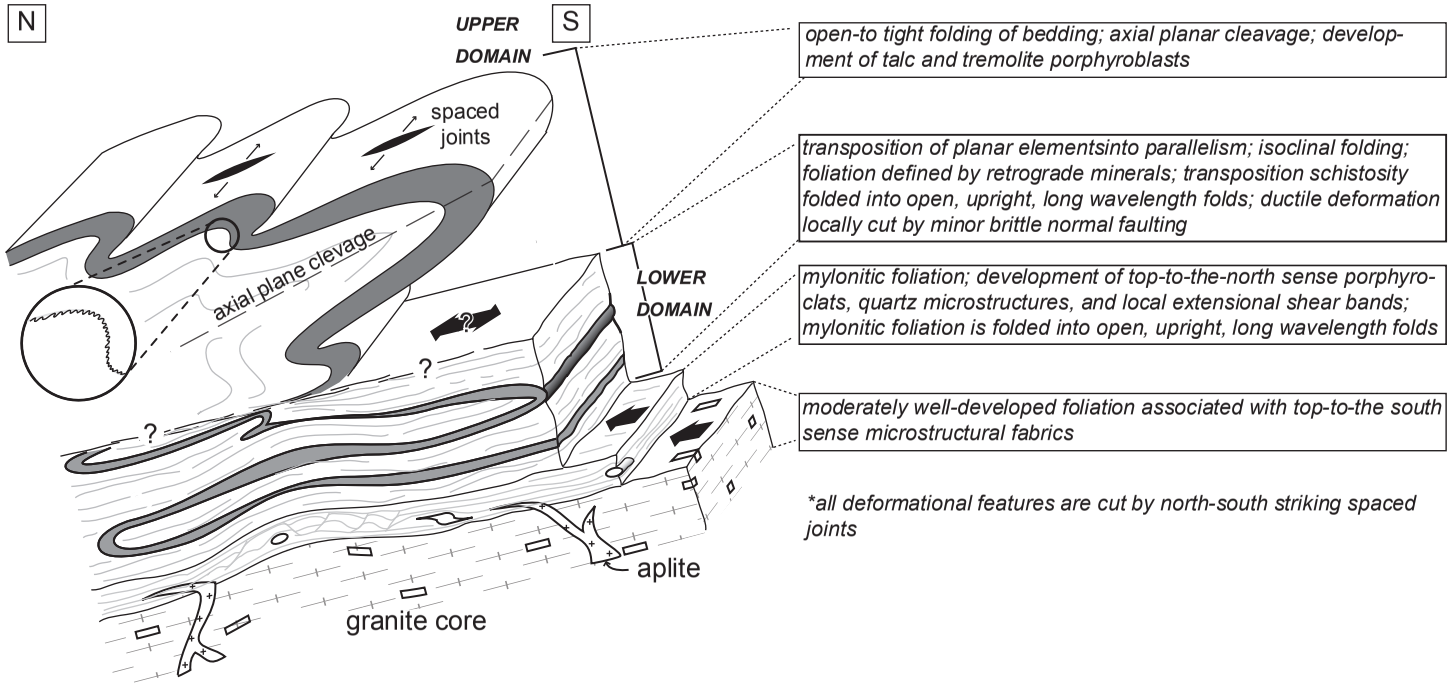


**Figure 3.9**
Schematic block diagram, looking eastward, of structural relationships among different domains of the carapace and core of the Changgo culmination.

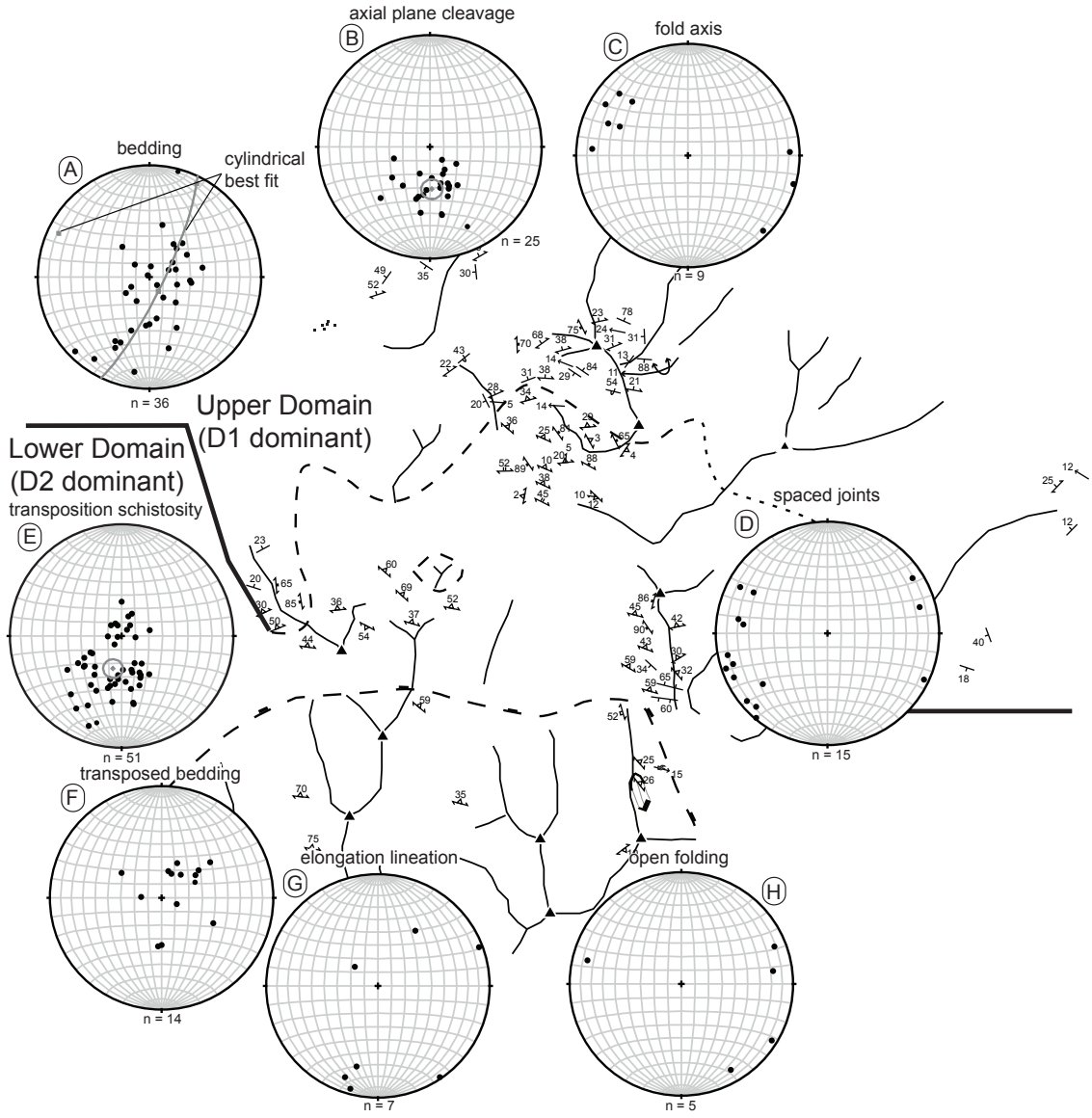


**Figure 3.10**
Summary of structural orientation fabric data from the upper domain (A,B,C, and D) and lower domain (D,E,F,G,and H) of the meta-sedimentary carapace. Data are presented in equal-area lower-hemispherical stereographic projections. A) Poles to bedding (upper domain). B) Poles to axial planar cleavage (upper domain). C) Fold hinges (upper domain). D) Poles to north-south striking, east-west extension-related joint set (upper and lower domains). E) Poles to transposition schistosity (lower domain). F) Poles to bedding preserved within the transposition foliation (lower domain). G) Mineral lineation defining stretch direction (lower domain). H) Fold hinges of low-amplitude long-wavelength folds (lower domain).

paleothermobarometric estimates in the Malashan and Kangmar areas, D1 has been interpreted as evidence for crustal thickening prior to main prograde metamorphism (Lee et al., 2000; Aoya et al., 2006; Kawakami et al., 2007).

Evidence of prograde metamorphism subsequent to fold development and crustal thickening in the Changgo area is preserved as talc and tremolite porphyroblasts at lower levels of the upper structural domain. The porphyroblasts overprint the dominant axial planar cleavage (Figure 3.8G) and therefore post-date the folding event. The talc porphyoblasts are commonly bent, however, and both talc and tremolite porphyroblasts have face-controlled calcite fringes indicative of rotation (Figure 3.8G), which suggests that they were subjected to strain after the development of the axial planar cleavage. A spaced secondary foliation that crosscuts the axial planar cleavage is visible in thin section (Figure 3.6G).

Spaced joints that strike roughly north-south (Figure 3.10D) overprint all other deformational features in the upper structural domain of the carapace. Similar joint sets in adjacent areas are interpreted to be related to large-scale east-west extension occurring throughout the Tibetan plateau (e.g., Godin, 2003; Gleeson and Godin, 2006).

### 3.4.3 Carapace - Lower domain

Deformation in the lower domain of the carapace is expressed as moderately north-dipping isoclinal folds (Figures 3.8H; 3.10E) and an associated transposition schistosity (Figure 3.7). Bedding, which is transposed into parallelism with the tectonic foliation (Figure 3.10F), can be recognized but only where there are significant compositional differences. Locally, a poorly-defined SSW-NNE elongation lineation (Figure 3.10G), defined by retrograde metamorphic minerals, is observed. In other parts of the North Himalayan antiform similarly described transposition foliations have been labeled S2 and have been interpreted to be related to a high-strain deformation event D2 (Lee et al., 2000, 2004; Aoya et al., 2006; Quigley et al., 2006).

The transposition schistosity is sub-horizontal-to-moderately north dipping throughout the map area (Figure 3.10E), indistinguishable from the attitude of the axial planar cleavage observed in the upper carapace domain. The similar orientation of the dominant foliations in the two structural domains of the Changgo culmination carapace may indicate a related genesis. It is possible that the transposition schistosity observed in the lower structural domain of the

carapace occurred in response to increased ductility due to slow progressive heating related to initial crustal thickening recorded by folds in the upper domain. In the lower structural domain the transposition schistosity is defined by a retrograde mineral assemblage. While this does not constrain the onset of deformation associated with the development of the transposition fabric, the retrograde-mineral-assemblage-defined foliation indicates that at least some deformation occurred after prograde metamorphism. This interpretation is supported by the rotation of porphyroblasts in the upper domain.

The transposition schistosity is folded locally by open, slightly inclined south-verging folds with roughly NNW-ESE trending fold axes (Figure 3.10H). There is no axial planar cleavage associated with this folding, but related large-scale warps are interpreted in cross-section (Figure 3.7). These structures may be related to the doming of the Changgo area and the development of the North Himalayan antiform.

Brittle deformation structures, including minor, roughly east-west striking normal faults and reverse faults (Figure 3.4), cross-cut all ductile fabrics in the lower structural domain of the carapace. These faults are not closely spaced and are only locally important. At most, they have accommodated a few meters of throw. These structures may reflect brittle accommodation at shallow structural levels of strain related to the late stages of acquisition of the domal geometry that is evident in the Changgo area. In studies of other culminations along the North Himalayan antiform, doming post-dates all ductile deformation and occurs after both muscovite and biotite became closed to Ar diffusion (Lee et al., 2000, 2006).

Similar to the upper structural domain of the carapace, north-south striking extensional joints overprint all other deformational features.

### 3.4.4 Changgo granite

The dominant deformation-related feature observed in the granitic core is a moderately well-developed foliation defined by a preferential alignment of mica and ductilely deformed quartz grains (see following section on quartz microstructures). The foliation is observed in the two older phases of the Changgo granite, but is crosscut by aplite dykes. The foliation observed in the core of the Changgo culmination has a similar orientation to the transposition schistosity observed in the overlying carapace, however, the two fabrics cannot be related unequivocally.

North-south striking extensional jointing is well-developed in the Changgo granite and appears to control the development of prominent north-south valleys in the area (Figure 3.3A).

### 3.4.5 Contact between the core and carapace

The contact between the granitic core and sedimentary carapace is a shear zone characterized by a well-developed mylonitic foliation (Figure 3.6A). The contact is only directly observed in one locale in the Changgo area, but has also been observed in the adjacent Kung Tang dome (Figure 3.2). The mylonitic foliation is approximately parallel to the transposition schistosity observed in the carapace making the actual extent of the shear zone difficult to define. However, the spatial extent of deformed aplite dykes and mylonitized leucogranite and pelitic schist shows that it is likely more than 300 m thick (Figures 3.6B, C). Near the contact, aplite dykes that cross-cut the foliation preserved in the older phases of the Changgo granite are themselves deformed by top-to-the north sense deformation within the shear zone and have acquired a mylonitic foliation.

The mylonitic foliation associated with the shear zone is folded (Figure 3.6A) into upright open folds with outcrop-scale (>10 m) wavelengths. These folds are similar to folds observed in the lower structural domain of the carapace and are also interpreted to be related to doming of the Changgo area. As in the previously described structural levels of the Changgo culmination, all deformational features are cut by north-south striking extensional joint sets.

## 3.5 Quartz *c*-axis fabrics

The strongly developed foliation within the porphyritic phase of the quartz-rich Changgo granite, and mylonitic foliation within quartzite and quartz-rich leucogranite in the shear zone at the core-cover contact, provide an opportunity to characterize the strain associated with the formation of these foliations using quartz ***c***-axis orientation analyses. Quartz crystallographic preferred orientations have been employed in the kinematic study of the Greater Himalayan sequence in Nepal to evaluate ductile strain between a top-to-the-south sense MCT and a top-to-the-north sense STDS (e.g. Grujic et al., 1996; Bhattacharya and Weber, 2004; Law et al., 2004, Chapter 2 of this thesis). The quartz-rich rocks in the Changgo area allow us to investigate northward changes in ductile strain across-strike from the previous studies within

the Greater Himalayan sequence that are cited above. Oriented specimens of foliated granite, mylonitic leucogranite, and pelitic schist for quartz ***c***-axis orientation analyses were collected at the sample locations shown in Figures 3.4 and 3.7. Quartz ***c***-axis orientations were measured optically in oriented thin sections that were cut parallel to lineation and perpendicular to foliation using a universal stage mounted on a petrographic microscope. All quartz *c*-axis orientation data are presented in equal-area lower-hemisphere stereographic projection onto a plane that is perpendicular to the foliation and parallel to the lineation. Because the domal structure of the Changgo area folds the ductile deformation fabric related to the formation of these quartz petrofabrics, all foliations and lineations have been unfolded about a southeast trending fold axis defined by changes in the foliation orientation in the granite that are interpreted to be the result of doming.

Specimens CH-13-2 and CH-123A (Figure 3.11A) are deformed porphyritic granite. Quartz in these samples is characterized by subgrain formation, grain boundary migration, and bulging (likely Regime 2 of Hirth and Tullis, (1992)). Both specimens yield weakly-defined asymmetric Type-1 cross-girdled patterns (Lister, 1977), dominated by rhomb <a> slip, that appear to show a general top-to-the-south shear sense. For specimen CH-123A the maximum elongation (shear) direction is 110˚ (SE), and for specimen CH-13-2 the maximum elongation (shear) direction is 223˚ (SSW).

Specimen CH-122A (Figure 3.11A) is from a quartzite lens within the shear zone at the northern outer-edge of the Changgo granite. Quartz in this specimen is characterized by extensive subgrain formation, grain boundary migration, and bulging (likely Regime 3 of Hirth and Tullis (1992)). The quartz *c*-axis pattern of CH-122A defines a symmetric Type-1 crossed girdle (Lister, 1977) that is characterized by rhomb <a> slip. Although no reliable shear sense can be determined from this pattern (see plot of individual axes), outcrop observations suggest a top-to-the-north shear sense (Figure 3.6D), therefore the maximum elongation (shear) direction in the specimen is 052˚ (NE).

Specimen LEUCO is from a leucogranite body within the shear zone at the core-carapace interface where it occurs extensively as felsenmeer. The specimen analyzed is not oriented. Quartz grains in LEUCO show evidence of grain boundary migration and bulging (Regime 2 of Hirth and Tullis (1992)) and yield a quartz *c*-axis pattern characterized by a Type-1 crossed-girdle

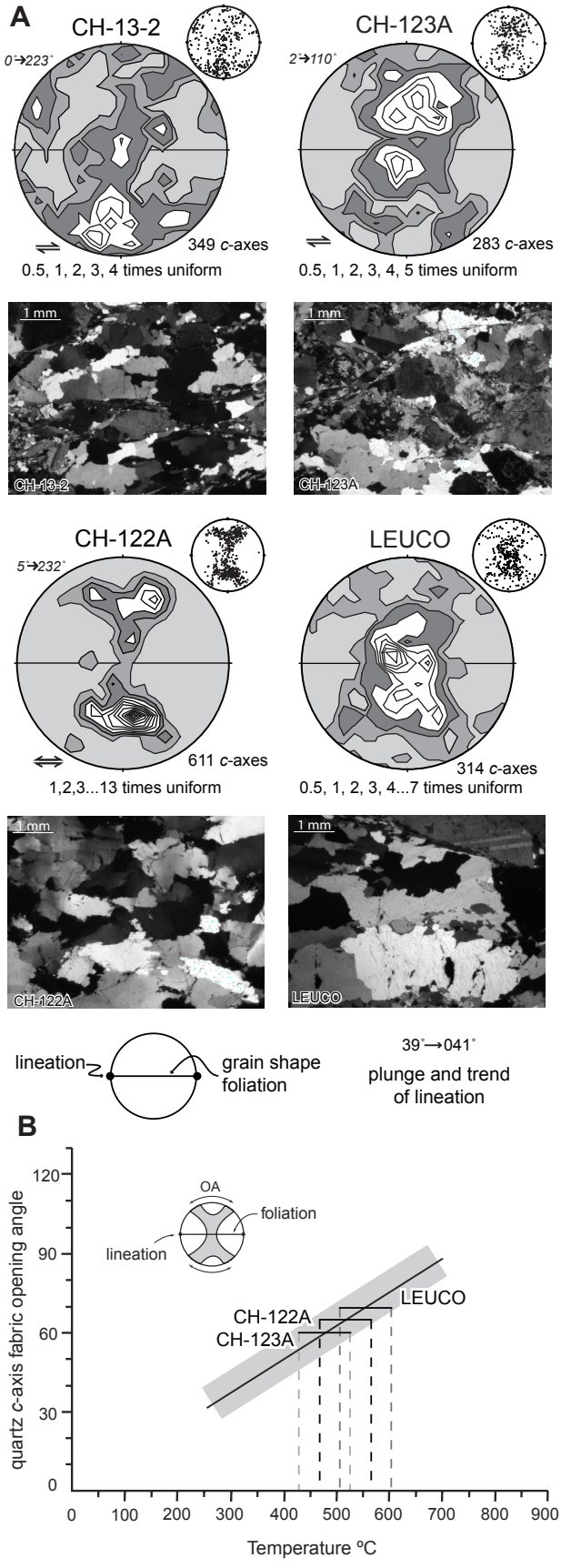


**Figure 3.11**
A) Quartz *c*-axis lattice preferred orientation diagrams of specimens from the deformed phase of the Changgo granite (CH-13-2 and CH-123A) and from the shear zone between the granite core and the meta-sedimentary carapace (CH-122A and LEUCO). Under each diagram is a cross-polarized photomicrograph of the quartz textures in that specimen (see text for discussion). B) Empirical relationship between opening-angle of a quartz *c*-axis pattern and temperature (modified from Law et. al., 2004). Suitable samples from this study are plotted. See text for discussion.

fabric (Lister, 1977). The fabric shows predominate slip in the prism <a> and rhomb <a> planes.

Quartz *c*-axis analysis of CH-14 (Figure 3.4) is not shown as it yielded a very diffuse pattern. This specimen was sampled from highly-strained porphyritic granite adjacent to undeformed aplite dykes. The broad dispersion of the *c*-axis fabric may reflect significant post-deformational recrystallization of the quartz related to heating during the emplacement of the dykes.

The opening angle of cross-girdled quartz *c*-axis fabrics can be related to the temperature at which the fabrics were developed (Tullis et al., 1973; Lister and Hobbs, 1980; Lister and Dornsiepen, 1982; Kruhl, 1998; Law et al., 1992, 2004). Empirical data indicates that an increase in temperature results in a corresponding linear increase the opening angle of a quartz *c*-axis fabric up to ~700˚C (Kruhl, 1998; Law et al., 2004). Deformation temperatures derived from the opening angles of quartz *c*-axis fabrics are estimated to be subject to an uncertainty of ±50˚C (Kruhl, 1998), which accounts for the range in strain rates and effects of hydrolytic weakening likely to be encountered during deformation (Law et al., 2004).

The quartz *c*-axis pattern derived for specimen CH-122A exhibits an average opening angle of approximately 67˚. This opening angle corresponds to a deformation temperature of ca. 520 ± 50˚C (Figure 3.11B). Specimens LEUCO and CH-123A also exhibit cross-girdled patterns with measurable opening angles, however, the quality of the quartz *c*-axis fabrics makes the use of the observed opening angles to determine deformation temperatures in these specimens suspect. LEUCO has an opening angle of approximately 70˚, which corresponds to a deformation temperature of *ca*. 555 ± 50˚C, while CH-123A yields an opening angle of approximately 60˚, which corresponds to a deformation temperature of *ca*. 480 ± 50˚C (Figure 3.11B). The deformation temperatures derived for specimens LEUCO and CH-123A are consistent with the temperature estimated from specimen CH-122A, which suggests that although suspect, the LEUCO and CH-123A quartz *c*-axis fabrics may reflect actual deformation conditions.

## 3.6 Geochronology and thermochronology

### 3.6.1 U–Pb geochronology

In order to constrain the crystallization age of the Changgo granite and the timing of

the deformation episodes observed in the Changgo area, U-Pb geochronology by sensitive high-resolution ion microprobe (SHRIMP) and conventional isotope dilution thermal ionization mass spectrometry (ID-TIMS) techniques was conducted on zircon and monazite separated from the different igneous phases. Specifically, specimens of the oldest (specimen KTG-9A) and youngest (specimen KTG-9C) phases of the Changgo granite and of a leucogranite (specimen LEUCO) that crops out within the shear zone at the core-cover contact, were analyzed. Additionally, preliminary U-Pb analyses were also carried out on a specimen of the deformed alkali-feldspar granite from the core of the Kung Tang culmination (specimen CH-133; Figure 3.3B) and more complete U-Pb analyses were conducted on specimens of undeformed alkali-feldspar and hornblende porphyritic dacite dykes (specimens CH-139B and CH-139C) that cut across the high-strain zone developed at the core-carapace contact in the Kung Tang area (Figure 3.3B).

#### 3.6.1.1 Analytical Techniques

Zircon and monazite were separated from 1-3 kg samples through standard gravity and magnetic techniques (crushing, grinding, WilfleyTM table, heavy liquids, FrantzTM isodynamic separator). Analytical procedures for specimens analyzed using the SHRIMP II at the Geological Survey of Canada (GSC) followed those outlined by Stern (1997). Standards and U-Pb calibration methods are as those reported by Stern and Amelin (2003). Zircon grains were cast and polished in 2.5 cm diameter epoxy mounts. Two separate mounts were made, IP448 and IP438, and analyzed over a 15 month period. The internal features of the grains were characterized with backscattered electrons (BSE) and cathodoluminescence using a Zeiss scanning electron microscope. Mounts were evaporatively coated in 10 nm of high-purity gold and spots selected for analysis were cleaned of surface common lead by rastering the ion beam for 2 minutes. Analyses were conducted using an $^{16}O-$ primary beam, projected onto the specimens at 10kV. For all zircon rim analyses and the analyses of cores from specimens CH-133, 139B, 139C, and LEUCO, the sputtered area used for analyses was approximately 9 x 12 μm with a beam current of *ca*. 2.2-2.6 nA. For core analyses from sample KTG-9A, the sputtered area was approximately 30 x 36 μm with a beam strength of *ca*. 6 nA. The count rates at ten masses were measured sequentially over 5-6 scans by a single electron multiplier and a pulse counting system with deadtime of 23 ns. Off-line data processing was facilitated utilizing customized

## Table 3.1 - U-Pb Data

SHRIMP II Data

| Spot Name | U (ppm) | Th (ppm) | $^{232}Th/^{238}U$ | $^{270}U/^{196}Zr$ | $\pm^{270}U/^{196}Zr$ | Pb*(ppm) | $^{204}Pb$ (ppb) | $^{204}Pb/^{206}Pb$ | $\pm^{204}Pb/^{206}Pb$ | $f(206)204$ | $^{208*}Pb/^{206*}Pb$ | $\pm^{208}Pb/^{206}Pb$ | $^{207*}Pb/^{235}U$ | $\pm^{207}Pb/^{235}U$ | $^{206}Pb/^{238}U$ | $\pm^{206}Pb/^{238}U$ | Corr Coeff | Apparent ages (Ma) $^{206}Pb/^{238}U$ | 1σ | $^{207}Pb/^{235}U$ | 1σ |
|---|---|---|---|---|---|---|---|---|---|---|---|---|---|---|---|---|---|---|---|---|---|
| ***KTG-9A*** | | | | | | | | | | | | | | | | | | | | | |
| 9068-5.1 | 22711 | 110 | 0.005 | 71.00 | 0.64 | 97 | 1 | 0.00001 | 0.00001 | 0.0002 | 0.00331 | 0.00066 | 0.0305 | 0.0015 | 0.00476 | 0.00016 | 0.7467 | 30.6 | 1.0 | 30.5 | 1.5 |
| 9068-6.1 | 11883 | 142 | 0.012 | 35.59 | 0.29 | 46 | 0 | 0.00001 | 0.00001 | 0.0002 | 0.00726 | 0.00122 | 0.0300 | 0.0022 | 0.00428 | 0.00011 | 0.4814 | 27.5 | 0.7 | 30.0 | 2.1 |
| 9068-11.1 | 10742 | 103 | 0.010 | 32.21 | 0.30 | 38 | 31 | 0.00082 | 0.00024 | 0.0143 | -0.02199 | 0.00906 | 0.0197 | 0.0028 | 0.00403 | 0.00010 | 0.3044 | 25.9 | 0.7 | 19.9 | 2.8 |
| 9068-10.1 | 11184 | 148 | 0.014 | 33.41 | 0.47 | 42 | 0 | 0.00001 | 0.00001 | 0.0002 | 0.00756 | 0.00115 | 0.0307 | 0.0024 | 0.00414 | 0.00010 | 0.4287 | 26.6 | 0.6 | 30.7 | 2.3 |
| 9068-9.1 | 5700 | 51 | 0.009 | 16.56 | 0.13 | 20 | 0 | 0.00001 | 0.00001 | 0.0002 | 0.01098 | 0.00265 | 0.0241 | 0.0013 | 0.00379 | 0.00007 | 0.4529 | 24.4 | 0.5 | 24.2 | 1.3 |
| 9068-9.2 | 19411 | 75 | 0.004 | 60.31 | 0.99 | 80 | 7 | 0.00009 | 0.00011 | 0.0016 | 0.00228 | 0.00402 | 0.0306 | 0.0018 | 0.00459 | 0.00016 | 0.6918 | 29.5 | 1.0 | 30.6 | 1.7 |
| 9068-12.1 | 15841 | 202 | 0.013 | 48.51 | 0.56 | 60 | 15 | 0.00026 | 0.00024 | 0.0046 | -0.00348 | 0.00898 | 0.0240 | 0.0026 | 0.00428 | 0.00014 | 0.4145 | 27.5 | 0.9 | 24.1 | 2.6 |
| 9068-13.1 | 13733 | 91 | 0.007 | 41.45 | 0.46 | 53 | 6 | 0.00012 | 0.00006 | 0.0021 | -0.00131 | 0.00239 | 0.0261 | 0.0015 | 0.00429 | 0.00011 | 0.5694 | 27.6 | 0.7 | 26.1 | 1.5 |
| 9068-18.1 | 10968 | 113 | 0.011 | 32.42 | 0.25 | 40 | 20 | 0.00051 | 0.00018 | 0.0088 | -0.01204 | 0.00680 | 0.0238 | 0.0020 | 0.00407 | 0.00010 | 0.4106 | 26.2 | 0.7 | 23.9 | 2.0 |
| 9068-5.2 c | 260 | 181 | 0.721 | 0.66 | 0.00 | 20 | 6 | 0.00036 | 0.00013 | 0.0063 | 0.21912 | 0.00653 | 0.5285 | 0.0307 | 0.06903 | 0.00117 | 0.4062 | 430 | 7 | 431 | 21 |
| 9068-10.2 c | 242 | 86 | 0.370 | 0.61 | 0.00 | 35 | 2 | 0.00006 | 0.00010 | 0.0011 | 0.12599 | 0.00435 | 1.3616 | 0.0419 | 0.13948 | 0.00177 | 0.5201 | 842 | 10 | 873 | 18 |
| 9068-11.2 c | 357 | 27 | 0.079 | 0.89 | 0.00 | 26 | 6 | 0.00027 | 0.00007 | 0.0047 | 0.02341 | 0.00290 | 0.5964 | 0.0183 | 0.07737 | 0.00099 | 0.5265 | 480 | 6 | 475 | 12 |
| 9068-12.2 c | 323 | 108 | 0.345 | 0.81 | 0.00 | 45 | 7 | 0.00020 | 0.00005 | 0.0034 | 0.21768 | 0.00800 | 1.4974 | 0.0568 | 0.12478 | 0.00307 | 0.7334 | 758 | 18 | 929 | 23 |
| 9068-13.2 c | 624 | 80 | 0.133 | 1.61 | 0.01 | 46 | 6 | 0.00013 | 0.00005 | 0.0023 | 0.04207 | 0.00294 | 0.6099 | 0.0279 | 0.07872 | 0.00232 | 0.7305 | 488 | 14 | 484 | 18 |
| 9068-16.2 c | 646 | 3 | 0.005 | 1.64 | 0.01 | 45 | 6 | 0.00014 | 0.00004 | 0.0024 | -0.00072 | 0.00141 | 0.5894 | 0.0141 | 0.07632 | 0.00099 | 0.6369 | 474 | 6 | 470 | 9 |
| 9068-7.1 c | 130 | 76 | 0.606 | 0.33 | 0.01 | 10 | 6 | 0.00075 | 0.00028 | 0.0130 | 0.18819 | 0.01152 | 0.5002 | 0.0499 | 0.07318 | 0.00171 | 0.3530 | 455 | 10 | 412 | 34 |
| 9068-6.2 c | 310 | 101 | 0.336 | 0.85 | 0.01 | 43 | 4 | 0.00012 | 0.00010 | 0.0021 | 0.11916 | 0.00994 | 1.3147 | 0.0676 | 0.13733 | 0.00205 | 0.4056 | 830 | 12 | 852 | 30 |
| 9068-16.1 | 20204 | 102 | 0.005 | 62.54 | 0.57 | 83 | 1 | 0.00001 | 0.00001 | 0.0002 | 0.00461 | 0.00135 | 0.0304 | 0.0013 | 0.00454 | 0.00016 | 0.8585 | 29.2 | 1.0 | 30.4 | 1.3 |
| ***CH-133B*** | | | | | | | | | | | | | | | | | | | | | |
| 9326-12.1 c | 559 | 74 | 0.137 | 1.26 | 0.01 | 45 | 20 | 0.00049 | 0.00016 | 0.0085 | 0.04343 | 0.00668 | 0.6765 | 0.0584 | 0.08513 | 0.00392 | 0.6321 | 527 | 23 | 525 | 36 |
| 9326-13.1 c | 5050 | 208 | 0.043 | 12.30 | 0.09 | 23 | 16 | 0.00074 | 0.00023 | 0.0128 | 0.01301 | 0.00885 | 0.0332 | 0.0031 | 0.00493 | 0.00007 | 0.2800 | 31.7 | 0.5 | 33.2 | 3.0 |
| 9326-3.1 c | 342 | 145 | 0.438 | 0.81 | 0.02 | 43 | 17 | 0.00047 | 0.00011 | 0.0081 | 0.13728 | 0.00551 | 1.1585 | 0.0441 | 0.12197 | 0.00197 | 0.5307 | 742 | 11 | 781 | 21 |
| 9326-4.1 c | 787 | 77 | 0.101 | 1.88 | 0.02 | 60 | 16 | 0.00029 | 0.00010 | 0.0050 | 0.03102 | 0.00398 | 0.6353 | 0.0258 | 0.08086 | 0.00105 | 0.4330 | 501 | 6 | 499 | 16 |
| 9326-5.1 c | 757 | 5 | 0.007 | 1.80 | 0.01 | 3 | 3 | 0.00116 | 0.00302 | 0.0201 | 0.20594 | 0.11549 | 0.0770 | 0.0251 | 0.00352 | 0.00023 | 0.3221 | 22.7 | 1.5 | 75.3 | 23.9 |
| 9326-6.1 c | 2140 | 11 | 0.005 | 5.19 | 0.33 | 54 | 14 | 0.00026 | 0.00008 | 0.0046 | 0.00066 | 0.00289 | 0.2225 | 0.0165 | 0.02778 | 0.00177 | 0.9111 | 177 | 11 | 204 | 14 |
| ***Leuco*** | | | | | | | | | | | | | | | | | | | | | |
| 9327-17.1 | 3049 | 128 | 0.043 | 7.42 | 0.11 | 16 | 4 | 0.00025 | 0.00033 | 0.0044 | 0.02072 | 0.01248 | 0.0398 | 0.0044 | 0.00552 | 0.00009 | 0.2699 | 35.5 | 0.6 | 39.7 | 4.3 |
| 9327-2.1 | 2761 | 122 | 0.046 | 6.65 | 0.07 | 14 | 5 | 0.00035 | 0.00025 | 0.0061 | 0.01639 | 0.00991 | 0.0342 | 0.0036 | 0.00553 | 0.00009 | 0.2672 | 35.6 | 0.6 | 34.1 | 3.6 |
| 9327-22.1 | 24376 | 761 | 0.032 | 63.89 | 0.56 | 161 | 4 | 0.00003 | 0.00003 | 0.0005 | 0.01007 | 0.00138 | 0.0468 | 0.0015 | 0.00726 | 0.00020 | 0.9113 | 46.6 | 1.3 | 46.4 | 1.5 |
| 9327-23.1 | 13591 | 480 | 0.037 | 34.02 | 0.28 | 80 | 1 | 0.00001 | 0.00001 | 0.0002 | 0.01456 | 0.00081 | 0.0436 | 0.0016 | 0.00644 | 0.00010 | 0.5548 | 41.4 | 0.7 | 43.3 | 1.5 |
| 9327-25.1 | 4198 | 172 | 0.042 | 10.29 | 0.09 | 22 | 0 | 0.00001 | 0.00016 | 0.0001 | 0.02138 | 0.00611 | 0.0385 | 0.0025 | 0.00579 | 0.00008 | 0.3316 | 37.2 | 0.5 | 38.4 | 2.5 |
| 9327-25.2 | 4238 | 118 | 0.029 | 10.49 | 0.13 | 23 | 7 | 0.00032 | 0.00021 | 0.0056 | 0.00289 | 0.00830 | 0.0370 | 0.0030 | 0.00591 | 0.00009 | 0.3037 | 38.0 | 0.6 | 36.9 | 3.0 |
| 9327-29.1 | 4180 | 149 | 0.037 | 10.20 | 0.48 | 21 | 10 | 0.00048 | 0.00046 | 0.0083 | 0.00334 | 0.01731 | 0.0325 | 0.0062 | 0.00567 | 0.00027 | 0.3681 | 36.4 | 1.7 | 32.5 | 6.1 |
| 9327-39.1 | 5617 | 369 | 0.068 | 13.77 | 0.15 | 30 | 11 | 0.00041 | 0.00018 | 0.0071 | 0.01604 | 0.00700 | 0.0349 | 0.0026 | 0.00581 | 0.00008 | 0.3073 | 37.3 | 0.5 | 34.8 | 2.5 |
| 9327-41.1 | 14339 | 569 | 0.041 | 36.38 | 0.27 | 87 | 2 | 0.00002 | 0.00006 | 0.0004 | 0.01418 | 0.00273 | 0.0426 | 0.0015 | 0.00666 | 0.00014 | 0.6670 | 42.8 | 0.9 | 42.3 | 1.5 |
| 9327-42.1 | 5932 | 97 | 0.017 | 14.49 | 0.17 | 30 | 9 | 0.00031 | 0.00014 | 0.0054 | 0.00243 | 0.00519 | 0.0368 | 0.0021 | 0.00569 | 0.00008 | 0.3844 | 36.6 | 0.5 | 36.7 | 2.0 |
| 9327-45.1 | 3311 | 116 | 0.036 | 7.92 | 0.08 | 17 | 2 | 0.00015 | 0.00023 | 0.0027 | 0.01622 | 0.00905 | 0.0359 | 0.0030 | 0.00549 | 0.00007 | 0.2696 | 35.3 | 0.4 | 35.8 | 3.0 |
| 9327-56.1 | 16061 | 455 | 0.029 | 40.96 | 0.34 | 96 | 11 | 0.00012 | 0.00007 | 0.0020 | 0.00791 | 0.00273 | 0.0423 | 0.0015 | 0.00659 | 0.00013 | 0.6547 | 42.3 | 0.9 | 42.1 | 1.5 |
| 9327-58.1 | 4322 | 173 | 0.041 | 10.44 | 0.37 | 22 | 9 | 0.00043 | 0.00016 | 0.0075 | 0.01386 | 0.00642 | 0.0365 | 0.0031 | 0.00566 | 0.00022 | 0.5526 | 36.4 | 1.4 | 36.4 | 3.1 |
| 9327-64.1 | 2918 | 149 | 0.053 | 6.92 | 0.05 | 15 | 7 | 0.00050 | 0.00049 | 0.0087 | 0.00731 | 0.01852 | 0.0317 | 0.0066 | 0.00559 | 0.00008 | 0.1963 | 36.0 | 0.5 | 31.7 | 6.5 |
| 9327-70.1 | 3179 | 583 | 0.190 | 7.64 | 0.06 | 17 | 9 | 0.00056 | 0.00033 | 0.0098 | 0.05500 | 0.01286 | 0.0335 | 0.0043 | 0.00560 | 0.00010 | 0.2636 | 36.0 | 0.7 | 33.4 | 4.2 |
| 9327-75.1 | 3897 | 160 | 0.043 | 9.39 | 0.07 | 20 | 4 | 0.00022 | 0.00039 | 0.0039 | 0.01324 | 0.01476 | 0.0332 | 0.0049 | 0.00553 | 0.00009 | 0.2346 | 35.6 | 0.6 | 33.2 | 4.9 |
| 9327-78.1 | 19098 | 519 | 0.028 | 49.11 | 0.78 | 120 | 7 | 0.00006 | 0.00005 | 0.0010 | 0.00862 | 0.00214 | 0.0438 | 0.0016 | 0.00694 | 0.00017 | 0.7520 | 44.6 | 1.1 | 43.5 | 1.5 |
| 9327-80.1 | 6656 | 172 | 0.027 | 16.35 | 0.19 | 36 | 6 | 0.00016 | 0.00018 | 0.0028 | 0.01026 | 0.00662 | 0.0387 | 0.0030 | 0.00593 | 0.00009 | 0.3280 | 38.1 | 0.6 | 38.6 | 2.9 |
| ***CH-139B*** | | | | | | | | | | | | | | | | | | | | | |
| 9328-15.1 | 4726 | 801 | 0.175 | 11.63 | 0.09 | 11 | 12 | 0.00107 | 0.00073 | 0.0185 | 0.03228 | 0.02780 | 0.0123 | 0.0044 | 0.00263 | 0.00005 | 0.1803 | 16.9 | 0.3 | 12.4 | 4.4 |
| 9328-3.1 c | 1195 | 411 | 0.356 | 2.89 | 0.06 | 95 | 17 | 0.00021 | 0.00006 | 0.0036 | 0.10975 | 0.00316 | 0.6188 | 0.0237 | 0.07909 | 0.00095 | 0.4271 | 491 | 6 | 489 | 15 |
| 9328-3.2 c | 441 | 246 | 0.576 | 1.04 | 0.02 | 37 | 10 | 0.00033 | 0.00024 | 0.0058 | 0.19829 | 0.05421 | 0.6219 | 0.2514 | 0.07673 | 0.01957 | 0.7186 | 477 | 118 | 491 | 171 |
| 9328-40.1 | 3162 | 227 | 0.074 | 7.74 | 0.06 | 8 | 2 | 0.00028 | 0.00045 | 0.0048 | 0.03464 | 0.01825 | 0.0179 | 0.0029 | 0.00258 | 0.00005 | 0.2316 | 16.6 | 0.3 | 18.0 | 2.9 |
| 9328-41.1 | 1414 | 360 | 0.263 | 3.48 | 0.03 | 4 | 2 | 0.00049 | 0.00190 | 0.0085 | 0.11668 | 0.07249 | 0.0210 | 0.0106 | 0.00252 | 0.00010 | 0.2037 | 16.2 | 0.7 | 21.1 | 10.6 |
| 9328-43.1 | 2208 | 81 | 0.038 | 5.29 | 0.08 | 5 | 4 | 0.00087 | 0.00079 | 0.0151 | 0.04625 | 0.03021 | 0.0202 | 0.0045 | 0.00252 | 0.00005 | 0.2180 | 16.2 | 0.3 | 20.3 | 4.5 |
| 9328-44.1 c | 305 | 92 | 0.310 | 0.73 | 0.01 | 43 | 7 | 0.00020 | 0.00016 | 0.0034 | 0.09586 | 0.00779 | 1.3254 | 0.0645 | 0.14235 | 0.00184 | 0.3820 | 858 | 10 | 857 | 29 |
| 9328-44.2 | 6236 | 159 | 0.026 | 15.65 | 0.17 | 16 | 1 | 0.00007 | 0.00025 | 0.0012 | 0.01863 | 0.00947 | 0.0204 | 0.0018 | 0.00287 | 0.00006 | 0.3643 | 18.5 | 0.4 | 20.5 | 1.8 |
| 9328-45.1# | 2551 | 61 | 0.025 | 6.20 | 0.04 | 13 | 5 | 0.00043 | 0.00060 | 0.0075 | 0.00453 | 0.02228 | 0.0362 | 0.0074 | 0.00559 | 0.00011 | 0.2160 | 35.9 | 0.7 | 36.1 | 7.3 |
| 9328-47.1 | 4529 | 525 | 0.120 | 11.25 | 0.16 | 12 | 9 | 0.00085 | 0.00058 | 0.0147 | 0.07045 | 0.02240 | 0.0249 | 0.0040 | 0.00282 | 0.00005 | 0.2370 | 18.2 | 0.3 | 25.0 | 4.0 |
| 9328-47.2 c | 537 | 16 | 0.030 | 1.28 | 0.02 | 4 | 1 | 0.00035 | 0.00063 | 0.0062 | 0.14372 | 0.02994 | 0.1024 | 0.0121 | 0.00754 | 0.00022 | 0.3590 | 48.5 | 1.4 | 99.0 | 11.2 |
| 9328-54.1 | 2232 | 29 | 0.014 | 5.43 | 0.07 | 5 | 7 | 0.00140 | 0.00073 | 0.0243 | 0.00041 | 0.02940 | 0.0142 | 0.0048 | 0.00252 | 0.00007 | 0.2062 | 16.2 | 0.5 | 14.3 | 4.8 |

## Table 3.1 continued

| | | | | | | | | | | | | | | | | | | | | |
|---|---|---|---|---|---|---|---|---|---|---|---|---|---|---|---|---|---|---|---|---|
| 9328-58.1# | 1738 | 221 | 0.131 | 4.24 | 0.07 | 7 | 5 | 0.00073 | 0.00051 | 0.0127 | 0.04595 | 0.01983 | 0.0296 | 0.0056 | 0.00446 | 0.00007 | 0.2095 | 28.7 | 0.5 | 29.6 | 5.5 |
| 9328-59.1 | 6336 | 50 | 0.008 | 15.93 | 0.29 | 16 | 1 | 0.00004 | 0.00021 | 0.0007 | 0.01697 | 0.00798 | 0.0197 | 0.0014 | 0.00270 | 0.00004 | 0.3491 | 17.4 | 0.3 | 19.8 | 1.4 |
| 9328-59.2 c | 546 | 80 | 0.152 | 1.31 | 0.02 | 67 | 2 | 0.00004 | 0.00008 | 0.0007 | 0.03499 | 0.02392 | 1.2449 | 1.2187 | 0.13006 | 0.08453 | 0.7476 | 788 | 501 | 821 | 795 |
| 9328-62.1 | 3635 | 238 | 0.068 | 8.93 | 0.06 | 9 | 3 | 0.00034 | 0.00051 | 0.0058 | 0.03066 | 0.01923 | 0.0166 | 0.0030 | 0.00260 | 0.00004 | 0.2177 | 16.7 | 0.3 | 16.7 | 3.0 |
| 9328-62.2# | 7873 | 820 | 0.108 | 19.76 | 0.31 | 20 | 3 | 0.00016 | 0.00026 | 0.0027 | 0.03800 | 0.01052 | 0.0186 | 0.0017 | 0.00278 | 0.00005 | 0.3140 | 17.9 | 0.3 | 18.7 | 1.7 |
| 9328-63.1 c | 493 | 106 | 0.223 | 1.18 | 0.01 | 62 | 4 | 0.00008 | 0.00008 | 0.0014 | 0.07504 | 0.00541 | 1.1669 | 0.0339 | 0.12792 | 0.00175 | 0.5735 | 776 | 10 | 785 | 16 |
| 9328-64.1 | 3804 | 135 | 0.037 | 9.37 | 0.07 | 9 | 14 | 0.00157 | 0.00085 | 0.0272 | -0.01585 | 0.03273 | 0.0127 | 0.0050 | 0.00263 | 0.00006 | 0.1814 | 16.9 | 0.4 | 12.8 | 5.0 |
| 9328-65.1 | 2807 | 1137 | 0.418 | 7.00 | 0.07 | 7 | 8 | 0.00128 | 0.00068 | 0.0221 | 0.11951 | 0.02674 | 0.0126 | 0.0037 | 0.00243 | 0.00005 | 0.1917 | 15.7 | 0.3 | 12.7 | 3.7 |
| 9328-65.2# | 2306 | 855 | 0.383 | 5.65 | 0.05 | 6 | 1 | 0.00010 | 0.00052 | 0.0017 | 0.14093 | 0.02446 | 0.0182 | 0.0031 | 0.00259 | 0.00004 | 0.2219 | 16.7 | 0.3 | 18.3 | 3.1 |
| ***CH-139C*** | | | | | | | | | | | | | | | | | | | | |
| 9329-10.1 | 6507 | 735 | 0.117 | 16.37 | 0.22 | 16 | 21 | 0.00135 | 0.00056 | 0.0234 | 0.03948 | 0.02419 | 0.016640 | 0.003850 | 0.00270 | 0.00006 | 0.2137 | 17.4 | 0.4 | 16.8 | 3.9 |
| 9329-12.1 | 5122 | 127 | 0.026 | 12.80 | 0.10 | 13 | 17 | 0.00138 | 0.00086 | 0.0239 | 0.00844 | 0.03243 | 0.020610 | 0.005310 | 0.00274 | 0.00008 | 0.2337 | 17.6 | 0.5 | 20.7 | 5.3 |
| 9329-14.1 | 3355 | 112 | 0.035 | 8.48 | 0.09 | 8 | 22 | 0.00281 | 0.00074 | 0.0488 | -0.00336 | 0.02940 | 0.011340 | 0.004590 | 0.00262 | 0.00008 | 0.1957 | 16.9 | 0.5 | 11.5 | 4.6 |
| 9329-14.2 c | 1498 | 1297 | 0.895 | 3.68 | 0.03 | 230 | 27 | 0.00016 | 0.00007 | 0.0027 | 0.28157 | 0.00384 | 1.186610 | 0.028270 | 0.13245 | 0.00166 | 0.6239 | 802 | 9 | 794 | 13 |
| 9329-17.1 | 4121 | 153 | 0.038 | 10.13 | 0.14 | 10 | 9 | 0.00092 | 0.00061 | 0.0160 | 0.03166 | 0.02325 | 0.020630 | 0.003700 | 0.00268 | 0.00005 | 0.2248 | 17.3 | 0.3 | 20.7 | 3.7 |
| 9329-17.2 c | 96 | 45 | 0.482 | 0.23 | 0.00 | 37 | 11 | 0.00038 | 0.00014 | 0.0067 | 0.15738 | 0.02360 | 8.081920 | 1.352450 | 0.33756 | 0.03704 | 0.7404 | 1875 | 181 | 2240 | 164 |
| 9329-2.1 | 10731 | 1692 | 0.163 | 27.05 | 0.22 | 30 | 9 | 0.00033 | 0.00017 | 0.0056 | 0.05974 | 0.00692 | 0.021060 | 0.001510 | 0.00288 | 0.00006 | 0.4003 | 18.5 | 0.4 | 21.2 | 1.5 |
| 9329-23.1 c | 372 | 159 | 0.441 | 0.90 | 0.01 | 32 | 10 | 0.00039 | 0.00026 | 0.0068 | 0.23634 | 0.01291 | 0.688000 | 0.055880 | 0.07570 | 0.00117 | 0.3097 | 470 | 7 | 532 | 34 |
| 9329-24.1 | 3300 | 308 | 0.097 | 8.08 | 0.11 | 8 | 23 | 0.00300 | 0.00088 | 0.0520 | 0.00501 | 0.03456 | 0.009980 | 0.005330 | 0.00261 | 0.00006 | 0.1652 | 16.8 | 0.4 | 10.1 | 5.4 |
| 9329-26.1 | 1099 | 60 | 0.056 | 2.60 | 0.02 | 3 | 11 | 0.00441 | 0.00272 | 0.0765 | 0.06639 | 0.10638 | 0.019880 | 0.015740 | 0.00253 | 0.00014 | 0.1917 | 16.3 | 0.9 | 20.0 | 15.8 |
| 9329-3.1 | 6534 | 878 | 0.139 | 16.78 | 0.16 | 16 | 51 | 0.00313 | 0.00076 | 0.0543 | -0.01089 | 0.02953 | 0.012730 | 0.004790 | 0.00277 | 0.00007 | 0.1873 | 17.9 | 0.4 | 12.9 | 4.8 |
| 9329-5.1 | 5747 | 447 | 0.080 | 14.67 | 0.12 | 15 | 9 | 0.00066 | 0.00060 | 0.0115 | 0.03738 | 0.02410 | 0.019180 | 0.003650 | 0.00272 | 0.00006 | 0.2407 | 17.5 | 0.4 | 19.3 | 3.7 |
| 9329-50.1 | 8167 | 92 | 0.012 | 20.53 | 0.15 | 24 | 8 | 0.00035 | 0.00017 | 0.0060 | 0.02248 | 0.00759 | 0.023920 | 0.001570 | 0.00317 | 0.00007 | 0.4435 | 20.4 | 0.4 | 24.0 | 1.6 |
| 9329-7.1 | 1886 | 62 | 0.034 | 4.64 | 0.07 | 5 | 0 | 0.00001 | 0.00001 | 0.0002 | 0.09797 | 0.00875 | 0.028470 | 0.002740 | 0.00261 | 0.00006 | 0.3589 | 16.8 | 0.4 | 28.5 | 2.7 |
| 9329-9.1 | 1194 | 522 | 0.452 | 2.90 | 0.04 | 3 | 13 | 0.00406 | 0.00130 | 0.0704 | 0.07720 | 0.05511 | 0.005190 | 0.008640 | 0.00288 | 0.00011 | 0.1479 | 18.6 | 0.7 | 5.3 | 8.7 |

Uncertainties reported at one sigma and are calculated by numerical propagation of all know sources of error [*Stern*, 1997]. Asterisk (*) refers to radiogenic Pb (Pb isotopes have been corrected using measured $^{204}$Pb). # indicates analyses excluded from weighed mean and regression analysis (comprises two anomalously old analyses and two analysis that were the second spots on a zircon grain within close proximity to the first spot). Spot name follows the convention x-y.z; where x = sample number and z = spot number. $f(206)^{204}$ refers to the mole fraction of total $^{206}$Pb that is due to common Pb calulated using the $^{204}$Pb-method; common Pb composition used is the surface blank (4/6: 0.05770; 7/6: 0.89500; 8/6: 2.13840).*refers to radiogenic Pb (corrected for common Pb). Discordance relative to origin = 100*(1-($^{206}$Pb/$^{238}$U age)/($^{207}$Pb/$^{206}$Pb age)). Calibration standard 6266; U = 910 ppm; Age = 559 Ma; $^{206}$Pb/$^{238}$U = 0.09059. Error in $^{206}$Pb/$^{238}$U calibration: 1.0%



### ID-TIMS data

| No. | Description | Wt (mg) | U (ppm) | Th $_b$ U | Pb$^R$ (pg) | Pb$_{com}^C$ (pg) | $^{207}$Pb/$^{204}$Pb | $^{206}$Pb/$^{238}$U | ±$^{206}$Pb/$^{238}$U | $^{207}$Pb/$^{235}$U | ±$^{207}$Pb/$^{235}$U | $^{206}$Pb/$^{238}$U age (Ma) | 2σ | $^{207}$Pb/$^{235}$U age (Ma) | 2σ | $^{207}$Pb/$^{206}$Pb age(Ma) | 2σ | Disc. (%) | Error corr. coeff. | Lab No. |
|---|---|---|---|---|---|---|---|---|---|---|---|---|---|---|---|---|---|---|---|---|
| **1** | **KTG-9A** | **Deformed alkali-feldspar porphyrytic granite, Changgo granite** | | | | | | | | | | | | | | | | | | |
| 1 | 1 ab, zr, lp | 0.001 | 504 | -0.05 | 33 | 0.9 | 158.488 | 0.07275 | 0.00017 | 0.5740 | 0.0034 | 452.7 | 1.0 | 460.6 | 2.2 | 500 | 11 | 9.9 | 0.54346 | dwd4817 |
| 2 | 1 ab, zr, lp | 0.001 | 436 | -0.10 | 11 | 0.7 | 92.493 | 0.05662 | 0.00013 | 0.5317 | 0.0048 | 355 | 0.8 | 432.9 | 3.2 | 872 | 17 | 60.9 | 0.53574 | dwd4818 |
| **2** | **KTG-9C** | **Undeformed aplite dyke, Changgo granite** | | | | | | | | | | | | | | | | | | |
| 1 | 1 mz | 0.001 | 14625 | 7.31 | 156 | 8.9 | 32.433 | 0.003470 | 0.000010 | 0.0220 | 0.0008 | 22.32 | 0.06 | 22.14 | 0.75 | 2.74 | 2.11 | -716.1 | 0.07014 | dwd5000 |
| 2 | 1 mz | 0.001 | 33635 | 2.21 | 204 | 25.8 | 29.117 | 0.003530 | 0.000013 | 0.0223 | 0.0010 | 22.70 | 0.08 | 22.44 | 1.00 | 0.00 | 16.73 | -716.1 | 0.06735 | dwd5001 |
| 3 | 1 mz | 0.001 | 18450 | 3.46 | 160 | 39.7 | 20.507 | 0.003550 | 0.000026 | 0.0227 | 0.0029 | 22.82 | 0.17 | 22.80 | 2.84 | 20.79 | 59.36 | -9.8 | 0.01302 | dwd5002 |
| 4 | 1 mz | 0.001 | 252 | 0.50 | 7 | 7.1 | 16.133 | 0.003110 | 0.000287 | 0.0308 | 0.0330 | 20.05 | 1.85 | 30.79 | 32.74 | 977.47 | 2020.78 | 98.1 | 0.03394 | dwd5003 |

Uncertainties reported at two sigma. Description: zr - zircon grain; mon - monazite; Ab - abraded; lp - long prism. Pb$^R$ is radiogenic Pb. Pb$^C$ is total measured common Pb assuming the isotopic composition of laboratory blank: 206/204 - 18.221; 207/204 - 15.612; 208/204 - 39.360 (errors 2%). Th/U is calculated from radiogenic 208Pb/206Pb ratio and 207Pb/206Pb age assuming concordance. Disc - % discordance for the given 207Pb/206Pb age. Uranium decay constants are from *Jaffey of et al.* [1971].

in-house software. The 1σ external errors of $^{206}Pb/^{238}U$ ratios reported in the data (Table 1) incorporate a ± 1.0% error in calibrating the standard zircon (see Stern and Amelin, 2003). No fractionation correction was applied to the Pb-isotope data as the maximum correction, which is 0.11 Ma as calculated using the method of Schärer (1984), is within analytical error. Pb isotopes were corrected for common lead using measured $^{204}Pb$. Isoplot v.3.5 (Ludwig, 2003) was used to generate concordia plots, calculate weighted means, and facilitate regression analyses. The error in weighted means and ellipses on concordia diagrams are reported at 2σ.

Fragments of the GSC laboratory standard zircon (Z6266, with $^{206}Pb/^{238}U$ age = 559 Ma) and Fish Canyon Tuff standard zircon (FCT - Z5567) were mounted with unknowns. Additionally, Temora 2 standard zircon (Z8539) was also mounted with unknowns in IP 448 (see data table for related samples). For mount IP 438, the weighted mean $^{206}Pb/^{238}U$ age of 7 SHRIMP analyses of laboratory standard Z6266 is 559.9 ± 5.2 Ma (95% conf.). Analyses of FCT zircons in the same mount to verify the U-Pb calibration yielded a $^{206}Pb/^{238}U$ age of 29.24 ± 1.93 Ma within error of the accepted 28.402 ± 0.023 Ma $^{206}Pb/^{238}U$ age of FCT (Schmitz and Bowring, 2001). 21 analyses of laboratory standard Z6266 in mount IP 448 yield a weighed mean $^{206}Pb/^{238}U$ age of 559.0 ± 1.8 Ma (95% conf.) Analyses of FCT zircons on the same mount were interspersed between the sample analyses to verify the accuracy of the U-Pb calibration. Using the calibration defined by the z6266 standard, the weighted mean $^{206}Pb/^{238}U$ age of nine SHRIMP analyses of FCT zircon is 28.1 ± 1.1 Ma (95% conf.). Analyses of another secondary zircon standard (Temora 2) were also used to verify the accuracy of the U-Pb calibration. Using the calibration defined by the z6266 standard, the weighted mean $^{206}Pb/^{238}U$ age of 11 SHRIMP analyses of Temora 2 zircon is 410.1 ± 4.9 Ma (95% conf.). The accepted $^{206}Pb/^{238}U$ age of Temora 2 is 416.5 ± 0.22 Ma, based on 21 isotope dilution fractions (Black et al., 2004).

ID-TIMS analyses were carried out at the Jack Satterly Geochronology Laboratory at the University of Toronto. Zircon grains were hand-picked from a non-magnetic fraction for clarity and lack of inclusions or cracks. Picked grains were abraded (e.g., Krogh, 1982), weighed by optical imaging (e.g., Matthews and Davis, 1999), and prepared chemically following the procedures of Krogh (1973) for analysis. Monazite grains were prepared for analyses using the same procedures as for the zircon, with the exception of abrasion, which was not carried out. During the chemical preparation of the monazite grains, which generally follows the procedure of

Krogh (1973), crystals were dissolved in Savillex vials using 6N HCl. Linear regression and error estimation and plotting were performed using Isoplot v. 3.5 (Ludwig, 2003).

#### 3.6.1.2 SHRIMP Results

U-Pb analyses on zircon separates from specimen KTG-9A constrain the age of the main phase of the Changgo intrusion. The results of these analyses also provide a minimum age for the onset of the deformation that is preserved throughout the granite. Zircon rims and cores were analyzed separately. Zircon grains from this specimen were hand-picked from a slightly magnetic fraction (3˚ side-slope on a FrantzTM isodynamic separator) for clarity and lack of inclusions or cracks. Zircon from this specimen are characterized by large low-U cores and ≤ 40 μm thick high-U rims (Figure 3.12A). Analyses of 8 cores yielded mostly concordant analyses with $^{206}Pb/^{238}U$ ages ranging between 426 ± 5 Ma and 845 ± 8 Ma (Table 1; Figure 3.12A). These ages are interpreted to reflect the ages of the various xenocrystic cores incorporated into the magma from its source material. This interpretation has also been made for similar results elsewhere along the North Himalayan belt (Aoya et al., 2005; Lee and Whitehouse, 2007). The age of rim growth around the xenocrysts is determined from 10 spot analyses on different zircon grains. Eight of the ten ages plot within error of concordia (Figure 3.12B). $^{206}Pb/^{238}U$ ages range between 29.4 ± 0.2 Ma and 24.0 ± 0.3 Ma (Table 1).

The range of ages between 24 and 29 Ma correlate with uranium content (Figure 3.12C) as has been previously demonstrated for high-uranium zircons analyzed using a SHRIMP instrument (Williams and Hergt, 2000). This is thought to reflect an analytical bias, one that may be exacerbated depending on the ion species used with the microprobe (Williams and Hergt, 2000). Discrepancies between SHRIMP and ID-TIMS $^{206}Pb/^{238}U$ measurements of the Sri Lankan zircon standard SL3 (3540 ppm) are small when an ion beam of $O_2$- is used, but large when O- is used (Williams, 1998). Williams and Hergt (2000) suggested that the effect of uranium concentrations on apparent age is only significant above a threshold of about 2500 ppm and that the magnitude of this effect is independent of zircon age. Data from the SHRIMP at the GSC suggest that the threshold may be closer to 2000 ppm. The $^{207}Pb$ corrected $^{206}Pb/^{238}U$ ages of rim spots in zircon from specimen KTG-9A are highly correlated with measured $270(UO_2)/196(Zr_2O)$ ratios, a proxy for uranium content (Figure 3.12C). Fitting a least-square regression line through

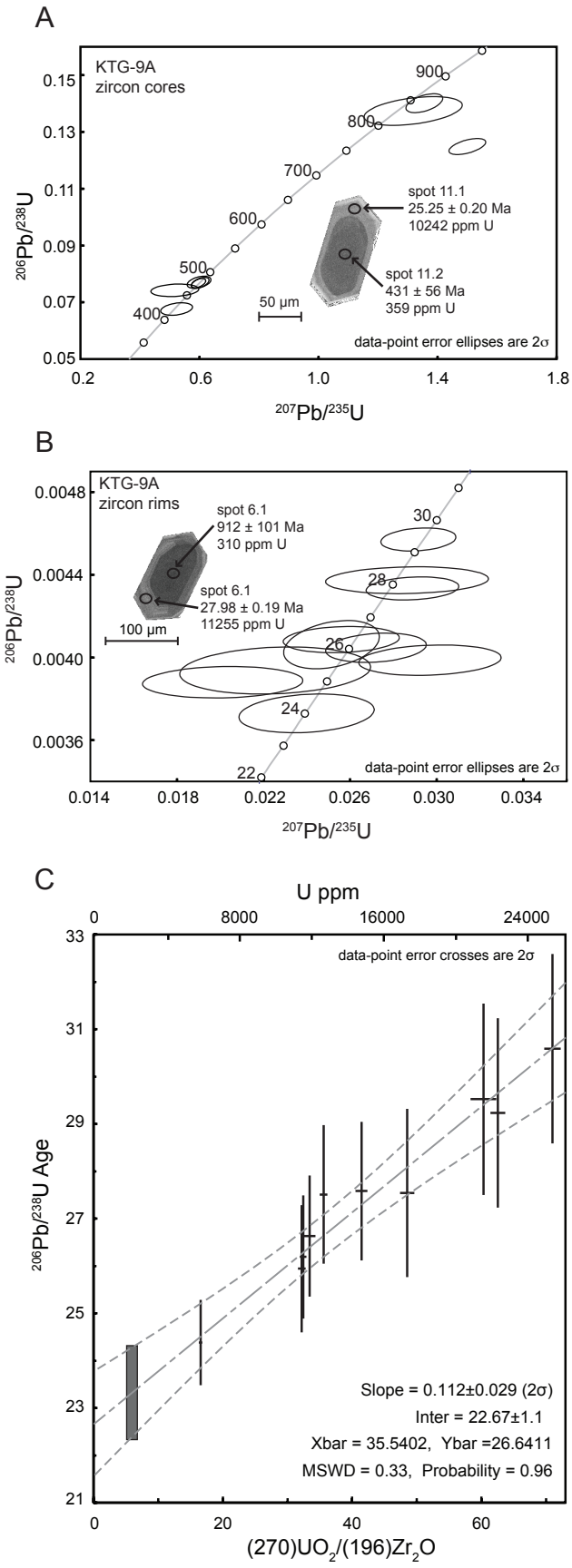


**Figure 3.12**
A) Concordia diagram for U-Pb analyses of zircon cores from specimen KTG-9A. Most results are within error of concordia; the spread in data is interpreted to reflect xenocrystic ages. Inset is a back-scattered electron microscopic image of a representative zircon with typical dark uranium-poor cores surrounded by bright uranium-rich rims. Black circles with adjacent $^{206}Pb/^{238}U$ ages represent the location and results of SHRIMP II analyses. B) Concordia diagram of U-Pb analyses of zircon rims separated from specimen KTG-9A. C) Plot of 270/196 (atomic weight - used as a proxy for uranium concentrations) against $^{206}Pb/^{238}U$ age. Regression analysis with error envelope used to determine the age of the specimen at a threshold of 2000 ± 300 ppm of uranium (error depicted as grey box with black outline).

the data allows an age for the zircon rims to be calculated at a threshold value of 2000 ppm. Errors in the age and 270($UO_2$)/196($Zr_2O$) weight ratios of each analyses are propagated through the regression using ISOPLOT (Ludwig, 2003) and are reflected in the calculated slope error. An error in the location of the threshold value of ± 300 ppm was assumed and propagated through the error analyses. For zircon rims from KTG-9A, the age calculated from a regression line (MSWD of 0.33) at ~2000 ppm of uranium is 23.5 ± 1.0 Ma (Figure 3.12C).

Analyses were also performed on zircons from the mylonitic, feldspar-augen leucogranite that crops out within the metasedimentary rocks in the shear zone at the contact between the core of the Changgo culmination and its carapace. Zircon from this specimen (LEUCO) has high uranium contents (up to ~25000 ppm) and shows evidence of reordering textures (Figure 3.13A). Analyses from 17 separate rim and core areas range in age from 46.6 ± 1.3 Ma to 35.2 ± 0.5 Ma (Table 1) (Figure 3.13B). As observed in rim data from specimen KTG-9A, the $^{207}Pb$ corrected $^{206}Pb/^{238}U$ ages of zircons from LEUCO have a positive linear relationship with uranium concentration (Figure 3.13C). Using the same regression and error propagation methods as described above, analyses from this sample yield a late Eocene age of 35.4 ± 0.4 Ma.

Analyses of the cores of zircon grains from the deformed core of the Kung Tang culmination (Figures 3.2, 3.3B) yield ages that range from ~20 Ma to 737 Ma (specimen CH-133B; Figures 3.3, 3.14; Table 1). Similar to the cores of other specimens analyzed by ion microprobe methods in this study, the spread in ages is thought to reflect the xenocrystic nature of these cores. The youngest analyzed core, which yields a $^{207}Pb$ corrected $^{206}Pb/^{238}U$ age of 19.7 ± 0.8 Ma, may actually be magmatic as it is similar to the age of zircon rim growth in the core of the Changgo dome. More analyses, including rim ages, are needed to properly constrain the age of the Kung Tang granite.

Specimens CH-139B and CH-139C are from two different phases of an undeformed alkali-feldspar and hornblende porphyritic dacite dyke intruding the deformed meta-sedimentary carapace of the Kung Tang dome (Figure 3.3B). Zircon grains separated from these specimens are characterized by large xenocrystic cores and ≤ 40 μm thick high-uranium overgrowths (Figures 3.15A, B, C, D). Analyses of zircon cores from CH-139B and CH-139C result in ages ranging between 1734 and 21 Ma (Figures 3.15A, B). While the majority of these cores are interpreted to be xenocrystic, the Miocene age may reflect inheritance from the same source as the Miocene

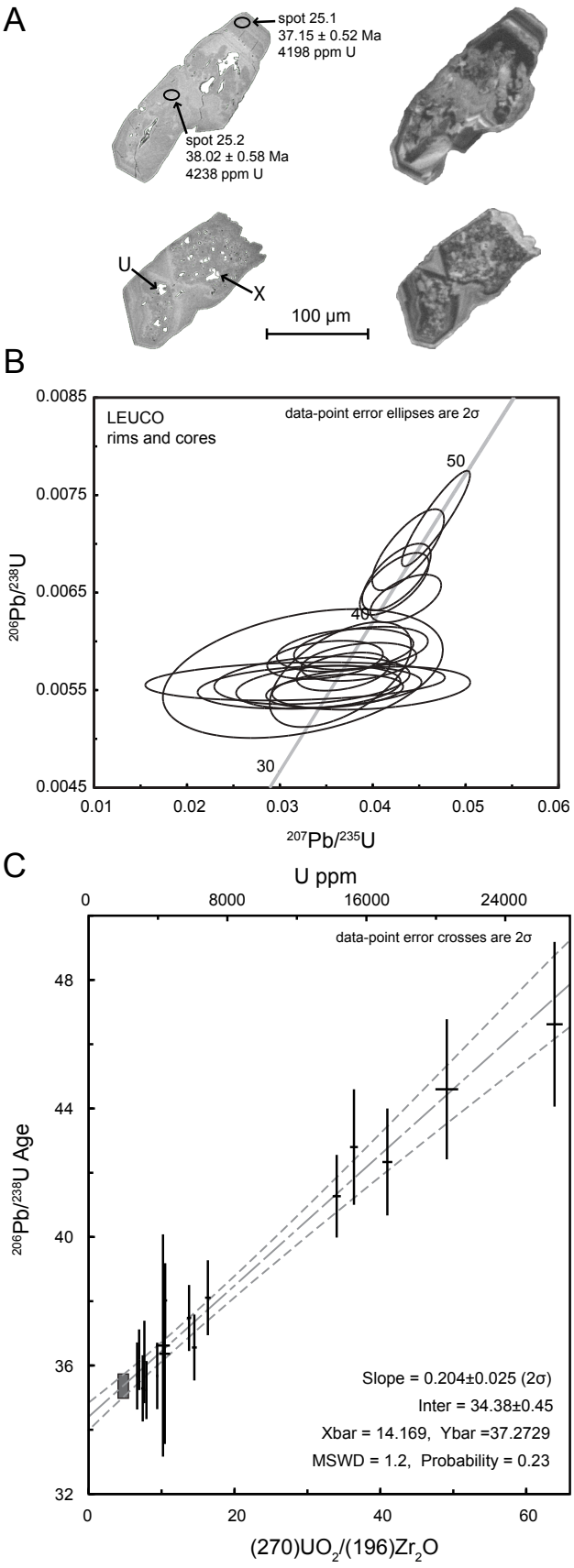


**Figure 3.13**
A) Back-scattered electron (left) and cathodoluminescence (right) photomicrographs of zircon separated from the specimen LEUCO. The zircons exhibit a partially metamict texture and local inclusions of discrete uranium-rich mineral phases: urananite-U; xenotime-X. Spot 25.1 and spot 25.2 are the locations of the analyses and $^{206}Pb/^{238}U$ ages that are shown. B) Concordia plots of rim and core analyses of zircons from specimen LEUCO. Error limits of all analyses include concordia. C) Plot and regression analysis of uranium concentration versus $^{206}Pb/^{238}U$ age for zircon specimens separated from LEUCO. Error in threshold and age determination through regression analyses depicted as grey box with black outline.

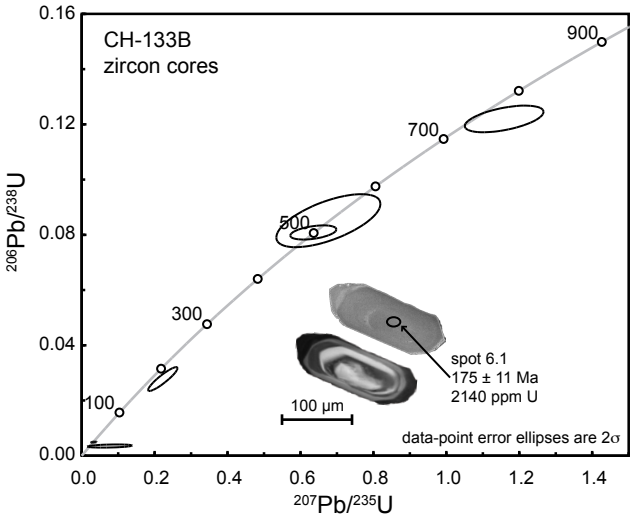


**Figure 3.14**
The results of SHRIMP II analyses of cores of zircon grains separated from specimen CH-133B of the main deformed phase of the Kung Tang granite. The spread in ages is interpreted to reflect a metasedimentary melt source. A representative zircon is shown as imaged by both back-scattered electron and cathodoluminescence. The age associated with the SHRIMP II analysis is a $^{206}Pb/^{238}U$ age.

zircon in the Kung Tang granite. Analyses of zircon rims yield weighted mean $^{207}Pb$ corrected $^{206}Pb/^{238}U$ ages of 16.9 ± 0.5 Ma and 17.2 ± 0.5 Ma for specimen CH-139B and 139C, respectively (Figures 3.15C, D; see Table 1 for exclusions). Two ages from zircon rims in specimen CH-139B have values of 35.9 ± 0.6 Ma and 28.6 ± 0.4 Ma and may reflect inherence or perhaps mixing of different age materials. All of the ages plot within error of concordia with the exception of one analysis from CH-139C (Figure 3.15D). Similar to specimens KTG-9A and LEUCO, the rims analyzed in zircon grains from specimens CH-139B and CH-139C show evidence for significant matrix effects due to high-uranium contents (Figures 3.15E, F). When the matrix effects are corrected back to a threshold of 2000 ± 300 ppm of uranium they yield $^{207}Pb$ corrected $^{206}Pb/^{238}U$ ages of 16.1 ± 0.4 Ma and 16.6 ± 0.3 Ma for CH-139B and CH-139C, respectively. These ages are within error and show that the two phases were formed over a relatively short time interval.

#### 3.6.1.3 ID-TIMS U–Pb analyses

Specimen KTG-9C is from an unfoliated post-D2 aplitic dyke (Figure 3.5B). This specimen was chosen to constrain the upper age limit for the development of the pervasive S2 foliation, which it cross-cuts, and a lower limit for D3-related deformation that has been observed to deform aplite dykes. Two single-zircon crystal fractions were analyzed and both yielded discordant results (Figure 3.16A). These results are interpreted as evidence for mixing of material between xenocrystic cores, presumably derived from the melt source, and new growth during crystallization preserved as rims around the core. This interpretation is supported by BSE microscopy, which shows that zircon from KTG-9C is characterized by bright, high-uranium rims developed around darker relatively-lower uranium-poor cores (Figure 3.16A).

---

**Figure 3.15**
A) Concordia diagram of the results of U-Pb analyses of zircon cores from specimen CH-139B. The spread in the data is interpreted to reflect the presence of older xenocrystic grains. Inset is a cathodoluminescence image of a representative zircon with typical dark uranium-poor cores surrounded by bright uranium-rich rims. Black circles with adjacent $^{206}Pb/^{238}U$ ages represent the location and result of a single SHRIMP II analysis. B) Concordia diagram of the results of U-Pb analyses of zircon cores from specimen CH-139C C) Results of SHRIMP II analyses of zircon rim material from specimen CH-139B. D) Concordia diagram showing the results of SHRIMP II analyses of zircon rims from specimen CH-139C. E) and F) Plots of uranium concentration versus $^{206}Pb/^{238}U$ age for CH-139B and CH-139C, respectively. Regression analyses with error envelopes used to determine the ages of the specimens at a threshold of 2000 ± 300 ppm of uranium are shown as dashed lines (error in threshold and age determination depicted as grey box with black outline).

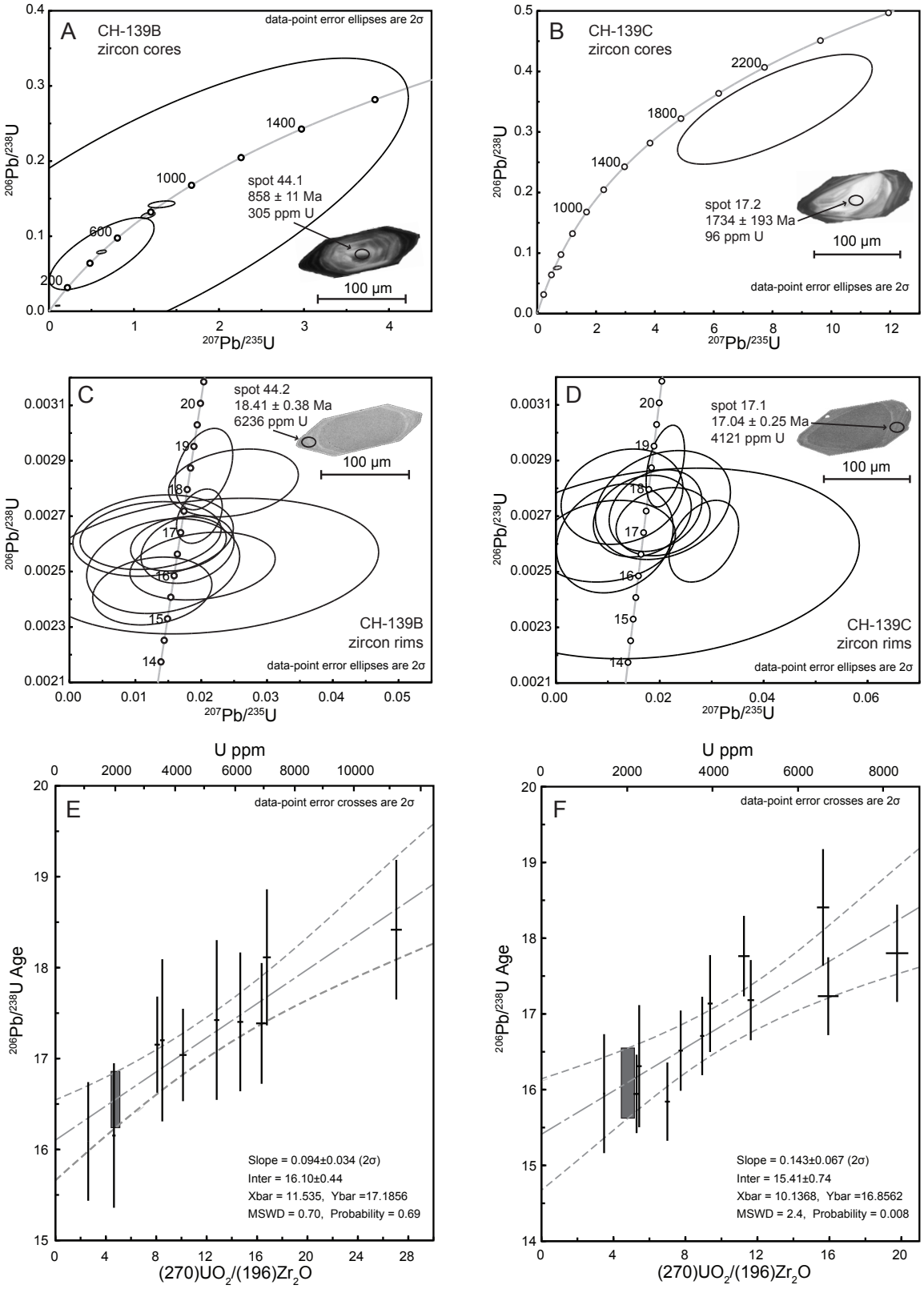
A
CH-139B
zircon cores
data-point error ellipses are 2σ
spot 44.1
858 ± 11 Ma
305 ppm U
100 µm
1400
1000
600
200
$^{206}Pb/^{238}U$
$^{207}Pb/^{235}U$
B
CH-139C
zircon cores
2200
1800
1400
1000
spot 17.2
1734 ± 193 Ma
96 ppm U
100 µm
data-point error ellipses are 2σ
C
spot 44.2
18.41 ± 0.38 Ma
6236 ppm U
100 µm
CH-139B
zircon rims
data-point error ellipses are 2σ
D
spot 17.1
17.04 ± 0.25 Ma
4121 ppm U
100 µm
CH-139C
zircon rims
data-point error ellipses are 2σ
U ppm
E
data-point error crosses are 2σ
$^{206}Pb/^{238}U$ Age
Slope = 0.094±0.034 (2σ)
Inter = 16.10±0.44
Xbar = 11.535, Ybar =17.1856
MSWD = 0.70, Probability = 0.69
$(270)UO_2/(196)Zr_2O$
F
data-point error crosses are 2σ
Slope = 0.143±0.067 (2σ)
Inter = 15.41±0.74
Xbar = 10.1368, Ybar =16.8562
MSWD = 2.4, Probability = 0.008

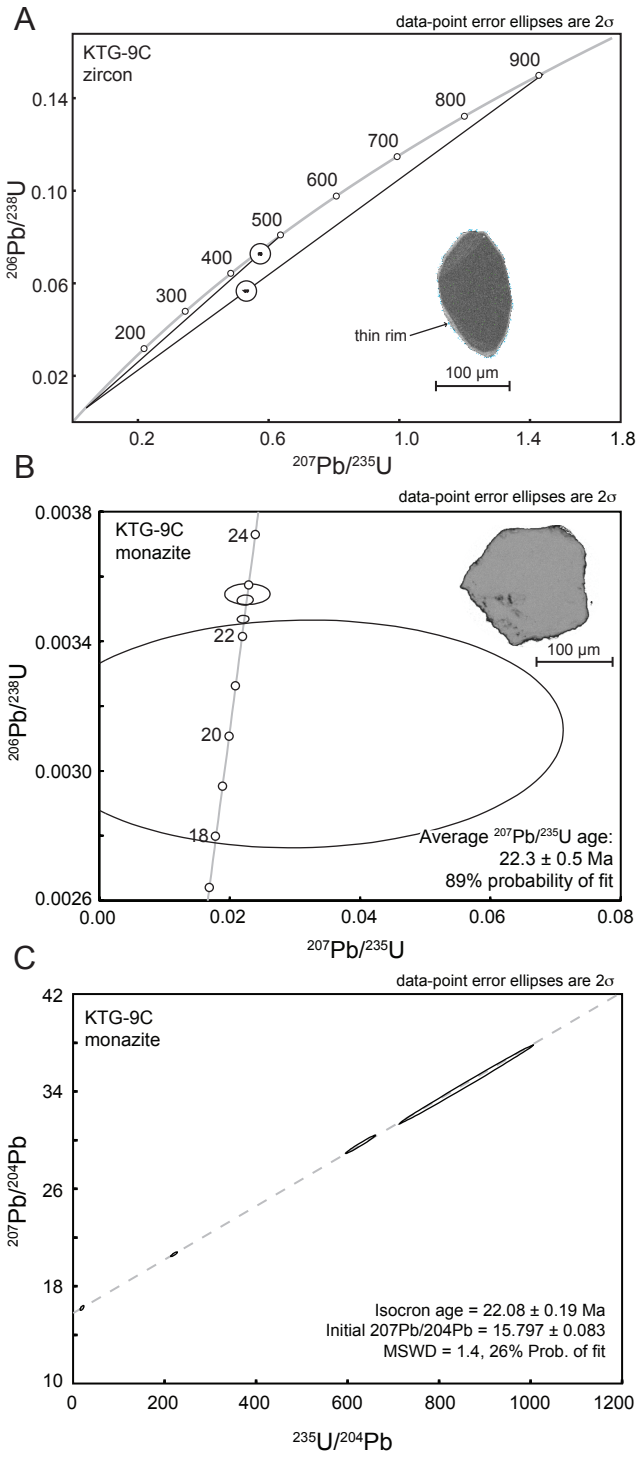


**Figure 3.16**
A) Discordant ID-TIMS analyses of abraded zircon separated from specimen KTG-9C. The results of these analyses are interpreted as evidence for mixing between old xenocrystic cores and new rim growth. Chords are drawn through a crystallization age of 23 Ma interpreted from SHRIMP data. The inset image of a zircon from specimen KTG-9C features a thin, high-uranium rim around a large, low-uranium core. Chords are drawn through the ca. 22 Ma age of the specimen as determined by analysis of uranium and lead in monazite from the same sample. B) Concordia plot of monazites from specimen KTG-9C, analyzed by ID-TIMS. C) $^{207}Pb$ versus $^{235}U$ isochron plot of monazite data normalized to $^{204}Pb$. MSWD; mean square weighted deviate.

Monazite separates from the same specimen, imaged using BSE techniques, are homogenous and do not show evidence for multiple growth generations (Figure 3.16B). The four U-Pb analyzed single crystals plot within error of concordia. However, only two of the error ellipses overlap (Figure 3.16B). When averaged, these analyses yield a $^{207}Pb/^{235}U$ age of 22.3 ± 0.5 Ma (89% probability of fit). Because the monazite from specimen KTG-9C is young and therefore relatively unradiogenic, the unknown composition of initial Pb adds significant uncertainty to the resultant ages. Furthermore, the degree of excess $^{206}Pb$ from fractionation of $^{230}Th/U$ is unknown. To avoid assumptions about the initial composition of common Pb and Th/U fractionation, the monazite data are plotted as a $^{207}Pb - ^{235}U$ isochron (Figure 3.16C). $^{204}Pb$ is used as a denominator in this plot to provide a simple reference isotope for the ratios as all $^{204}Pb$ can be attributed to common Pb (the data are corrected for blank contributions). This yields an isochron age of 22.08 ± 0.19 Ma, where the linear spread apparent in the data reflects a mixture between pure radiogenic Pb and a common Pb component. We interpret this age to mark the emplacement of the aplite dykes. It assumes that there is no significant bias from fractionation and decay of $^{231}Pa$.

### 3.6.2 $^{40}Ar/^{39}Ar$ thermochronology

$^{40}Ar/^{39}Ar$ analyses were carried out at the Queen's University Argon Geochronology laboratory. $^{40}Ar/^{39}Ar$ analysis of biotite and muscovite from specimens of Changgo granite yields ages that are significantly younger than those obtained through U-Pb analysis. Therefore, the results of $^{40}Ar/^{39}Ar$ analysis are interpreted as cooling ages and not crystallization ages. Three analyzed specimens are from within the granite, two of the dominant magmatic phase and one of the late aplitic phase (for localities see Figure 3.4). Data from these specimens are supplemented by three $^{40}Ar/^{39}Ar$ analyses of specimens from within the meta-sedimentary cover (see Figure 3.4 for localities). Mica separates were obtained through standard mechanical separation techniques and hand-picked under a binocular macroscope for clarity and lack of inclusions or inter-growth. (See appendices for analytical methods and full data tables.)

Specimen KT-202 is from the margins of a ca. 18 cm thick quartz vein within the lower domain of the meta-sedimentary carapace (Figure 3.4). A sieved fraction of muscovite with an average grain diameter of 420 ± 50 μm was used for $^{40}Ar/^{39}Ar$ laser step-heating analysis.

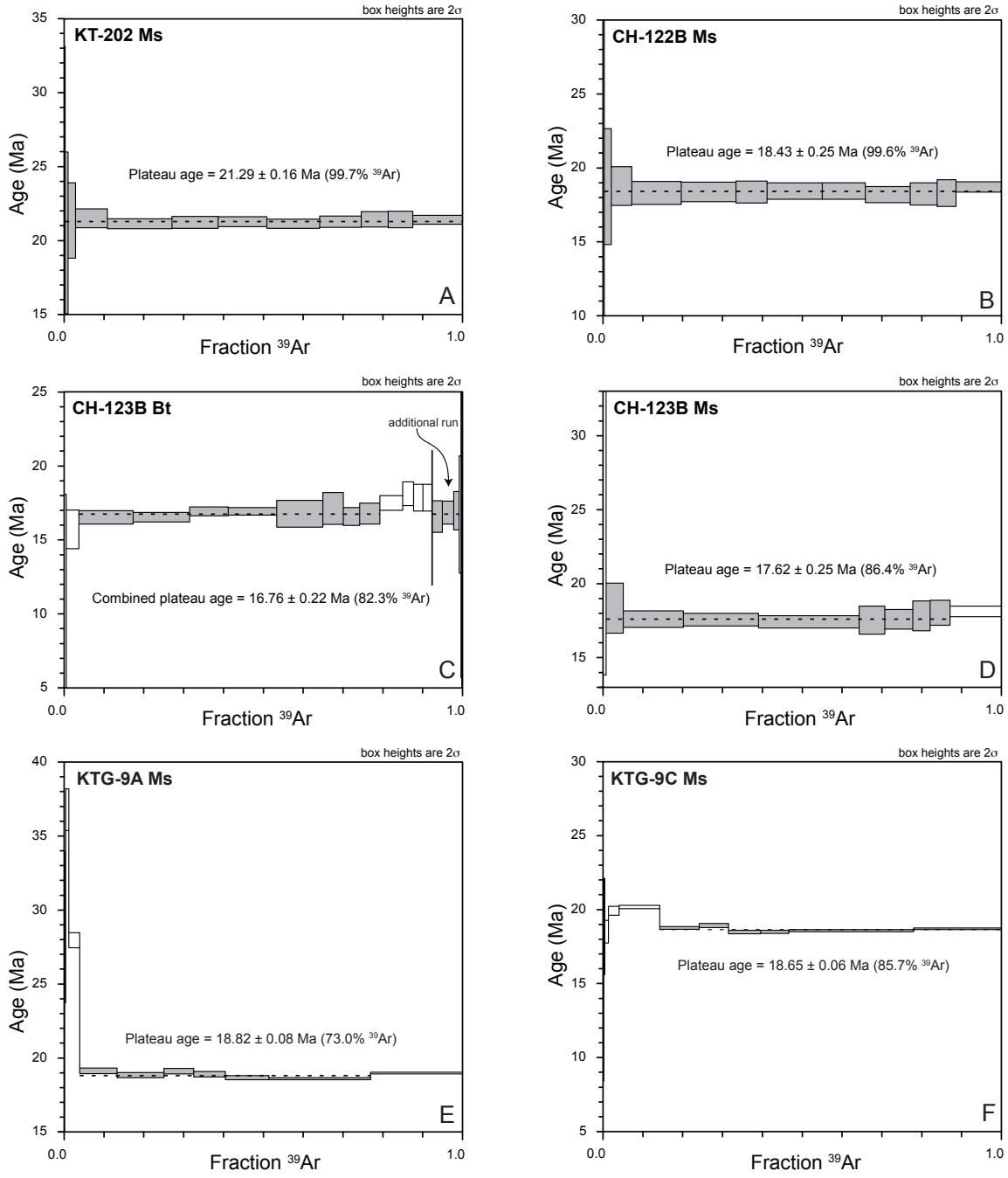


**Figure 3.17**
Results of $^{40}Ar/^{39}Ar$ thermochronologic analyses of muscovite and biotite separated from specimens collected across the Changgo area (see Figure 3.4 for sample locations). All analyses define broad plateaus and, when corrected for closure temperature variations due to grain size differences, indicate that cooling was earliest in the metasedimentary carapace and then proceeded into the interior of the Changgo granite.

$^{40}Ar/^{39}Ar$ analysis produced a well-defined age plateau, comprising 99.7% of released $^{39}Ar$, at 21.29 ± 0.16 Ma (Figure 3.17A). Specimen CH122B is from a pelitic schist within the shear zone that marks the boundary between the granite and the metasedimentary carapace. Muscovite with an average grain diameter of approximately 340 ± 50 μm was separated from specimen CH-122B. The results of $^{40}Ar/^{39}Ar$ laser step-heating analysis of these muscovite grains delineate a well-defined plateau, which consists of 100% of released $^{39}Ar$, at 18.43 ± 0.25 Ma (Figure 3.17B).

Specimens CH-123B and KTG-9A are from the deformed porphyritic phase of the Changgo granite while specimen KTG-9C is from an undeformed aplitic dyke. Biotite and muscovite from CH-123B were selected from a 425 μm-250 μm sieved fraction with an average grain size of 340 ± 50 μm. Biotite from this specimen yields a plateau age of 16.76 ± 0.22 Ma (82.3% of released $^{39}Ar$, Figure 3.17C), while muscovite from the same specimen yields a plateau age of 17.62 ± 0.25 Ma (86.4% of released $^{39}Ar$, Figure 3.17D). Muscovite from specimens KTG-9A and KTG-9C was picked from a 425+ μm sieved size fraction in which most grains had a circular disc shape with a diameter of approximately 1.5 mm and 1 mm, respectively. $^{40}Ar/^{39}Ar$ analyses of muscovite from KTG-9A and KTG-9C yield well-defined plateau profiles that correspond to cooling ages of 18.82 ± 0.08 Ma (73.0% of released $^{39}Ar$) for specimen KTG-9A, the porphyritic older phase (Figure 3.17E), and 18.65 ± 0.06 Ma (85.7% released $^{39}Ar$) for specimen KTG-9C, the aplitic younger phase (Figure 3.17F).

### 3.6.3 Significance of geochronologic and thermochronologic results

The results of the geochronometric and thermochronometric analyses undertaken in this study provide robust constraints on the evolution of the Changgo culmination and adjacent areas. Mylonitic leucogranite, observed in both the Changgo and Kung Tang domes, has an Eocene crystallization age of *ca.* 35 Ma. This age provides the earliest evidence of a protracted melt history in the North Himalayan antiform, adding significantly to previous work by Lee and Whitehouse (2007) who reported Eocene migmatization within the Mabja/Sakya dome. Similar to the model proposed by Godin et al., (2001) for the Eocene evolution of the Kali Gandaki valley in adjacent Nepal, the generation of leucogranitic melt in the Changgo and Kung Tang environ is interpreted to be a consequence of heating during initial crustal thickening. Evidence of crustal thickening is preserved as folded bedding in the upper domain in the Changgo culmination. In

a recent U-Pb study of the Kampa dome using SHRIMP spot analyses, Quigley et al., (2008) report three Eocene ages from metamict zircon, which they attribute to lead-loss. If the data from Quigley et al., (2008), which range in uranium content of zircon from ~7000 to 16,000 ppm and in age from ~52 to 32, are processed to compensate for high-uranium concentrations in the same manner as the data from the Changgo, they yield an age of 17.5 ± 4.9 Ma at a threshold of 2000 ± 300 ppm uranium. Thus, the zircon ages reported by Quigley et al., (2008) are reinterpreted by us to be Miocene. The results of analyses from specimen KTG-9A suggests that the main phase of the Changgo granite intruded at 23.5 ± 1.0 Ma, perhaps concurrently with top-to-the south displacement. The deformed granite phase is cut by unfoliated aplite dykes that yield a monazite age of 22.08 ± 0.19 Ma. The age of the aplite dykes constrains the end of top-to-the-south deformation in the granite to less than 22.08 ± 0.19 Ma ago whereas the youngest displacement along the top-to-the-north shear zone between the core and carapace, within which the dykes are deformed, must post-date this.

We interpret the difference in muscovite cooling ages within the granite core to reflect variations in the size of the grains analyzed, which show a correlation from older large grains to younger small ones. Estimation of the closure temperature of the muscovite from each specimen was calculated using the equations of Dodson (1973) with biotite parameters from Grove and Harrison (1996) and muscovite parameters from Hames and Bowring (1994). Errors for muscovite parameters have not been published, in this study we estimate ± 6% error in the activation energy, and ± 75% in the coefficient of diffusion, which compares to published values of ± 3% error in the activation energy and +65% and -30% for the diffusion coefficient of biotite (Grove and Harrison 1996). The cooling rate estimate of 80 ± 20˚C/Ma, as defined for the Nar and Manaslu regions (Godin et al., 2006b) *ca*. 40 km to the south of the Changgo area was used initially in the calculations. The cooling rate was later refined through iterative calculation of closure temperatures to be 62 ± 10˚C/Ma. The closure temperature estimates for each specimen are presented in Table 2.

The closure temperatures and plateau ages of specimens from within the granite core of the Changgo culmination, along with the crystallization of the main granite phase at 23.5 ± 1.0 Ma define a first order cooling rate for the Changgo area of 62 ± 10˚C/Ma (Figure 3.17A). The calculated rate assumes a crystallization temperature of 720 ± 65˚C/Ma for the Changgo granite

**Table 3.2 - Calculated Ar closure temperatures**

| Specimen | Mineral(s) | Sieve size | Median grain size | Closure Temperature | error |
|---|---|---|---|---|---|
| CH-123B | Biotite | 425-250 μm | 337 μm | 341 | ±16 |
| KT-202 | Muscovite | 425-250 μm | 420 μm | 421 | ±24 |
| CH-122B | Muscovite | 425-250 μm | 337 μm | 414 | ±25 |
| CH-123B | Muscovite | 425-250 μm | 337 μm | 414 | ±25 |
| KTG-9A | Muscovite | 425+ μm | 1500 μm | 469 | ±23 |
| KTG-9C | Muscovite | 425+ μm | 1000 μm | 453 | ±23 |

*error in median grain size is ±100 μm; closure temperature calculated with a cooling rate of ~62 ±11 ˚C/Ma; temperatures reported in ˚C (see text for discussion)

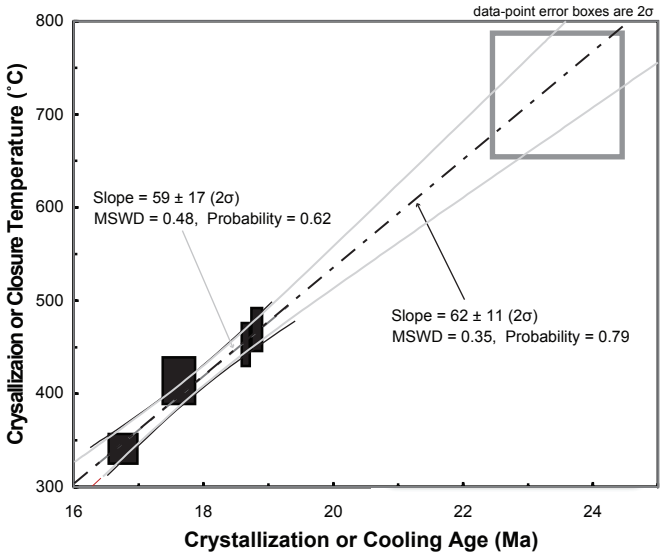


**Figure 3.18**
First order cooling rate of the Changgo granite between 23 Ma and 16 Ma. Grey box indicates U-Pb crystallization age and interpreted temperature of emplacement (Zhang et al., 2004). Black boxes indicate $^{40}Ar/^{39}Ar$ cooling age and closure temperature. Black dashed line indicates weighted linear regression calculated using estimates for crystallization of the Changgo granite with error envelop depicted with thin grey lines. Grey dashed line indicates weighted linear regression calculated using only argon cooling data; error envelope is shown as thin black lines. Isoplot 3.5 (Ludwig, 2003) was used to calculate regression lines and error envelopes.

taken from estimates by Zhang et al., (2004) for the crystallization of four two-mica granites within the North Himalayan antiform. If the U-Pb datum is excluded, the resultant regression calculation yields a cooling rate of 60 ± 13˚C/Ma that is not significantly different than that calculated by including the U-Pb datum.

The closure temperature estimate for muscovite grains in specimen CH-122B, which came from within the shear zone at the contact between the core and cover, is 414 ± 25˚C. Thus, the shear zone cooled through 414 ± 25˚C by *ca*. 18.43 Ma. Temperature of deformation estimated using quartz petrofabrics from the same outcrop indicates that deformation took place at 520 ± 50˚C. The closure temperature estimate for specimen CH-122B is significantly lower than the deformation temperature, which indicates that the deformation within the shear zone took place before ~18.43 Ma. Because movement in the shear zone affects aplite dykes of known age, the cessation of deformation related to ductile shearing can be constrained between 22.08 Ma (the age of the dykes) and 18.43 Ma. Furthermore, in the Kung Tang area, a large undeformed porphyritic dyke cross-cuts metasedimentary rocks in the shear zone that marks the core-cover contact. Two phases of this dyke (specimens CH-139B and C) yield indistinguishable crystallization ages of 16.1 ± 0.4 Ma and 16.6 ± 0.3 Ma (Figure 3.15E, F), which shows that displacement along the shear zone must have ceased by this time.

When grain-size is considered, the cooling ages from the Changgo culmination decrease towards its center; similar to the Kangmar dome (Lee et al., 2000). This apparent pattern of younging towards the center of the culmination is consistent with models of exhumation due to crustal-scale folding or faulting and paired erosion, diapirism, and some models of mid-crustal lateral flow (Hauck et al., 1998; Lee et al., 2001; Beaumont et al., 2004). The restricted spatial distribution, structural depth, and number of thermochronologic samples from the Changgo area, however, make extrapolation from cooling data to tectonic processes uncertain.

## 3.7 Discussion

### 3.7.1 Structural Evolution of the Changgo culmination

The geologic mapping and microstructural and isotopic analyses in this study constrain interpretations of the tectonic evolution of the Changgo culmination. The geochronologic and

thermochronologic data provide a temporal context for our structural mapping and microstructural fabric observations that, when integrated with other data from across the orogen, have important implications for the understanding of the evolution of the Himalayan-Tibetan system.

The tectonic evolution of the Changgo dome is summarized in Figure 3.19. Initial crustal thickening, expressed as large-scale, south-verging folding and thrusting within the TSS, resulted in dynamo-thermal metamorphism, partial melting of the mid-crust, and the formation and emplacement of leucogranite bodies at ~35 Ma (Figure 3.19A). More voluminous melt generation, coupled with retrograde metamorphism, occurred during the lateral southward-directed ductile extrusion of the mid-crust. The Changgo granite was intruded syn-tectonically at this time (Figure 3.19B). These interpretations are consistent with those of Lee et al., (2000, 2004, 2006), Aoya et al., (2006), and Quigley et al., (2006) who also concluded that an early vertical thickening and horizontal shortening phase was followed by regional metamorphism and subsequent horizontal stretching and vertical thinning (assuming plane strain as suggested by the quartz *c*-axis fabrics), mainly coincident with melt generation.

The main phase of the Changgo pluton was emplaced during southward-directed ductile flow of the mid-crust (Figure 3.19B). This deformation is expressed microstructurally in the orientation of quartz *c*-axes and macroscopically as a well-defined tectonic foliation. The top-to-the-south shear sense reflected in the quartz microstructures is the same as that reported in published petrofabric data from the central Nepalese Himalaya south of the Changgo area (Bouchez and Pêcher, 1976; Chapter 2 of this thesis), which are interpreted to be related to Miocene motion on the Main Central thrust fault (Chapter 2 of this thesis). The intrusion of 22.08 ± 0.19 Ma aplite dykes constrains the ductile top-to-the-south deformation in the Changgo culmination to be older than Early Miocene (Figure 3.19C), the same as the constraints on the latest ductile top-to-the-north displacement along the South Tibetan detachment system in central

**Figure 3.19**
Diagrammatic portrayal of the evolution of the Changgo culmination. A) Crustal thickening, metamorphism, and leucogranite melt generation due to south-verging thrusting and folding. B) Emplacement of the main phase of the Changgo granite during south-verging mid-crustal deformation above the MCT (Main Central thrust). C) Post-kinematic intrusion of aplitic dykes (shown in white). D) Cooling of carapace rocks, during north-verging shearing associated with displacement along the STDS (South Tibetan detachment system). E) Displacement across the STDS ceases. Continued cooling of the Changgo granite persisted during uplift and exhumation. Regional uplift occurs along the North Himalayan antiform.

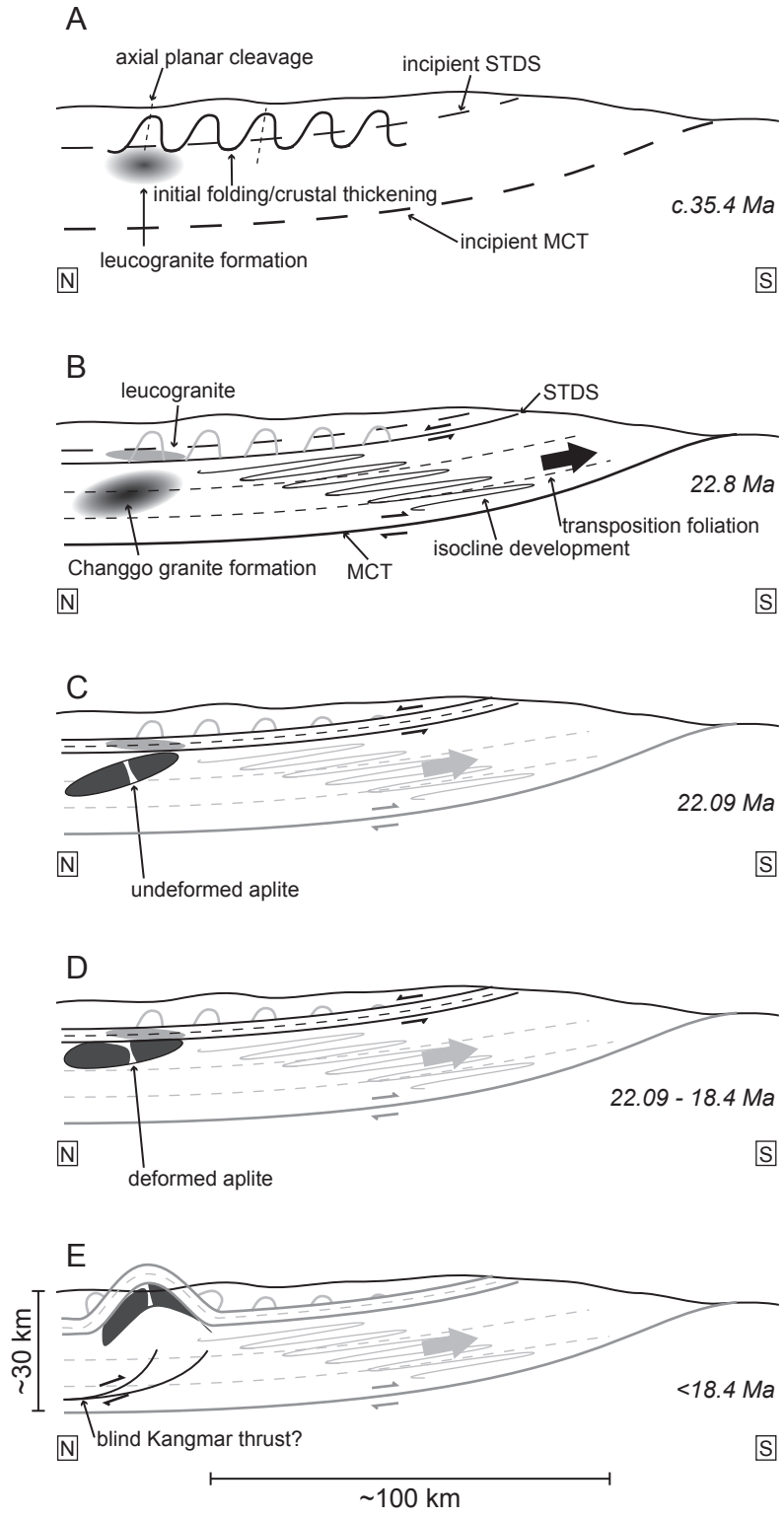
A
axial planar cleavage
incipient STDS
initial folding/crustal thickening
c.35.4 Ma
incipient MCT
leucogranite formation
N
S
B
leucogranite
STDS
22.8 Ma
transposition foliation
isocline development
Changgo granite formation
MCT
N
S
C
22.09 Ma
N
S
undeformed aplite
D
22.09 - 18.4 Ma
N
S
deformed aplite
E
~30 km
<18.4 Ma
N
blind Kangmar thrust?
S
~100 km

Nepal (Godin et al., 2001). Thus, the timing and shear sense of deformation in the Changgo granite is kinematically congruent with that in the exhumed Greater Himalayan sequence exposed in the frontal Himalaya.

Subsequent to southward-directed ductile flow of the mid-crust, the top of the Changgo pluton was deformed between 22.1 and 18.4 Ma by top-to-the-north ductile shear (Figure 3.19D). In the field, this deformation is manifested as a > 300 m thick shear zone straddling the boundary between the granitic core and its sedimentary carapace, in a relationship similar to the STDS in the Manaslu Himal to the south (Searle and Godin, 2003). Because of the similarities in character and structural position and age (i.e., a top-to-the-north-sense shear zone, above a mid-crustal melt-bearing zone, within the TSS) we interpret the shear zone between the Changgo granite and its sedimentary carapace to be the northerly equivalent to the STDS. A similar interpretation has also been made in the Kampa dome (Quigley et al., 2006). Based on stratigraphic level within the TSS, Aoya et al., (2006) and Kawakami et al., (2007) have interpreted a similar shear zone in the nearby Malashan area (Figure 3.2) to be a different detachment within the TSS. Although the stratigraphic levels of the granitic intrusions and the shear zones in the Changgo and Malashan areas (in Jurassic strata) are different relative to the STDS in the frontal Himalaya (in Cambrian - Ordovician strata), tectonic reconstructions have shown that the TSS, which occurs in its hanging wall of the STDS, was folded prior to displacement along the STDS (Godin et al., 1999a; Searle and Godin, 2003). Therefore the structural level of the STDS will not be everywhere constant. Kawakami et al., (2007) argue that to link the detachment observed in the Malashan area to the STDS, the STDS must dip at ~30˚ to the north, which they suggest is too shallow for a normal fault. A recent study of the STDS in the Dzakaa Chu region of southern Tibet (just north and east of Mt. Everest), however, supports the interpretation of Searle et al., (2003) and shows that the STDS actually dips at an angle of less than 35˚ (Cottle et al., 2007). We therefore speculate that the top-to-the-north shear zone described in the Malashan area is the STDS. Our interpretation is supported by reconnaissance fieldwork on the Kung Tang culmination, adjacent to the Malashan area (Figure 3.2), where a shear zone similar to that observed in the Changgo area and described in the Malashan region and Kampa area is also observed.

Subsequent to displacement along the STDS, which likely ended by *ca*. 18.4 Ma, and certainly by 16.55 ± 0.25 Ma, the Changgo culmination acquired the domal geometry it currently

exhibits and was exhumed subsequently by erosion (Figure 3.19E). Formation of the culmination appears to have been associated with the large-wavelength, low-amplitude folding of older structures perhaps reflecting large-scale vertical thickening and the development of the North Himalayan antiform. Local minor brittle normal faults may represent the final stages of doming or may be younger and independent of the entire process.

### 3.7.2 The post ca. 20 Ma Evolution of the Himalayan orogenic wedge

Exhumation of the Chako antiform, a metamorphic culmination in adjacent north-central Nepal (Figure 3.2), has been attributed to crustal warping in response to a decrease in orogenic critical taper at ca.16 Ma (Godin et al., 2006b). The large wavelength folding of tectonic foliation in the Changgo area is interpreted to be similarly related to crustal thickening by buckling that created a thrust-wedge-taper steep enough to propagate the tip of the wedge farther into the foreland. Out-of-sequence vertical thickening in the Changgo area at ~18 Ma may have increased the thrust-wedge taper enough to propagate thrusting towards the foreland to form the Chako antiform at ~16 Ma (Godin et al., 2006b) and subsequently into the main Himalayan front at ~ 14 Ma (Vannay and Hodges, 1996; Godin et al., 2001).

The lateral expansion of a foreland thrust-fold wedge can be compared to the spreading of an ice sheet and analyzed in terms of gravitational potential and a critical-taper thrust-fold wedge (Price, 1972; Elliot, 1976; Chapple, 1978; Davis et al., 1983; Platt, 1986). The basic parameters controlling the propagation of the thrust-fold wedge are the rheology of the material in the wedge and the dip and strength of the detachment at its base (Chapple, 1978; Suppe, 2007).

The role of gravitational potential in explaining Himalayan tectonics has been explored previously. Hodges et al., (1996) discussed the gravitational extrusion of mid-crustal material southwards from beneath the Tibetan plateau by concurrent displacement along both the Himalayan basal detachment and the STDS in response to crustal thickening and increased gravitational potential under the plateau while Godin et al., (2006b) evoked critical taper theory to explain the exhumation of the Chako antiform. Furthermore, Kohn (2008) has argued that P-T-t data from the frontal Himalaya are best explained by critical taper theory. Here we invoke gravitational potential to elucidate the diachronous, post-20 Ma, out-of-sequence deformation history across the frontal Himalaya and the subsequent activation of the Main Boundary thrust

(Figure 3.20). Restoration of the critical orogenic taper by out-of-sequence vertical thickening possibly related to blind thrusting, crustal buckling, or inflation of the plateau, after motion along the Main Central thrust had ceased by ca. 21 Ma in central Nepal (Godin et al., 2006a), is interpreted to have thickened the crust in the Changgo area and, paired with erosion, led to the exhumation of the Changgo granite.

Our interpretation of the early Miocene (*ca*. 20 - 12 Ma) evolution of the Himalayan front is based upon an important simplifying assumption - mica cooling ages are assumed to record erosional exhumation driven by crustal thickening. The variations in $^{40}Ar/^{39}Ar$ cooling ages are interpreted to reflect the diachronous nature of displacement within a complex convergent system that, although part of a single framework on longer timescales, appears to operate in distinct segments over shorter time-scales (e.g., Price, 1988). To explore the post-20 Ma diachroneity in deformation and exhumation along the Himalayan front we examine, in detail, two well-constrained transects: 1) across the Annapurna/Manaslu Himal in central Nepal and adjacent southern Tibet, and 2) across eastern Nepal and southern Tibet near the Everest region.

The southward extrusion and rapid erosion of Greater Himalayan sequence rocks from

---

**Figure 3.20**
Diagrammatic regional model of the early Miocene (20-12 Ma) evolution of southern Tibet and the frontal Himalayan in adjacent Nepal. Left side – central Nepal (Annapurna region), right side – eastern Nepal (Everest region). A) Southward extrusion of ductile mid-crustal rocks terminates with final displacement along the MCT and STDS. B) Continuing displacement along the STDS and MCT accompanies southward extrusion of ductile mid-crustal infrastructure of the orogen. C) Out-of-sequence buckling of the proximal hinterland leading to rapid erosional exhumation and cooling of mid-crustal rocks. The Changgo area cooled at ~18.8 Ma. Subsequently deformation propagated southward towards the foreland uplifting the Chako antiform at ~16 Ma. D) Final displacement along the STDS and the MCT terminates extrusion and partial exhumation (significant cooling) of the Himalayan metamorphic slab ends by ~16 Ma. The MCT and STDS may have remained active longer here than in central Nepal because the mid-crustal zone was significantly thicker and took longer to cool. Temperature controlled rheology is effectively the extrusion stop-valve. E) Thrust duplexing beneath the MCT uplifted the Greater Himalayan sequence. Localized thrusting on the north-dipping limb of the Chako antiform and Changgo culmination. Probable time of initiation of east-west extension in the Tibetan plateau. The increase in gravitational potential due to crustal thickening leads to the initiation of displacement on the Main Boundary thrust (MBT). F) Initiation of duplexing beneath the MCT uplifts the Greater Himalayan sequence. Localized out-of-sequence buckling farther east is reflected in cooling of the Kampa dome. G) Lateral spreading of the orogenic wedge by southward propagation of thrusting along the MBT. East-west extension in the hinterland also begins at this time. H) Out-of-sequence motion across the Kangmar thrust fault in southern Tibet increases the gravitational potential and drives lateral spreading into the foreland. East-west extension in the Tibetan plateau is underway at this time.

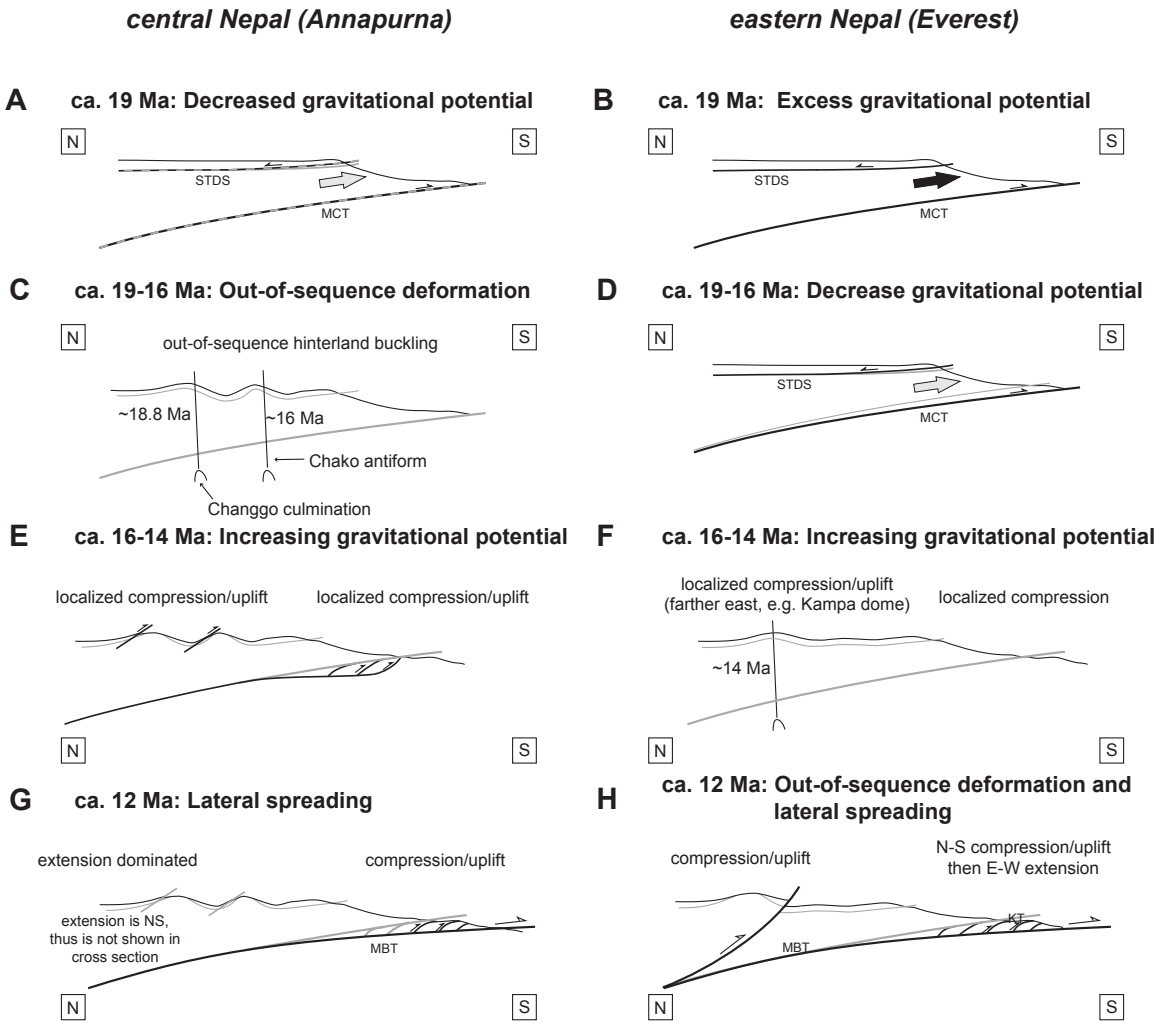
central Nepal (Annapurna)
eastern Nepal (Everest)
A
ca. 19 Ma: Decreased gravitational potential
N
S
STDS
MCT
B
ca. 19 Ma: Excess gravitational potential
N
S
STDS
MCT
C
ca. 19-16 Ma: Out-of-sequence deformation
N
out-of-sequence hinterland buckling
S
~18.8 Ma
~16 Ma
Chako antiform
Changgo culmination
D
ca. 19-16 Ma: Decrease gravitational potential
N
S
STDS
MCT
E
ca. 16-14 Ma: Increasing gravitational potential
localized compression/uplift
localized compression/uplift
N
S
F
ca. 16-14 Ma: Increasing gravitational potential
localized compression/uplift
(farther east, e.g. Kampa dome)
localized compression
~14 Ma
N
S
G
ca. 12 Ma: Lateral spreading
extension dominated
compression/uplift
extension is NS,
thus is not shown in
cross section
MBT
N
S
H
ca. 12 Ma: Out-of-sequence deformation and
lateral spreading
compression/uplift
N-S compression/uplift
then E-W extension
KT
MBT
N
S
Grey: past event
Black: active event
MCT, Main Central thrust
STDS, South Tibetan detachment system
KT, Kangmar thrust
MBT, Main Basal thrust

beneath southern Tibet, which was ongoing *ca*.19 Ma, reduced the gravitational potential required to drive thrust and fold deformation farther south in central Nepal (Figure 3.20A). It also resulted in the cessation of movement along both the MCT (Godin et al., 2006a) and STDS (Godin et al., 2006b). However, in eastern Nepal, during the same time interval, gravitational potential was still sufficient to drive southward extrusion of Greater Himalayan sequence rocks and displacement along the MCT and the STDS (see Godin et al., 2006a and references therein) (Figure 3.20B). Between *ca*. 19 and 16 Ma the locus of deformation in central Nepal shifted back toward the hinterland in southern Tibet (Figure 3.20C). This out-of-sequence deformation, which was manifested in the ~18.8 Ma cooling of the Changgo granite eventually increased the gravitational potential across the thrust-fold wedge and deformation then shifted back toward the foreland and the tip of the thrust-fold wedge with the development of the Chako antiform at *ca*.16 Ma (Figure 3.20C) (Godin et al., 2006b). In the eastern Nepal transect the southward extrusion of the mid-crust waned due to southward extrusion of Greater Himalayan sequence rocks. This resulted in a decrease in gravitational potential between *ca*.19 and 16 Ma and cessation of displacement along the STDS (Hodges et al., 1998; Cottle et al., 2007) (Figure 3.20D). The MCT and STDS may have been active longer in the Everest region, relative to central Nepal, because the mid-crustal rock layer that was extruded and exhumed in the Everest region is significantly thicker than that in the Annapurna region and would thus would have taken longer to cool. Cooling of the mid-crustal layers as it was extruding may have acted as a "stop-valve" by increasing its viscosity. $^{40}Ar/^{39}Ar$ data from the Everest region records significant cooling by *ca*.16 Ma (Hubbard and Harrison, 1989; Hodges et al., 1998), which is likely due to erosional exhumation of the Greater Himalayan sequence. Between *ca*. 16 and 14 Ma, the orogenic wedge continued to expand southward into central Nepal with the southward propagation of thrusting and folding and the initiation of thrust duplexing within the Lesser Himalayan sequence (e.g. DeCelles et al., 2001; Robinson et al., 2006; Pearson and DeCelles, 2005). This deformation extended under the extruded mid-crust beginning at *ca*. 15-14 Ma (Figure 3.20E) driving its uplift, erosional exhumation, and cooling (Vannay and Hodges, 1996; Godin et al., 2001). During this interval gravitational potential in eastern Nepal does not appear to have been sufficient to drive thrusting and folding southwards (Figure 3.20F). Farther east of the Everest region, out-of-sequence deformation in southern Tibet is reflected in the initiation of cooling in the Kampa and Kangmar

domes at 15-14 Ma (Lee et al., 2000; Quigley et al., 2006). We speculate that the uplift of these domes is related to initial displacement on the Kangmar thrust.

At *ca*.12 Ma, in central Nepal, lateral gravitational spreading involved growth of the orogenic wedge and was marked by the further development of the thrust duplex in the Lesser Himalayan sequence and by the southward propagation of the Main Boundary thrust fault (e.g., Meigs et al., 1995) (Figure 3.20G). At *ca*.12 Ma in eastern Nepal, gravitational potential within the orogenic wedge was restored by out-of-sequence displacement along the Kangmar thrust in southern Tibet. The North Himalayan antiform was uplifted by the vertical component of the thrusting. The resulting increase in gravitational potential was sufficient to drive thrusting southwards, where it was manifested as thrust duplexing within Lesser Himalayan strata. Eventually, southward lateral spreading involved the initiation of the Main Boundary thrust (Figure 3.20H).

Clear differences in the timing of the post-20 Ma tectonic evolution between the central and eastern Nepalese Himalaya and adjacent portions of Tibet can be explained by teh differences in teh timing of termination of extrusion of the Greater Himalayan sequence and ensuing tectonic thickening. It is interpreted that the reorganization of the orogenic wedge between ~20 Ma and ~12 Ma reflects the transfer of southward transport from the MCT to the Main Boundary thrust.

## 3.8 Conclusions

The Changgo culmination comprises a core of multiphase granite surrounded by deformed meta-sedimentary carapace. There is evidence for multiple deformational events in the Changgo area, although a number of these are minor. After initial crustal thickening and melt production in the Eocene at 35.4 ± 0.4 Ma, the main phase of the granitic core crystallized at 23.5 ± 1.0 Ma late-syn-kinematically during top-to-the-south-sense shearing of the Greater Himalayan sequence. This shearing had ended by 22.08 ± 0.19 Ma, the time of intrusion of the undeformed aplite dykes that cross-cut the transposition fabric associated with it. These two dates constrain the end of top-to-the-south deformation in the Greater Himalayan sequence to between 23.5 ± 1.0 Ma and 22.08 ± 0.19 Ma. The contact between the carapace and core of the culmination in the Changgo area is interpreted to be a strand of the STDS. This fault is marked by a > 300 m thick shear zone with macroscopic top-to-the-north shear sense indicators. The shear strain

associated with the fault deforms the 22.08 ± 0.19 Ma aplitic dykes, pre-dates cooling through mica argon closure temperatures of 414 ± 21˚C, at *ca*. 18.43 ± 0.53 Ma, and is demonstrably cut by undeformed porphyritic dykes at 16.6 ± 0.3 Ma. Subsequent crustal thickening, through crustal-scale buckling, blind thrusting, or ductile inflation, drove the erosional exhumation of the Changgo area and imparted the present-day domal geometry. This thickening is interpreted to be related to out-of-sequence deformation and crustal thickening in response to a reduction in gravitational potential in central Nepal. The same process can explain the diachroniety of exhumation/cooling that exists along the North Himalayan antiform and results in the lateral expansion of the Himalayan-Tibetan orogen.

## Acknowledgements

This project was funded by a Natural Science and Engineering Research Council of Canada Discovery grant to L. Godin and Canada Graduate Scholarship to K. Larson. Support for geochronologic analyses was provided by a GSA Research Grant to K. Larson. D. Watts and J. Wolters are thanked for processing and providing access to the ASTER images of Tibet. Logistical support in Beijing was provided through collaboration with D. Lin and J. Han of the Chinese Academy of Science. Assistance in the field was provided by Y. Najman, C. Fulong, and N. Portelance. Field logistics were arranged through Shigatse Travels. K. Kwok, S. Kamo, M. Hamilton, and J. Eliades are thanked for their help with specimen preparation, separation, and analysis at the University of Toronto. T. Pestaj and N. Rayner are thanked for their assistance with SHRIMP analyses at the Geological Survey of Canada. Support in the Queen's Argon Laboratory was provided by D. Archibald. This chapter has benefited through discussions and reviews by R.A. Price, R.L. Brown, and D. Grujic.

# Chapter 4

# Relationships between displacement and distortion in orogens: linking the Himalayan foreland and hinterland in central Nepal

## 4.1 Abstract

The Greater Himalayan sequence, as exposed in the Manaslu-Himal Chuli Himalaya along the Budhi Gandaki and Dauradi valleys, comprises a ~43 km thick layer of exhumed mid-crustal rocks. This estimate is ~20 km thicker than previous estimates in the same area because of a reinterpretation of the location of the Main Central thrust fault - the base of the Greater Himalayan sequence. The rocks in the hanging wall of the Main Central thrust are deformed pervasively and are characterized by a conspicuous transposition foliation, a Cenozoic metamorphic history, and Neogene cooling history. Quartz *c*-axis deformation fabrics indicate that deformation across the Greater Himalayan sequence occurred at high temperatures ranging from ~450˚C near its base to ~640˚C within the migmatitic upper portion. Vorticity analyses show evidence of almost equal contributions of coaxial and non-coaxial components of deformation throughout the lower-to-middle portion of the Greater Himalayan sequence. $^{40}Ar/^{39}Ar$ thermochronology indicates that all material in the hanging wall of the Main Central thrust was exhumed in the Neogene.

Greater Himalayan sequence rocks exposed in this portion of central Nepal can be separated into distinct upper and lower parts. Peak metamorphic temperatures across the migmatitic upper part are essentially isothermal, perhaps because of thermal buffering during anatexis, whereas metamorphic pressure estimates across the same section define an apparent metamorphic pressure gradient of 620 bars/km, double that expected for normal continental crust. This abnormal pressure gradient can be attributed to 50% post-metamorphic tectonic thinning of the upper Greater Himalayan sequence. In contrast, in the lower part of the Greater Himalayan sequence metamorphic pressure and temperature decrease with structural depth. This is interpreted to be the result of the progressive downward expansion of the metamorphic shear zone at the base of the Greater Himalayan sequence. This downward migration of the Main Central thrust, which involved thrust slice subcretion, was coeval with the tectonic exhumation of

the overlying mid-crustal package.

Deformation in the upper portion of the Greater Himalayan sequence was characterized by extending flow (i.e. extension in the direction of flow), expressed as vertical thinning with commensurate horizontal extension, whereas deformation in the lower portion of the Greater Himalayan sequence was characterized by compressing flow; compression in the direction of flow expressed as vertical thickening and horizontal compression. Extending flow is a characteristic feature of displacement and distortion in deep orogenic hinterlands, and compressing flow is characteristic of displacement and distortion in orogenic foreland regions. The transition between the upper and lower Greater Himalayan sequence thus represents a fundamental transition between hinterland-style deformation, involving processes such as lateral mid-crustal flow, and foreland-style deformation and processes such as critical thrust-fold wedge taper. Both types of processes are essential to maintaining an overall orogenic wedge through different methods of material transfer.

## 4.2 Introduction

### 4.2.1 Kinematic compatibility in orogens

The stark contrast in style of deformation between the deep interior of the hinterland of an orogen and the shallower regions of its foreland belies the fact that these disparate geologic domains generally form at the same time in response to the same regional plate-tectonic framework. The foreland thrust and fold belt is an expanding critical-taper wedge within which detached supracrustal strata, deformed by listric thrust faulting and thrust-related folding, are compressed horizontally and thickened vertically as they are displaced over the under-riding craton and foreland sediments. Lateral growth of the wedge, induced by plate convergence, a high topographic gradient, and associated gravitational spreading, is accommodated within the wedge by horizontal shortening in the direction of displacement. This relationship between displacement and distortion is characteristic of compressing flow (Price, 1972). In contrast, the combination of recumbent folding, shallowly dipping transposition foliation, pronounced stretching , and foreland directed shear in the deep (mid-to lower crustal) metamorphic core of an orogen involves a relationship between displacement and distortion - extension in the direction of flow - that is

characteristic of extending flow (Price, 1972).

Compressing flow and extending flow are simple conceptual models of the kinematics of flow that were used by Nye (1952) to analyze the deformation in ice sheets and glaciers. As with ice sheets and glaciers, gravitationally driven lateral spreading in orogenic belts involves a continuum between extending flow in the metamorphic core zone beneath the topographically highest parts of an orogen and compressing flow in the topographically lower foreland region. This distinction between displacement and distortion during lateral gravitational spreading, which reconciles the disparities in style of deformation between the metamorphic core zone and foreland thrust and fold belt, also implies that during orogenesis diachronous tectonic overprinting occurs as rock moves from a geographic domain of extending flow into an adjacent domain of compressing flow (or vise versa).

Dynamic relationships between displacement and distortion within the hinterland and foreland of the Himalaya-Tibet orogen are evident in both thermo-mechanical mathematical models of lateral mid-crustal extrusive flow (e.g. Beaumont et al., 2001; Beaumont et al., 2004; Beaumont et al., 2006) and models of critical wedge taper (e.g. Bollinger et al., 2006; Kohn, 2008) that have been proposed to explain the evolution of the India-Asia collision. The kinematic transition between the hinterland and foreland is not the focus of these models, however, and as such both the details and the conceptual framework of this transition remain enigmatic. Understanding the kinematic transition between the hinterland and foreland regions of the Himalaya, the prototypical continent-continent collision, is critical to elucidating orogenesis in general.

### 4.2.2 The Himalaya

The geology of the Himalayan arc is commonly described in terms of three discrete, fault-bounded tectonostratigraphic rock assemblages that were identified by Heim and Gansser (1939) and have subsequently been mapped along its entire length (see Hodges, 2000; Yin and Harrison, 2000 and references therein). The three assemblages have been interpreted as comprising sediment that was originally deposited as parts of a southward-tapering continental margin wedge of supracrustal sedimentary rocks that accumulated along the northern former margin of India (Searle et al., 2006) and subsequently was scraped off of the under-riding Indian

continent and deformed by the over-riding Asian continent. The structurally lowest assemblage, the Lesser Himalayan sequence, consists of unmetamorphosed to low metamorphic-grade rocks. The overlying Greater Himalayan sequence, which has been displaced southward over the Indian craton along Main Central thrust (Figure 4.1), consists of exhumed greenschist to upper amphibolite, and locally granulite, grade metamorphic rocks. The structurally highest domain, the Tethyan sedimentary sequence, is underlain by the South Tibetan detachment system, a network of top-to-the-north normal sense detachment faults that can be mapped along the length of the orogen (Figure 4.1; Hodges, 2000). The Tethyan sedimentary sequence consists generally of an unmetamorphosed assemblage of Paleozoic to Mesozoic passive margin strata.

The deformational history of the Greater Himalayan sequence and the Lesser Himalayan sequence currently is the subject of intense debate ( e.g., Grujic et al., 1996; Parrish and Hodges, 1996; Hodges, 2000; Catlos et al., 2001; Martin et al., 2005; Robinson and Pearson, 2006; Searle et al., 2006; Caddick et al., 2007; Harris, 2007; Chambers et al., 2008; Searle et al., 2008; Chapter 2 of this thesis). The initial view of Himalayan geology was that the Greater Himalayan sequence was thrust over the Lesser Himalayan sequence along the Main Central thrust during the early Miocene (Gansser, 1964). While the concept of the Main Central thrust has largely endured, the timing of displacement across it, and the definition of the exact boundary between the Greater Himalayan sequence and Lesser Himalayan sequence are controversial (for a review of the Main Central thrust controversy see Searle et al., 2008). It is important to state from the outset, therefore, that we follow the definition of the Main Central thrust proposed by Searle et al. (2008) who suggest that the logical criterion for recognizing the thrust is that it is a zone of high ductile shear strain separating rocks typical of the Lesser Himalayan sequence below, from rocks of the Greater Himalayan sequence above. The lower portion of the latter commonly comprises an inverted metamorphic sequence along the front of the high Himalaya. Above the Main Central thrust all rocks record evidence of Cenozoic Himalayan metamorphism and cooling and some degree of pervasive ductile shear strain, while below it rocks are unmetamorphosed-to-weakly metamorphosed, characterized by sedimentary structures such as primary bedding, oscillatory ripple marks, and cross-bedding, and record Paleozoic to Precambrian cooling ages. By definition (e.g., Gansser, 1964) everything above the Main Central thrust belongs to the Greater Himalayan sequence, and as such, using the Searle et al. (2008) definition of the Main Central thrust, requires

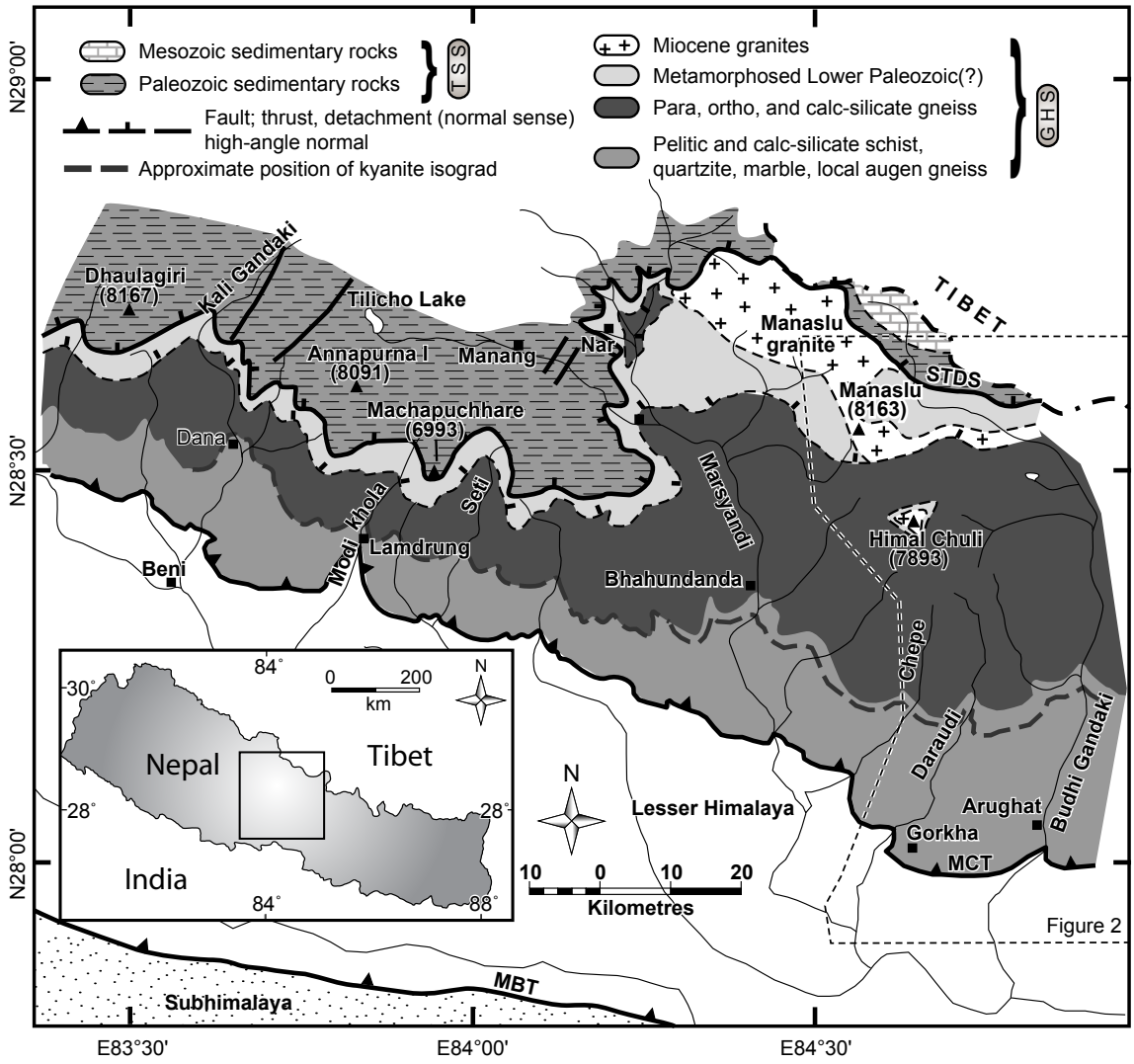


**Figure 4.1**
Simplified geologic map of central Nepal (modified from Searle et al., 2008). Location of this map is depicted in the inset map of Nepal. TSS, Tethyan sedimentary sequence; GHS, Greater Himalayan sequence; STDS, South Tibetan detachment system; MCT, Main Central thrust; MBT, Main Boundary thrust.

that rocks considered part of the Lesser Himalayan sequence by previous researchers (e.g., Colchen et al., 1986) be part of the Greater Himalayan sequence.

There are two petrologically distinct lithologic domains within the Greater Himalayan sequence in central Nepal. The upper Greater Himalayan sequence is distinguished by the occurrence of migmatitic paragneiss and orthogneiss. While local anatectite crystallization ages of *ca*. 35 Ma have been reported from the Kali Gandaki valley (Godin et al., 2001; Figure 4.1) most anatectite crystallization ages from within the upper Greater Himalayan sequence have been dated at *ca*. 22-22.5 Ma (Nazarchuk, 1993; Hodges et al., 1996; Godin et al., 2001), and are approximately synchronous with metamorphic monazite ages from the same structural level (Catlos et al., 2001; Kohn et al., 2001). In contrast, the lower Greater Himalayan sequence contains very little if any anatectite and, moreover, metamorphic monazite ages are progressively younger with depth below the migmatitic upper portion. Although monazite ages from the lower Greater Himalayan sequence in central Nepal have been interpreted as dating prograde metamorphism, studies by Bollinger and Janots (2006) and Martin et al. (2007) have demonstrated that some Himalayan monazite may have formed through retrograde metamorphic reactions or may have been effected by post-crystallization alteration.

The migmatitic upper portion of the Greater Himalayan sequence has been interpreted as ductile rock that was extruded laterally from beneath the Tibetan plateau whereas the non-migmatitic lower portion has been interpreted as a downward expanding shear zone at the base of this layer (Searle et al., 2008; Chapter 2 of this thesis). It is the relationship between the upper and lower portions of the Greater Himalayan sequence, in the hanging wall of the Main Central thrust fault, that we seek to elucidate.

Herein we present the results of our mapping analysis of a transect across the Greater Himalayan sequence in the Budhi Gandaki valley and Daraudi valley of the Manaslu-Himal Chuli Himalaya in central Nepal (Figure 4.1). This portion of central Nepal has been the subject of several previous geologic studies that have cumulatively generated a substantial structural, thermochronometric, thermobarometric and microstructural database (e.g., Bouchez and Pêcher, 1981; Deniel et al., 1987; Hodges et al., 1988; Copeland et al., 1990, 1991; Guillot et al., 1994, 1995; Harrison et al., 1999; Kohn et al., 2001; Wobus et al., 2003, 2005). Our study focuses on the transition between the migmatitic portion of the Greater Himalayan sequence and the non-

migmatitic metamorphic rocks of the lower Greater Himalayan sequence and the relationship between displacement and distortion associated with the emplacement of the metamorphic rocks of the Greater Himalayan sequence between the Tethyan sedimentary sequence and the Lesser Himalayan sequence.

## 4.3 Manaslu–Himal Chuli Himalaya

We recognize three fault-bounded tectonostratigraphic domains in the Manaslu–Himal Chuli Himalaya: the Lesser Himalayan sequence, the Greater Himalayan sequence, and the Tethyan sedimentary sequence, but our focus in this study is on the evolution of the Greater Himalayan sequence and only it will be discussed in detail.

### 4.3.1 The Greater Himalayan sequence

The top of the Greater Himalayan sequence is marked by the uppermost top-to-the-north sense detachment fault within the South Tibetan detachment system (Searle and Godin, 2003). In the Manaslu–Himal Chuli Himalaya the upper part of the Greater Himalayan sequence is amphibolite-grade, diopside-bearing calc-silicate schist with locally abundant phlogopitic marble (Figure 4.2). The calc-silicate schist locally contains boudinaged pods of anatectic quartz, feldspar, and tourmaline. The schist, which comprises the Nilgiri, Pi, and Annapurna formations of Colchen et al. (1986), is pervasively deformed and commonly preserves top-to-the-north sense C-S-C′ fabrics (Figure 4.3A). Structurally below the calc-silicate schist is quartz-rich mica schist (Figure 4.2) that is likely equivalent to the Sanctuary Formation of Colchen et al. (1986). The Chokang arm of the Manalsu pluton intrudes the quartz mica schist and locally contains large rafts of the country rock within it (Figure 4.3B). Pervasive deformation within both the Chokang arm and the quartz mica schist involves top-down-to-the-north sense shear.

Granitic orthogneiss crops out subjacent to the quartz mica schist in the Budhi Gandaki valley (Figure 4.2). The quartz + biotite + K-feldspar ± garnet orthogneiss, which commonly contains alkali-feldspar augen up to 10 cm in length, locally hosts feldspar + quartz ± biotite ±

**Figure 4.2**
Geologic map of the Manaslu-Himal Chuli Himalaya. All geological data are from this study with the exception of the location of geologic contacts on the Manaslu massif, which are transcribed from Colchen et al., (1986). A-A', B-B', C-C', and D-D' are lines of section depicted in Figure 4. Geologic data are projected onto line D-D' from a north-northwest trending line that follows the Himal Chuli-Manaslu ridge.

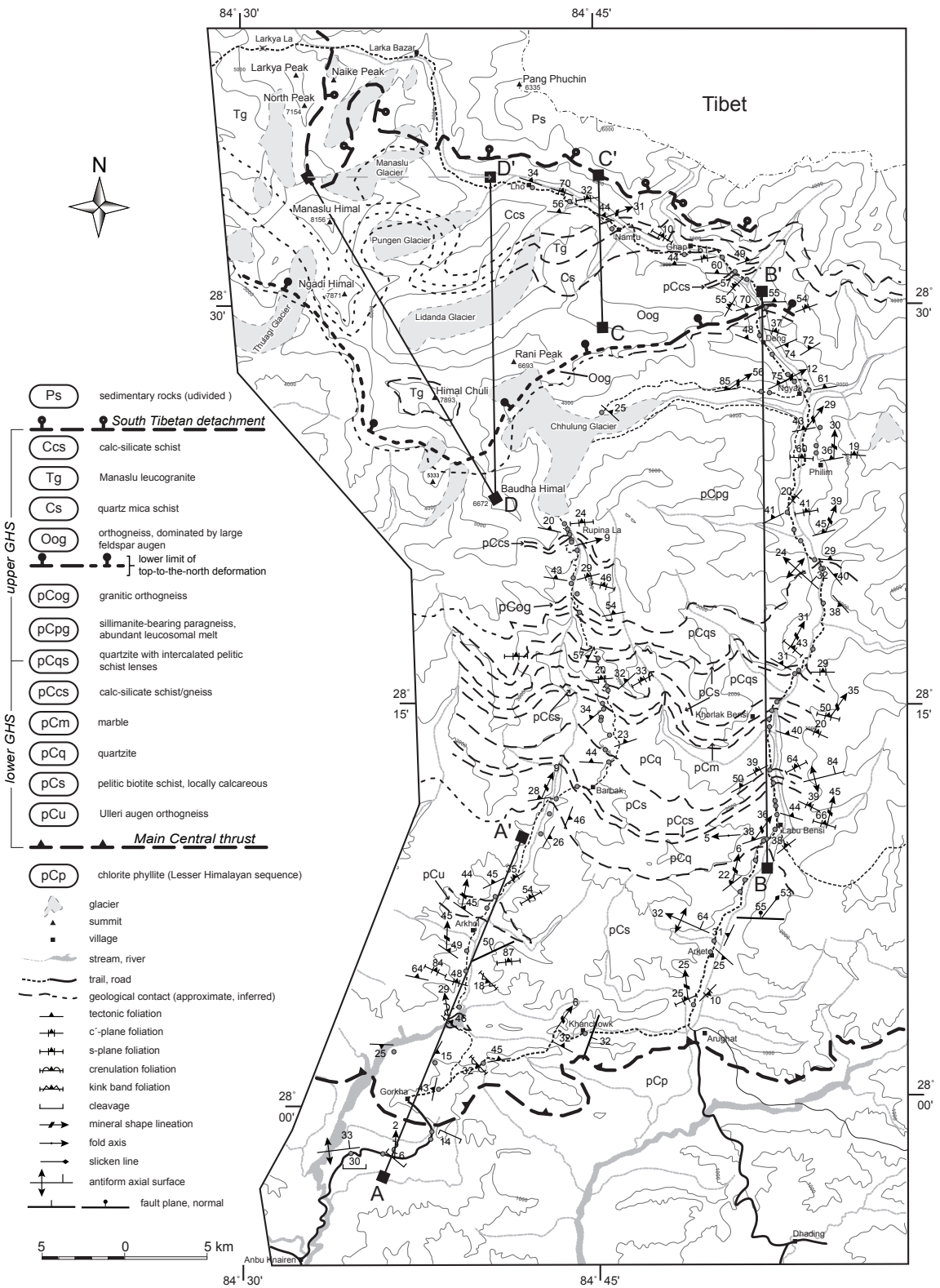
84° 30'
84° 45'
28° 30'
28° 15'
28° 00'
Tibet
Larkya La
Larka Bazar
Larkya Peak
Naike Peak
North Peak
7154
Pang Phuchin
6335
Manaslu Glacier
Manaslu Himal
8156
Pungen Glacier
Ngadi Himal
7871
Tsulegi Glacier
Lidanda Glacier
Rani Peak
6693
Himal Chuli
7893
Chhulung Glacier
Baudha Himal
6672
Rupina La
Namru
Ghap
Deng
Ngyak
Philim
Khorlak Bensi
Baibak
Labu Bensi
Arkhol
Arkete
Khandbowk
Arughat
Gorkha
Dhading
Anbu Khairen
N
A
A'
B
B'
C
C'
D
D'
Ps
Tg
Ccs
Cs
Oog
pCcs
pCpg
pCog
pCqs
pCcs
pCm
pCq
pCs
pCu
pCp
sedimentary rocks (udivided )
South Tibetan detachment
calc-silicate schist
Manaslu leucogranite
quartz mica schist
orthogneiss, dominated by large feldspar augen
lower limit of top-to-the-north deformation
granitic orthogneiss
sillimanite-bearing paragneiss, abundant leucosomal melt
quartzite with intercalated pelitic schist lenses
calc-silicate schist/gneiss
marble
quartzite
pelitic biotite schist, locally calcareous
Ulleri augen orthogneiss
Main Central thrust
chlorite phyllite (Lesser Himalayan sequence)
upper GHS
lower GHS
glacier
summit
village
stream, river
trail, road
geological contact (approximate, inferred)
tectonic foliation
c´-plane foliation
s-plane foliation
crenulation foliation
kink band foliation
cleavage
mineral shape lineation
fold axis
slicken line
antiform axial surface
fault plane, normal
5 0 5 km

tourmaline ± muscovite anatectite. The upper portion of the orthogneiss preserves C-S-C′ fabrics that indicate a top-to-the-north sense of shear (Figure 4.3C). Near the base of the orthogneiss top-to-the-north sense deformation is recorded as single C′ shear bands that cut across the main foliation (Figure 4.3D). These shear bands are interpreted to mark the lower limit of meso-scale deformation related to displacement across the South Tibetan detachment system.

Structurally below the orthogneiss in the Manaslu–Himal Chuli Himalaya is a 7-8 km thick unit of sillimanite-bearing paragneiss (Figures 4.2, 4.4). The paragneiss, which consists of quartz + k-feldspar + biotite + garnet ± muscovite, contains significant quantities of quartz + k-feldspar ± garnet ± tourmaline anatectite, locally with biotite melanosomes (Figure 4.3E). In the upper portion of the paragneiss, anatectite content by volume can be as high as 40% (Figure 4.3E); the anatectite proportion decreases down structural section. Ductile deformation within the paragneiss is recorded by top-to-the-south sense C-S-C′ fabrics (Figure 4.3F).

Subjacent to the sillimanite paragneiss in the Manaslu–Himal Chuli Himalaya is a 5 km thick unit of quartzite with intercalated lenses of anatectite-bearing pelitic gneiss (Figures 4.2, 4.4). Kyanite occurs locally within the anatectite pods. Previous researchers mapped the Main Central thrust at the base of this unit (e.g., Colchen et al., 1986; Hodges et al., 1988; Copeland et al., 1991). The rock units that occur below the quartzite with intercalated pelitic gneiss have been referred to previously as part of the Midlands Group (Hashimoto, 1973; Colchen et al., 1986). This is a ~15 km thick layer of metasedimentary rock, with minor igneous intercalations, metamorphosed at greenschist facies near its base and amphibolite facies near its top. Thick

**Figure 4.3**
Photographic illustrations of the Greater Himalayan sequence. A) Calc-silicate schist within the South Tibetan detachment system with a C-S-C' fabric recording top-to-the-north shear sense. View to the west. Pen is approximatley 15 cm long. B) A raft of pelitic schist in a cliff-face exposure of the Chokkang arm of the Manaslu pluton. View to the west. C) Granitic augen orthogneiss with a well-developed C-C' fabric recording a top-to-the-north sense of shear. View is to the west. The end of the pencil in the photo is approximately 3 cm long. D) Granitic orthogneiss cut by a top-to-the-north sense shear band. View is to the west; lens cap is 58 mm in diameter. The photo image has been flipped about a vertical axis to maintain a constant north-south direction throughout the figure. E) Anatectite-bearing sillimanite-grade paragneiss. View is to the west. F) Migmatitic paragneiss with a C-S fabric that records a top-to-the-south sense of shear. View is to the west. The photo image has been flipped about a vertical axis to maintain a consistent north-south orientation. G) Well-developed C-S-C' fabric in a pelitic schist in the lower Greater Himalayan sequence. The lens cap is 58 mm in diameter; view is to the northwest. H) Folded lens of quartz arenite within chloritic phyllitic slate in the footwall of the Main Central thrust fault ~2km south of Gorkha. View is to the north; lens cap is 58 mm in diameter..

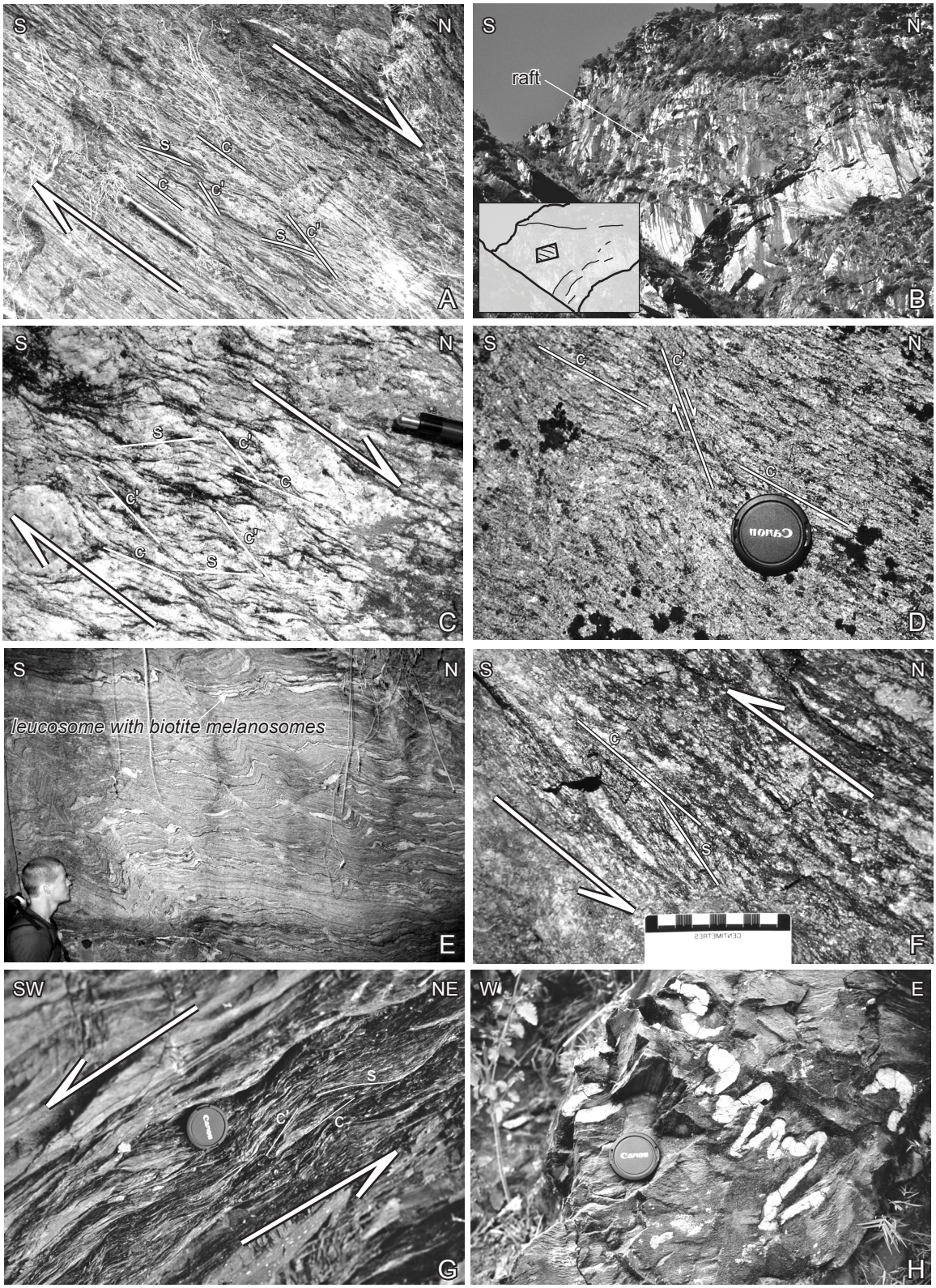
S
N
S
C
C'
S
C'
A
S
N
raft
B
S
N
S
C'
C
C'
C'
C
S
C
S
N
C
C'
C
C
Canon
D
S
N
leucosome with biotite melanosomes
E
S
N
C
S
F
SW
NE
S
C'
C
G
W
E
Canon
H

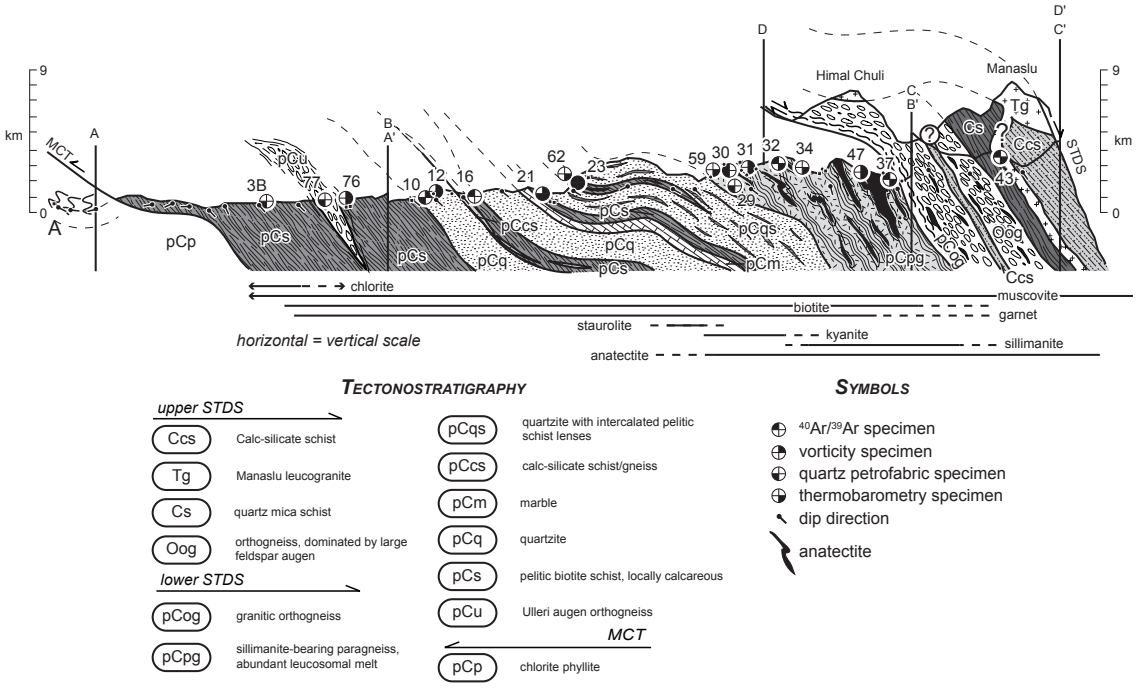


**Figure 4.4**
Composite vertical geological section along the lines A-A', B-B', C-C', and D-D' (locations in Figure 2). Vertical black lines depict ends of section lines. Specimen sample locations are identified by number. STDS, South Tibetan detachment system; MCT, Main Central thrust.

quartzite bands, which dominate the upper Midlands Group are separated by layers of calc-silicate schist, marble and pelitic schist (Figures 4.2, 4.4). The lower portion of the Midlands Group consists of garnet-bearing pelitic quartz mica schist that decreases in metamorphic grade towards the south and becomes a muscovite chlorite phyllitic schist at its base. All of the rocks within the Midlands Group are pervasively deformed; C-S-C′ fabrics, which are observed in most outcrops, consistently yield a top-to-the-south sense of shear (Figure 4.3G). The Ulleri augen orthogneiss occurs as a local lenticular mass within the meta-sedimentary rocks of the lower Midlands Group (Figures 4.2, 4.4). In the Daraudi valley it is approximately 1.5 km thick and contains K-feldspar augen up to 2 cm in length.

The Main Central thrust in the Manaslu–Himal Chuli Himalaya, as defined by Searle et al. (2008), occurs just south of the villages of Gorkha and Arughat (Figure 4.2). Rocks of the Lesser Himalayan sequence that crop out in the immediate footwall of the Main Central thrust consist of sub-biotite grade chlorite phyllite or phyllitic slate with abundant sand grains of k-felspar and quartz. Unlike structures in the hanging wall of the Main Central thrust, planar and linear features in the footwall have not been transposed and features such as bedding, though folded, are still recognizable (Figure 4.3H).

## 4.4 Deformation and Microstructures

The entire Greater Himalayan sequence has been sheared pervasively. All planar and linear features are transposed into a single tectonic foliation that, although folded locally (Figure 4.4), dips predominantly towards the north (Figure 4.2). At the outcrop scale, C-S-C′ fabrics throughout the entire lower Greater Himalayan sequence record a top-to-the-south deformational shear sense. Near the base of the orthogneiss in the upper Greater Himalayan sequence a change in C-S-C′ fabrics defines a reversal in shear sense that marks the lower boundary of the South Tibetan detachment system.

Bouchez and Pêcher (1981) reported quartz *c*-axis preferred orientations for a number of specimens collected from the lower portion of the Greater Himalayan sequence across much of central Nepal. The quartz *c*-axis fabrics that they reported define asymmetric type-1 cross-girdled patterns with a predominantly top-to-the-south sense of shear (Bouchez and Pêcher, 1981). Similar results were also reported from the Kali Gandaki valley in the Dhaulagiri Himal (Figure

4.1; Chapter 2 of this thesis). The consistency of the quartz *c*-axis fabrics from central Nepal has been interpreted to indicate that no large post-kinematic strain has affected the *c*-axis orientations (Bouchez and Pêcher, 1981; Chapter 2 of this thesis).

### 4.4.1 Microstructures and quartz *c*-axis fabrics

Oriented specimens of quartz-rich rocks were collected for quartz *c*-axis orientation analyses from across the Greater Himalayan sequence along the Budhi Gandaki and Daraudi valleys (Figure 4.1). These analyses, which complement the analyses of Bouchez and Pêcher (1981) expand significantly the area sampled for quartz-rich specimens in the upper half of the Greater Himalayan sequence. Quartz *c*-axis orientation measurements were made manually using a universal stage mounted on an optical microscope. All microstructural and crystal fabric data reported here are from thin sections cut perpendicular to foliation and parallel to lineation. The orientation data are presented in equal-area projection from the lower hemisphere as viewed towards the west; top-to-the-south (i.e. thrust-sense motion) is indicated by a sinistral shear sense and top-to-the-north (i.e. normal-sense motion) is indicated by a dextral shear sense. The following descriptions of the mineral assemblages, microstructures and quartz *c*-axis fabrics of the specimens collected begin with the structurally lowest specimen and move progressively structurally higher.

#### 4.4.1.1 Lower Greater Himalayan sequence

Rocks of the lower Greater Himalayan sequence as defined in this study, part of the Midlands Group and associated with the Lesser Himalayan sequence of Hashimoto (1973), Colchen et al., (1986), and Copeland et al., (1991), are pervasively deformed, but unlike overlying rocks do not include abundant anatectite.

The structurally lowest specimen, MS-3B (Figure 4.5A), is from a thin garnet-bearing quartz + biotite + muscovite + feldspar meta-sandstone lens located just north of the town of Arughat (Figure 4.2). The foliation is defined by biotite, muscovite and ductilely deformed quartz grains. Mica crystals also are aligned with weakly developed shear bands, which indicate a top-to-the-south shear sense. The size of individual quartz grains in the specimen is controlled by the distance between mica-rich layers. Boundaries of adjacent quartz grains are locally

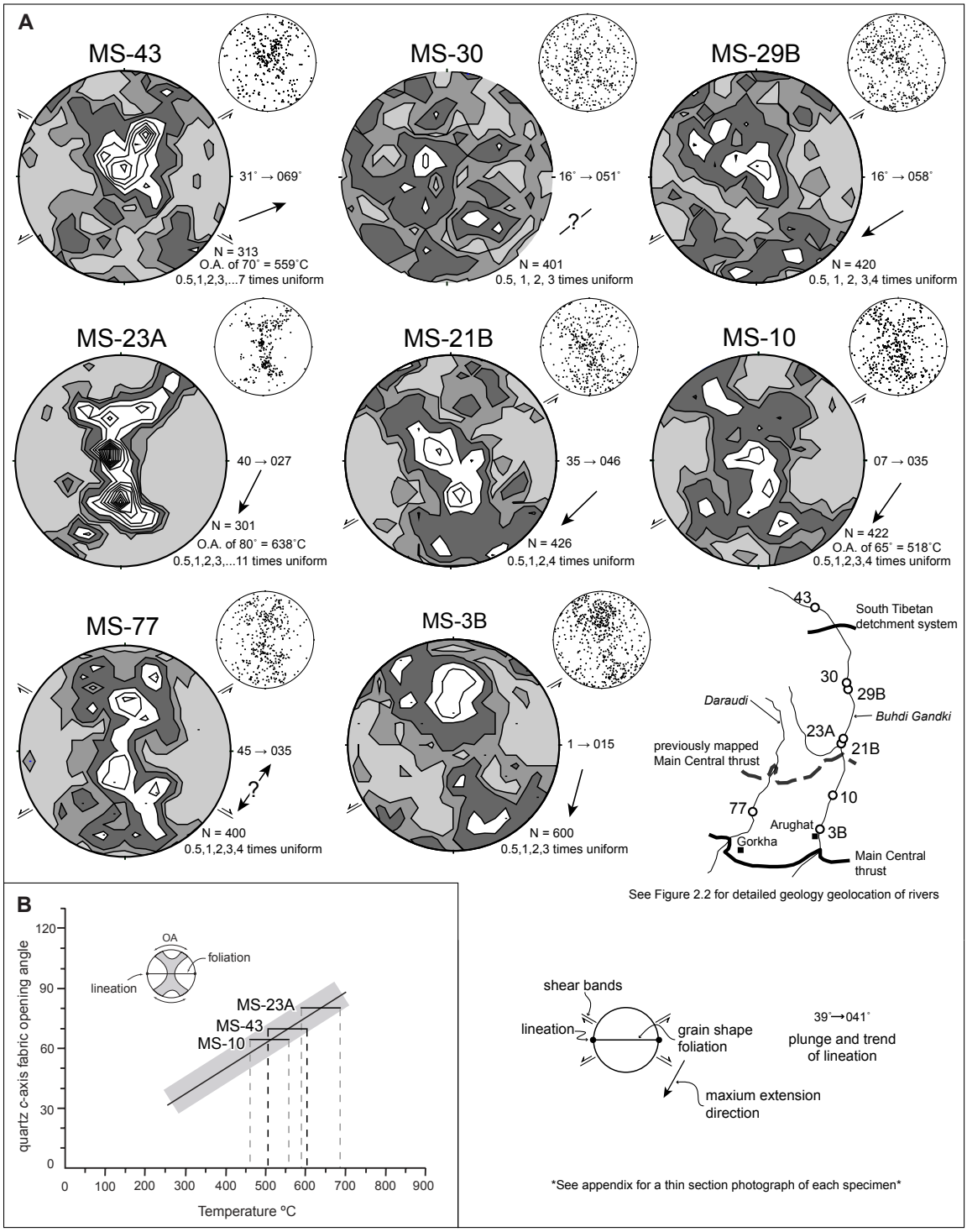


**Figure 4.5**
Quartz petrofabric analyses. A) Quartz c-axis orientation data are presented in equal-area projection from the lower hemisphere with the foliation striking east-west and vertical and the lineation horizontal. Data are contoured at 0.5, 1, 2, 3... times uniform. Contour and scatter plots were created using STEREONET 6.3.3 developed by R.W. Allmendinger. B) A graph depicting the relationship between quartz c-axis fabric opening angle and deformation temperature (modifed from Law et al., 2004). Fabric opening angles (O.A.) of three specimen from this study are plotted on the diagram.

lobate, but dominantly define a foam-type texture. The lobate grain boundaries may indicate low temperature grain boundary migration (Regime 1 of Hirth and Tullis, 1992), while the granoblastic foam texture of the quartz grains may indicate grain boundary area reduction through static recrystallization. Quartz *c*-axes in specimen MS-3B define a weakly developed asymmetric type 1 cross-girdle fabric with a top-to-the-south-southwest shear sense. The quartz petrofabric is dominated by rhomb <a> slip (Figure 4.5A).

Specimen MS-77 is from an outcrop of the Ulleri augen orthogneiss located structurally above specimen MS-3B (Figure 4.4). Where sampled, the Ulleri augen orthogneiss is a quartz + feldspar + biotite + muscovite + amphibole L-tectonite. The foliation and lineation are defined by aligned biotite and muscovite mica crystals and ductilely deformed quartz grains that commonly occur as ribbons. A well-developed grain-shape lineation that plunges 45˚ towards N035˚ indicates that stretching took place along a northeast-southwest azimuth. Definitive shear sense indicators were not observed in thin section; a conjugate set of weakly-developed shear bands show both a top-to-the-north and top-to-the-south sense of shear. Boundaries between adjacent quartz grains in the specimen are locally lobate and subgrain boundaries are observed internally. These features are indicative of low temperature grain boundary migration and subgrain formation (likely Regime 2 recrystallization of Hirth and Tullis, 1992). As in specimen MS-3B, the quartz grains in MS-77 take on a granoblastic texture locally indicating grain boundary area reduction through static recrystallization. Quartz *c*-axis orientations in specimen MS-77 appear to define a fabric that appears to be characteristic of constrictional strain (Figure 4.5A; Lister and Hobbs, 1980). The *c*-axis pattern is relatively symmetric about the foliation plane with both prism <a> and rhomb <a> slip and only minor evidence for basal <a> slip.

The next structurally higher specimen, MS-10, is from a quartz + biotite + feldspar + muscovite schist. Aligned biotite grains and ductilely deformed quartz grains define the lineation and foliation. Quartz grains in specimen MS-10 show evidence for minor subgrain formation whereas the interface between adjacent quartz grains is locally lobate. Those features are characteristic of low temperature grain boundary migration and subgrain recrystallization (Regime 2 recrystallization of Hirth and Tullis, 1992). The quartz grains commonly have a granoblastic texture indicating some degree of grain boundary area reduction through static recrystallization. The quartz *c*-axis pattern in specimen MS-10 appears to define an asymmetric type-1 crossed-

girdled pattern with a top-to-the-southwest shear sense (Figure 4.5A); prism <a> and rhomb <a> are the dominant slip systems. Moderately well-developed shear bands observed in the specimen also indicate a top-to-the-south shear sense.

#### 4.4.1.2 Mid-to-upper Greater Himalayan sequence

Specimen MS-21B is from an outcrop of quartzite situated just above the Main Central thrust as mapped in previous studies of the map-area (e.g., Colchen et al., 1986; Hodges et al., 1988; Copeland et al., 1991). The muscovite-bearing quartzite has both a foliation and lineation defined by aligned, ductilely deformed quartz grains and muscovite. Quartz within this specimen commonly contains subgrains and locally the interface between individual grains is lobate. These features indicate subgrain formation and low temperature grain boundary migration characteristic of Regime 2 recrystallization of Hirth and Tullis (1992). As with the structurally lower specimens, quartz grains in MS-21B also have a slight granoblastic texture indicating grain boundary area reduction through static recrystallization. Shear bands, marked by aligned mica grains, indicate a top-to-the south shear sense. Quartz *c*-axis orientations in specimen MS-21B define a weak type-1 crossed-girdle pattern, dominated by prism <a> slip, with an asymmetry indicating a top-to-the-southwest shear sense (Figure 4.5A).

Specimen MS-23A is from a slightly higher structural position than specimen MS-21B (Figure 4.4). It consists of kyanite-grade quartzite containing minor (less than 2% total) biotite and muscovite. Quartz grains in this specimen show evidence of internal sub-grain formation and amoeboid grain boundaries, features indicative of subgrain recrystallization and high temperature grain boundary migration, respectively, that are characteristic of Regime 3 recrystallization of Hirth and Tullis (1992). Quartz *c*-axis preferred orientations are aligned in a well-defined type-1 crossed-girdle pattern (Figure 4.5A). No shear bands were observed in thin-section, however, the quartz *c*-axis fabric has a top-to-the-southwest asymmetry indicating a top-to-the-southwest shear sense. The slip preserved in the quartz petrofabric pattern is dominantly along the prism <a> and rhomb <a> slip systems.

Specimens MS-29B and MS-30 were collected within 750 meters (Figure 4.4) of one another just above the sillimanite-in isograd. Specimen MS-29B is a quartz + muscovite + biotite + sillimanite ± garnet + quartz-k feldspar anatectite paragneiss with a foliation that is defined

predominantly by mica alignment and a mineral lineation, which consists of elongate muscovite and biotite grains and ductilely deformed quartz. Quartz grains within specimen MS-29B show evidence of internal subgrain formation and have lobate-to-amoeboidal grain boundaries. These features indicate subgrain rotation recrystallization and high temperature grain boundary migration indicative of Regimes 2 and/or 3 recrystallization of Hirth and Tullis (1992). The quartz *c*-axis orientations in specimen MS-29B are aligned in a weakly defined type-1 crossed-girdle pattern with a top-to-the-southwest asymmetry (Figure 4.5A). The most prominent slip system appears to be prism <a>; however, both rhomb <a> and basal <a> slip is apparent in the petrofabric pattern. The quartz *c*-axes measured in specimen MS-30, in contrast, have no discernible organized pattern (Figure 4.5A). Specimen MS-30 is from an anatectite-bearing quartz + muscovite + biotite meta-sandstone; anatectite pods consist of quartz, feldspar, and cm-scale garnet clusters. Quartz grains, which are confined between closely spaced layers of mica, show internal subgrains and have interlobate-to-amoeboid boundaries between grains. These features indicate subgrain formation and high temperature grain boundary migration recovery processes, which are characteristic of Regimes 2 and/or 3 recrystallization of Hirth and Tullis (1992). Specimen MS-30 contains ~35% muscovite that occurs as discrete layers. The lack of crystallographic preferred orientation of quartz grains may indicate that strain was preferentially partitioned along the mica layers during deformation. A similar lack of preserved quartz *c*-axis fabric has been observed in a specimen sampled in the Dhaulagiri Himal where deformation is interpreted to have been preferentially partitioned into chlorite-rich layers (Chapter 2 of this thesis).

#### 4.4.1.3 Upper Greater Himalayan sequence

The structurally highest specimen, MS-43, is muscovite-rich granite from the Chokkang arm of the Manaslu pluton (Figure 4.4) within the South Tibetan detachment zone. The granite is deformed pervasively and contains a foliation defined by aligned muscovite and ductilely-deformed quartz grains and a lineation that consists of aligned muscovite grains. Quartz in the specimen contains subgrains and has interlobate-to-amoeboid grain boundaries. These characteristics indicate subgrain formation and high-temperature grain boundary migration, features that are associated with Regimes 2 and/or 3 recrystallization of Hirth and Tullis (1992).

The quartz *c*-axes in specimen MS-43 define a type-2 cross-girdle pattern displaying dominant prism <a> and rhomb <a> slip (Figure 4.5A). The two major concentrations of *c*-axes in the fabric appear to define an asymmetry consistent with a top-to-the-northeast sense of shear (Figure 4.5A).

#### 4.4.1.4 Temperature of deformation

Assuming that critical resolved shear stress values for glide systems are primarily controlled by temperature, rather than strain rate or hydrolytic weakening, the opening angle of cross-girdled quartz *c*-axis fabrics can be related to the temperature at which the fabrics were developed (Kruhl, 1998; Law et al., 2004). Empirical observations show that the opening angle of the quartz *c*-axis pattern increases approximately linearly with deformation temperature between ~300 and 650˚C (Kruhl, 1998; Law et al., 2004). At temperatures higher than ~650˚C opening angles increase more rapidly with temperature, perhaps reflecting the increasing importance of prism <c> slip (Law et al., 2004). Kruhl (1998) estimated that deformation temperatures determined from quartz *c*-axis fabric opening angles are subject to an uncertainty of ± 50˚C.

Three of the specimens analyzed for quartz *c*-axis orientation data yield fabric-opening angles suitable for deformation temperature determination. The structurally lowest specimen with a quartz *c*-axis pattern appropriate for deformation temperature analysis is MS-10. It has an opening angle of ~65˚, which corresponds to a deformation temperature of 518 ± 50˚C (Figure 4.5B). Specimen MS-23A was collected from the middle of the Greater Himalayan sequence (Figure 4.4) and yields a quartz *c*-axis fabric with an opening angle of ~80˚, which corresponds to a deformation temperature of 638 ± 50˚C (Figure 4.5B). Specimen MS-43, from near the top of the Greater Himalayan sequence, has an opening angle of ~70˚, which corresponds to deformation temperature of 559 ± 50˚C (Figure 4.5B). The deformation temperatures are generally consistent with observed metamorphic mineral assemblages. Specimen MS-10 came from near the staurolite-in isograd, specimen MS-23A, which yielded the highest deformation temperature was taken from within the sillimanite zone, and specimen MS-43 was from near the top of the Greater Himalayan sequence within which diopside porphyroblasts are observed (Colchen et al., 1986). These estimated deformation temperatures are consistent with those estimated by using the quartz *c*-axis fabrics published by Bouchez and Pêcher (1981), from the Daraudi and Budhi Gandaki valleys, which, near the structural level of MS-10, are 520 ± 50˚C and 450 ± 50˚C respectively.

Quartz *c*-axis fabrics of Bouchez and Pêcher (1981) from a structurally lower position in the adjacent Chepe valley (Figure 4.1) that is comparable to MS-3B indicate deformation temperatures between 445 ± 50˚C and 425 ± 50˚C. The estimated deformation temperatures from the middle and upper Greater Himalayan sequence in the Manaslu-Himal Chuli Himalaya are comparable to those from other studies along the Himalaya (e.g., Law et al., 2004; Chapter 2 of this thesis). Comparisons between deformation temperatures estimated from quartz *c*-axis orientation fabrics and those estimated geochemically from metamorphic mineral assemblages are discussed in a later section of this paper.

### 4.4.2 Vorticity

Analysis of the rotation of rigid porphyroclasts while they are imbedded in penetratively deformed rock can be used to estimate the relative importance of simple shear and pure shear components during deformation (e.g., Passchier, 1987; Simpson and De Paor, 1993, 1997; Wallis, 1995). Specimens of penetratively deformed rocks for vorticity analysis were collected along the valleys of the Budhi Gandaki and and Daraudi rivers (Figure 4.1) Other studies of vorticity carried out along the Himalayan arc have used the relationship of the aspect ratio of a clast and its orientation with respect to the tectonic foliation to estimate a mean kinematic vorticity number, $W_m$ (e.g., Law et al., 2004; Carosi et al., 2006; Jessup et al., 2006; Carosi et al., 2007; Chapter 2 of this thesis). Mean kinematic vorticity, which describes the bulk rotation of material lines coincident with the principal strain axes (Carosi et al., 2007), ranges between values of 0 for pure shear strain and 1 for simple shear strain. Equal contributions to strain from both pure shear and simple shear components occurs at a mean kinematic vorticity number of 0.71 (Law et al., 2004).

In this study we use the Rigid Grain Net (RGN) method of estimating $W_m$ (Jessup et al., 2007). The RGN relates the aspect ratio and long axis orientation of porphyroclasts to $W_m$ (Figure 4.6). It is an integration of the $W_m$ determination methods of Passchier (1987), Simpson and De Paor (1993; 1997), and Wallis (1995) for tailless porphyroclasts and is therefore subject to the same inherent assumptions: (1) the porphyroclasts have undergone no internal deformation; (2) the matrix surrounding the clast was homogeneously deformed; (3) sufficient strain has developed to allow all clasts to reach a stable sink position; and (4) there has been no mechanical interaction between rigid porphyroclasts. Microscopic inspection of thin sections cut from porphyroclast-

bearing specimens collected during this study indicate that only four such specimens appear to meet all of the assumptions necessary for vorticity analysis by the RGN method. Although rigid porphyroclast rotation-based determinations of $W_m$ assume a minimum of monoclinic symmetry (Law et al., 2004), they do not assume plane strain deformation and remain valid for 3-dimensional strains (Law et al., 2004). However, the quartz *c*-axis patterns obtained from our specimens have crossed-girdles, which indicate plane strain deformation conditions (Lister and Hobbs, 1980; Schmid and Casey, 1986).

#### 4.4.2.1 Lower Greater Himalayan sequence

The structurally lowest specimen from which an estimate of mean kinematic vorticity was obtained is specimen MS-76, a quartz + biotite + garnet ± muscovite schist (see Figure 4.4 for location). Analysis of 55 grains of garnet yields a $W_m$ between 0.50 and 0.68 and indicates a pure shear component representing 52-67% of the total recorded deformation (Figure 4.6A). The next structurally lowest specimen estimate is from a quartz + feldspar + biotite + muscovite + garnet meta-sandstone (MS-12A), in which garnet porphyroclasts are embedded within a ductilely deformed quartz-dominated matrix and show no internal deformation. On the basis of the aspect ratio and orientation of 165 grains of garnet the $W_m$ value for specimen MS-12A is estimated to be between 0.71 and 0.73, which indicates a pure shear strain component of 48-50% (Figure 4.6B). The distribution of data points in the RGN from specimen MS-12A should be interpreted with caution, however, as the break between porphyroclasts that rotate freely and those that have found a stable sink position (see Jessup et al., 2007) is defined by only two measurements. This may indicate that the strain in the specimen was insufficient to allow the porphyroclasts to reach stable sink positions or, alternatively, that few porphyroclasts were present in the specimen that have an aspect ratio sufficient to have a stable sink position in the dominant flow type. We prefer the later interpretation as specimen MS-12 is pervasively deformed, as is all surrounding material.

#### 4.4.2.2 Mid-to-upper Greater Himalayan sequence

Specimen MS-21A is from a quartz + muscovite + biotite + garnet schist (see Figure 4.4 for sample location). Based on 83 garnet porphyroclasts, the $W_m$ is between 0.72 and 0.83, which corresponds to a pure shear deformational component of 38-48% (Figure 4.6C). Specimen

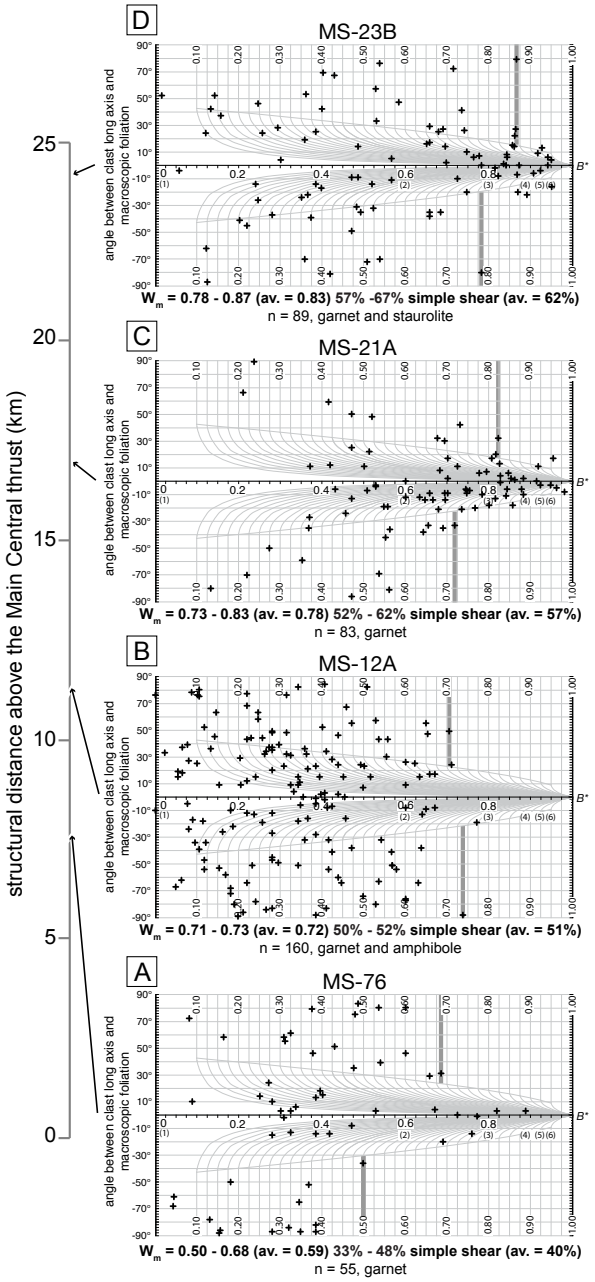


**Figure 4.6**
Vorticity analyses of four specimens from the lower to middle Greater Himalayan sequence based on the Rigid Grain Net method of Jessup et al. (2007). The location of each specimen is shown in Figure 4. The angle between the long axis of a porphyroclast and the foliation is plotted on the vertical axis. B*,which is a function of the aspect ratio of the porphyroclast (, where Mn, short axis of clast; Mx, long axis of clast), is plotted on the horizontal axis. Thick, dark grey vertical lines show the approximate boundary between freely spinning porphyroclasts and those that have entered a “stable sink” position (refer to text). The data are presented in relative structural position with the structurally lowest specimen at the bottom and the structurally highest specimen at the top.

MS-23B, which was sampled just above MS-21A (Figure 4.4), is a staurolite-bearing quartz + biotite + muscovite + kyanite schist. The orientation and aspect ratios of 89 undeformed staurolite and kyanite porphyroclasts measured in specimen MS-23B yield $W_m$ values, as determined on the RGN, between 0.78 and 0.87 (Figure 4.6D). These $W_m$ values indicate a pure shear strain component of 33 to 43% of the total recorded deformation, indistinguishable from those recorded in MS-21A.

The vorticity estimates indicate that there is significant, and in most cases almost equal, contributions of both pure shear and simple shear components to the total recorded deformation across the lower to middle Greater Himalayan sequence.

## 4.5 Metamorphic thermobarometry

Metamorphic mineral assemblages in the Manaslu-Himal Chuli Himalaya that include garnet + biotite + muscovite + quartz ± plagioclase ± sillimanite/kyanite are suitable for the application of microprobe-based petrochemical estimates of metamorphic thermobarometry. Compositions of coexisting mineral phases were measured using the Camebax MBX electron microprobe at Carleton University, Canada. Minerals in mutual contact were analyzed both in the core and near the rim of zoned garnet crystals (see appendix for mineral composition data).

In this study we follow the suggestion of Wu and Cheng (2006) who, after an extensive comparative review of geothermometers based on Fe-Mg partitioning between garnet and biotite, recommend the use of the Holdaway (2000) calibration, which has an estimated random error of ± 25˚C. For all geobarometry specimens except MS-31 we used the garnet-biotite-plagioclase-quartz (GBPQ) geobarometer of Wu et al. (2004a). For specimen MS-31 we used the garnet-muscovite-plagioclase-quartz (GMPQ) geobarometer of Wu et al. (2004b) because the anorthite ratio in this specimen was below the calibrated threshold for the GBPQ barometer. The geobarometers of Wu et al., (2004a, b) were chosen because both are empirical calibrations based on the Holdaway (2001) calibration of the garnet-alumino silicate-quartz-plagioclase (GASP) barometer (Wu et al., 2004a, b), recommended by Wu and Cheng (2006), which is internally consistent with the Holdaway (2000) geothermometer. Both the GBPQ and GMPQ are calibrated to within 0.5 kbar of the Holdaway (2001) geobarometer and have associated estimated random errors of 1.2 and 1.4 kbars, respectively (Wu et al., 2004a, b).

### 4.5.1 Textures and Garnet zoning

All specimens analyzed for thermobarometry exhibit a strong tectonic foliation. Garnet in the structurally lowest specimen (MS-76) have spiral inclusion trails in their cores that appear to be at least partially continuous with the matrix foliation that wraps around them (Figure 4.7A), and therefore record syn-deformational garnet growth. Garnet in specimens sampled from the middle portion of the Greater Himalayan sequence (i.e., MS-12B, MS-21A, MS-62, and MS-59) appear in two forms: 1) small sub-to-anhedral garnet grains that may be the result of mechanical break-up of larger grains or of crystallographically-controlled dissolution during metamorphic reactions (Figure 4.7B) or 2) inclusion-rich (sometimes spiral pattern) cores with thick, inclusion-free, euhedral-to-subhedral overgrowths and associated pressure shadows (Figure 4.7C). The latter type of garnet is most common. Garnet grains in specimens sampled from the upper portion of the Greater Himalayan sequence (i.e. MS-31, MS-32B, MS-34, MS-47, MS-37) are commonly asymmetric with a well-defined long axis and display poikiolitic inclusions of quartz, biotite, plagioclase and muscovite (Figure 4.7D). Garnet with similar characteristics have been described in the Everest region and are interpreted to have formed through 1) growth of inclusion-rich cores during nucleation; 2) growth of inclusion free rims during a second garnet growth phase; and 3) removal of garnet rim/core material through a combination of fracturing and pressure solution during late-stage penetrative shearing and foliation development (Jessup et al., 2006).

Rim-to-core microprobe traverses across garnet grains, expressed as mole fractions of spessartine, grossular, pyrope, and almandine and Fe/(Fe+Mg) show evidence of limited zonation. The lack of a typical prograde zonation (e.g. Yardley, 1977) may indicate a re-equilibration of chemical components in the garnet during heating subsequent to their original growth. Similar flat chemical profiles across garnet grains collected from the middle of the Greater Himalayan sequence in the Everest region are interpreted to record thermal overprinting subsequent to original growth (Jessup et al., 2008).

In the garnet analyzed in this study, a slight increase is commonly noted in Mn content and Fe/(Fe+Mg) ratios (Figure 4.8). Our sample area in central Nepal overlaps with the case-study examples of retrograde net transfer reactions (ReNTR) described by Kohn and Spear (2000) and the subsequent work of Kohn et al. (2001), who also incorporate corrections for ReNTR in their pressure-temperature estimates. Where our sample locations overlap those of Kohn et al. (2001)

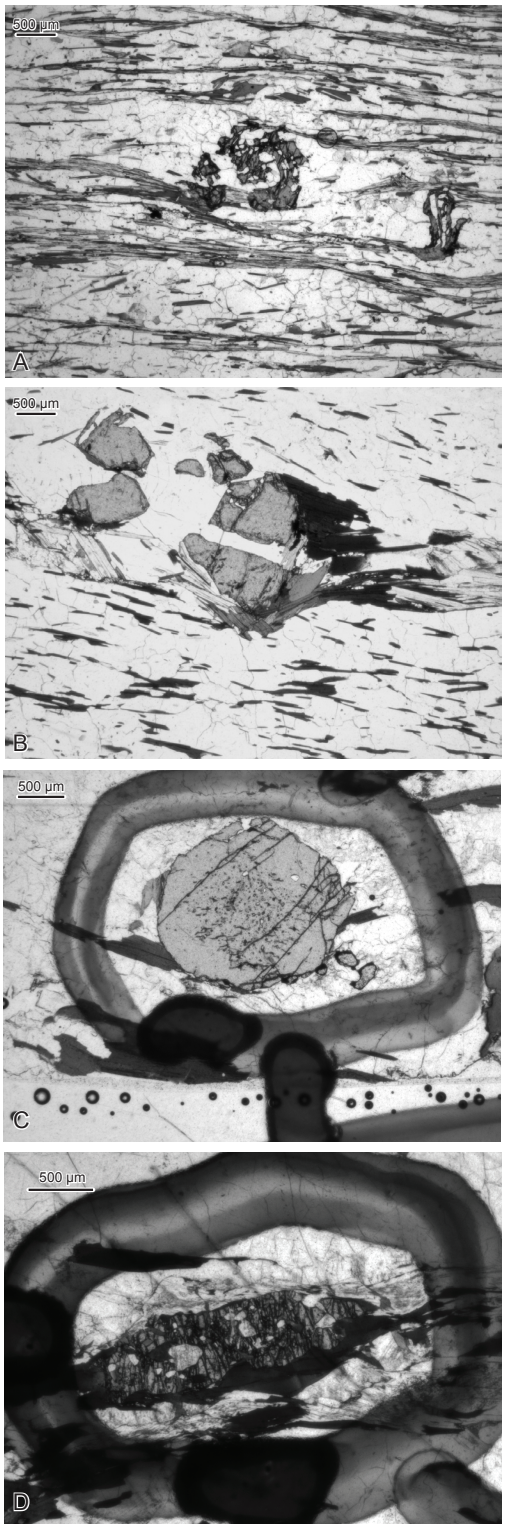


**Figure 4.7**
Photomicrographs of garnet textures in the Greater Himalayan sequence. A) Syntectonic garnet, from the lower Greater Himalayan sequence (specimen MS-76). The sigmoidial inclusion pattern indicates a top-to-the-south shear sense. B) Garnet fragments from the lower portion of the Greater Himalayan sequence in specimen MS-12A. The fragmentation is interpreted to have occured mechanically, during deformation, and is

therefore pre-tectonic with respect to the latest stage of deformation, but not nessessarily with respect to displacement on the major faults. C) Garnet porphyroclast in specimen MS-52, collected from the middle Greater Himalayan sequence. Note the inclusion-rich core and a relatively thick inclusion free rim. D) A garnet porphyroclast in specimen MS-32 from the upper Greater Himalayan sequence. Note the numerous inclusions and elongate morphology.

---

and Kohn and Spear (2000) our thermobarometric estimates are entirely consistent with their reported P-T values. Additionally, the temperatures and pressures calculated from compositional data from the specimens collected in this study are consistent with observed mineral assemblages. Thus, our data do not appear to be affected significantly by ReNTR.

### 4.5.2 Thermobarometric Results

Thermobarometric estimates from this study are summarized in Table 1. The P-T estimates show that the metamorphic minerals equilibrated chemically while the upper portion of the Greater Himalayan sequence was buried at depths ranging between ~14 and ~31 km through direct measurement; up to ~40 km through indirect measurement (assuming a crustal gradient of 270 bars/km) and at temperatures of approximately 625˚C. The relatively constant temperatures in the upper portion of the Greater Himalayan sequence are interpreted by Hodges et al. (1988) to reflect thermal buffering during anatexis. Garnet-biotite thermometry indicates that metamorphic temperatures are slightly lower in the lower portion of the Greater Himalayan sequence, than those reported for the upper portion (Table 1). Pressure data from the lower Greater Himalayan sequence were not obtained due to a lack of suitable mineral phases.

Metamorphic temperature estimates are within error of, but slightly higher than deformation temperatures estimated using quartz *c*-axis petrofabrics. Specimens MS-23A and MS-62 were collected from similar structural levels (Figure 4.4) and yield a deformation temperature of 638 ± 50˚C and a garnet-biotite temperature of 666 ± 25˚C, respectively. Similarly, the deformation temperature for specimen MS-10 is interpreted to be 518 ± 50˚C while the metamorphic temperature estimate of nearby specimen MS-12 is 595 ± 25˚C. The general agreement between deformation temperatures and metamorphic temperature estimates is interpreted to indicate that deformation and metamorphism took place under similar conditions. However, deformation temperatures are slightly lower, though not significantly so, than peak metamorphic temperatures. This may indicate that the deformation continued post-peak

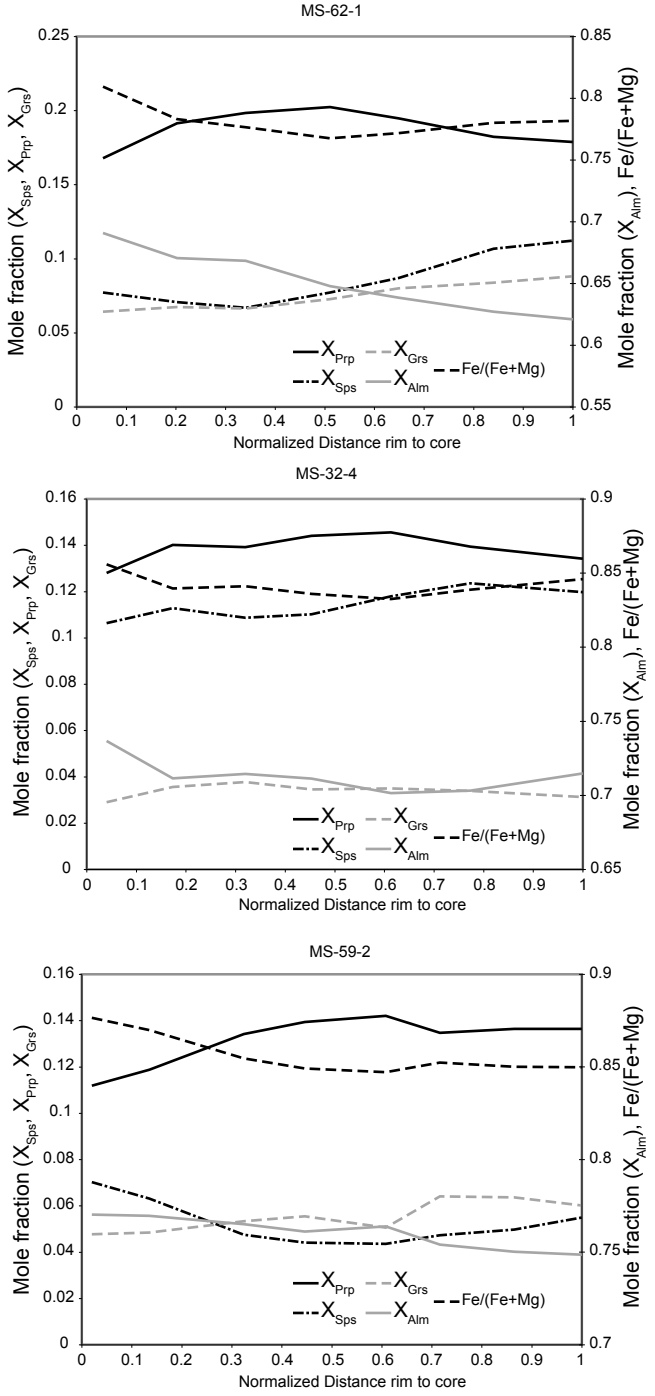


**Figure 4.8**
Chemical zoning of garnet porphyroclasts. Distances along microprobe traverses from the rim to the core have been normalized such that 0 is located at the rim and 1 indicates the centre of the garnet. See text for discussion. $X_{Prp}$, pyrope; $X_{Grs}$, grossular; $X_{Sps}$, spessertine; $X_{Alm}$, almandine

## Table 4.1 - Geothermobarometic Estimates

| Specimen | GBMAQ | | GBPQ | | †Estimated depth of burial |
|---|---|---|---|---|---|
| | (˚C) | (Bar) | (˚C) | (Bar) | |
| MS-37 | | | 615 | 3899 | 14 km |
| MS-47 | | | 629 | 4068 | 15 km |
| MS-34r | | | 620 | 4266 | 16 km |
| MS-32B-2 | | | 642 | 4597 | 17 km |
| MS-32B-2c | | | 660 | 4788 | 18 km |
| MS-31 | 581 | 5657 | | | 21 km |
| MS-59 | | | 604 | 5275 | 20 km |
| MS-62 | | | 666 | 8421 | 31 km |
| MS-21A | | | 632 | 9477* | 35 km |
| MS-12 | | | 595 | 10875* | 40 km |
| MS-76 | | | 610 | 9308* | 34 km |

Specimens are listed in correct relative structural positions.
*Calculated using fourth order polynomial fit (Figure 4.10A).
†Assuming an average crustal pressure gradient of 270 bars/km.

metamorphism. Because of a lack of suitable specimens it is not known whether deformation temperatures are systematically lower than metamorphic temperatures or if discrepancy between the two geothermometers simply reflects variance within error.

## 4.6 $^{40}Ar/^{39}Ar$ Thermochronology

In order to constrain the post-metamorphic cooling history in the Manaslu-Himal Chuli Himalaya, a suite of specimens was collected from across the study area for $^{40}Ar/^{39}Ar$ analyses of muscovite and biotite (Figure 4.4). Whole mica grains from these specimens were mechanically separated through standard crushing procedures and handpicked from sieved size-fractions under an optical microscope to eliminate grains with inclusions or mineral inter-growths. Cooling ages for irradiated muscovite and biotite aliquots were obtained through laser step-heating analysis (see the data repository for complete analytical procedures and data tables) and errors are reported at 1σ. The $^{40}Ar/^{39}Ar$ results for the muscovite and biotite specimens analyzed from the study area are presented in Table 2.

Previous investigations of the $^{40}Ar/^{39}Ar$ thermochronologic characteristics of the Manaslu-Himal Chuli Himalaya have delineated an interval of conspicuously young cooling ages, *ca*. 3 Ma (Copeland et al., 1990; Copeland et al., 1991; Wobus et al., 2003, 2005) in the middle of the Greater Himalayan sequence. The young cooling ages and their spatial distribution may be related to out-of-sequence thrusting (Wobus et al., 2005) or uplift due to under-plating and duplexing of the mid-crust (Bollinger et al., 2006). All $^{40}Ar/^{39}Ar$ cooling ages reported previously from the Greater Himalayan sequence, nonetheless, are Cenozoic (Copeland et al., 1990; 1991; Wobus et al., 2003) whereas $^{40}Ar/^{39}Ar$ cooling ages from the Lesser Himalayan sequence are Paleozoic and older (Wobus et al., 2003).

5.1 Muscovite

Three muscovite specimens have been analyzed by the $^{40}Ar/^{39}Ar$ technique and the corresponding ages are shown in Table 2 and Figure 4.9. These specimens were obtained from three distinct rock types and locations and show a range in their plateau age between 15.18 ± 0.18 M and 3.07 ± 0.20 Ma with age increasing at higher structural level. The structurally highest specimen, MS-43, was sampled from the Chhokang arm of the Manaslu pluton (Figure 4.4). Specimen MS-30 was sampled from a sillimanite-grade meta-sandstone while the structurally

**Table 4.2 - Thermochronology ages and calculated Ar closure temperatures**

| Specimen | Lab # | Mineral | Plateau Age (Ma) | err (1σ) | Isochron Age (Ma) | err (1σ) | Closure Temperature (°C) | err |
|---|---|---|---|---|---|---|---|---|
| MS-43 | KL-12 | Ms | 15.18 | 0.18 | 15.50 | 0.31 | 432 | 24 |
| MS-37 | KL-5 | Bt | 12.43 | 0.15 | 12.63 | 0.27 | 345 | 16 |
| MS-32B | KL-6 | Bt | 4.46 | 0.09 | 4.53 | 0.12 | 345 | 16 |
| MS-30 | KL-8 | Ms | 4.34 | 0.14 | 4.47 | 0.31 | 345 | 16 |
| MS-30 | KL-9 | Bt | 2.60 | 0.15 | 2.93 | 0.68 | 418 | 25 |
| MS-23B | KL-10 | Ms | 3.07 | 0.20 | 2.98 | 0.56 | 418 | 25 |
| MS-23B | KL-11 | Bt | 3.83 | 0.12 | 3.90 | 0.52 | 345 | 16 |
| MS-16 | KL-7 | Bt | 53.89 | 0.41 | 50.52 | 4.36 | 332 | 20 |

Closure temperatures calculated based on the equations of Dodson (1973) using cooling rate of 80°C/Ma as estimated by Godin et al., (2006b) for the Nar area (Figure 4.1) with an estimated error of ±20°C/Ma. Biotite (Bt) parameters and errors are from Grove and Harrison (1996). Muscovite (Ms) parameters are from Hames and Bowring (1994) with estimated error in the activation energy of ± 6% and coefficient of diffusion error of ±75%.

**Figure 4.9**
$^{40}Ar/^{39}Ar$ analyses of muscovite (ms) and biotite (bt) specimens from across the Greater Himalayan sequence. The interpreted plateau age is depicted as a dashed line. Heating steps included in calculation of the plateau age for each specimen are grey-filled.

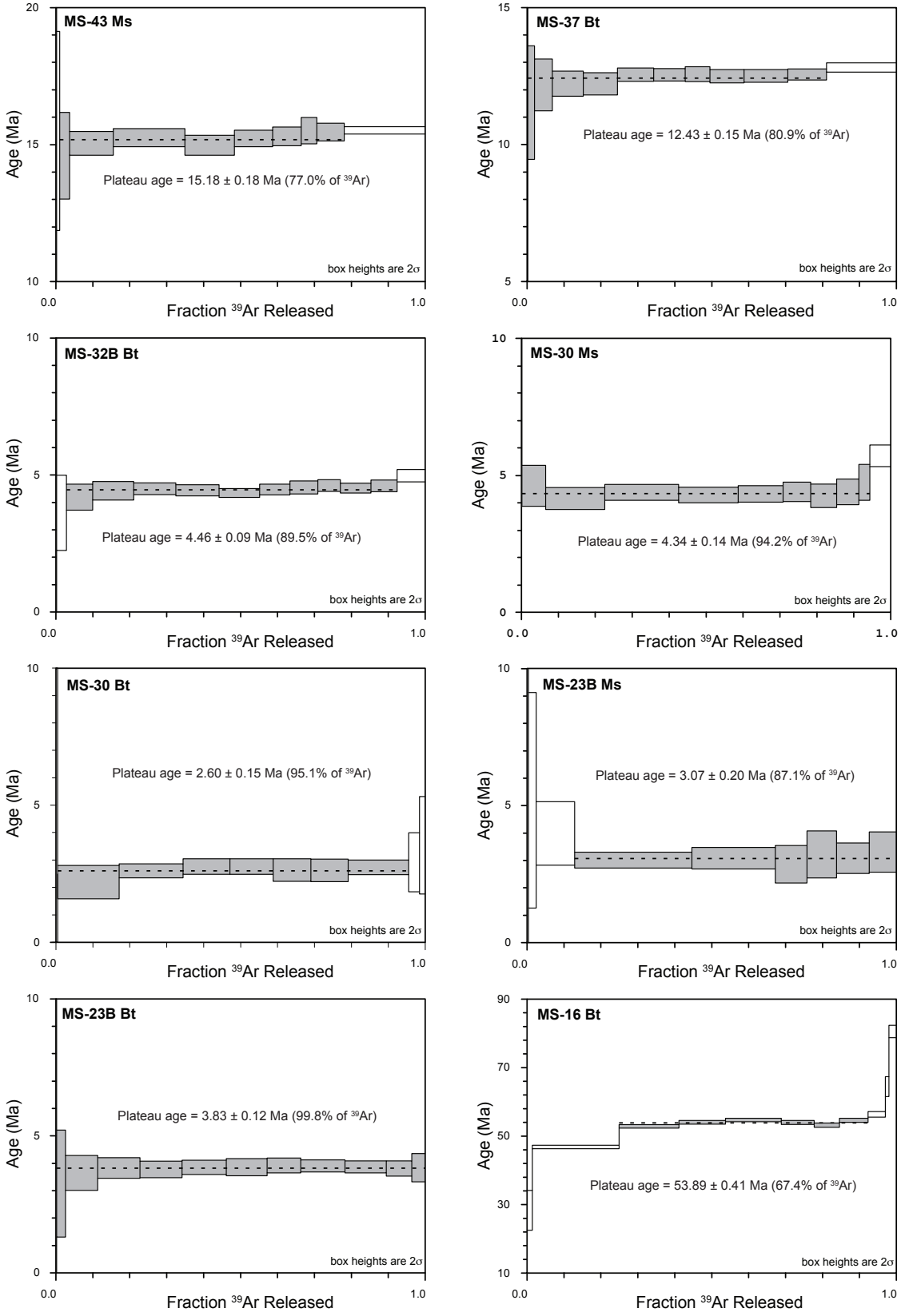
MS-43 Ms
Plateau age = 15.18 ± 0.18 Ma (77.0% of 39Ar)
box heights are 2σ
Age (Ma)
Fraction 39Ar Released
MS-37 Bt
Plateau age = 12.43 ± 0.15 Ma (80.9% of 39Ar)
box heights are 2σ
Age (Ma)
Fraction 39Ar Released
MS-32B Bt
Plateau age = 4.46 ± 0.09 Ma (89.5% of 39Ar)
box heights are 2σ
Age (Ma)
Fraction 39Ar Released
MS-30 Ms
Plateau age = 4.34 ± 0.14 Ma (94.2% of 39Ar)
box heights are 2σ
Age (Ma)
Fraction 39Ar Released
MS-30 Bt
Plateau age = 2.60 ± 0.15 Ma (95.1% of 39Ar)
box heights are 2σ
Age (Ma)
Fraction 39Ar Released
MS-23B Ms
Plateau age = 3.07 ± 0.20 Ma (87.1% of 39Ar)
box heights are 2σ
Age (Ma)
Fraction 39Ar Released
MS-23B Bt
Plateau age = 3.83 ± 0.12 Ma (99.8% of 39Ar)
box heights are 2σ
Age (Ma)
Fraction 39Ar Released
MS-16 Bt
Plateau age = 53.89 ± 0.41 Ma (67.4% of 39Ar)
box heights are 2σ
Age (Ma)
Fraction 39Ar Released

lowest specimen, MS-23B, was sampled from a kyanite-bearing paragneiss (Figure 4.4).

The muscovite analyses yield generally well-behaved age spectra with a flat release profiles (Figure 4.9). $^{40}Ar/^{39}Ar$ versus $^{36}Ar/^{40}Ar$ correlation ages are also reported in Table 2 and do not differ significantly from the interpreted plateau age.

5.2 Biotite

Five biotite separates from the Greater Himalayan sequence have been analyzed using the $^{40}Ar/^{39}Ar$ technique and the resulting plateau ages (Figure 4.9), which range from 53.89 ± 0.41 Ma to 2.60 ± 0.15 Ma, are reported in Table 2 with associated isochron ages and rock types.

With the exception of specimen MS-16, all biotite specimens yield flat, well-behaved age spectra (Figure 4.9) that define plateau ages indistinguishable from $^{40}Ar/^{39}Ar$ versus $^{36}Ar/^{40}Ar$ correlation ages (Table 2). $^{39}Ar$ release spectra for specimen MS-16 appear to define a pseudo-plateau at 53.89 ± 0.41 Ma that comprises 67.4% of released $^{39}Ar$. When compared to muscovite and hornblende cooling ages reported from nearby locations reported by Copeland et al., (1991) the biotite cooling age of ~53 Ma is anomalously high. It may reflect the presence of excess $^{40}Ar$ as indicated by the initial $^{40}Ar/^{36}Ar$ ratio for specimen MS-16 (c. 558 compared to an atmospheric ratio of ~295). The biotite age for specimen MS-23B may also reflect contamination by excess argon as it yields an age that is statistically older than that determined for muscovite from the same specimen, 3.07 ± 0.20 Ma versus 3.83 ± 0.12 Ma (Figure 4.9).

## 4.7 Discussion

### 4.7.1 Strain in the hanging wall of the Main Central thrust

Field mapping and subsequent structural analysis of specimens collected from across the Greater Himalayan sequence show that the exhumed mid-crust of the Himalaya has been deformed pervasively and all planar and linear features transposed into parallelism with a dominant tectonic foliation (Figure 4.3). Crystallographic preferred orientation of quartz grains and mean kinematic vorticity estimates based on rigid porphyroclast orientations indicate that rock mapped as part of the Greater Himalayan sequence was deformed in a general non-coaxial regime at high temperature. These observations support the conclusion that the Midlands Group lies in the hanging wall of the Main Central thrust. Furthermore, the results of the $^{40}Ar/^{39}Ar$

analyses undertaken in this study confirm those produced by Copeland et al. (1990, 1991) and are also consistent with the findings of Wobus et al. (2003), which exhibit a stark contrast between the thermal histories of the footwall and hanging wall as mapped in this study. In the footwall of the Main Central thrust $^{40}Ar/^{39}Ar$ cooling ages range between Paleozoic and Proterozic (Figure 4.9C; Copeland et al., 1991; Wobus et al., 2003), whereas in the hanging wall of the Main Central thrust, excluding specimens affected by excess argon, the oldest ages are interpreted to be Oligocene based on the minimum age of an inclined age spectra (Copeland et al., 1991). The sharp contrast between rocks that cooled through the argon blocking temperature of muscovite, biotite, and hornblende in the Cenozoic and those that preserve evidence of much older cooling support our mapped location of the Main Central thrust. The same break in cooling ages marks the Physiographic Transition 2 of Wobus et al. (2003).

### 4.7.2 Geothermobarometric Implications

When combined with thermobarometric data from the Manaslu-Himal Chuli Himalaya reported by Hodges et al. (1988) and Kohn et al. (2001), the P-T data obtained during this study help constrain profiles of metamorphic pressures and temperatures across the entire Greater Himalayan sequence (Figures 4.10A, B). The data of Kohn et al. (2001) have been re-calculated using the Holdaway (2000) thermometer and the GBPQ barometer of Wu et al., (2004a) to facilitate the comparison of those pressure and temperature estimates with data from this study. We have not recalculated the estimated pressures and temperatures reported by Hodges et al. (1988), however, because mineral composition data were not available for the rocks analyzed by them. Disparities between metamorphic pressure-temperature estimates from this study and those of Hodges et al. (1988) may reflect the use of different garnet-biotite thermometer calibrations and barometers.

Estimated metamorphic temperatures increase slightly up-structural-section from near the bottom of the Greater Himalayan sequence, while estimates from the middle and upper portions of the Greater Himalayan sequence are relatively constant (Figure 4.10B). Pressure estimates, in contrast, vary systematically with structural position with maximum pressures near the base of the migmatite-bearing portion of the Greater Himalayan sequence (Figure 4.10A). From that maximum, pressures decrease, almost linearly, structurally upward and downward but at different

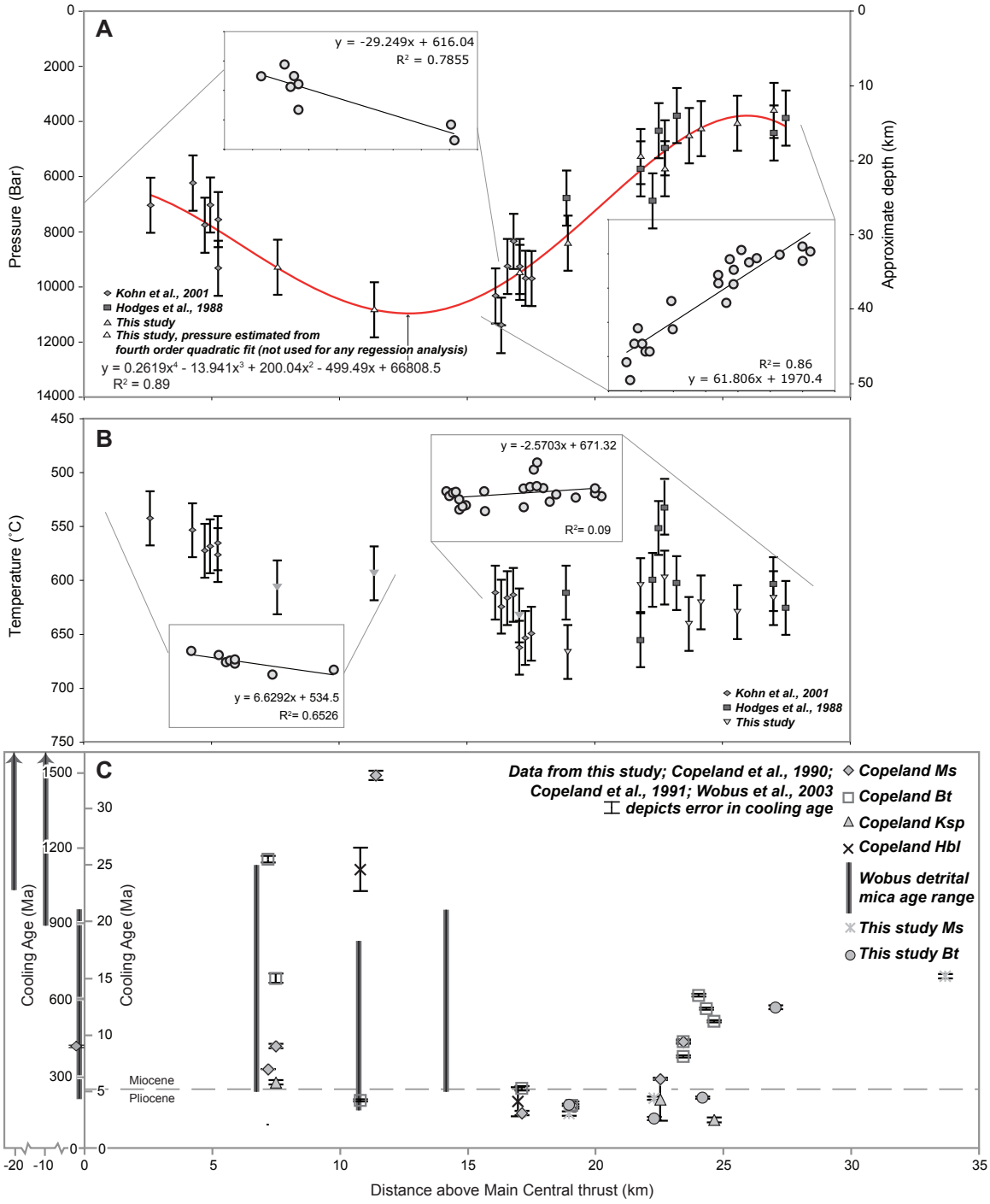


**Figure 4.10**
Variations in metamorphic pressure, temperature, and $^{40}Ar/^{39}Ar$ cooling data with respect to structural position in the Manaslu-Himal Chuli Himalaya. A) Metamorphic pressure estimates (with associated error) from this study (triangles) and from previously published studies within the same area (squares, Hodges et al., 1988; diamonds, Kohn et al., 2001). A fourth order polynomial fitted to the metamorphic pressure estimates has been used to estimate pressures for specimens that only yeilded temperature estimates in this study (white-filled triangles). Linear regression through geobarometry data from the upper Greater Himalayan sequence and lower Greater Himalayan sequence

provide an estimate of the apparent metamorphic pressure gradient recorded in these rocks. B) Metamorphic temperature estimates from this study (triangles), Hodges et al., (1988), and Kohn et al., (2001) with associated error bars. Linear regresson of data from the lower Greater Himalayan sequence shows an inverted apparent temperature field gradient, whereas temperatures in the upper Greater Himalayan sequence are approximately flat. Data from Hodges et al., (1988) are calculated using a different garnet-biotite exhange thermometer, which may account for the apparent disparity displayed in some of those specimens (see text). C) $^{40}Ar/^{39}Ar$ cooling ages of muscovite (Ms), biotite (Bt), K-felspar (Ksp), and hornblende (Hbl) from this study, and also from Copeland et al., (1990), Copeland et al. (1991), and Wobus et al., (2003) with associated error bars, plotted against structural position within the Greater Himalayan sequence. Notice the abrupt change in cooling ages across the Main Central thrust.

---

slopes. The pressure estimates are modeled with a fourth-order quadratic equation with an $R^2$ value of 0.89 (Figure 4.10A). The quadratic model for the data allows the estimation of pressures for specimens from this study (specimens: MS-76, MS-12B, MS-21A) within which the mineral assemblage was appropriate only for a temperature estimate. The pressures estimated using the quadratic model help fill in a conspicuous gap in pressure data; however, because they are less reliable, they are not used to estimate pressure/structural position ratios that are discussed later in this paper.

All P-T data points from this study and previous studies carried out in the Daraudi and Budhi Gandaki valleys are plotted against structural position in Figures 4.10A, B. The structural position of each specimen is estimated based on a vertical geologic section drawn across the Manaslu-Himal Chuli Himalaya (Figure 4.4). Previous estimates of the structural depth of specimens did not accommodate the complex geometry of the Greater Himalayan sequence in this area, which includes large-scale post-metamorphic upright open folding (Figure 4.4); instead structural depth was estimated from horizontal distance from a reference point using an assumed constant dip of the exhumed mid-crustal layer. Assuming a uniform dip of ~30˚, Hodges et al. (1988) concluded that their pressure data define an apparent pressure gradient of 270 bar/km, consistent with that predicted assuming a lithostatic load with the average density of gneissic rocks (~2750 kg/m$^3$). When our data are combined with those of Hodges et al. (1988) and Kohn et al. (2001), and the structural position of each specimen is interpreted on the basis of our cross-section (Figure 4.4), the pressure data from the upper half of the Greater Himalayan sequence define a gradient of ~ 620 bar/km, more than twice the predicted gradient assuming a lithologic density of ~2750 kg/m$^3$. Similar results, 540 bar/km, have been reported by Fraser et al. (2000) for the adjacent Langtang Himalaya.

The apparent pressure gradient defined by the metamorphic thermobarometric data from the upper portion of the Greater Himalayan sequence can be explained in a number of ways. 1) The estimated pressures may have been recorded by the diachronous 'locking in' of metamorphic pressure at different levels in the upper Greater Himalayan sequence. No geochronologic control on the timing of metamorphism in the upper portion of the Greater Himalayan sequence in central Nepal is available except for a few Early Miocene Th-Pb monazite dates reported by Kohn et al. (2001) and Catlos et al. (2001). The specimens dated were collected from the lowest portion of the upper Greater Himalayan sequence and thus do not constrain the age of metamorphism across the rest of the exhumed mid-crust. Better geochronologic constraints can be derived, however, on variations in the timing of peak metamorphic temperatures. Hodges et al., (1988) suggested that the partial melting of the crustal rocks that fed the Manaslu intrusive complex thermally buffered the upper Greater Himalayan sequence and is responsible for the relatively flat thermal profile across it (Figure 4.10B; Hodges et al. 1988). In the adjacent Nar area (Figure 4.1) Godin et al. (2006a) reported that migmatites in the Greater Himalayan sequence coalesce up-section into dykes that represent the feeder system of the 23-19 Ma (Harrison et al., 1999) Manaslu intrusive complex. While this does not provide direct control on the timing of the pressures recorded in the metamorphic mineral assemblages, it does indicate that peak temperatures across the Greater Himalayan sequence, upon which paleogeobarometric measurements are partially based, were achieved relatively synchronously. 2) A higher-than-expected apparent pressure gradient can also be explained by post-metamorphic tectonic thinning of the crust (e.g., Lee et al., 2004). Post-metamorphic stretching parallel with the foliation in the upper Greater Himalayan sequence is consistent with the presence of pre-to-syn tectonic garnets and deformation temperatures that appear to be lower than metamorphic temperature estimates. It is also consistent with observations from the Everest region (Hubbard, 1996; Jessup et al., 2006) and NW India (Vannay and Grasemann, 2001) that support post-metamorphic layer-parallel stretching of the mid-crust. For the pressure gradient to be double that expected by present thicknesses, the upper portion of the Greater Himalayan sequence would have to have been thinned vertically by ~50%. Evidence of thinning in the upper Greater Himalayan sequence is indicated by vorticity estimates that show a significant pure shear strain component (Figure 4.6) and by published estimates of shortening perpendicular to the boundaries of the Greater Himalayan sequence including 25-32% for the

Dhaulagiri Himal of central Nepal (Chapter 2 of this thesis), 10-30% in the Everest region (Law et al., 2004), and ~ 43% in the Sutlej valley of NW India (Vannay and Grasemann, 2001). The values reported from the Dhaulagiri Himal and Everest region are minimum values, however, as the finite strain in those studies was measured using recrystallized quartz grains (e.g., Wallis et al., 1993). If the cross-girdle shape of the quartz petrofabrics measured in upper Greater Himalayan sequence does indicate plane strain conditions, as modeled by Lister and Hobbs (1980), a vertical thinning of 50% would require commensurate horizontal elongation of 100%.

In contrast to the upper part of the Greater Himalayan sequence the lower Greater Himalayan sequence displays an inverse metamorphic pressure gradient (Figure 4.10A), where specimens from structurally lower levels record lower pressures than those from higher structural levels. A similar trend is also observed in the metamorphic temperature estimates from the same rocks (Figure 4.10B). Monazite crystals in the lower Greater Himalayan sequence have been dated in the Daraudi and adjacent Marsyandi (Figure 4.1) valleys of the Manaslu-Himal Chuli Himalaya; there is a general downward decrease in monazite ages in the structural section (Catlos et al., 2001; Kohn et al., 2001). While these dates should be regarded with caution (e.g., Bollinger and Janots, 2006; Martin et al., 2007), they indicate that monazite growth, and perhaps metamorphism in the lower Greater Himalayan sequence, was diachronous. Catlos et al. (2001) attribute similar P-T-t data from the Marsyandi valley to the progressive accretion of thrust slices beneath the upper Greater Himalayan sequence produced by the downward migration of the Main Central thrust through time. The P-T-t data imply that diachronous metamorphism in the lower Greater Himalaya sequence took place at consistently shallower and cooler crustal levels. Such a model requires exhumation coincident with the metamorphism of the lower Greater Himalayan sequence.

### 4.7.3 Displacement and distortion of the mid-crust

The simple shear conceptual model that is commonly used to depict ductile flow in rocks (e.g. Ramsay and Huber, 1983) consists of laminar flow that involves neither shortening nor stretching within the rock mass in the direction of flow. This conceptual model is an idealized special situation marking the boundary between two general states: compressing flow, which involves shortening in the direction of flow, and extending flow which involves extension in

the direction of flow. While the compressing flow and extending flow conceptual models are commonly used to describe variations in patterns of gravitationally driven flow in glaciers and ice sheets (Nye, 1951, 1952; Patterson, 2000) they are also useful in depicting gravitationally influenced ductile flow of rock within evolving mountain belts (Price, 1972).

#### 4.7.3.1 The Prandtl Cell

The Prandtl cell is a graphical illustration of slip lines and flow lines within plastic material that is either being compressed in the direction of flow or being extended in the direction of flow (Figure 4.11; Prandtl, 1924; Nádai, 1950; Kanizay, 1962). These two types of Prandtl cells can be used to conceptualize displacement and distortion in the hinterland and foreland regions of an orogen. The deep hinterland is characterized by extending flow and the lateral extrusion of hot ductile rock, while the shallow foreland is characterized by compressing flow and the intrusion of formerly hot cooling rock. The boundary, or transition, between these flow-type domains corresponds to a region of simple shear where rock is neither extending nor compressing in the direction of flow. As the orogen evolves so does this boundary; it shifts through time with changing themal regimes (ductility) and tectonic loading. Furthermore, rock that moves through this boundary is subject to tectonic overprinting and the obliteration of any record of the transition itself.

#### 4.7.3.2 The Himalayan hinterland-foreland transition and the growth of the orogenic wedge

The change of elevation across the orogen from the Tibetan plateau southwards to the Indian craton paired with a northward-dipping Main Himalayan thrust forms a natural wedge. The Tibetan plateau, which comprises the back of the wedge, appears to be in a steady-state gravitational equilibrium (Fielding et al., 1994). If crustal thickening occurs (by tectonic under-plating or internal deformation), it must be accommodated by extending flow - vertical thinning and lateral horizontal spreading within the hot ductile crust below the plateau. At the southern edge of the plateau, extrusion of the hot ductile mid-crustal rock from beneath the South Tibetan detachment system has driven the expansion of the foreland thrust and fold belt, which is characterized by compressing flow - vertical thickening and horizontal shortening. Thus,

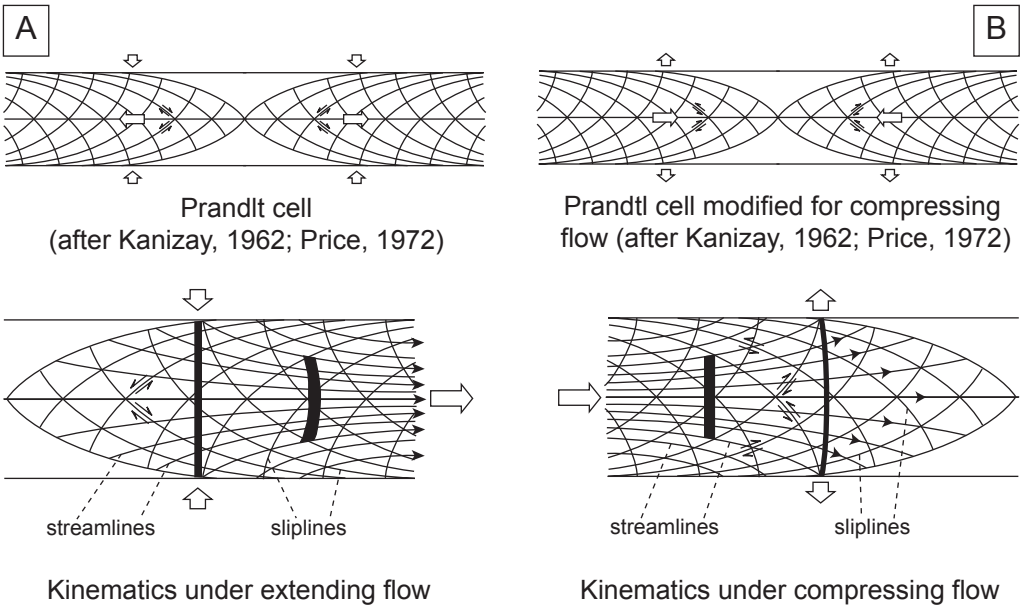


**Figure 4.11**
Sliplines and streamlines illustrating distortion and displacement during ductile flow within the Prandtl cell; A) for extending flow, B) for compressing flow.

lateral flow across the entire orogen, driven by the gravitational potential gradient between the high standing plateau and the topographically lower Indian craton, involves both extending and compressing flow components.

The change in apparent metamorphic paleo-pressure gradients between the upper and lower Greater Himalayan sequence in this study can be attributed to the fundamentally different character of flow-type recorded in the two domains. The Prandtl cell model for extending flow is consistent with observations in the upper part of the Greater Himalayan sequence in which apparent pressure gradient data indicate vertical thinning and horizontal stretching (assuming plane strain deformation) during lateral flow out from beneath the Tibetan plateau (Figure 4.12A). As the spreading mid-crustal rock emerged from beneath the edge of the plateau and began intruding its southern flank there was a transition from extending flow to compressing flow (Figure 4.12A). This transition was likely linked to cooling, reduced ductility and rheologic strengthening of the mid-crust, which was manifested as a transformation into a semi-rigid indenter.

The location of the transition from extending flow to compressing flow adjusted in response to changes in the orogenic wedge. Subsequent to initial horizontal spreading of the weak, partially-molten mid-crustal layer, i.e. channel flow (Grujic et al., 1996; Beaumont et al., 2001), deformation proceeded out-of-sequence to restore lost gravitational potential at the back of the wedge (Figure 4.12B). The restoration of the orogenic wedge, which occurred between 18-12 Ma (Chapter 3 of this thesis), led to the exhumation of the North Himalayan antiform (Godin et al., 2006a; Chapter 3 of this thesis). During that time the transition between regions of extending flow and compressing flow shifted toward the hinterland (Figure 4.12B). Crustal thickening and uplift of the southern margin of the plateau drove the southward lateral growth of the foreland thrust-fold belt and the initiation of the Main Boundary thrust at *ca*. 10 Ma (Figure 4.12C; Meigs et al., 1995). It also caused the transition from extending flow to compressing flow to migrate back towards the foreland. Concurrent with foreland propagating deformation in the frontal Himalaya, continuing crustal thickening and lateral mid-crustal extrusion in southern Tibet may have been accommodated through horizontal lateral flow toward southeast Asia and the Indo-China block (Figure 4.12C; Clark and Royden, 2000; Clark et al., 2005; Burchfiel et al., 2008).

The boundary between the upper Greater Himalayan sequence and the lower Greater

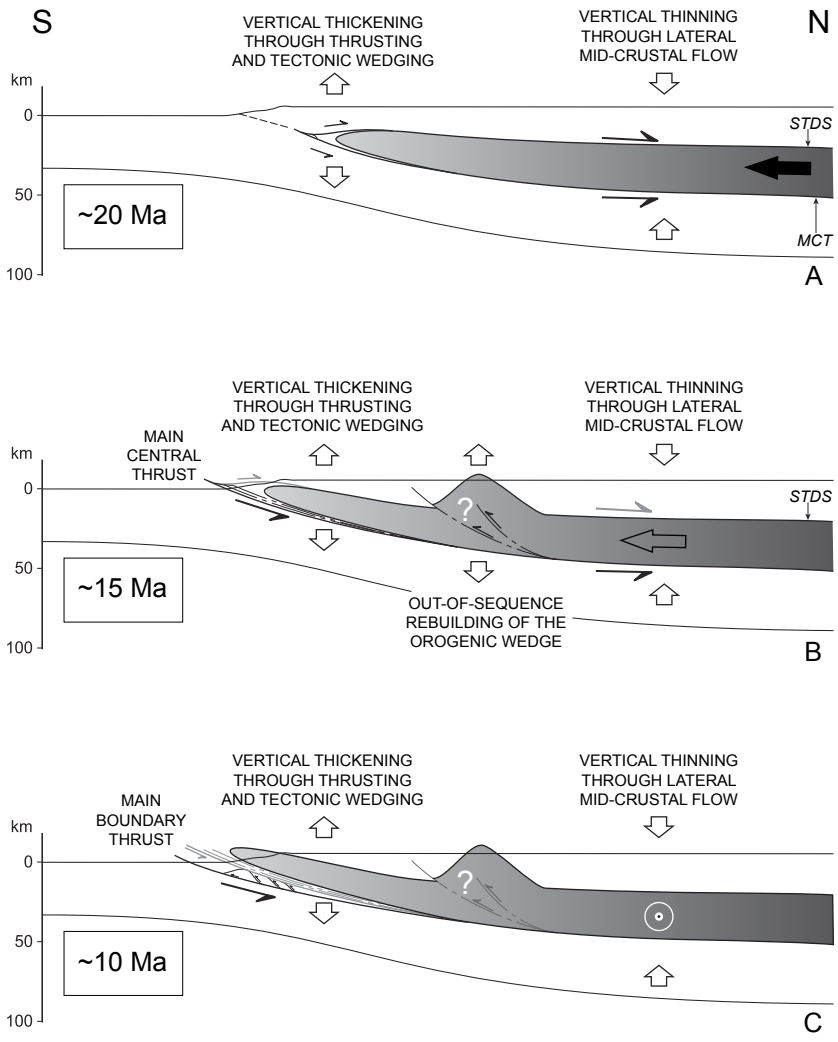


**Figure 4.12**
Model of the evolution of the Himalayan-Tibetan orogen between *ca*. 20 Ma and *ca*. 10 Ma. A) At *ca*. 20 Ma extending flow during vertical thinning and lateral extrusion of hot ductile mid-crustal rock from beneath the Tibetan plateau. The extruded rock cools as it spreads laterally along the Main Central thrust and intrudes rocks to the south. Tectonic wedging of the cooled mid-crustal plug into the foreland, which produces vertical thickening and horizontal shortening, involves compressing flow. B) At *ca*. 15 Ma deformation steps back towards the hinterland of the orogen rebuilding the Himalayan orogenic wedge. At this time compressing flow deformation extends back to at least the North Himalayan antiform. C) At *ca*. 10 Ma, after the orogenic critical taper has been rebuilt, deformation advances into the foreland and initiates displacement along the Main Boundary thrust. At this time vertical thinning beneath the Tibetan plateau is synchronous with lateral flow towards the Indo-China block (out-of-plane toward the viewer). STDS, South Tibetan detachment system; MCT, Main Central thrust.

Himalayan sequence in central Nepal is interpreted to mark the transition between hinterland-style extending flow above and foreland-style compressing flow below. The transition between the two involved cooling and stiffening of the intruding mid-crustal layer plus subcretion of footwall strata by the downward-expanding basal detachment, which produced thickening of the advancing critical-taper wedge as required to compensate for erosional removal from the tip of the wedge and lateral expansion of the wedge without loss of critical taper.

## 4.8 Conclusions

The Greater Himalayan sequence in the Manaslu-Himal Chuli Himalaya is a pervasively deformed layer of upper-greenschist to upper-amphibolite metamorphic grade mid-crustal rocks. Field and microstructural data outline a shear sense reversal near the top of the sequence from top-to-the-south sense deformation that dominates most of the Greater Himalayan sequence to top-to-the-north sense deformation that is related to the South Tibetan detachment system. Microstructural analysis of the migmatite-bearing upper portion of the Greater Himalayan sequence indicates that there deformation outlasted metamorphism. This interpretation is supported by an apparent metamorphic pressure gradient of 620 bar/km, which is double the expected 270 bar/km, and is interpreted to indicate post-metamorphic vertical thinning of up to 50%. Foliation-perpendicular thinning during deformation is also implied by vorticity data that show a significant contribution of pure shear deformation across the Greater Himalayan sequence. Vertical thinning in the upper part of the Greater Himalayan sequence stands in contrast with deformation in the lower part of the Greater Himalayan sequence. The lower Greater Himalayan sequence is interpreted to comprise thrust slices that formed beneath and carried forward the Greater Himalayan sequence as the Main Central thrust expanded down structural section with time. This deformation is consistent with vertical thickening and horizontal compression at the frontal tip of the mid-crust.

Failure to recognized the fundamentally different tectonic domains within which the tectonometamorphic data has been gathered in the past from the Greater Himalayan sequence has hindered our understanding of the evolution of the Himalaya. It is proposed that the fundamental change in deformation style between the upper and lower parts of the Greater Himalayan sequence marks the transition from hinterland-style deformation or extending flow

(i.e. channel flow) - extension in the direction of tectonic transport, to foreland-style deformation or compressing flow (i.e. critical taper wedge) - compression in the direction of transport.

## Acknowledgements

This project was funded through a Natural Science and Engineering Research Council of Canada Discovery grant to L. Godin. Financial support for K. Larson was provided through a Canada Graduate Scholarship. Local logistical support in Nepal was organized by Teke Tamang of Peke Peak Trekking and provided by Asta, Sure, Ralesh, Pradap, Yo Singgi, Forpa, and Kami Tamang. Support in the Queen's Argon Laboratory was provided by D. Archibald and at Carleton University by Peter Jones. Dr. C.Wu is thanked for assistance with thermobarometric calculations. This paper has benefited through discussions with and informal reviews by D.A. Kellett, R.L. Brown and D. Grujic and proof-reading by N. Portelance.

# Chapter 5

# Summary Conclusions

The research presented in this thesis has provided the basis for better understanding the tectonometmorphic evolution of the Greater Himalayan sequence and for answering the two main questions posed in this first chapter of this work: 1) What are the kinematic characteristics (i.e. structural framework, deformation history) of the Greater Himalayan sequence? and 2) By what process(es) has the Greater Himalayan sequence been translated laterally from beneath the Tibetan plateau and exhumed from mid-crustal depths?

## 5.1 Kinematic Framework

### 5.1.1 The Main Central thrust

The Main Central thrust fault is defined as the structural break/strain gradient above which all rocks are transposed, have been subject to Cenozoic metamorphism, and generally yield Neogene (certainly Cenozoic) cooling ages (Searle et al., 2008). All rocks above the Main Central thrust, i.e. in the immediate hanging wall, belong to the Greater Himalayan sequence (Gansser, 1964), while those rocks below, i.e. in the immediate footwall, belong to the Lesser Himalayan sequence (Gansser, 1964).

Previous studies in the Dhaualagiri-Annapurna and Manaslu-Himal Chuli Himalaya of central Nepal map the Main Central thrust fault near the base of a thick migmatitic paragneiss unit, sometimes referred to as Formation I (e.g. Colchen et al., 1986), which commonly coincides with the kyanite-in isograd (e.g. Colchen et al., 1986; Hodges et al., 1988; Vannay and Hodges, 1996). Rocks both above and below the inferred fault, however, are highly strained, of similar metamorphic grade, and exhibit Cenozoic cooling histories (Copeland et al., 1991). Based on the definition of the Main Central thrust as proposed by Searle et al., (2008) we map the fault more than 8 km structurally below those previous interpretations. This new location for the fault requires that a package of rock often referred to, at least in part, as the Main Central thrust shear zone (e.g., Arita, 1983) and formerly considered to be of Lesser Himalayan sequence affinity (e.g. Hashimoto, 1973; Colchen et al., 1986; Parrish and Hodges 1996) be part of the Greater

Himalayan sequence.

The Main Central thrust, as it is mapped in this study, is structurally below the inferred surface trace of the Ramgarh thrust in the region (see Pearson and DeCelles, 2005). The presence of the Ramgarh thrust in central Nepal is based largely on inferred stratigraphic repetition (Pearson and DeCelles, 2005), however, no evidence for repeated stratigraphy has been observed in this study. Furthermore there is no discrete concentration of strain anywhere near the proposed location of the Ramgarh thrust (another identifying criteria of Pearson and DeCelles, 2005). The only possible location for the Ramgarh thrust in central Nepal is coincident with the Main Central thrust fault at the base of the Greater Himalayan sequence. It is therefore interpreted that the Ramgarh thrust and the Main Central thrust are the same. This field-based interpretation supports an earlier conceptual model (Searle et al., 2008) that arrived at the same conclusion.

### 5.1.2 Deformation of the Greater Himalayan sequence

All rocks above the Main Central thrust, and below the South Tibetan detachment system, are pervasively deformed. C/S/C' fabrics are observed throughout the Greater Himalayan sequence and record a dominant top-to-the south shear sense in the bottom and middle portions of the package. In the upper portion of the Greater Himalayan sequence, however, C/S/C' fabrics record a shear sense reversal and indicate a top-to-the-north sense of shear. These field observations are confirmed through quartz petrofabric analyses, which, in addition to indicating the sense of shear during deformation, indicate that deformation took place at temperatures between ~450 – 650˚C. These deformation temperatures are similar to those estimated for the metamorphic conditions just prior to/or during extrusion of the mid-crust at similar structural levels, which indicates that the deformation observed in the Greater Himalayan sequence is related to its lateral extrusion between the Main Central thrust and South Tibetan detachment system. This interpretation is also consistent with the above-noted shear sense reversal.

Mean kinematic vorticity ($W_m$) estimates from across the Greater Himalayan sequence indicate significant contributions of pure shear to the finite strain. $W_m$ values range between 0.50 and 0.87, which correspond to pure shear contributions, relative to simple shear, of between 67% and 33%, respectively, with larger pure shear values generally present at deeper structural levels. Pure shear during deformation would enhance the rate of lateral extrusion relative to

entirely simple shear (Law et al., 2004; Jessup et al., 2006), as horizontal extension would be commensurate with the vertically oriented flattening component.

### 5.1.3 The upper and lower Greater Himalayan sequence

The Greater Himalayan sequence in central Nepal can be separated into an upper and lower portion each with a distinct displacement and distortion history. The upper portion of the Greater Himalayan sequence consists generally of migmatitic sillimanite metamorphic-grade paragneiss and orthogneiss. Metamorphic pressure estimates from this portion of the Greater Himalayan sequence are interpreted to have been achieved coevally. Paleogeobarometric estimates define an apparent pressure gradient of ~62 MPa/km; approximately twice that expected for regular continental crust (~27 MPa/km). This apparent pressure gradient is interpreted to record post-metamorphic thinning of the mid-crust by 50%, likely during its extrusion from beneath southern Tibet. Quartz *c*-axis preferred orientations indicate that deformation in the upper Greater Himalayan sequence occurred under plain strain conditions and as such vertical thinning of the mid-crust would result in commensurate horizontal extension. Vertical thinning and paired horizontal extension is characteristic of extending flow or extending in the direction of tectonic transport. This style of ductile deformation is commonly observed in the deep hinterland regions of orogens.

The lower Greater Himalayan sequence, in contrast, consists dominantly of paragneiss and schist that decrease in metamorphic grade from kyanite grade at its top to biotite grade at its base; anatectite is only abundant locally. Estimates of metamorphic conditions define apparent paleogeothermal and paleogeobarometric gradients that decrease with structural depth. Additionally, monazite ages, interpreted to date peak metamorphism (Kohn et al., 2001; Catlos et al., 2001) in the lower Greater Himalayan sequence, decrease with increased structural depth. The metamorphic condition and age estimates are interpreted to indicate that the lower Greater Himalayan sequence was accreted as foreland propagating and exhuming thrust slices beneath the previously extruded upper Greater Himalayan sequence as the Main Central thrust migrated downward structurally with time. The addition of thrust slices increased the vertical thickness of the Greater Himalayan sequence while coevally accommodating horizontal compression. These features, vertical thickening and horizontal compression, are characteristic of compressing flow or

shortening in the direction of tectonic transport. This style of deformation is commonly observed in the foreland regions of orogens.

## 5.2 Lateral extrusion and exhumation of the Greater Himalayan sequence

Previous models proposed to explain the evolution of the Himalaya have generally been variations of one of two end-members: 1) mid-crustal lateral (channel) flow (e.g. Grujic et al., 1996; Beaumont et al., 2001, 2004; Searle et al., 2006) or 2) critical wedge taper (e.g. DeCelles et al., 2001; Kohn, 2008; Robinson, 2008). In both models deformation occurs in response to lateral gravitational gradients. The new kinematic, paleogeothermobarometric, and geochronologic data presented in this study indicate that both lateral mid-crustal flow and critical taper processes were active during the development of the Himalaya.

At a first order observational scale the topographic profile from cratonic India south of the Main Frontal thrust northward to the Tibetan plateau defines a southward tapering orogenic wedge with the Main Himalayan thrust as its basal detachment. During episodes of in-sequence deformation the back of the orogenic wedge undergoes vertical thinning and lateral spreading in order to transfer material to the toe of the wedge. The transfer of material from the back of the wedge drives horizontal compression and vertical thickening at the front of the wedge thereby reducing the taper angle.

At the back of the Himalayan orogenic wedge vertical thinning and horizontal spreading, extending flow, appears to have been accomplished through ductile lateral (channel) flow of the mid-crust. Evidence of this is preserved in the upper portion of the Greater Himalyan sequence. As the laterally extruded material was translated southward over India it cooled and passed through a kinematic transition where compressing flow became the dominant flow type. This transition marks the change from displacement and distortion characteristic of deep orogenic hinterlands to that characteristic of foreland regions. Deformation that occurred in the foreland portion of the orogen, as recorded in lower portion of the Greater Himalayan sequence, was characterized by vertical thickening and horizontal compression typical of critical taper wedge style deformation.

The kinematic transition between regions of compressing and extending flow did not remain static with respect to material points through time. Rather it migrated as the wedge

changed shape and the locus of deformation adjusted to maintain a preferred wedge geometry. In central Nepal, lateral mid-crustal flow between the South Tibetan detachment system and the Main Central thrust ceased by ~19 Ma. The cessation may reflect insufficient orogenic potential to continue to drive deformation southward. Subsequently, deformation stepped out-of-sequence, toward the hinterland, to restore the orogenic potential, resulting in the exhumation of the Changgo culmination at ~18 Ma. Restoring the orogenic potential, or the preferred geometry of the orogenic wedge, was accomplished through compressing flow (vertical thickening, horizontal compression) and therefore reflects a migration of the kinematic transition between the hinterland and foreland. After the Changgo culmination had been exhumed, deformation proceeded to migrate back toward the foreland as recorded in the ~16 Ma exhumation of the Chako antiform (Godin et al., 2006b), the exhumation of the frontal Himalaya at ~14 Ma (Vannay and Hodges, 1996) and eventually the initiation of the Main Boundary thrust at ~10-12 Ma (Meigs et al., 1995).

The evolution of the Himalaya records both extending flow and compressing flow and as such different models, i.e. lateral mid-crustal flow and critical wedge taper, are applicable to different portions of the orogen at different times. The kinematic transition between those two different styles of deformation within the Greater Himalayan sequence, hitherto unrecognized has been the source of significant scientific consternation among Himalayan geologists. Recognition of this transition allows us to better understand the evolution of the Himalaya and the structural link between orogenic hinterlands and forelands in general.

## 5.3 Future Research Considerations

While this study represents a significant contribution to understanding the geology of central Nepal and adjacent Tibet and provides insight into the processes that may have governed the evolution of the Himalaya and other continent-continent collisions there yet remains many questions to be explored and topics to research:

- Along-strike and across-strike quantification of strain within the Greater Himalayan sequence:
    - * Strain demonstrably changes across the Greater Himalayan sequence in single transect and the Greater Himalayan sequence itself changes character along the strike

of the orogen (e.g. Everest region vs. Dhaulagiri region);

* Understanding lateral variations in strain may provide insight into the processes that governed the evolution of the exhumed mid-crust of the mountain belt.

• Geologic study of the Kung Tang culmination and the southern flank of the Changgo culmination:

* Investigation of the Kung Tang area would provide a test for the model proposed for the Changgo culmination and the North Himalayan antiform;

* Accessing the southern flank of the Changgo dome may provide the means to better constrain the late doming history of the area and across-strike characterization of the South Tibetan detachment zone.

• The use of Raman spectroscopy to estimate metamorphic temperatures in calcite-bearing rocks not amenable to traditional P-T estimation methods (particularly in the calc-silicate rich Greater Himalayan sequence rocks exposed in the Kali Gandaki valley):

* Raman-based temperature estimates would help constrain metamorphic conditions through the entire Greater Himalayan sequence;

* Raman spectroscopy may allow the estimation of metamorphic temperatures in the South Tibetan detachment zone in the Kali Gandaki valley, which commonly occurs within calc-silicate units.

• U-Pb geochronologic analyses of zircon and monazite from the migmatitic Greater Himalayan sequence rock exposed in the Budhi Gandki and Dauradi valleys:

* Derive constraints for the age of metamorphism (is it diachronous?);

* Date the crystallization ages of migmatites (are they all related to the Manaslu granite?);

* Constrain age of deformation through cross-cutting relationships (is it syn-or-post metamorphism?).

• Examination of the hinterland/foreland transition across the orogen:

* The concept and significance of the hinterland-foreland transition in the Himalaya was introduced in this thesis and as such there are many opportunities to identify the transition in areas both along-strike, and across-strike, to help elucidate its significance to the evolution of the orogen.

# References

Ahmad, T., N. Harris, M. Bickle, H. Chapman, J. Bunbury, and C. Prince (2000), Isotopic constraints on the structural relationships between Lesser Himalayan series and High Himalayan crystalline series, Garhwal Himalaya*, Tectonophysics, 112*, 467-477.

Aoya, M., S. R. Wallis, T. Tawakami, J. Lee, Y. Wang, and H. Maeda (2006), The Malashan gneiss dome in south Tibet: comparative study with the Kangmar dome with special reference to kinematics of deformation and origin of associated granites, in *Channel Flow, Ductile Extrusion and Exhumaiton in Continental Collision Zones*, edited by R.D. Law, M. P. Searle, and L. Godin, Geological Society, London, Special Publication 268, 471-495.

Aoya, M., S. R. Wallis, K. Terada, J. Lee, T. Kawakami, Y. Wang, and M. Heizler (2005), North-south extension in the Tibetan crust triggered by granite emplacement*, Geology, 33*, 853-856.

Arita, K. (1983), Origin of the inverted metamorphism of the lower Himalayas, central Nepal*, Tectonophysics, 95*, 43-60.

Bailey, C. M., B. E. Francis, and E. E. Fahrney (2004), Strain and vorticity analysis of transpressional high-strain zones from the virginia piedmont, USA, in *Flow Processes in Faults and Shear Zones*, edited by G. I. Alsop, R. E. Holdsworth, K. J. W. McCaffrey, and M. Hand, Geological Society, London, Special Publication 224, 249-264.

Beaumont, C., R. A. Jamieson, M. H. Nguyen, and B. Lee (2001), Himalayan tectonics explained by extrusion of a low-viscosity crustal channel coupled to focused surface denudation*, Nature, 414*, 738-742.

Beaumont, C., R. Jamieson, M. Nguyen, and S. Medvedev (2004), Crustal channel flows: 1. Numerical models with applications to the tectonics of the Himalayan-Tibetan orogen*, Journal of Geophysical Research, 109,* B06406, doi:10.1029/2003JB002809.

Beaumont, C., M. H. Nguyen, R. A. Jamieson, and S. Ellis (2006), Crustal flow modes in large hot orogens, in *Channel Flow, Ductile Extrusion and Exhumation in Continental Collisional Zones*, edited by R. D. Law, M. P. Searle, and L. Godin, Geological Society, London, Special Publication 268, 91-146.

Bhattacharya, A. R. and K. Weber (2004), Fabric development during shear deformation in the Main Central Thrust Zone, NW-Himalaya, India*, Tectonophysics, 387*, 23-46.

Bird, P. (1991), Lateral extrusion of lower crust from under high topography, in the isostatic limit*, Journal of Geophysical Research, 96*, 10275-10286.

Black, J. P., S. L. Kamo, D. W. Allen, J. N. Aleinikoff, J. W. Valley, R. Mundi, I. H. Campbell, R. J. Korsh, I. S. Williams, and C. Foudoulis (2004), Improved $^{206}Pb/^{238}U$ microprobe geochronology by monitoring of a trace-element-related matrix effect; SHRIMP, ID-TIMS, ELA-ICP-MS and oxygen isotope documentation for a series of zircon standards*, Chemical Geology, 205*, 115-140.

Bodenhausen, J. W. A. and C. G. Egeler (1971), On the geology of the upper Kali Gandaki valley, Nepalese Himalayas, I*., Proceedings Akademic van Wetenschappen, 74*, 526-538.

Bollinger, L. and E. Janots (2006), Evidence for Mio-Pliocene retrograde monazite in the Lesser Himalaya, far western Nepal*, European Journal of Mineralogy, 18*, 289-297.

Bollinger, L., P. Henry, and J. -P. Avouac (2006), Mountain building in the Nepal Himalaya: Thermal and kinematic model*, Earth and Planetary Science Letters, 244*, 58-71.

Bordet, P. (1961)*,* Recherches géologiques dans l'Himalaya du Népal, région du Makalu, 275 pp., *C.N.R.S., Paris*.

Bordet, P. (1979), Geology of the Tibetan slab (central Nepal Himalaya), in *Structural Geology of the Himalaya*, edited by P. S. Saklani, pp. 229-246, Today and Tomorow's Printers and Publishers, New Delhi, India.

Bordet, P. (1977), Géologie de la dalle du Tibet (Himalaya central). Geology of the Tibet Slab, Central Himalayas; Livre à la mémoire de Albert F. de Lapparent (1905-1975) *consacré aux Recherches géologiques dans les chaînes alpines de l'Asie du Sud-Ouest. Mémoire Hors Serie - Société Géologique De France*, 235-250.

Bordet, P., R. Mouterde, and M. Remy (1964), Sur la stratigraphie des séries affleurant dans la vallée de la Kali Gandaki (Nepal central). *Compte Rendus Hebdomadaires des Séances de l'Académie des Sciences, 259*, 414-416.

Bordet, P., M. Colchen, D. Krummenacher, P. LeFort, R. Mouterde, and M. Remy (1971), Recherches géologiques dans l'Himalaya du Népal: région de la Thakhola, *Éditions Du Centre National De La Recherche Scientifique*, 279 pp., Paris, France.

Bouchez, J. L. (1978), Preferred orientations of quartz axes in some tectonites; kinematic inferences, *Tectonophysics, 49*, T25-T30.

Bouchez, J. L. and A. Pêcher (1976), Microstructures and quartz preferred orientations in quartzites of the Annapurna area (central Nepal), in the proximity of the main central thrust, *Himalayan Geology, 6*, 118-131.

Bouchez, J. and A. Pecher (1981), The Himalayan Main Central thrust pile and its quartz-rich tectonites in Central Nepal, *Tectonophysics, 78*, 23-509.

Brookfield, M. E. (1993), The Himalayan passive margin from Precambrian to Cretaceous, *Sedimentary Geology, 84*, 1-35.

Brown, R. L. and J. H. Nazarchuk (1993), Annapurna detachment fault in the greater himalaya of central Nepal, in *Himalayan Tectonics*, vol. 74, edited by P. J. Treloar and M. P. Searle, pp. 461-473, Geological Society Special Publication.

Burchfiel, B. C., L. H. Royden (1985), North-south extension within the convergent Himalayan region, *Geology, 13 (10)*, 679-682.

Burchfiel, B. C., C. Zhilian, K. V. Hodges, L. Yuping, L. H. Royden, D. Changrong, and X. Jiene (1992), The South Tibetan detachment system, Himalaya orogen: extension contemporaneous with and parallel to shortening in a collisional mountain belt, *Geological Society of America, Special Paper 269*, 1-41.

Burchfiel, B. C., L. H. Royden, Van Der Hilst, R. D., B. H. Hager, Z. Chen, R. W. King, C. Li, J. Lu, H. Yao, and E. Kirby (2008), A geological and geophysical context for the Wenchuan earthquake of 12 May 2008, Sichuan, People's Republic of China, *GSA Today, 18*, 7-11.

Burg, J. -P. and G. M. Chen (1984), Tectonics and structural zonation of southern Tibet, China, *Nature, 311*, 219-223.

Burg, J. -P., M. Guirand, G. M. Chen, and G. C. Li (1984), Himalayan metamorphism and deformations in the North Himalayan Belt (southern Tibet, China), *Earth and Planetary Science Letters, 69*, 391-400.

Caddick, M. J., M. J. Bickle, N. B. W. Harris, T. J. B. Holland, M. S. A. Horstwood, R. R. Parrish, and T. Ahmad (2007), Burial and exhumation history of a Lesser Himalayan schist; recording the formation of an inverted metamorphic sequence in NW India, *Earth and Planetary Science Letters, 264*, 375-390.

Carosi, R., C. Montomoli, D. Rubatto, and D. Visona (2006), Normal-sense shear zones in the core of the Higher Himalayan Crystallines (Bhutan Himalaya): Evidence for extrusion?, in *Channel Flow, Ductile and Exhumation in Continental Collision Zones*, edited by R. D. Law, M. P. Searle, and L. Godin, Geological Society, London, Special Publication 268, 425-444.

Carosi, R., C. Montomoli, and D. Visona (2007), A structural transect in the Lower Dolpo: Insights on the tectonic evolution of Western Nepal, *Journal of Asian Earth Sciences, 29*, 407-423.

Catlos, E., M. Harrison, M. Kohn, M. Grove, F. Ryerson, C. Manning, and B. Upreti (2001), Geochronologic and thermobarometric constraints on the evolution of the Main Central Thrust, central Nepal Himalaya, *Journal of Geophysical Research-Solid Earth, 106*, 16177-16204.

Catlos, E. J., T. M. Harrison, C. E. Manning, M. Grove, S. M. Rai, M. S. Hubbard, and B. N. Upreti (2002), Records of the evolution of the Himalayan orogen from in situ Th-Pb ion microprobe dating of monazite: eastern Nepal and western Garhwal, *Journal of Asian Earth Sciences, 20*, 459-479.

Catlos, E. J., C. S. Dubey, T. M. Harrison, and M. E. Edwards (2004), Late Miocene movement within the Himalayan Main Central Thrust shear zone, Sikkim, north-east India, *Journal of Metamorphic Geology, 22*, 207-226.

Chambers, J., T. Argles, M. Horstwood, N. Harris, R. Parrish, and T. Ahmad (2008), Tectonic implications of Paleoproterzoic anatexis and Late Miocene metamorphism in the Lesser Himalayan Sequence, Sutlej Valley, NW India, *Journal of the Geological Society, London, 165*,

725-737.

Chapple, W. (1978), Mechanics of thin-skinned fold-and-thrust belts, *Geological Society of America Bulletin, 89*, 1189-1198.

Chen, Z., Y. Liu, K. V. Hodges, B. C. Burchfiel, L. H. Royden, and C. Deng (1990), The Kangmar dome: A metamorphic core complex in southern Xizang (Tibet)*, Science, 250*, 1552-1556.

Clark, M. K. and L. H. Royden (2000), Topographic ooze: Building the eastern margin of Tibet by lower crustal flow*, Geology, 28*, 703-706.

Clark, M. K., M. A. House, L. H. Royden, K. X. Whipple, B. C. Burchfiel, X. Zhang, and W. Tang (2005), Late Cenozoic uplift of southeastern Tibet*, Geology, 33*, 525-528.

Colchen, M., P. LeFort, and A. Pecher (1986), Carte géologique Annapurna-Manaslu-Ganesh, Himalaya du Népal.

Coleman, M. E. (1996), Orogen-parallel and orogen-perpendicular extension in the central Nepalese Himalayas*, Geological Society of America Bulletin, 108*, 1594-1607.

Copeland, P. and T. M. Harrison (1990), Episodic rapid uplift in the Himalaya revealed by $^{40}Ar/^{39}Ar$ analysis of detrital K-feldspar and muscovite, Bengal fan*, Geology, 18*, 354-357.

Copeland, P., T. M. Harrison, K. V. Hodges, P. Maruéjol, P. LeFort, and A. Pêcher (1991), An Early Pliocene thermal disturbance of the Main Central Thrust, central Nepal: Implications for Himalayan tectonics*, Journal of Geophysical Research, 96*, 8475-8500.

Cottle, J., M. Jessup, D. Newell, M. P. Searle, R. Law, and M. Horstwood (2007), Structural insights into the early stages of exhumation along an orogen-scale detachement: The South Tibetan Detachment System, Dzakaa Chu section, Eastern Himalaya*, Journal of Structural Geology, 29*, 1781-1797.

Culshaw, N., C. Beaumont, and R. Jamieson (2006), The orogenic superstructure-infrastructure concept: Revisited, quantified, and revived*, Geology, 34*, 733-734.

Davis, D., J. Suppe, and F. A. Dahlen (1983), Mechanics of fold-and-thrust belts and accretionary

wedges, *Journal of Geophysical Research, 88*, 1153-1172.

DeCelles, P., G. Gehrels, J. Quade, T. Ojha, P. Kapp, and B. Upreti (1998), Neogene foreland basin deposits, erosional unroofing, and the kinematic history of the Himalayan fold-thrust belt, western Nepal, *Geological Society of America Bulletin, 110*, 2-21.

DeCelles, P. G., G. E. Gehrels, J. Quade, B. LaReau, and M. Spurlin (2000), Tectonic implications of U-Pb zircon ages of the Himalayan orogenic belt in Nepal, *Science, 288*, 497-499.

DeCelles, P. G., D. M. Robinson, J. Quade, T. P. Ojha, C. N. Garzione, P. Copeland, and B. N. Upreti (2001), Stratigraphy, structure, and tectonic evolution of the Himalayan fold-thrust belt in western Nepal, *Tectonics, 20*, 487-509.

DeCelles, P. G., D. M. Robinson, and G. Zandt (2002), Implications of shortening in the Himalayan fold-thrust belt for uplift of the Tibetan Plateau, *Tectonics, 21*, doi:10.1029/2001TC001322.

Deniel, C., P. Vidal, A. Fernandez, P. LeFort, and J. -P. Peucat (1987), Isotopic study of the Manaslu granite (Himalaya, Nepal): inferences on the age and source of Himalayan leucogranites, *Contributions to Mineralogy and Petrology, 96*, 78-92.

Dodson, M. H. (1973), Closure temperature in cooling geochronological and petrological systems, *Contributions to Mineralogy and Petrology, 40*, 259-274.

Elliot, D. (1976), The motion of thrust sheets, *Journal of Geophysical Research, 81*, 949-963.

Ferry, J. and F. Spear (1978), Experimental calibration of partitioning of Fe and Mg between biotite and garnet, *Contributions to Mineralogy and Petrology, 66*, 113-117.

Fielding, E., B. Isacks, M. Barazangi, and M. Duncan (1994), How flat is Tibet?, *Geology, 22*, 163-167.

Fraser, G., B. Worley, and M. Sandiford (2000), High-precision geothermobarometry across the High Himalayan metamorphic sequence, Langtang Valley, Nepal, *Journal of Metamorphic Geology, 18*, 665-681.

Fuchs, G. (1964), Beitrag zur Kenntnis des Palaozoikums und Mesozoikums der tibetischen Zone in Dolpo (Nepal Himalaja), *Sonderabdruck aus den Verhandlungen der Geologischen Bundesanstalt, 1*, 6-9.

Fuchs, G. (1967), Zum Bau des Himalaya. The structure of the Himalayas, *Denkschriften - Osterreichische Akademie der Wissenschaften, Mathematisch-Naturwissenschaftliche Klasse, 113*, 211.

Gansser, A. (1964), *Geology of the Himalayas*, 289 pp., John Wiley and Sons, London.

Garzanti, E. (1999), Stratigraphy and sedimentary history of the Nepal Tethys Himalaya passive margin, *Journal of Asian Earth Sciences, 17*, 805-827.

Gehrels, G. E., P. G. DeCelles, A. Martin, T. P. Ojha, G. Pinhassi, and B. N. Upreti (2003), Initiation of the Himalayan orogen as an Early Paleozoic thin-skinned thrust belt, *GSA Today, 13*, 4-9.

Gleeson, T. and L. Godin (2006), The Chako antiform: A folded segment of the Greater Himalayan sequence, Nar valley, Central Nepal Himalaya, *Journal of Asian Earth Sciences, 27*, 717-734.

Godin, L., R. Brown, S. Hanmer, and R. Parrish (1999a), Back folds in the core of the Himalayan orogen: An alternative interpretation, *Geology, 27*, 151-154.

Godin, L., R. L. Brown, and S. Hanmer (1999b), High strain zone in the hanging wall of the Annapurna detachment, central Nepal Himalaya, in *Himalaya and Tibet: Mountain Roots to Mountain Tops*, edited by A. M. Macfarlane, R. Sorkhabi, and J. Quade, Geological Society of America, Special Paper 328, 199-210.

Godin, L., R. R. Parrish, R. L. Brown, and K. Hodges (2001), Crustal thickening leading to exhumation of the metamorphic core of the central Nepal Himalaya: Insight from U-Pb geochronology and $^{40}Ar/^{39}Ar$ thermochronology, *Tectonics, 20*, 729-747.

Godin, L. (2003), Structural evolution of the Tethyan sedimentary sequence in the Annapurna area, central Nepal Himalaya, *Journal of Asian Earth Sciences, 22*, 307-328.

Godin, L., D. Grujic, R. D. Law, and M. P. Searle (2006a), Channel flow, ductile extrusion and exhumation in continental collision zones: An introduction, in *Channel Flow, Ductile Extrusion and Exhumation in Continental Collision Zones*, edited by R. D. Law, M. P. Searle, and L. Godin, Geological Society, London, Special Publication 268, 1-23.

Godin, L., T. Gleeson, M. P. Searle, T. D. Ullrich, and R. Parrish (2006b), Locking of southward extrusion in favour of rapid crustal-scale buckling of the Greater Himalayan sequence, Nar valley, central Nepal, in *Channel Flow, Ductile Extrusion and Exhumation in Continental Collision Zones*, edited by R. D. Law, M. P. Searle, and L. Godin, Geological Society, London, Special Publication 268, 269-292.

Godin, L., D. Kellett, and K. P. Larson (2007), Orogenic superstructure behaviour and mid-plastic flow in the central Nepal Himalaya, *EOS Transactions AGU, 88*, Fall meeting Supplement, Abstract T31D-0672.

Goscombe, B., D. Gray, and M. Hand (2006), Crustal architecture of the Himalayan metamorphic front in eastern Nepal*, Gondwana Research, 10*, 232-255.

Grasemann, B., H. Fritz, and J. Vannay (1999), Quantitative kinematic flow analysis from the Main Central Thrust Zone (NW-Himalaya, India): implications for a decelerating strain path and the extrusion of orogenic wedges*, Journal of Structural Geology, 21*, 837-853.

Green, O. R., M. P. Searle, R. I. Corfield, R. M. Corfield (2008), Cretaceous-Tertiary Carbonate Platform Evolution and the Age of the India-Asia Collision along the Ladakh Himalaya (Northwest India). *Journal of Geology, 116 (4),* 331-353.

Grove, M. and M. Harrison (1996), $^{40}$Ar* diffusion in Fe-rich biotite*, American Mineralogist, 81,* 940-951.

Grujic, D. (2006), Channel flow and continental collision tectonics: an overview, in *Channel Flow, Ductile Extrusion and Exhumation in Continental Collision Zones*, edited by R. D. Law, M. P. Searle, and L. Godin, Geological Society, London, Special Publication 268, 25-37.

Grujic, D., M. Casey, C. Davidson, L. S. Hollister, R. Kundig, T. Pavlis, and S. Schmid (1996), Ductile extrusion of the Higher Himalayan Crystalline in Bhutan: evidence from quartz

microfabrics, *Tectonophysics, 260*, 21-43.

Grujic, D., L. S. Hollister, and R. R. Parrish (2002), Himalayan metamorphic sequence as an orogenic channel: insight from Bhutan, *Earth and Planetary Science Letters, 198*, 177-191.

Guillot, S., K. V. Hodges, P. LeFort, and A. Pêcher (1994), New constraints on the age of the Manaslu leucogranite: evidence for episodic tectonic denudation in the central Himalayas, *Geology, 22*, 559-562.

Guillot, S., P. L. Fort, A. Pêcher, M. Barman, and J. Aprahamian (1995), Contact metamorphism and depth of emplacement of the Manaslu granite (central Nepal). Implications for Himalayan orogenesis, *Tectonophysics, 241*, 99-119.

Guitang, P., D. Jun, Y. Dongsheng, and W. Liquan (2004), Geological Map of the Qinghai–Xizang (Tibet) Plateau and Adjacent Areas, *1:1,500,000*.

Hames, W. and S. Bowring (1994), An empirical evaluation o the argon diffusion geometry in muscovite, *Earth and Planetary Science Letters, 124*, 161-167.

Harris, N. (2007), Channel flow and the Himalayan-Tibetan Orogen; a critical review, *Journal of the Geological Society, London, 164*, 511-523.

Harris, N. and J. Massey (1994), Decompression and anatexis of Himalayan metapelites, *Tectonics, 13*, 1537-1546.

Harris, N., M. Caddick, J. Kosler, S. Goswami, D. Vance, and A. G. Tindle (2004), The pressure-temperature-time path of migmatites from the Sikkim Himalaya, *Journal of Metamorphic Geology, 22*, 249-264.

Harrison, T. M., K. D. McKeegan, and P. LeFort (1995), Detection of inherited monazite in the Manaslu leucogranite by $^{208}Pb/^{232}Th$ ion microprobe dating; crystallization age and tectonic implications, *Earth and Planetary Science Letters, 133*, 271-282.

Harrison, M., F. J. Ryerson, P. L. Fort, A. Yin, O. Lovera, and E. Catlos (1997), A late Miocene-Pliocene origin for the Central Himalayan inverted metamorphism, *Earth and Planetary Science Letters, 146*, E1-E7.

Harrison, T. M., M. Grove, K. D. McKeegan, C. D. Coath, O. M. Lovera, and P. LeFort (1999), Origin and episodic emplacement of the Manaslu intrusive complex, central Himalaya, *Journal of Petrology, 40*, 3-19.

Hashimoto, S. (1973), Buri Gandaki region, in *Geology of the Nepal Himalayas*, edited by Yoshihide Ohta and Chikara Akiba, pp. 147-157, Saikon Publishing Co., Sapporo, Japan.

Hauck, M. L., K. D. Nelson, L. D. Brown, W. Zhao, and A. R. Ross (1998), Crustal structure of the Himalayan orogen at ~90° east longitude from Project INDEPTH deep reflection profiles, *Tectonics, 17*, 481-500.

Hetényi, G. (2007), *Evolution of deformation of the Himalayan prism: from imaging to modeling*, 2007, 400 pp., Ph.D. Thesis, l'Université Paris.

Heim, A. and A. Gansser (1939), *Central Himalayas: Geological Observations of the Swiss Expedition, 1936*, 245 pp., Memoir Society Helvetica Science.

Hirth, G. and J. Tullis (1992), Dislocation creep regimes in quartz aggregates, *Journal of Structural Geology, 14*, 145-159.

Hodges, K. V. (2000), Tectonics of the Himalaya and southern Tibet from two perspectives, *Geological Society of America Bulletin, 112*, 324-350.

Hodges, K. (2006), A synthesis of the Channel Flow-Extrusion hypothesis as developed for the Himalayan-Tibetan system, in *Channel Flow, Ductile Extrusion and Exhumation in Continental Collision Zones*, edited by R. D. Law, M. P. Searle, and L. Godin, Geological Society, London, Special Publication 268, 71-90.

Hodges, K. V., M. S. Hubbard, and D. S. Silverberg (1988), Metamorphic constraints on the thermal evolution of the central Himalayan orogen, *Philosophical Transactions of the Royal Society of London. Series A, Mathematical and Physical Sciences, 326*, 257-277.

Hodges, K. V., P. LeFort, and A. Pêcher (1988), Possible thermal buffering by crustal anatexis in collisional orogens: thermobarometric evidence from the Nepalese Himalaya, *Geology, 16*, 707-710.

Hodges, K. V., R. R. Parrish, T. B. Housh, D. R. Lux, B. C. Burchfiel, L. H. Royden, and Z. Chen (1992), Simultaneous Miocene extension and shortening in the Himalayan orogen, *Science, 258*, 1466-1470.

Hodges, K. V., R. R. Parrish, and M. P. Searle (1996), Tectonic evolution of the central Annapurna Range, Nepalese Himalayas, *Tectonics, 15*, 1264-1291.

Hodges, K. V., S. Bowring, K. Davidek, D. Hawkins, and M. Krol (1998), Evidence for rapid displacement of Himalayan normal faults and the importance of tectonic denudation in the evolution of mountain ranges, *Geology, 26*, 483-486.

Holdaway, M. (2000), Application of new experimental and garnet Margules data to the garnet-biotite geothermometer, *American Mineralogist, 85*, 881-892.

Holdaway, M. (2001), Recalibration of the GASP geobarometer in light of recent garnet and plagioclase activity models and versions of the garnet-biotite geothermometer, *American Mineralogist, 86*, 1117-1129.

Hubbard, M. S. (1989), Thermobarometric constraints on the thermal history of the Main Central Thrust Zone and the Tibetan Slab, eastern Nepal Himalaya, *Journal of Metamorphic Geology, 7*, 19-30.

Hubbard, M. S. and T. M. Harrison (1989), $^{40}Ar/^{39}Ar$ age constraints on deformation and metamorphism in the Main Central Thrust Zone and Tibetan Slab, eastern Nepal Himalaya, *Tectonics, 8*, 865-880.

Hubbard, M. S. (1996), Ductile shear as a cause of inverted metamorphism: example from the Nepal Himalaya, *Journal of Geology, 104*, 493-499.

Jamieson, R. A., C. Beaumont, S. Medvedev, and M. H. Nguyen (2004), Crustal channel flow: 2. Numerical models with implications for metamorphism in the Himalayan-Tibetan orogen, *Journal of Geophysical Research, 109*, doi: 10.1029/2003JB002811.

Jamieson, R., C. Beaumont, M. Nguyen, and D. Gruijic (2006), Provenance of the Greater Himalayan Sequence and associated rocks: predictions of channel flow models.

Jessup, M. J., R. D. Law, M. P. Searle, and M. S. Hubbard (2006), Structural evolution and vorticity of flow during extrusion and exhumation of the greater himalayan slab, mount everest massif, Tibet/Nepal: Implications for orogen-scale flow partitioning, in *Channel Flow, Ductile Extrusion and Exhumation in Continental Collision Zones*, edited by R. D. Law, M. P. Searle, and L. Godin, Geological Society, London, Special Publication 268, 379-413.

Jessup, M. J., R. D. Law, and C. Frassi (2007), The Rigid Grain Net (RGN): An alternative method for estimating mean kinematic vorticity number ($W_m$), *Journal of Structural Geology, 29*, 411-421.

Jimenez-Munt, I., M. Fernandez, J. Verges, and J. Platt (2008), Lithosphere structure underneath the Tibetan Plateau inferred from elevation, gravity and geoid anomalies, *Earth and Planetary Science Letters, 267*, 276-289.

Kanagawa, K. (1992), MacStrain, *2.4*. computer program.

Kanizay, S. P. (1962), Mohr's Theory of Strength and Prandtl's Compressed Cell in Relation to Vertical Tectonics, *414–B*, 1-16.

Kawakami, T., M. Aoya, S. R. Wallis, J. Lee, K. Terada, Y. Wang, and M. Heizler (2007), Contact metamorphism in the Malashan dome, North Himalayan gneiss domes, southern Tibet: an example of shallow extensional tectonics in the Tethys Himalaya, *Journal of Metamorphic Geology, 25*, 831-853.

Kellett, D. A.-M. and L. Godin (2009), Pre-Miocene deformation of the Himalayan superstructure, Hidden Valley, central Nepal, *Journal of the Geological Society, London, 166,* 261-274, doi:10.1144/0016-76492008-097.

King, J., N. Harris, T. Argles, R. Parrish, B. Charlier, S. Sherlock, and H. F. Zhang (2007), First field evidence of southward ductile flow of Asian crust beneath southern Tibet, *Geology, 35*, 727-730.

Kohn, M. J. (2008), P-T-t data from central Nepal support critical taper and repudiate large-scale channel flow of the Greater Himalayan Sequence, *Geological Society of America Bulletin, 120*, 259-273.

Kohn, M. J. and F. Spear (2000), Retrograde net transfer reaction insurance for pressure-temperature estimates, *Geology, 28*, 1127-1130.

Kohn, M. J., E. J. Catlos, F. J. Ryerson, and T. M. Harrison (2001), Pressure-temperature-time path discontinuity in the Main Central thrust zone, central Nepal, *Geology, 29*, 571-574.

Kohn, M. J., M. S. Wieland, C. D. Parkinson, and B. N. Upreti (2005), Five generations of monazite in Langtang gneisses; implications for chronology of the Himalayan metamorphic core, *Journal of Metamorphic Geology, 23*, 399-406.

Krogh, T. E. (1973), A low contamination method for hydrothermal decomposition of zircon and extraction of U and Pb for isotopic age determinations, *Geochimica et Cosmochimica Acta, 37*, 485-494.

Krogh, T. E. (1982), Improved accuracy of U-Pb ages by the creation of more concordant systems using an air abrasion technique, *Geochimica et Cosmochimica Acta, 46*, 637-649.

Kruhl, J. H. (1998), Reply: Prism- and basal-plane parallel subgrain boundaries in quartz: a microstructural geothermabarometer, *Journal of Metamorphic Petrology, 16*, 142-146.

Larson, K. P. and L. Godin (2009), Kinematics of the Greater Himalayan sequence, Dhaulagiri Himal: implications for the structural framework of central Nepal, *Journal of the Geological Society, London, 166*, 25-43.

Larson, K. P., L. Godin, W. J. Davis, and D. W. Davis (submitted, September 2008), Out-of-sequence deformation and expansion of the Himalayan orogenic wedge: insight from the Changgo culmination, south-central Tibet, *Tectonics*.

Law, R. D., S. S. Morgan, M. Casey, A. G. Sylvester, and M. Nyman (1992), The Papoose Flat pluton of eastern California: a re-assessment of its emplacement history in the light of new microstructural and crystallographic fabric observations, *Transactions of the Royal Society of Edinburgh: Earth Sciences, 83*, 361-375.

Law, R. D., M. P. Searle, and R. L. Simpson (2004), Strain, deformation temperatures and vorticity of flow at the top of the Greater Himalayan Slab, Everest Massif, Tibet, *Journal of the*

*Geological Society, London, 161*, 305-320.

Law, R. D., M. P. Searle, and L. Godin (Eds.) (2006)*, Channel Flow, Ductile Extrusion and Exhumation in Continental Collision Zones*, Special Publication 268, 620 pp., Geological Society, London.

Lee, J., B. R. Hacker, W. S. Dinkage, Y. Wang, P. Gans, A. Calvert, J. Wan, W. Chen, A. E. Blythe, and W. McClelland (2000), Evolution of the Kangmar Dome, southern Tibet: Structural, petrologic, and thermochronologic constraints*, Tectonics, 19*, 872-895.

Lee, J., B. R. Hacker, and Y. Wang (2004), Evolution of North Himlayan gneiss domes: structural and metamorphic studies in Mabja Dome, southern Tibet*, Journal of Structural Geology, 26*, 2297-2316.

Lee, J., W. McClelland, Y. Wang, A. E. Blythe, and M. O. McWilliams (2006), Oligocene—Miocene middle crustal flow in southern tibet: Geochronology of mabja dome, in *Channel Flow, Ductile Extrusion and Exhumation in Continental Collisional Zones*, edited by Richard D. Law, Michael P. Searle, and Laurent Godin, Geological Society, London, Special Publication 268, pp. 445-469.

Lee, J. and M. J. Whitehouse (2007), Onset of mid-crustal extensional flow in southern Tibet: Evidence from U/Pb zircon ages*, Geology, 35*, 45-48.

LeFort, P. (1975), Himalayas, the collided range: present knowledge of the continental arc, *American Journal of Science, 275*, 1-44.

LeFort, P. (1986), Metamorphism and magmatism during the Himalayan collision, in *Collision Tectonics*, edited by M. P. and Ries Coward A.C., Geological Society, London, Special Publication 19, 159-172.

LeFort, P., A. Pêcher, and B. N. Upreti (1986), A section through the Tibetan Slab in central Nepal (Kali Gandaki valley): mineral chemistry and thermobarometry of the Main Central thrust zone*, Science de la Terre, Mémoire 47*, 211-228.

LeFort, P., M. Cuney, C. Deniel, C. France-Lanord, S. M. F. Sheppard, B. N. Upreti, and P. Vidal

(1987), Crustal generation of the Himalayan leucogranites, *Tectonophysics, 134*, 39-57.

Lisle, R. J. (1985), *Geological Strain Analysis; a Manual for the Rf/phi Technique*, Pergamon Press, Oxford, United Kingdom (GBR), United Kingdom (GBR).

Lister, G. (1977), Crossed-girdle *c*-axis fabrics in quartzites plastically deformed by plane strain and progressive simple shear, *Tectonophysics, 39*, 51-54.

Lister, G. S. and B. E. Hobbs (1980), The simulation of fabric development during plastic deformation and its application to quartzite; the influence of deformation history, *Journal of Structural Geology, 2*, 355-370.

Lister, G. S. and U. F. Dornsiepen (1982), Fabric transitions in the Saxony granulite terrain, *Journal of Structural Geology, 4*, 81-93.

Liu, G. and G. Einsele (1994), Sedimentary history of the Tethyan basin in the Tibetan Himalayas, *Geol Rundsch, 83*, 32-61.

Ludwig, K. R. (2003), *User's Manual for Isoplot 3.00a Geochronological Toolkit for Excel*, Berkeley Geochronological Center Special Publication 4, 71 pp.

Macfarlane, A. M. (1995), An evaluation of the inverted metamorphic gradient at Langtang National Park, Central Nepal Himalaya, *Journal of Metamorphic Geology, 13*, 595-612.

Martin, A., G. Gehrels, and P. DeCelles (2007), The tectonic significance of (U, Th)/Pb ages of monazite inclusions in garnet from the Himalaya of central Nepal, *Chemical Geology, 244,* 1-24.

Martin, A. J., P. G. DeCelles, G. E. Gehrels, P. J. Patchett, and C. Isachsen (2005), Isotopic and structural constraints on the location of the Main Central thrust in the Annapurna Range, central Nepal Himalaya, *Geological Society of America Bulletin, 117*, 926-944.

Matthews, W. and W. J. Davis (1999), A practical image analysis technique for estimating the weight of abraded mineral fractions used in U-pb dating, *Radiogenic Age and Isotopic Studies: Report 12*, pp. 1-7, Geological Survey of Canada, Current Research 1999-F.

McQuarrie, N., D. Robinson, S. Long, T. Tobgay, D. Grujic, G. Gehrels, M. Ducea (2008),

Preliminary stratigraphic and structural architecture of Bhutan: implications for the along strike architecture of the Himalayan system, *Earth and Planetary Science letters, 272,* 105-117.

Meigs, A. J., D. W. Burbank, and R. A. Beck (1995), Middle-late Miocene (>10Ma) formation of the Main Boundary thrust in the western Himalaya*, Geology, 23*, 423-426.

Nadai, A. (1952)*, Theory of Fracture and Flow in Solids*, vol. 1, 572 pp., McGraw-Hill, New York.

Nazarchuk, J. H. (1993), Structure and geochronology of the Greater Himalaya, Kali Gandaki region, west-central Nepal, Carleton University.

Nelson, K. D. et al. (1996), Partially molten middle crust beneath southern Tibet: Synthesis of project INDEPTH results*, Science, 274*, 1684-1688.

Nye, J. F. (1951), The flow of glaciers and ice-sheets as a problem in plasticity*, Proceedings of the Royal Society, London, Series A, 207*, 554-572.

Nye, J. F. (1952), The mechanics of glacier flow*, Journal of Glaciology, 2*, 82-93.

Pande, I. C. (1950), A geological note on the Ramgarh area, Dist. Nainital (U. P.)*, Quarterly Journal of the Geological, Mining and Metallurgical Society of India, 22*, 15-23.

Parrish, R. R. and K. V. Hodges (1996), Isotopic constraints on the age and provenance of the Lesser and Greater Himalayan sequences, Nepalese Himalaya*, Geological Society of America Bulletin, 108*, 904-911.

Passchier, C. W. (1987), Stable positions of rigid objects in non-coaxial flow; a study in vorticity analysis; Shear criteria in rocks*, Journal of Structural Geology, 9*, 679-690.

Passchier, C. W. and R. Trouw A.J. (2005)*, Microtectonics*, 2nd ed., 366 pp., Springer.

Patterson, W. S. B. (2000), Physics of Glaciers - 3rd edition, Butterworth-Heinemann, Oxford, 481p.

Paudel, L. P. and K. Arita (2000), Tectonic and polymetamorphic history of the Lesser Himalaya in central Nepal*, Journal of Asian Earth Sciences, 18*, 561-584.

Pearson, O. N. and P. G. DeCelles (2005), Structural geology and regional tectonic significance of the Ramgarh thrust, Himalayan fold-thrust belt of Nepal*, Tectonics, 24*, 1-26.

Pêcher, A. (1978), *Déformation et métamorphisme associés à une zone de cisaillement: exemple du grand chevauchement central Himalayen (MCT)*, 354 pp., Université de Grenoble, France.

Pêcher, A. (1989), The metamorphism in the Central Himalaya*, Journal of Metamorphic Geology, 7*, 31-41.

Pêcher, A. and P. Le Fort (1977), Origin and significance of the Lesser Himalayan augen gneisses, in *Ecologie et Géologie De l'Himalaya*, 268, pp. 319-329, Sèvres, Paris.

Platt, J. (1986), Dynamics of orogenic wedges and the uplift of high-pressure metamorphic rocks, *Geological Society of America Bulletin, 97*, 1037-1053.

Platt, J. and J. Behrmann (1986), Structures and fabrics in a crustal-scale shear zone, Betic Cordillera, SE Spain*, Journal of Structural Geology, 8*, 15-33.

Prandtl, L. , Spannungsverteilung in plastischen Korpern*, First International Congress on Applied Mechanics, Delft*, 54.

Price, R. A. (1972), The Distinction Between Displacement and Distortion in Flow, and the Origin of Diachronism in Tectonic Overprinting in Orogenic Belts*, Section 3 International Geological Congress, 24*, 545-551.

Price, R. A. (1988), The mechanical paradox of large overthrusts*, Geological Society of America Bulletin, 100*, 1898-1908.

Quigley, M., Y. Liangjun, L. Xiaohan, C. J. L. Wilson, M. Sandiford, and D. Phillips (2006), $^{40}Ar/^{39}Ar$ thermochronology of the Kampa Dome, southern Tibet: Implications for tectonic evolution of the North Himalayan gneiss domes*, Tectonophysics, 421*, 297.

Quigley, M. C., Y. Liangjun, C. Gregory, A. Corvino, M. Sandiford, C. J. L. Wilson, and L. Xiaohan (2008), U-Pb SHRIMP zircon geochronology*, Tectonophysics, 446*, 97-113.

Ramsay, J. G. and M. I. Huber (1983)*, The Techniques of Modern Structural Geology, 1: Strain*

*Analysis*, Academic Press, London.

Richards, A., T. Argles, N. Harris, R. Parrish, T. Ahmad, G. Darbyshire, E. Draganits (2005), Himalayan architecture constrained by isotopic tracers from clastic sediments, *Earth and Planetary Science Letters, 236,* 773-796.

Richards, A., R. Parrish, N. Harris, T. Argles, L. Zhang (2006), Correlation of lithotectonic units across the eastern Himalaya, Bhutan, *Geology, 34,* 341-344.

Robinson, D. M. (2008), Forward modeling the kinematic sequence of the central Himalayan thrust belt, western Nepal, *Geosphere, 4,* 785-801.

Robinson, D. M., P. G. DeCelles, C. N. Garzione, O. N. Pearson, T. M. Harrison, and E. J. Catlos (2001), The kinematic evolution of the Nepalese Himalaya interpreted from Nd isotopes*, Earth and Planetary Science Letters, 192*, 507-521.

Robinson, D. M., P. G. DeCelles, C. N. Garzione, O. N. Pearson, T. M. Harrison, and E. J. Catlos (2003), Kinematic model for the Main Central thrust in Nepal*, Geology, 31*, 359-362.

Robinson, D. M., P. G. DeCelles, and P. Copeland (2006), Tectonic evolution of the Himalayan thrust belt in western Nepal: implications for channel flow models*, Geological Society of America Bulletin, 118*, 865-885.

Robinson, D. M. and O. N. Pearson (2006), Exhumation of Greater Himalayan rock along the Main Central Thrust in Nepal: implications for channel flow, in *Channel Flow, Ductile Extrusion and Exhumation in Continental Collisional Zones*, edited by Richard D. Law, Michael P. Searle, and Laurent Godin, Geological Society, London, Special Publication 268, pp. 255-267.

Schärer, U. (1984), The effect of initial $^{230}$Th disequilibrium on young U-Pb ages: the Makalu case, Himalaya*, Earth and Planetary Science Letters, 67*, 191-204.

Schärer, U., R. -. Xu, and C. J. Allègre (1986), U-(Th)-Pb systematics and ages of Himalayan leucogranites, South Tibet*, Earth and Planetary Science Letters, 77*, 35-48.

Schelling, D. D. (1992), The tectonostratigraphy and structure of the eastern Nepal Himalaya*, Tectonics, 11*, 925-943.

Schmid, S. M. and M. Casey (1986), Complete fabric analysis of some commonly observed quartz *c*-axis patterns; Mineral and rock deformation; laboratory studies; the Paterson volume, *Geophysical Monograph, 36*, 263-286.

Schmitz, M. D. and S. A. Bowring (2001), U-Pb zircon and titanite systematics of the Fish Canyon Tuff: an assessment of high-precision U-Pb geochronology and its application to young volcanic rocks, *Geochimica et Cosmochimica Acta, 65*, 2571-2587.

Searle, M. P. and A. Rex (1987), Thermal model for the Zanskar Himalaya, *Journal of Metamorphic Geology*, 7, 127-134.

Searle, M. P. (1999), Extensional and compressional faults in the Everest-Lhotse massif, Khumbu Himalaya, Nepal, *Journal of the Geological Society of London, 156*, 27-240.

Searle, M. P., B. F. Windley, M. P. Coward, D. J. W. Cooper, A. J. Rex, D. Rex, T. Li, X. Xiao, M. Q. Jan, V. C. Thakur, (1987), The closing of Tethys and the tectonics of the Himalaya, *Geological Society of America Bulletin, 98*, 678-701.

Searle, M. P. and L. Godin (2003), The South Tibetan detachment system and the Manaslu leucogranite: a structural reinterpretation and restoration of the Annapurna - Manaslu Himalaya, Nepal, *Journal of Geology, 111*, 505-524.

Searle, M. P., R. L. Simpson, R. D. Law, R. R. Parrish, and D. J. Waters (2003), The structural geometry, metamorphic and magmatic evolution of the Everest massif, High Himalaya of Nepal-South Tibet, *Journal of the Geological Society, London, 160*, 345-366.

Searle, M. P. and A. G. Szulc (2005), Channel flow and ductile extrusion of the high Himalayan slab-the Kanchenjunga-Darjeeling profile, Sikkim Himalaya, *Journal of Asian Earth Sciences, 25*, 173-185.

Searle, M. P., R. D. Law, and M. J. Jessup (2006), Crustal structure, restoration and evolution of the Greater Himalaya in Nepal-South tibet: Implications for channel flow and ductile extrusion of the middle crust, in *Channel Flow, Ductile Extrusion and Exhumation in Continental Collision Zones*, edited by R. D. Law, M. P. Searle, and L. Godin, Geological Society, London, Special Publication 268, 355-378.

Searle, M. P., R. Law, L. Godin, K. P. Larson, M. J. Streule, J. Cottle, and M. Jessup (2008), Defining the Himalayan Main Central Thrust in Nepal, *Journal of the Geological Society, 165*, 523-534.

Shimamoto, T. and Y. Ikeda (1976), A simple algebraic method for strain estimation from deformed ellipsoidal objects; 1, Basic theory, *Tectonophysics, 36*, 315-337.

Shrestha, S. B., J. N. Shrestha, and S. R. Sharma (1987), Geological map of far western Nepal, *1:250,000*, 1.

Simpson, C. and D. G. De Paor (1993), Strain and kinematic analysis in general shear zones, *Journal of Structural Geology, 15*, 1-20.

Simpson, C. and D. G. De Paor (1997), Practical analysis of general shear zones using the porphyroclast hyperbolic distribution method: An example from the scandinavian caledonides, in *Evolution of Geological Structures in Micro- to Macro- Scales*, edited by S. Segupta, pp. 169-184.

Srivastava, P. and G. Mistra (1994), Thrust geometries and deep structure of the outer and Lesser Himalaya, Kumaon and Garhwal (India): implications for evolution of the Himalayan fold-and-thrust belt, *Tectonics, 13*, 89-109.

Srivastava, P. and G. Mitra (1996), Deformation mechanisms and inverted thermal profile in the North Almora Thrust mylonite zone, Kumaon Lesser Himalaya, India, *Journal of Structural Geology, 18*, 27-39.

Stern, R. A. (1997), The GSC Sensitive High Resolution Ion Microprobe (SHRIMP): analytical techniques and performance evaluation, current research, *Radiogenic Age and Isotope Studies: Report 10*, pp. 1-31, Geological Survey of Canada, Ottawa.

Stern, R. and Y. Amelin (2003), Assessment of errors in SIMS zircon U-Pb geochronology using a natural zircon standard and NIST SRM 610 glass, *Chemical Geology, 197*, 111-142.

Stocklin, J. (1980), Geology of Nepal and its regional frame, *Journal of the Geological Society of London, 137*, 1-34.

Suppe, J. (2007), Absolute fault and crustal strength from wedge tapers, *Geology, 35*, 1127-1120.

Tullis, J., J. M. Christie, and D. T. Griggs (1973), Microstructures and Preferred Orientations of Experimentally Deformed Quartzites, *Geological Society of America Bulletin, 84*, 297-314.

Upreti, B. N. (1996), Stratigraphy of the western Nepal Lesser Himalaya; a synthesis, *Journal of Nepal Geological Society, 13*, 11-28.

Valdiya, K. S. (1980), *Geology of the Kumaon Lesser Himalaya*, 291 pp., Wadia Institute of Himalayan Geology, Dehra Dun, India.

Vannay, J. and K. V. Hodges (1996), Tectonometamorphic evolution of the Himalayan metamorphic core between the Annapurna and Dhaulagiri, central Nepal, *Journal of Metamorphic Geology, 14*, 635-656.

Vannay, J. and B. Grasemann (2001), Himalayan inverted metamorphism and syn-convergence extension as a consequence of a general shear extrusion, *Geological Magazine, 138*, 253-276.

Wallis, S. (1992), Vorticity analyasis in a metachert from the Sanbagawa Belt, SW Japan, *Journal of Structural Geology, 14*, 271-280.

Wallis, S. (1995), Vorticity analysis and recognition of ductile extension in the Sanbagawa belt, SW Japan, *Journal of Structural Geology, 17*, 1077-1093.

Wallis, S. R., J. P. Platt, and S. D. Knott (1993), Recognition of syn-convergence extension in accretionary wedges with examples from the Calabrian Arc and the Eastern Alps, *American Journal of Science, 293*, 463-494.

Watts, D. R., N. B. W. Harris, and The 2002 NASA GLENN SOARS Working Group (2005), Mapping granite and gneiss in domes along the North Himalayan antiform with ASTER SWIR band ratios, *Geological Society of America Bulletin, 117*, 879-886.

Webb, A. A. G., A. Yin, M. Harrison, J. Celerier, and W. Burgess (2007), The leading edge of the Greater Himalayan Crystalline complex revealed in the NW Indian Himalaya: Implications for the evolution of the Himalayan orogen, *Geology, 35*, 955-958.

White, J. C., D. C. Copeland, M. R. St-Onge, N. Wodijka, and D. J. Scott (2004), Channel flow in the paleoproterozic: the kinematics of cratonic collision and exhumation, SW Baffin Island,

Canada, Channel flow, ductile extrusion and exhumation of lower-mid crust in continental collision zones, London, December 6-7, 2004.

Williams, I. S. (1998), U-Th-Pb geochronology by ion microprobe, in *Applications of Microanalytical Techniques to Understanding Mineralizing Processes*, vol. 7, edited by M. A. McKibben, W. C. Shanks III, and I. W. Ridley, pp. 1-35. Williams, I. S. and J. M. Hergt (2000), U–Pb dating of tasmanian dolerites: A cautionary tale of SHRIMP analysis of high-U zircon, in *Beyond 2000: New Frontiers in Isotope Geoscience, Lorne, 2000, Abstracts and Proceedings*, edited by J. D. Woodhead, J. M. Hergt, and W. P. Noble, pp. 185-188, Eastern Press, Victoria, Australia.

Williams, P. F. and D. Jiang (2005), An investigation of lower crustal deformation: Evidence for channel flow and its implications for tectonics and structural studies*, Journal of Structural Geology, 27*, 1486-1504.

Williams, P. F., D. Jiang, and S. Lin (2006), Interpretation of deformation fabrics of infrastructure zone rocks in the context of channel flow and other tectonic models, in *Channel Flow, Ductile Extrusion and Exhumation in Continental Collision Zones*, edited by R. D. Law, M. P. Searle, and L. Godin, Geological Society, London, Special Publication 268, 221-235.

Wobus, C. W., K. V. Hodges, and K. X. Whipple (2003), Has focused denudation sustained active thrusting at the Himalayan topographic front?*, Geology, 23*, 861-864.

Wobus, C., A. Heimsath, K. Whipple, and K. Hodges (2005), Active out-of-sequence thrust faulting in the central Nepalese Himalaya*, Nature, 434*, 1008-1011.

Wolters, J. (2006), *Remote sensing of gneiss domes and granite in southern Tibet*, 79 pp. Ohio State University.

Wu, C., J. Zhang, and L. Ren (2004a), Empirical garnet-biotite-plagioclase-quartz (GBPQ) geobarometry in medium- to high-grade metapelites*, Journal of Petrology, 45*, 1907-1921.

Wu, C., J. Zhang, and L. Ren (2004b), Empirical garnet-muscovite-plagioclase-quartz geobarometry in medium- to high-grade metapelites*, Lithos, 78*, 319-332.

Wu, C. and B. Cheng (2006), Valid garnet-biotite (GB) geothermometry and garnet-aluminum silicate-plagioclase-quartz (GASP) geobarometry in metapelitic rocks*, Lithos, 89*, 1-23.

Xypolias, P. and S. Kokkalas (2006), Heterogeneous ductile deformation along a mid-crustal extruding shear zone: an example from the \ldots*, Geological Society London Special Publications*.

Yardley, B. W. D. (1977), An empirical study of diffusion in garnet*, American Mineralogist, 62*, 793-800.

Yin, A. and T. M. Harrison (2000), Geologic evolution of the Himalayan-Tibetan orogen*, Annual Reviews in Earth and Planetary Science, 28*, 211-280.

Zhang, H., N. Harris, R. R. Parrish, S. Kelley, L. Zhang, N. Rogers, T. Argles, and J. King (2004), Causes and consequences of protracted melting of the mid-crust exposed in the North Himalayan antiform*, Earth and Planetary Science Letters, 228*, 195-212.

# Appendix A - Thermochronology Methods

Specimens and flux-monitors (standards) were wrapped in Al-foil and loaded into an 11.5 cm long and 2.0 cm diameter irradiation container, and then irradiated with fast neutrons in position 5C of the McMaster Nuclear Reactor (Hamilton, Ontario) for 9 hours. A group of flux monitors (7 in total) were located at approximately every 0.5 cm along the irradiation container and J-values for individual samples were determined by interpolation.

For total-fusion of monitors and step-heating of the unknowns, specimens were mounted in an aluminum sample-holder, beneath the sapphire view-port of a small stainless-steel chamber connected to an ultra-high vacuum purification system. An 8W Lexel continuous argon-ion laser was used for step-heating by de-focusing the laser beam to cover the entire sample and heating for approximately 3 minutes at increasing power settings. The evolved gas, after purification using an SAES C50 getter, was admitted to an on-line, MAP 216 mass spectrometer, with a Bäur Signer source and an electron multiplier (set to a gain of 100 over the Faraday), and analyzed in static mode. Blanks, measured routinely, were subtracted from the subsequent sample gas-fractions.

Measured argon-isotope peak heights were extrapolated to zero-time, normalized to the $^{40}Ar/^{39}Ar$ atmosphere ratio (295.5), and corrected for neutron-induced $^{40}Ar$ from potassium and $^{39}Ar$ and $^{36}Ar$ from calcium. Dates and errors were calculated using formulae given by Dalrymple et al. (1981), and the constants recommended by Steiger and Jäger (1977). Errors shown represent the analytical precision at $2\sigma$, assuming that the error in the J-value is zero. A conservative estimate of error in the J-value is 0.5% and can be added for inter-sample comparison. Intra-laboratory standard MAC-83 Biotite (24.36 Ma referenced to FCT sanidine at 28.02 Ma; Renne et al. 1998) was used as the monitor for laser step-heating analyses.

## References

Dalrymple, G. B., E. C. Alexander, Jr., M. A. Lanphere, and G. P. Kraker (1981), Irradiation of samples for $^{40}Ar/^{39}Ar$ dating using the Geological Survey TRIGA Reactor. *U.S. Geological Survey, Professional Paper 1176*.

Renne, P. R., C. C. Swisher, A. L. Deino, D. B. Karner, T. L. Owens, and D. J. DePaolo (1998),

Intercalibration of standards, absolute ages and uncertainties in $^{40}Ar/^{39}Ar$ dating, *Chemical Geology, 145*, 117-152.

Steiger, R. H., and E. Jäger (1977), Subcommission on geochronology: Conventional use of decay constants in geo- and cosmo- chronology. *Earth and Planetary Science Letters, 36*, 359-362.

# Appendix B - Changgo Culmination (Chapter 3) Thermochrology Data

## KL-4: KT-202 Mu HP

Run date: 2007/12/18 Can/Pos: 208/5 J Value: 0.003436
Printed: 2008/01/29 Mass: 0.0 mg ± 0.000010

Volume 39K: 9.56 x 1E-10 cm3 NTP Approx. % K
Integrated Age: 21.28 ± 0.17 Ma % Ca

Initial 40/36: 283.84 ± 43.86 (MSWD = 0.37, isochron between 0.55 and 1.89)
Correlation Age: 21.39 ± 0.39 Ma (100.0% of 39Ar, steps marked by >) MSWD 0.348

Plateau Age: 21.29 ± 0.16 Ma ( 99.7% of 39Ar, steps marked by <) Mod. err. 0.22

| Power | 36Ar/40Ar | 39Ar/40Ar | r | Ca/K | %40Atm | %39Ar | 40Ar*/39K | Age |
|---|---|---|---|---|---|---|---|---|
| 0.50 | 0.003083±0.000312 | 0.033655±0.000959 | 0.027 | 1.864 | 91.00 | 0.27 | 2.647±2.735 | 16.34±16.80 |
| < 1.00 | 0.002074 0.000349 | 0.116196 0.002246 | 0.011 | 1.522 | 61.07 | 0.76 | 3.332 0.892 | 20.54 5.46 |
| < 1.50 | 0.001515 0.000223 | 0.159356 0.001987 | 0.013 | 0.445 | 44.55 | 1.84 | 3.466 0.416 | 21.36 2.55 |
| < 2.00 | 0.000790 0.000075 | 0.219588 0.001324 | 0.008 | 0.060 | 23.19 | 8.04 | 3.491 0.103 | 21.51 0.63 |
| < 2.50 | 0.000460 0.000045 | 0.251827 0.001035 | 0.006 | 0.015 | 13.50 | 16.21 | 3.431 0.055 | 21.14 0.34 |
| < 3.00 | 0.000428 0.000055 | 0.253466 0.001373 | 0.009 | 0.011 | 12.55 | 11.58 | 3.446 0.068 | 21.24 0.41 |
| < 3.50 | 0.000458 0.000044 | 0.250416 0.001217 | 0.008 | 0.011 | 13.43 | 12.20 | 3.453 0.055 | 21.28 0.34 |
| < 4.00 | 0.000368 0.000041 | 0.259614 0.001448 | 0.007 | 0.008 | 10.79 | 13.29 | 3.433 0.051 | 21.16 0.31 |
| < 5.00 | 0.000284 0.000055 | 0.265232 0.001393 | 0.005 | 0.006 | 8.32 | 10.38 | 3.454 0.064 | 21.29 0.39 |
| < 6.00 | 0.000218 0.000074 | 0.268743 0.001990 | 0.004 | 0.003 | 6.40 | 6.81 | 3.481 0.086 | 21.45 0.53 |
| < 7.00 | 0.000165 0.000081 | 0.273452 0.001876 | 0.001 | 0.002 | 4.84 | 6.17 | 3.479 0.091 | 21.44 0.56 |
| < 7.00 | 0.000123 0.000043 | 0.277291 0.001299 | 0.002 | 0.001 | 3.61 | 12.45 | 3.475 0.049 | 21.41 0.30 |

| Power | 40Ar | 39Ar | 38Ar | 37Ar | 36Ar | Blank 40Ar | Atmos 40/36 |
|---|---|---|---|---|---|---|---|
| 0.50 | 0.795±0.006 | 0.026±0.001 | 0.001±0.000 | 0.009±0.001 | 0.003±0.000 | 0.033 | 287.137 |
| < 1.00 | 0.660 0.004 | 0.073 0.001 | 0.001 0.000 | 0.019 0.001 | 0.002 0.000 | 0.033 | 287.137 |
| < 1.50 | 1.144 0.006 | 0.178 0.002 | 0.003 0.000 | 0.014 0.001 | 0.002 0.000 | 0.033 | 287.137 |
| < 2.00 | 3.555 0.008 | 0.774 0.004 | 0.010 0.001 | 0.008 0.001 | 0.003 0.000 | 0.033 | 287.137 |
| < 2.50 | 6.235 0.010 | 1.561 0.006 | 0.020 0.001 | 0.005 0.001 | 0.003 0.000 | 0.033 | 287.137 |
| < 3.00 | 4.434 0.011 | 1.115 0.005 | 0.014 0.001 | 0.003 0.001 | 0.002 0.000 | 0.033 | 287.137 |
| < 3.50 | 4.727 0.009 | 1.175 0.005 | 0.015 0.001 | 0.003 0.001 | 0.003 0.000 | 0.033 | 287.137 |
| < 4.00 | 4.965 0.010 | 1.279 0.006 | 0.016 0.001 | 0.003 0.000 | 0.002 0.000 | 0.033 | 287.137 |
| < 5.00 | 3.806 0.009 | 1.000 0.005 | 0.013 0.001 | 0.002 0.000 | 0.001 0.000 | 0.033 | 287.137 |
| < 6.00 | 2.473 0.009 | 0.655 0.004 | 0.008 0.001 | 0.001 0.000 | 0.001 0.000 | 0.033 | 287.137 |
| < 7.00 | 2.207 0.007 | 0.594 0.003 | 0.008 0.001 | 0.001 0.000 | 0.001 0.000 | 0.033 | 287.137 |
| < 7.00 | 4.361 0.010 | 1.198 0.005 | 0.015 0.001 | 0.001 0.000 | 0.001 0.000 | 0.033 | 287.137 |

Measured volumes are x 1E-10 cm3 NTP. All errors are 2 x standard error. Intrim13 28-Mar-02

**KL-4: KT-202 Mu HP**

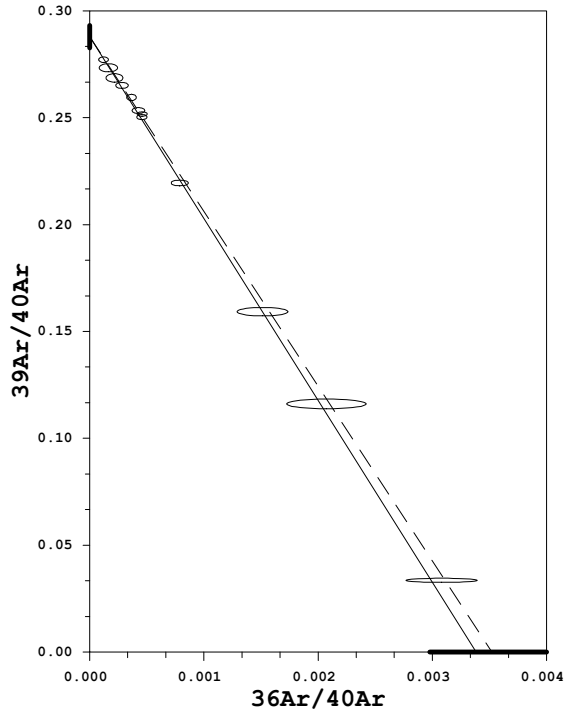


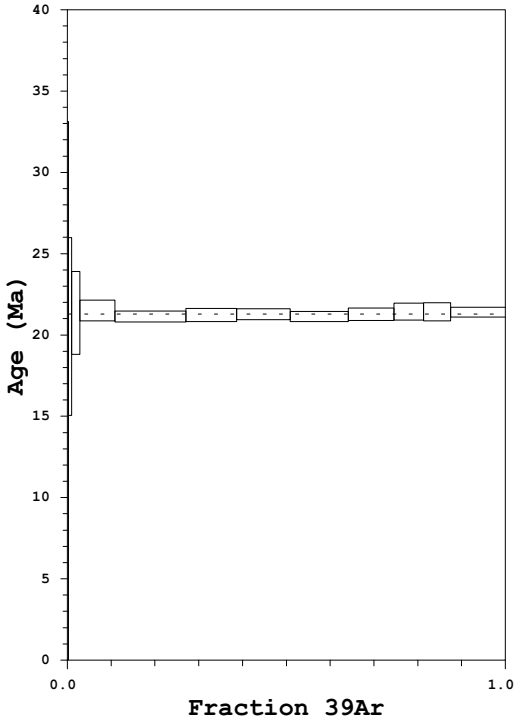


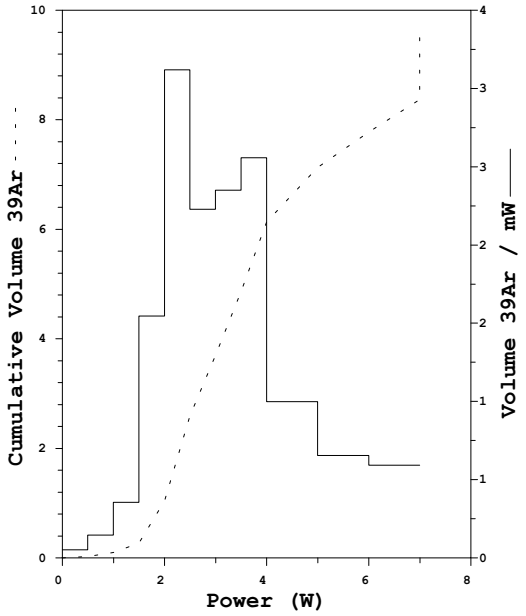


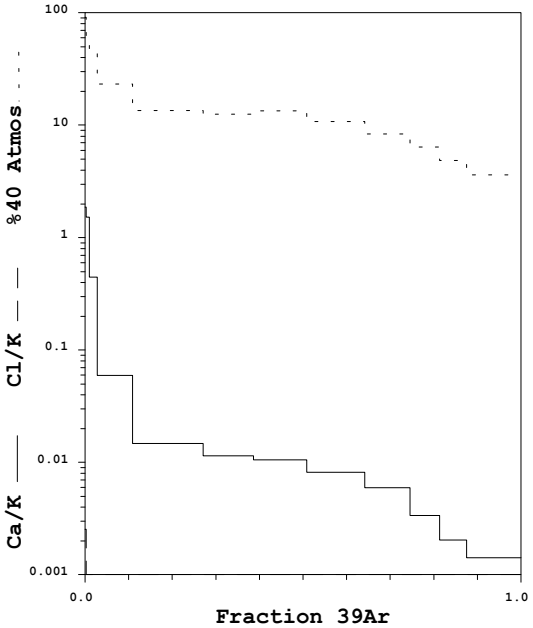


Measured volumes are x 1E-10 cm3 NTP. All errors are 2 x standard error. Intrim13 28-Mar-02

## KL-3: CH-122B Mu HP

**Run date:** 2007/12/17 **Can/Pos:** 208/4 **J Value:** 0.003435
**Printed:** 2008/01/29 **Mass:** 0.0 mg ± 0.000020

**Volume 39K:** 9.08 x 1E-10 cm3 NTP **Approx. % K**
**Integrated Age:** 18.42 ± 0.26 Ma 12.44% Ca

**Initial 40/36:** 286.74 ± 23.49 (MSWD = 0.48, isochron between 0.53 and 1.94)
**Correlation Age:** 18.77 ± 0.53 Ma ( 99.6% of 39Ar, steps marked by >) **MSWD** 0.412

**Plateau Age:** 18.43 ± 0.25 Ma ( 99.6% of 39Ar, steps marked by <) **Mod. err.** 0.30

| Power | 36Ar/40Ar | 39Ar/40Ar | r | Ca/K | %40Atm | %39Ar | 40Ar*/39K | Age |
|---|---|---|---|---|---|---|---|---|
| 0.50 | 0.003185±0.000217 | 0.021922±0.000569 | 0.014 | 0.016 | 94.07 | 0.38 | 2.679±2.928 | 16.52±17.98 |
| < 1.00> | 0.002414 0.000203 | 0.094269 0.001250 | 0.010 | 0.019 | 71.13 | 1.71 | 3.041 0.639 | 18.75 3.92 |
| < 1.50> | 0.001934 0.000100 | 0.140555 0.000931 | 0.016 | 0.002 | 56.91 | 5.16 | 3.048 0.213 | 18.79 1.31 |
| < 2.00> | 0.001701 0.000071 | 0.167376 0.000796 | 0.021 | 0.000 | 50.01 | 12.45 | 2.972 0.127 | 18.32 0.78 |
| < 2.50> | 0.001409 0.000070 | 0.195647 0.001039 | 0.012 | 0.000 | 41.38 | 13.74 | 2.983 0.108 | 18.39 0.66 |
| < 3.00> | 0.001477 0.000076 | 0.189006 0.001091 | 0.013 | 0.000 | 43.39 | 7.76 | 2.982 0.121 | 18.39 0.74 |
| < 3.50> | 0.001483 0.000057 | 0.187776 0.000839 | 0.019 | 0.000 | 43.57 | 13.86 | 2.992 0.092 | 18.45 0.56 |
| < 4.00> | 0.001235 0.000064 | 0.212145 0.001048 | 0.021 | 0.001 | 36.28 | 10.84 | 2.993 0.092 | 18.45 0.56 |
| < 5.00> | 0.001161 0.000065 | 0.222423 0.001060 | 0.014 | 0.003 | 34.09 | 11.26 | 2.953 0.088 | 18.21 0.54 |
| < 6.00> | 0.001020 0.000096 | 0.236101 0.001584 | 0.014 | 0.003 | 29.93 | 6.74 | 2.959 0.123 | 18.24 0.75 |
| < 7.00> | 0.000937 0.000119 | 0.243355 0.001884 | 0.009 | 0.000 | 27.49 | 4.72 | 2.971 0.147 | 18.32 0.90 |
| < 7.50> | 0.000413 0.000053 | 0.288960 0.001596 | 0.008 | 0.001 | 12.10 | 11.38 | 3.038 0.057 | 18.73 0.35 |

| Power | 40Ar | 39Ar | 38Ar | 37Ar | 36Ar | Blank 40Ar | Atmos 40/36 |
|---|---|---|---|---|---|---|---|
| 0.50 | 1.606±0.007 | 0.035±0.001 | 0.002±0.000 | 0.001±0.000 | 0.005±0.000 | 0.024 | 287.137 |
| < 1.00> | 1.675 0.005 | 0.156 0.002 | 0.003 0.000 | 0.002 0.000 | 0.004 0.000 | 0.024 | 287.137 |
| < 1.50> | 3.370 0.008 | 0.472 0.003 | 0.007 0.000 | 0.001 0.000 | 0.007 0.000 | 0.024 | 287.137 |
| < 2.00> | 6.812 0.014 | 1.138 0.005 | 0.016 0.001 | 0.001 0.000 | 0.012 0.000 | 0.024 | 287.137 |
| < 2.50> | 6.438 0.011 | 1.256 0.006 | 0.018 0.001 | 0.001 0.000 | 0.009 0.000 | 0.024 | 287.137 |
| < 3.00> | 3.773 0.007 | 0.710 0.004 | 0.010 0.001 | 0.001 0.000 | 0.006 0.000 | 0.024 | 287.137 |
| < 3.50> | 6.765 0.012 | 1.267 0.005 | 0.018 0.001 | 0.001 0.000 | 0.010 0.000 | 0.024 | 287.137 |
| < 4.00> | 4.693 0.011 | 0.991 0.004 | 0.014 0.001 | 0.001 0.000 | 0.006 0.000 | 0.024 | 287.137 |
| < 5.00> | 4.653 0.009 | 1.030 0.004 | 0.014 0.001 | 0.002 0.000 | 0.006 0.000 | 0.024 | 287.137 |
| < 6.00> | 2.635 0.008 | 0.616 0.004 | 0.008 0.001 | 0.002 0.000 | 0.003 0.000 | 0.024 | 287.137 |
| < 7.00> | 1.797 0.005 | 0.431 0.003 | 0.006 0.001 | 0.001 0.000 | 0.002 0.000 | 0.024 | 287.137 |
| < 7.50> | 3.633 0.009 | 1.041 0.005 | 0.013 0.001 | 0.001 0.000 | 0.002 0.000 | 0.025 | 287.137 |

**Measured volumes are x 1E-10 cm3 NTP.** **All errors are 2 x standard error.** **Intrim13 28-Mar-02**

**KL-3: CH-122B Mu HP**

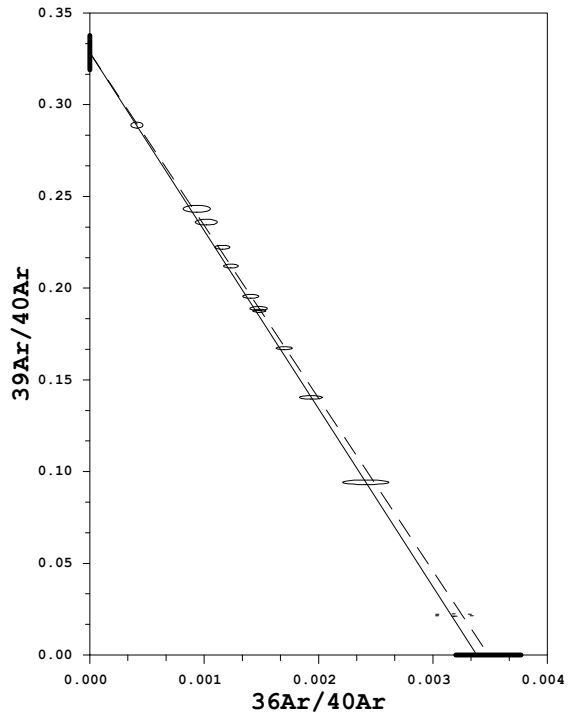


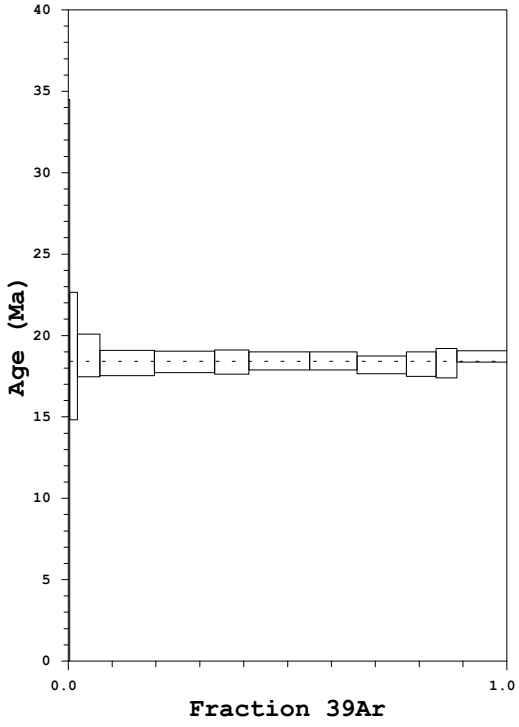


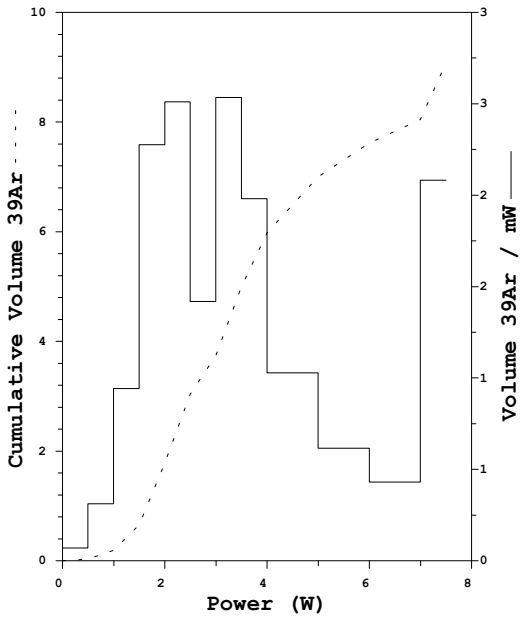


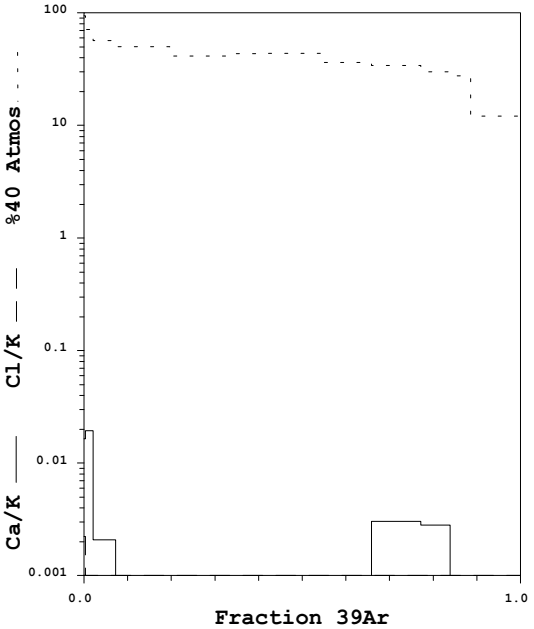


Measured volumes are x 1E-10 cm3 NTP. All errors are 2 x standard error. Intrim13 28-Mar-02

## KL-13: CH-123B Mu HP

**Run date:** 2008/01/26 **Can/Pos:** 208/2 **J Value:** 0.003431
**Printed:** 2008/01/29 **Mass:** 0.0 mg ± 0.000020

**Volume 39K:** 6.57 x 1E-10 cm3 NTP **Approx. % K**
**Integrated Age:** 17.73 ± 0.24 Ma **% Ca**

**Initial 40/36:** 286.43 ± 46.78 (MSWD = 0.69, isochron between 0.42 and 2.15)
**Correlation Age:** 17.78 ± 0.74 Ma ( 86.4% of 39Ar, steps marked by >) **MSWD** 0.414

**Plateau Age:** 17.62 ± 0.25 Ma ( 86.4% of 39Ar, steps marked by <) **Mod. err.** 0.34

| Power | 36Ar/40Ar | 39Ar/40Ar | r | Ca/K | %40Atm | %39Ar | 40Ar*/39K | Age |
|---|---|---|---|---|---|---|---|---|
| 0.75 | 0.002851±0.000224 | 0.040707±0.000860 | 0.014 | 0.040 | 84.15 | 0.78 | 3.869±1.628 | 23.79±9.94 |
| < 1.50> | 0.001857 0.000139 | 0.151361 0.001626 | 0.019 | 0.023 | 54.63 | 4.30 | 2.981 0.275 | 18.36 1.69 |
| < 2.00> | 0.001250 0.000065 | 0.220480 0.001238 | 0.027 | 0.002 | 36.70 | 15.11 | 2.860 0.089 | 17.62 0.55 |
| < 2.50> | 0.000780 0.000062 | 0.269566 0.001497 | 0.013 | 0.003 | 22.87 | 18.87 | 2.854 0.070 | 17.58 0.43 |
| < 3.00> | 0.000919 0.000059 | 0.257541 0.001099 | 0.010 | 0.002 | 26.95 | 25.28 | 2.828 0.069 | 17.42 0.42 |
| < 3.50> | 0.000887 0.000135 | 0.259040 0.002234 | 0.011 | 0.000 | 26.00 | 6.44 | 2.849 0.156 | 17.55 0.96 |
| < 4.50> | 0.000686 0.000098 | 0.278981 0.002269 | 0.009 | 0.005 | 20.10 | 7.01 | 2.858 0.107 | 17.60 0.66 |
| < 5.50> | 0.000461 0.000163 | 0.298132 0.003291 | 0.004 | 0.004 | 13.51 | 4.36 | 2.897 0.165 | 17.84 1.01 |
| < 7.00> | 0.000347 0.000140 | 0.306252 0.002873 | 0.002 | 0.000 | 10.16 | 4.98 | 2.931 0.138 | 18.05 0.85 |
| 7.50 | 0.000208 0.000060 | 0.318734 0.001911 | 0.002 | 0.000 | 6.08 | 12.86 | 2.945 0.058 | 18.14 0.36 |

| Power | 40Ar | 39Ar | 38Ar | 37Ar | 36Ar | Blank 40Ar | Atmos 40/36 |
|---|---|---|---|---|---|---|---|
| 0.75 | 1.294±0.006 | 0.052±0.001 | 0.002±0.000 | 0.001±0.000 | 0.004±0.000 | 0.029 | 287.137 |
| < 1.50> | 1.905 0.007 | 0.285 0.003 | 0.004 0.000 | 0.002 0.000 | 0.004 0.000 | 0.028 | 287.137 |
| < 2.00> | 4.562 0.013 | 1.000 0.005 | 0.014 0.001 | 0.001 0.000 | 0.006 0.000 | 0.028 | 287.137 |
| < 2.50> | 4.668 0.011 | 1.249 0.006 | 0.016 0.001 | 0.001 0.000 | 0.004 0.000 | 0.029 | 287.137 |
| < 3.00> | 6.532 0.011 | 1.673 0.006 | 0.022 0.001 | 0.001 0.000 | 0.006 0.000 | 0.029 | 287.137 |
| < 3.50> | 1.676 0.006 | 0.426 0.003 | 0.006 0.001 | 0.001 0.000 | 0.002 0.000 | 0.029 | 287.137 |
| < 4.50> | 1.695 0.006 | 0.464 0.003 | 0.006 0.001 | 0.001 0.000 | 0.001 0.000 | 0.029 | 287.137 |
| < 5.50> | 0.998 0.005 | 0.288 0.003 | 0.004 0.000 | 0.001 0.000 | 0.001 0.000 | 0.029 | 287.137 |
| < 7.00> | 1.109 0.005 | 0.330 0.003 | 0.004 0.000 | 0.001 0.000 | 0.001 0.000 | 0.029 | 287.137 |
| 7.50 | 2.708 0.006 | 0.851 0.005 | 0.011 0.001 | 0.001 0.000 | 0.001 0.000 | 0.029 | 287.137 |

**Measured volumes are x 1E-10 cm3 NTP.** **All errors are 2 x standard error.** **Intrim13 28-Mar-02**

**KL-13: CH-123B Mu HP**

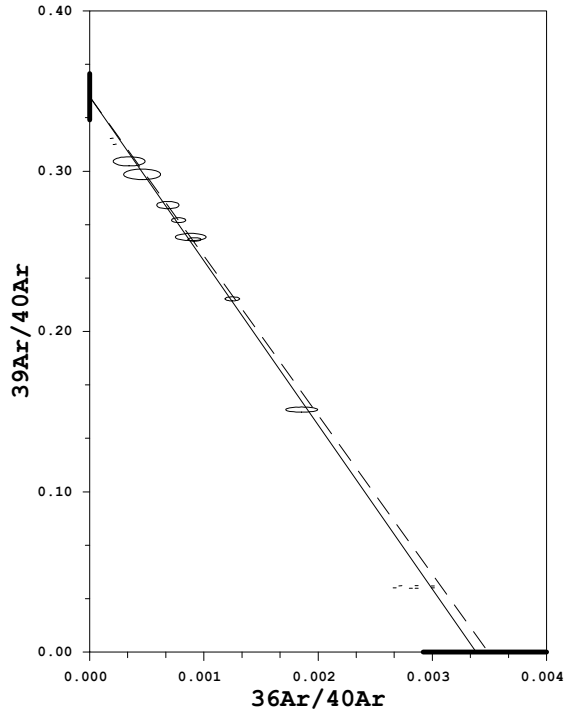


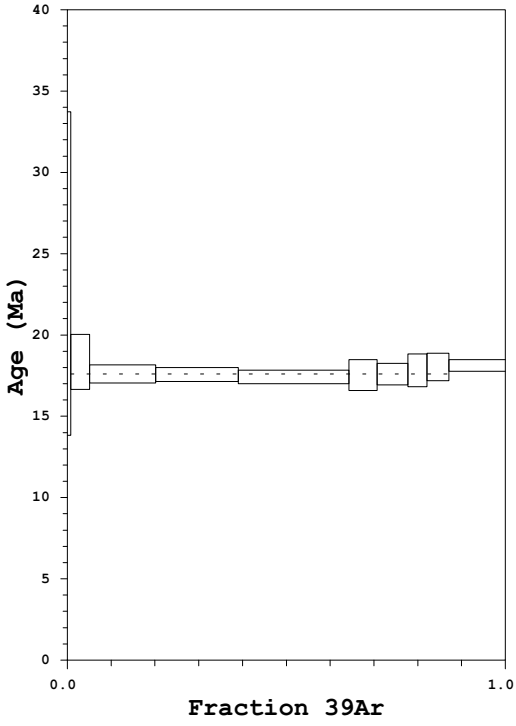


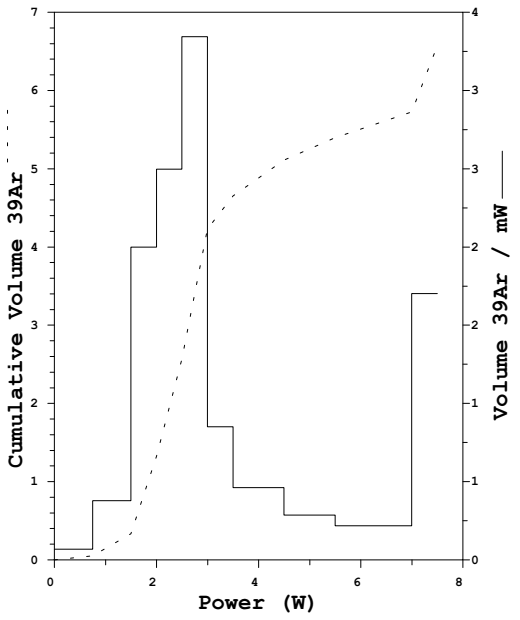


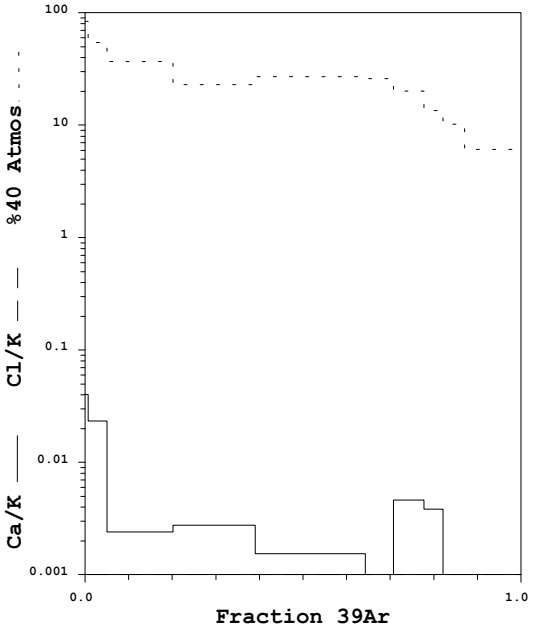


Measured volumes are x 1E-10 cm3 NTP. All errors are 2 x standard error. Intrim13 28-Mar-02

## KL-1: CH-123B Bt HP

**Run date:** 2007/12/08 **Can/Pos:** 208/1 **J Value:** 0.003430
**Printed:** 2008/01/29 **Mass:** 0.0 mg ± 0.000020

**Volume 39K:** 14.91 x 1E-10 cm3 NTP **Approx.** % K
**Integrated Age:** 16.82 ± 0.20 Ma % Ca

**Initial 40/36:** 285.25 ± 23.81 (MSWD = 0.36, isochron between 0.53 and 1.94)
**Correlation Age:** 16.95 ± 0.35 Ma ( 82.3% of 39Ar, steps marked by >) **MSWD** 0.703

**Plateau Age:** 16.76 ± 0.22 Ma ( 82.3% of 39Ar, steps marked by <) **Mod. err.** 0.17

| Power | 36Ar/40Ar | 39Ar/40Ar | r | Ca/K | %40Atm | %39Ar | 40Ar*/39K | Age |
|---|---|---|---|---|---|---|---|---|
| 0.50 | 0.003107±0.000176 | 0.045677±0.000870 | 0.010 | 0.075 | 91.68 | 0.53 | 1.794±1.143 | 11.07±7.03 |
| 1.00 | 0.002293 0.000090 | 0.126369 0.000892 | 0.027 | 0.029 | 67.50 | 3.23 | 2.552 0.213 | 15.72 1.30 |
| < 1.50> | 0.001509 0.000050 | 0.206331 0.000936 | 0.017 | 0.011 | 44.31 | 13.60 | 2.685 0.073 | 16.54 0.45 |
| < 1.75> | 0.000969 0.000046 | 0.265600 0.001201 | 0.013 | 0.008 | 28.41 | 14.14 | 2.687 0.053 | 16.55 0.33 |
| < 2.00> | 0.000374 0.000050 | 0.323367 0.001727 | 0.015 | 0.009 | 10.94 | 9.70 | 2.751 0.048 | 16.94 0.30 |
| < 2.50> | 0.000424 0.000040 | 0.318004 0.001776 | 0.014 | 0.016 | 12.41 | 12.20 | 2.751 0.041 | 16.94 0.25 |
| < 3.00> | 0.000407 0.000039 | 0.322989 0.015931 | 0.203 | 0.018 | 11.90 | 11.59 | 2.724 0.147 | 16.78 0.90 |
| < 3.50> | 0.000444 0.000078 | 0.312389 0.016129 | 0.212 | 0.010 | 12.98 | 5.08 | 2.782 0.175 | 17.13 1.07 |
| < 4.00> | 0.000471 0.000090 | 0.319737 0.005875 | 0.027 | 0.023 | 13.77 | 4.12 | 2.693 0.098 | 16.59 0.60 |
| < 5.00> | 0.000407 0.000085 | 0.322810 0.009681 | 0.033 | 0.018 | 11.90 | 5.10 | 2.726 0.116 | 16.79 0.71 |
| 6.00 | 0.000381 0.000071 | 0.312138 0.004508 | 0.032 | 0.011 | 11.12 | 5.69 | 2.844 0.081 | 17.51 0.49 |
| 7.00 | 0.000293 0.000114 | 0.310230 0.007582 | 0.013 | 0.023 | 8.55 | 2.78 | 2.945 0.132 | 18.13 0.81 |
| 8.00 | 0.000476 0.000142 | 0.296201 0.004138 | 0.022 | 0.025 | 13.90 | 2.33 | 2.902 0.148 | 17.87 0.91 |
| 8.50 | 0.000476 0.000142 | 0.296201 0.004138 | 0.022 | 0.025 | 13.90 | 2.33 | 2.902 0.148 | 17.87 0.91 |
| < 1.50> | 0.001584 0.000114 | 0.197435 0.001585 | 0.019 | 0.007 | 46.53 | 2.52 | 2.694 0.173 | 16.60 1.06 |
| < 3.00> | 0.000691 0.000122 | 0.290782 0.002808 | 0.008 | 0.000 | 20.23 | 2.87 | 2.737 0.128 | 16.86 0.78 |
| < 4.50> | 0.000755 0.000199 | 0.281581 0.003165 | 0.007 | 0.011 | 22.11 | 1.41 | 2.759 0.211 | 17.00 1.29 |
| 5.50 | 0.001143 0.000528 | 0.243783 0.006354 | 0.010 | 0.021 | 33.51 | 0.43 | 2.717 0.646 | 16.74 3.96 |
| 7.50 | 0.001672 0.001091 | 0.199176 0.005760 | 0.014 | 0.009 | 49.11 | 0.18 | 2.540 1.623 | 15.65 9.95 |
| 8.00 | 0.001825 0.001040 | 0.199121 0.007759 | 0.016 | 0.054 | 53.60 | 0.18 | 2.314 1.550 | 14.26 9.51 |

| Power | 40Ar | 39Ar | 38Ar | 37Ar | 36Ar | Blank 40Ar | Atmos 40/36 |
|---|---|---|---|---|---|---|---|
| 0.50 | 1.779±0.006 | 0.080±0.001 | 0.004±0.000 | 0.002±0.000 | 0.006±0.000 | 0.035 | 287.137 |
| 1.00 | 3.863 0.010 | 0.485 0.003 | 0.013 0.001 | 0.004 0.000 | 0.009 0.000 | 0.035 | 287.137 |
| < 1.50> | 9.930 0.016 | 2.043 0.009 | 0.047 0.002 | 0.005 0.001 | 0.016 0.000 | 0.036 | 287.137 |
| < 1.75> | 8.036 0.013 | 2.123 0.009 | 0.048 0.002 | 0.004 0.000 | 0.008 0.000 | 0.036 | 287.137 |
| < 2.00> | 4.551 0.015 | 1.456 0.006 | 0.032 0.001 | 0.003 0.000 | 0.002 0.000 | 0.036 | 287.137 |
| < 2.50> | 5.814 0.016 | 1.832 0.009 | 0.041 0.002 | 0.006 0.001 | 0.003 0.000 | 0.037 | 287.137 |
| < 3.00> | 5.438 0.165 | 1.740 0.066 | 0.039 0.002 | 0.007 0.001 | 0.003 0.000 | 0.036 | 287.137 |
| < 3.50> | 2.484 0.106 | 0.763 0.021 | 0.017 0.001 | 0.002 0.000 | 0.001 0.000 | 0.036 | 287.137 |
| < 4.00> | 1.976 0.019 | 0.619 0.009 | 0.014 0.001 | 0.003 0.000 | 0.001 0.000 | 0.036 | 287.137 |
| < 5.00> | 2.414 0.034 | 0.765 0.020 | 0.019 0.001 | 0.003 0.000 | 0.001 0.000 | 0.036 | 287.137 |
| 6.00 | 2.782 0.026 | 0.855 0.009 | 0.035 0.001 | 0.002 0.000 | 0.001 0.000 | 0.037 | 287.137 |
| 7.00 | 1.384 0.015 | 0.417 0.009 | 0.022 0.001 | 0.003 0.000 | 0.001 0.000 | 0.036 | 287.137 |
| 8.00 | 1.218 0.012 | 0.350 0.003 | 0.018 0.001 | 0.002 0.000 | 0.001 0.000 | 0.036 | 287.137 |
| 8.50 | 1.218 0.012 | 0.350 0.003 | 0.018 0.001 | 0.002 0.000 | 0.001 0.000 | 0.036 | 287.137 |
| < 1.50> | 1.940 0.006 | 0.378 0.003 | 0.009 0.001 | 0.001 0.000 | 0.003 0.000 | 0.029 | 287.137 |
| < 3.00> | 1.512 0.006 | 0.430 0.004 | 0.009 0.001 | 0.001 0.000 | 0.001 0.000 | 0.029 | 287.137 |
| < 4.50> | 0.781 0.004 | 0.211 0.002 | 0.004 0.001 | 0.001 0.000 | 0.001 0.000 | 0.029 | 287.137 |
| 5.50 | 0.292 0.003 | 0.064 0.001 | 0.001 0.000 | 0.001 0.000 | 0.001 0.000 | 0.029 | 287.137 |
| 7.50 | 0.167 0.002 | 0.028 0.001 | 0.001 0.000 | 0.001 0.000 | 0.000 0.000 | 0.029 | 287.137 |
| 8.00 | 0.165 0.003 | 0.027 0.001 | 0.001 0.000 | 0.001 0.000 | 0.000 0.000 | 0.029 | 287.137 |

**Measured volumes are x 1E-10 cm3 NTP.** **All errors are 2 x standard error.** **Intrim13 28-Mar-02**

**KL-1: CH-123B Bt HP**

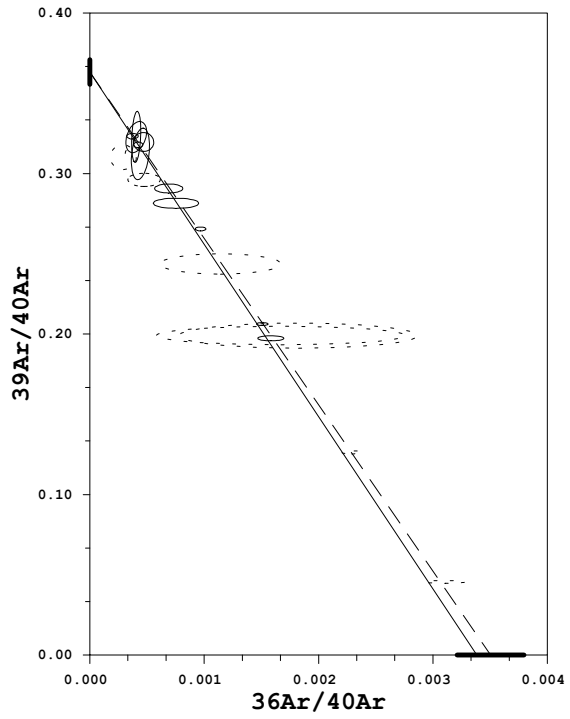


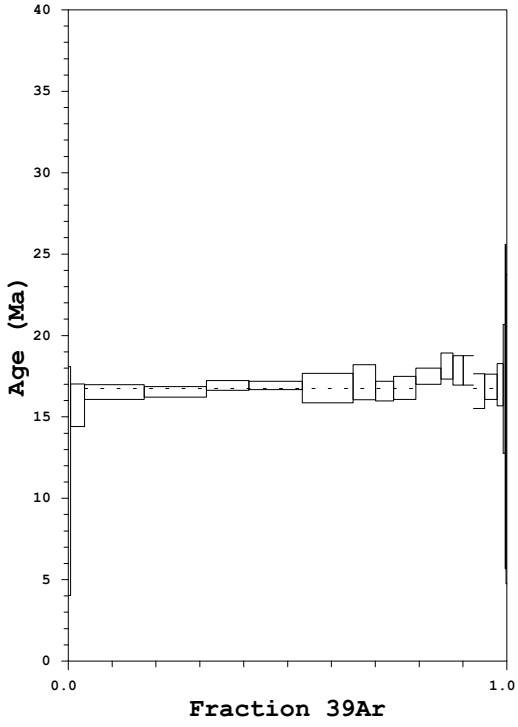


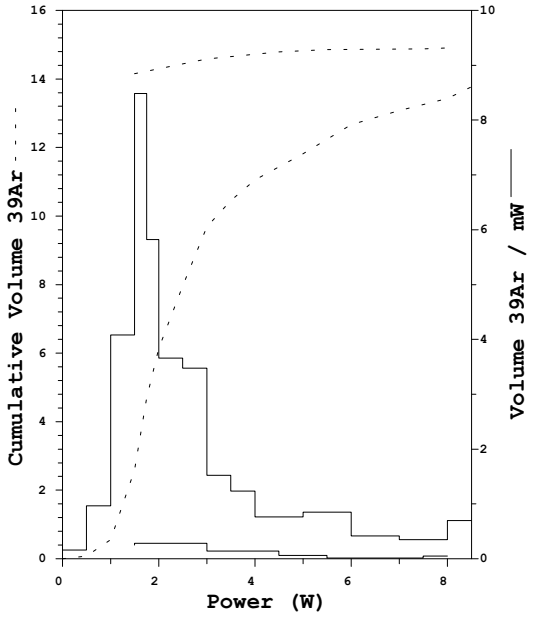


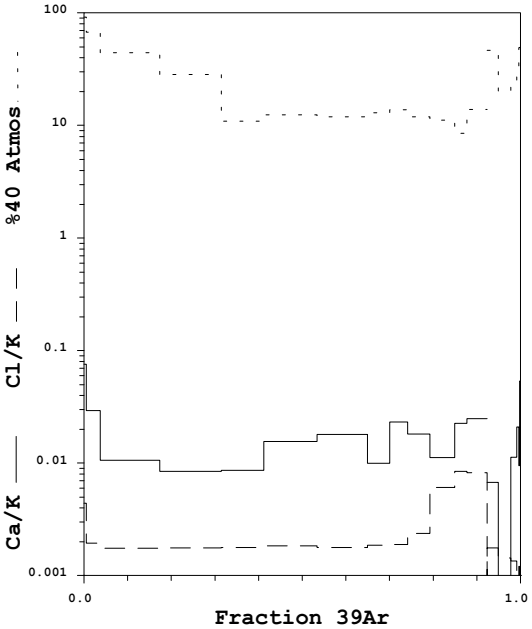


Measured volumes are x 1E-10 cm3 NTP. All errors are 2 x standard error. Intrim13 28-Mar-02

## DK05-7: KTG-9C Mu hp

**Run date:** 2006/09/11 **Can/Pos:** 202/11 **J Value:** 0.002599
**Printed:** 2008/01/29 **Mass:** 0.0 mg ± 0.000006

**Volume 39K:** 55.20 x 1E-10 cm3 NTP **Approx.** % K
**Integrated Age:** 18.83 ± 0.06 Ma % Ca

**Initial 40/36:** 290.42 ± 76.73 (MSWD = 13.03, isochron between 0.29 and 2.41)
**Correlation Age:** 18.68 ± 0.25 Ma ( 85.7% of 39Ar, steps marked by >) **MSWD** 9.406

**Plateau Age:** 18.65 ± 0.06 Ma ( 85.7% of 39Ar, steps marked by <) **Mod. err.** 0.11

| Power | 36Ar/40Ar | 39Ar/40Ar | r | Ca/K | %40Atm | %39Ar | 40Ar*/39K | Age |
|---|---|---|---|---|---|---|---|---|
| 2.00 | 0.002759±0.000240 | 0.063160±0.000783 | 0.019 | 0.032 | 81.37 | 0.20 | 2.925±1.128 | 13.66±5.25 |
| 3.00 | 0.001555 0.000316 | 0.133520 0.001278 | 0.009 | 0.020 | 45.75 | 0.32 | 4.049 0.701 | 18.89 3.25 |
| 4.00 | 0.000910 0.000101 | 0.184059 0.001011 | 0.007 | 0.007 | 26.74 | 0.86 | 3.972 0.165 | 18.53 0.76 |
| 5.00 | 0.000576 0.000043 | 0.194125 0.000575 | 0.007 | 0.004 | 16.93 | 2.67 | 4.274 0.067 | 19.93 0.31 |
| 6.00 | 0.000370 0.000015 | 0.205694 0.000318 | 0.007 | 0.001 | 10.87 | 10.23 | 4.330 0.023 | 20.19 0.11 |
| < 6.50> | 0.000217 0.000014 | 0.232545 0.000397 | 0.006 | 0.001 | 6.38 | 9.93 | 4.024 0.020 | 18.77 0.09 |
| < 7.00> | 0.000336 0.000021 | 0.221911 0.000428 | 0.006 | 0.001 | 9.86 | 7.33 | 4.059 0.029 | 18.93 0.14 |
| < 7.50> | 0.000195 0.000020 | 0.237760 0.000439 | 0.003 | 0.001 | 5.71 | 8.07 | 3.964 0.026 | 18.49 0.12 |
| < 8.00> | 0.000186 0.000017 | 0.238328 0.000469 | 0.005 | 0.000 | 5.46 | 7.05 | 3.965 0.023 | 18.50 0.11 |
| < 8.50> | 0.000151 0.000011 | 0.239833 0.000354 | 0.004 | 0.001 | 4.43 | 31.34 | 3.984 0.016 | 18.58 0.07 |
| < 8.50> | 0.000050 0.000008 | 0.245525 0.000518 | 0.005 | 0.001 | 1.48 | 22.00 | 4.012 0.013 | 18.72 0.06 |

| Power | 40Ar | 39Ar | 38Ar | 37Ar | 36Ar | Blank 40Ar | Atmos 40/36 |
|---|---|---|---|---|---|---|---|
| 2.00 | 2.105±0.008 | 0.112±0.001 | 0.004±0.000 | 0.001±0.000 | 0.006±0.000 | 0.367 | 287.699 |
| 3.00 | 1.691 0.006 | 0.178 0.001 | 0.003 0.001 | 0.001 0.000 | 0.004 0.000 | 0.367 | 287.699 |
| 4.00 | 2.650 0.006 | 0.480 0.002 | 0.007 0.001 | 0.001 0.000 | 0.003 0.000 | 0.049 | 287.699 |
| 5.00 | 7.688 0.010 | 1.484 0.004 | 0.020 0.001 | 0.002 0.000 | 0.005 0.000 | 0.049 | 287.699 |
| 6.00 | 27.659 0.019 | 5.682 0.008 | 0.073 0.001 | 0.002 0.000 | 0.011 0.000 | 0.049 | 287.699 |
| < 6.50> | 23.777 0.020 | 5.516 0.008 | 0.070 0.001 | 0.002 0.001 | 0.006 0.000 | 0.049 | 287.699 |
| < 7.00> | 18.410 0.017 | 4.074 0.007 | 0.052 0.001 | 0.001 0.000 | 0.007 0.000 | 0.050 | 287.699 |
| < 7.50> | 18.925 0.015 | 4.486 0.007 | 0.057 0.001 | 0.001 0.000 | 0.004 0.000 | 0.049 | 287.699 |
| < 8.00> | 16.488 0.017 | 3.916 0.006 | 0.049 0.001 | 0.001 0.000 | 0.004 0.000 | 0.049 | 287.699 |
| < 8.50> | 72.713 0.047 | 17.415 0.023 | 0.218 0.003 | 0.004 0.001 | 0.011 0.001 | 0.050 | 287.699 |
| < 8.50> | 49.880 0.068 | 12.224 0.019 | 0.152 0.002 | 0.003 0.001 | 0.003 0.000 | 0.050 | 287.699 |

**Measured volumes are x 1E-10 cm3 NTP.** **All errors are 2 x standard error.** **Intrim13 28-Mar-02**

**DK05-7: KTH-9C Mu hp**

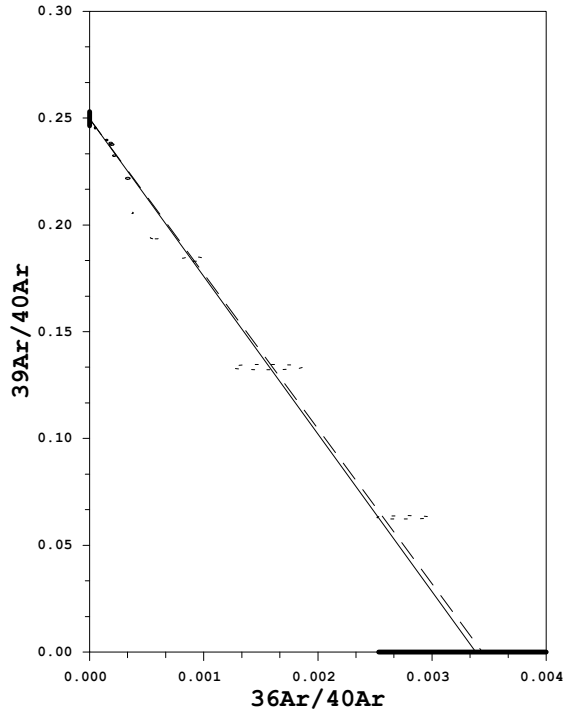


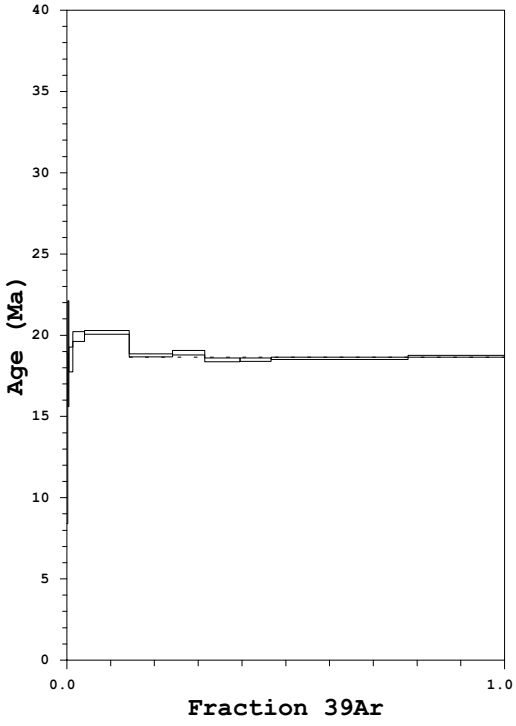


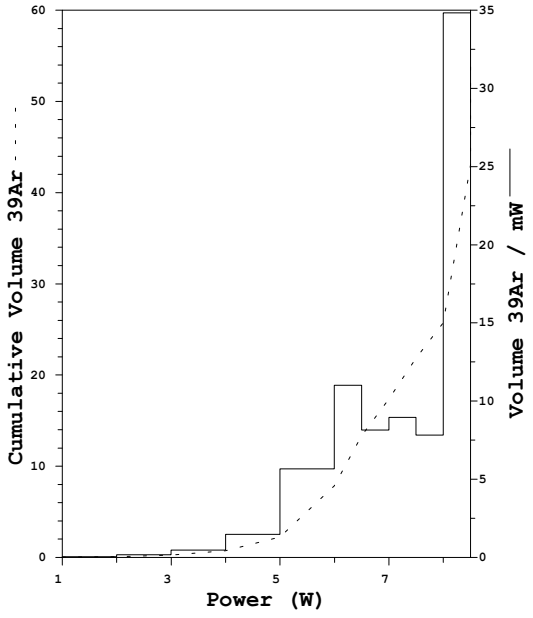


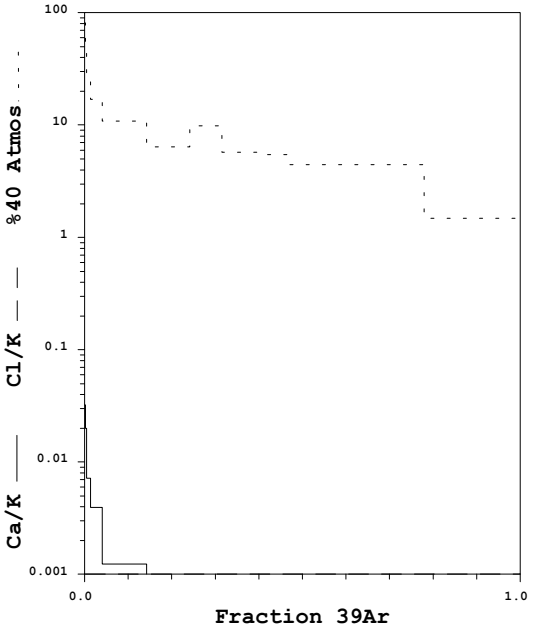


Measured volumes are x 1E-10 cm3 NTP. All errors are 2 x standard error. Intrim13 28-Mar-02

## DK05-8: KTG-9A Mu hp

**Run date:** 2006/09/12 **Can/Pos:** 202/10 **J Value:** 0.002597
**Printed:** 2008/01/29 **Mass:** 0.0 mg ± 0.000006

**Volume 39K:** 41.06 x 1E-10 cm3 NTP **Approx.** % K
**Integrated Age:** 19.28 ± 0.07 Ma % Ca

**Initial 40/36:** 326.41 ± 29.99 (MSWD = 5.61, isochron between 0.29 and 2.41)
**Correlation Age:** 18.48 ± 0.26 Ma ( 73.0% of 39Ar, steps marked by >) **MSWD** 10.804

**Plateau Age:** 18.82 ± 0.08 Ma ( 73.0% of 39Ar, steps marked by <) **Mod. err.** 0.17

| Power | 36Ar/40Ar | 39Ar/40Ar | r | Ca/K | %40Atm | %39Ar | 40Ar*/39K | Age |
|---|---|---|---|---|---|---|---|---|
| 2.00 | 0.002889±0.000197 | 0.027970±0.000456 | 0.006 | 0.028 | 85.31 | 0.13 | 5.228±2.083 | 24.33±9.63 |
| 3.00 | 0.001534 0.000241 | 0.093244 0.000902 | 0.005 | 0.016 | 45.21 | 0.31 | 5.862 0.766 | 27.26 3.54 |
| 4.00 | 0.000990 0.000091 | 0.089148 0.000594 | 0.005 | 0.008 | 29.18 | 0.74 | 7.935 0.308 | 36.80 1.41 |
| 5.00 | 0.001013 0.000042 | 0.116481 0.000413 | 0.010 | 0.004 | 29.83 | 2.78 | 6.015 0.110 | 27.96 0.51 |
| < 6.00> | 0.000766 0.000025 | 0.188295 0.000359 | 0.015 | 0.002 | 22.51 | 9.34 | 4.109 0.041 | 19.15 0.19 |
| < 6.50> | 0.000754 0.000024 | 0.192061 0.000329 | 0.012 | 0.001 | 22.16 | 11.80 | 4.046 0.038 | 18.86 0.18 |
| < 7.00> | 0.000422 0.000027 | 0.213366 0.000488 | 0.008 | 0.001 | 12.38 | 7.48 | 4.103 0.040 | 19.12 0.18 |
| < 7.50> | 0.000501 0.000027 | 0.209894 0.000437 | 0.006 | 0.001 | 14.71 | 7.94 | 4.059 0.040 | 18.92 0.18 |
| < 8.00> | 0.000514 0.000020 | 0.211609 0.000389 | 0.008 | 0.001 | 15.10 | 10.90 | 4.007 0.030 | 18.68 0.14 |
| < 8.50> | 0.000228 0.000011 | 0.233549 0.000327 | 0.007 | 0.001 | 6.69 | 25.51 | 3.993 0.016 | 18.61 0.07 |
| 8.50 | 0.000115 0.000010 | 0.237027 0.000380 | 0.003 | 0.001 | 3.37 | 23.06 | 4.076 0.014 | 18.99 0.07 |

| Power | 40Ar | 39Ar | 38Ar | 37Ar | 36Ar | Blank 40Ar | Atmos 40/36 |
|---|---|---|---|---|---|---|---|
| 2.00 | 1.994±0.005 | 0.054±0.001 | 0.003±0.001 | 0.001±0.000 | 0.006±0.000 | 0.078 | 287.699 |
| 3.00 | 1.452 0.004 | 0.129 0.001 | 0.003 0.001 | 0.001 0.000 | 0.003 0.000 | 0.077 | 287.699 |
| 4.00 | 3.506 0.006 | 0.307 0.002 | 0.005 0.001 | 0.001 0.001 | 0.004 0.000 | 0.078 | 287.699 |
| 5.00 | 9.923 0.012 | 1.151 0.004 | 0.016 0.001 | 0.002 0.000 | 0.011 0.000 | 0.077 | 287.699 |
| < 6.00> | 20.557 0.020 | 3.860 0.006 | 0.052 0.001 | 0.002 0.001 | 0.017 0.001 | 0.078 | 287.699 |
| < 6.50> | 25.455 0.020 | 4.878 0.007 | 0.065 0.001 | 0.001 0.000 | 0.020 0.001 | 0.078 | 287.699 |
| < 7.00> | 14.565 0.016 | 3.092 0.006 | 0.040 0.001 | 0.001 0.001 | 0.007 0.000 | 0.078 | 287.699 |
| < 7.50> | 15.700 0.014 | 3.280 0.006 | 0.042 0.001 | 0.001 0.000 | 0.009 0.000 | 0.078 | 287.699 |
| < 8.00> | 21.365 0.017 | 4.505 0.007 | 0.058 0.001 | 0.001 0.001 | 0.012 0.000 | 0.078 | 287.699 |
| < 8.50> | 45.249 0.030 | 10.544 0.013 | 0.133 0.002 | 0.002 0.001 | 0.011 0.000 | 0.077 | 287.699 |
| 8.50 | 40.308 0.026 | 9.530 0.014 | 0.119 0.002 | 0.003 0.001 | 0.005 0.000 | 0.078 | 287.699 |

**Measured volumes are x 1E-10 cm3 NTP.** **All errors are 2 x standard error.** **Intrim13 28-Mar-02**

**DK05-8: KTH-9A Mu hp**

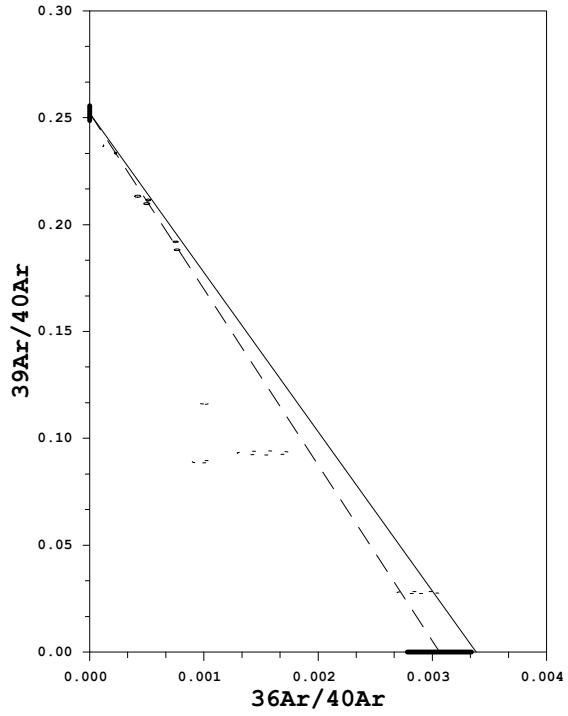


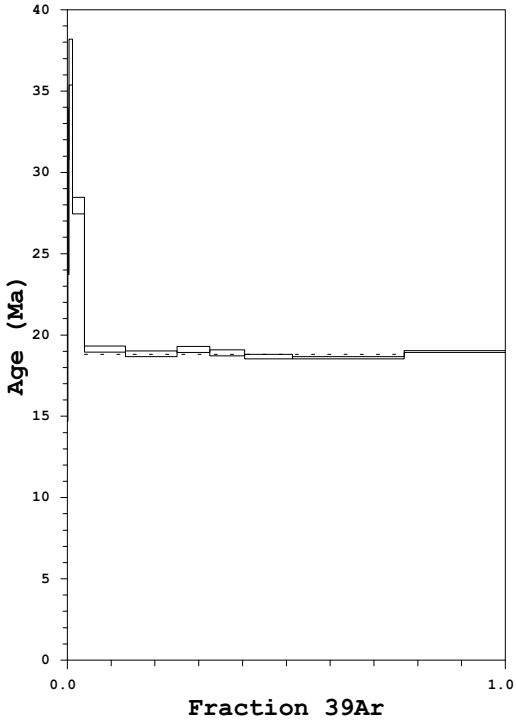


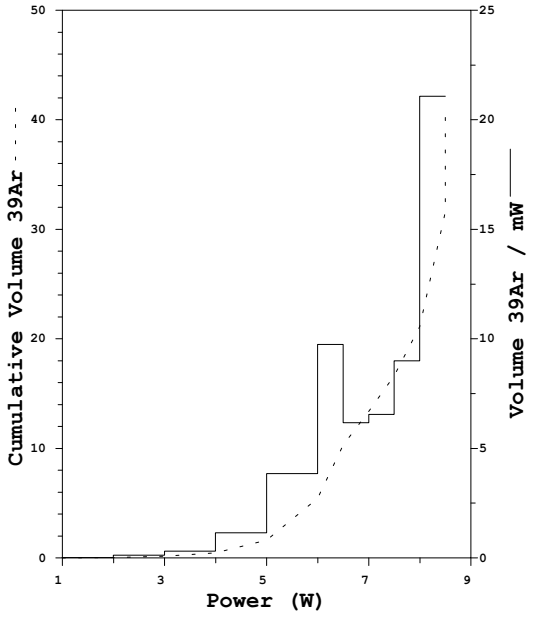


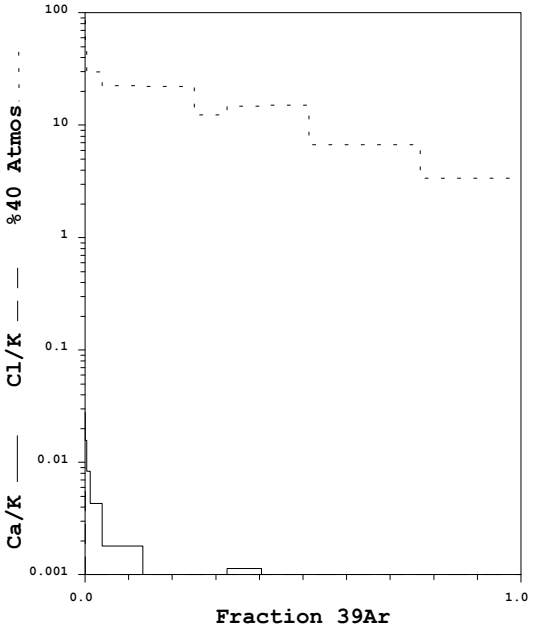


Measured volumes are x 1E-10 cm3 NTP. All errors are 2 x standard error. Intrim13 28-Mar-02

# Appendix C - Manaslu-Himal Chuli Himalaya (Chapter 4) Thermochronology Data

## KL-5: MS-37 Bt HP

**Run date:** 2007/12/18 **Can/Pos:** 208/6 **J Value:** 0.003438
**Printed:** 2008/01/29 **Mass:** 0.0 mg ± 0.000022

**Volume 39K:** 26.71 x 1E-10 cm3 NTP **Approx.** % K
**Integrated Age:** 12.50 ± 0.14 Ma % Ca

**Initial 40/36:** 286.86 ± 21.59 (MSWD = 0.26, isochron between 0.50 and 2.00)
**Correlation Age:** 12.63 ± 0.27 Ma ( 80.9% of 39Ar, steps marked by >) **MSWD** 0.630

**Plateau Age:** 12.43 ± 0.15 Ma ( 80.9% of 39Ar, steps marked by <) **Mod. err.** 0.11

| Power | 36Ar/40Ar | 39Ar/40Ar | r | Ca/K | %40Atm | %39Ar | 40Ar*/39K | Age |
|---|---|---|---|---|---|---|---|---|
| 0.50 | 0.003259±0.000138 | 0.022012±0.000406 | 0.012 | 0.019 | 96.23 | 0.21 | 1.686±1.855 | 10.43±11.44 |
| < 1.00> | 0.002813 0.000102 | 0.090475 0.000624 | 0.013 | 0.007 | 82.88 | 1.82 | 1.867 0.336 | 11.54 2.07 |
| < 1.50> | 0.002274 0.000086 | 0.166479 0.000727 | 0.023 | 0.003 | 66.85 | 4.84 | 1.971 0.153 | 12.18 0.94 |
| < 2.00> | 0.001889 0.000055 | 0.223450 0.000907 | 0.015 | 0.002 | 55.44 | 8.40 | 1.978 0.074 | 12.22 0.46 |
| < 2.50> | 0.001307 0.000069 | 0.310440 0.001178 | 0.014 | 0.002 | 38.27 | 9.23 | 1.977 0.067 | 12.22 0.41 |
| < 3.00> | 0.000788 0.000049 | 0.377796 0.001675 | 0.012 | 0.001 | 23.02 | 9.80 | 2.031 0.039 | 12.55 0.24 |
| < 3.50> | 0.000678 0.000047 | 0.393920 0.001708 | 0.013 | 0.001 | 19.79 | 8.53 | 2.030 0.036 | 12.55 0.22 |
| < 4.00> | 0.000681 0.000057 | 0.392553 0.001897 | 0.011 | 0.001 | 19.89 | 6.69 | 2.035 0.044 | 12.58 0.27 |
| < 5.00> | 0.000639 0.000052 | 0.401158 0.001580 | 0.012 | 0.001 | 18.66 | 9.24 | 2.022 0.039 | 12.50 0.24 |
| < 6.00> | 0.000648 0.000050 | 0.399624 0.001472 | 0.012 | 0.001 | 18.90 | 11.85 | 2.024 0.038 | 12.51 0.23 |
| < 7.00> | 0.000653 0.000043 | 0.397064 0.001401 | 0.012 | 0.001 | 19.07 | 10.48 | 2.032 0.033 | 12.56 0.20 |
| 7.50 | 0.000682 0.000034 | 0.385047 0.001316 | 0.012 | 0.001 | 19.92 | 18.90 | 2.074 0.027 | 12.82 0.17 |

| Power | 40Ar | 39Ar | 38Ar | 37Ar | 36Ar | Blank 40Ar | Atmos 40/36 |
|---|---|---|---|---|---|---|---|
| 0.50 | 2.583±0.007 | 0.057±0.001 | 0.004±0.000 | 0.001±0.000 | 0.009±0.000 | 0.033 | 287.137 |
| < 1.00> | 5.426 0.009 | 0.490 0.003 | 0.014 0.001 | 0.002 0.000 | 0.016 0.001 | 0.033 | 287.137 |
| < 1.50> | 7.835 0.015 | 1.301 0.005 | 0.029 0.001 | 0.002 0.000 | 0.018 0.001 | 0.033 | 287.137 |
| < 2.00> | 10.138 0.013 | 2.258 0.009 | 0.046 0.002 | 0.002 0.000 | 0.020 0.001 | 0.033 | 287.137 |
| < 2.50> | 8.050 0.013 | 2.482 0.008 | 0.047 0.001 | 0.002 0.000 | 0.011 0.001 | 0.034 | 287.137 |
| < 3.00> | 7.044 0.013 | 2.637 0.010 | 0.050 0.001 | 0.002 0.000 | 0.006 0.000 | 0.033 | 287.137 |
| < 3.50> | 5.889 0.012 | 2.295 0.009 | 0.043 0.001 | 0.002 0.000 | 0.004 0.000 | 0.033 | 287.137 |
| < 4.00> | 4.642 0.010 | 1.800 0.008 | 0.033 0.001 | 0.001 0.000 | 0.004 0.000 | 0.033 | 287.137 |
| < 5.00> | 6.260 0.012 | 2.485 0.008 | 0.046 0.002 | 0.002 0.000 | 0.004 0.000 | 0.034 | 287.137 |
| < 6.00> | 8.048 0.015 | 3.186 0.010 | 0.058 0.002 | 0.002 0.000 | 0.006 0.000 | 0.034 | 287.137 |
| < 7.00> | 7.169 0.012 | 2.819 0.009 | 0.051 0.001 | 0.001 0.000 | 0.005 0.000 | 0.034 | 287.137 |
| 7.50 | 13.298 0.018 | 5.083 0.016 | 0.093 0.002 | 0.002 0.000 | 0.010 0.000 | 0.034 | 287.137 |

**Measured volumes are x 1E-10 cm3 NTP.** **All errors are 2 x standard error.** **Intrim13 28-Mar-02**

**KL-5: MS-37 Bt HP**

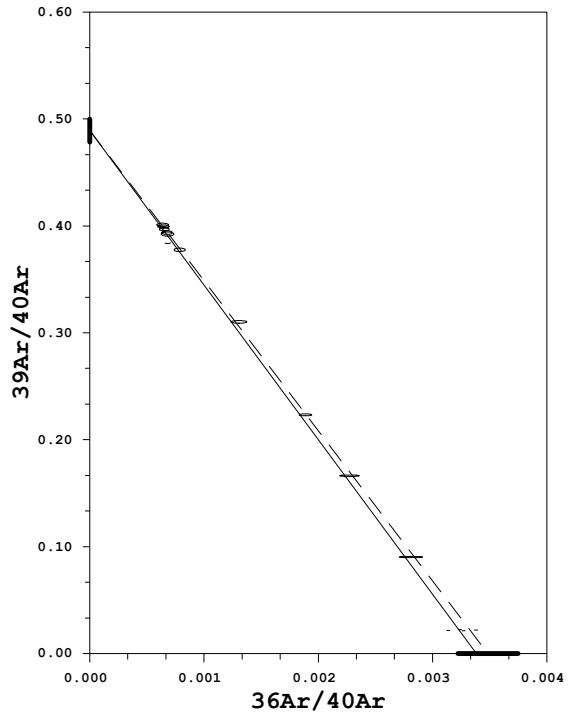


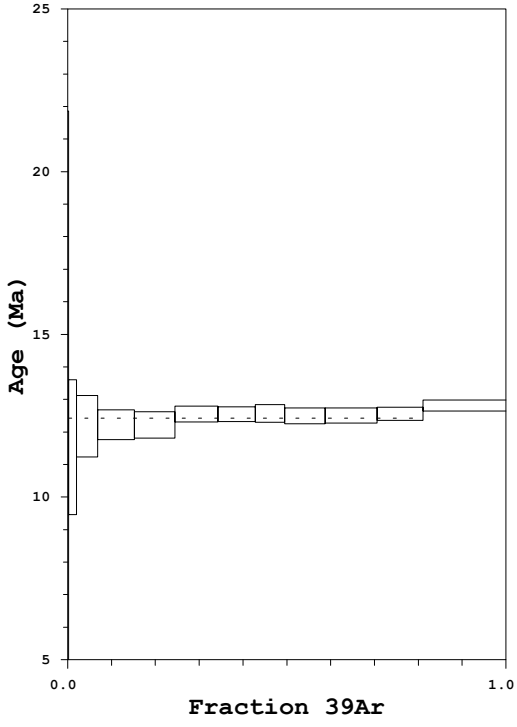


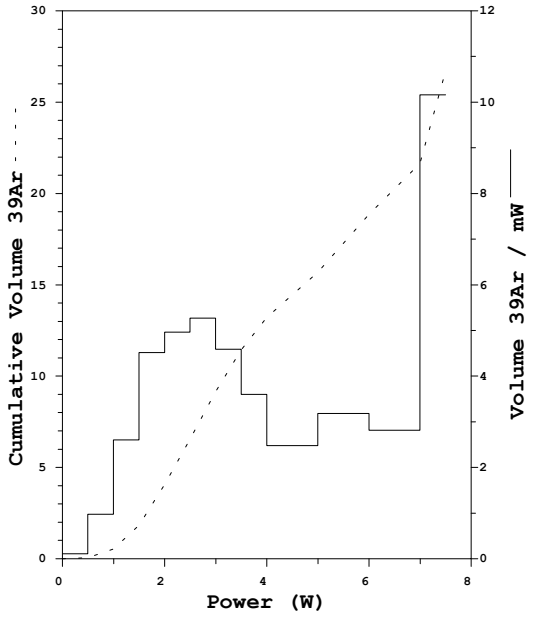


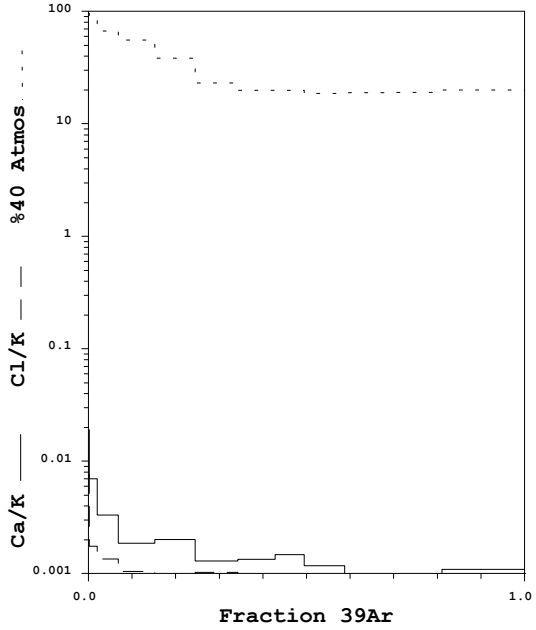


Measured volumes are x 1E-10 cm3 NTP. All errors are 2 x standard error. Intrim13 28-Mar-02

## KL-6: MS-32B Bt HP

**Run date:** 2007/12/19 **Can/Pos:** 208/7 **J Value:** 0.003439
**Printed:** 2008/01/29 **Mass:** 0.0 mg ± 0.000022

**Volume 39K:** 28.53 x 1E-10 cm3 NTP **Approx.** % K
**Integrated Age:** 4.47 ± 0.09 Ma % Ca

**Initial 40/36:** 291.01 ± 17.10 (MSWD = 0.80, isochron between 0.50 and 2.00)
**Correlation Age:** 4.53 ± 0.12 Ma ( 89.5% of 39Ar, steps marked by >) **MSWD** 0.889

**Plateau Age:** 4.46 ± 0.09 Ma ( 89.5% of 39Ar, steps marked by <) **Mod. err.** 0.07

| Power | 36Ar/40Ar | 39Ar/40Ar | r | Ca/K | %40Atm | %39Ar | 40Ar*/39K | Age |
|---|---|---|---|---|---|---|---|---|
| 0.50 | 0.003364±0.000150 | 0.028989±0.000515 | 0.014 | 0.033 | 99.33 | 0.23 | 0.203±1.536 | 1.26±9.52 |
| 1.00 | 0.003100 0.000107 | 0.143521 0.000975 | 0.023 | 0.011 | 91.20 | 2.66 | 0.585 0.222 | 3.63 1.37 |
| < 1.50> | 0.002694 0.000077 | 0.301386 0.001430 | 0.023 | 0.005 | 78.86 | 7.07 | 0.678 0.076 | 4.20 0.47 |
| < 2.00> | 0.002346 0.000078 | 0.429007 0.001512 | 0.022 | 0.004 | 68.41 | 11.13 | 0.716 0.054 | 4.43 0.34 |
| < 2.50> | 0.001683 0.000081 | 0.692199 0.002515 | 0.028 | 0.003 | 48.68 | 11.42 | 0.727 0.035 | 4.50 0.22 |
| < 3.00> | 0.001365 0.000091 | 0.832060 0.003279 | 0.021 | 0.002 | 39.31 | 11.72 | 0.718 0.032 | 4.45 0.20 |
| < 3.50> | 0.001272 0.000077 | 0.889592 0.003936 | 0.028 | 0.002 | 36.56 | 10.97 | 0.702 0.026 | 4.35 0.16 |
| < 4.00> | 0.001120 0.000101 | 0.927296 0.003987 | 0.018 | 0.001 | 32.14 | 8.17 | 0.722 0.032 | 4.47 0.20 |
| < 4.50> | 0.001064 0.000121 | 0.934449 0.005045 | 0.020 | 0.002 | 30.53 | 7.59 | 0.734 0.039 | 4.55 0.24 |
| < 5.00> | 0.001038 0.000110 | 0.930600 0.004446 | 0.018 | 0.001 | 29.77 | 6.12 | 0.746 0.035 | 4.62 0.22 |
| < 6.00> | 0.000987 0.000096 | 0.970107 0.004867 | 0.026 | 0.001 | 28.29 | 8.27 | 0.731 0.030 | 4.53 0.18 |
| < 7.00> | 0.001027 0.000108 | 0.936476 0.005175 | 0.017 | 0.001 | 29.47 | 7.07 | 0.744 0.034 | 4.61 0.21 |
| 7.50 | 0.001002 0.000107 | 0.876465 0.003956 | 0.015 | 0.001 | 28.80 | 7.57 | 0.804 0.036 | 4.98 0.23 |

| Power | 40Ar | 39Ar | 38Ar | 37Ar | 36Ar | Blank 40Ar | Atmos 40/36 |
|---|---|---|---|---|---|---|---|
| 0.50 | 2.344±0.007 | 0.067±0.001 | 0.006±0.000 | 0.002±0.000 | 0.008±0.000 | 0.033 | 287.137 |
| 1.00 | 5.351 0.012 | 0.765 0.005 | 0.032 0.002 | 0.002 0.001 | 0.017 0.001 | 0.033 | 287.137 |
| < 1.50> | 6.789 0.012 | 2.032 0.009 | 0.071 0.002 | 0.003 0.001 | 0.019 0.001 | 0.033 | 287.137 |
| < 2.00> | 7.527 0.012 | 3.196 0.010 | 0.106 0.002 | 0.003 0.001 | 0.018 0.001 | 0.033 | 287.137 |
| < 2.50> | 4.838 0.010 | 3.280 0.009 | 0.101 0.002 | 0.002 0.000 | 0.008 0.000 | 0.033 | 287.137 |
| < 3.00> | 4.153 0.009 | 3.366 0.010 | 0.100 0.002 | 0.002 0.001 | 0.006 0.000 | 0.033 | 287.137 |
| < 3.50> | 3.644 0.010 | 3.150 0.011 | 0.091 0.002 | 0.002 0.001 | 0.005 0.000 | 0.033 | 287.137 |
| < 4.00> | 2.618 0.007 | 2.348 0.007 | 0.069 0.001 | 0.002 0.001 | 0.003 0.000 | 0.033 | 287.137 |
| < 4.50> | 2.414 0.008 | 2.179 0.009 | 0.065 0.002 | 0.002 0.001 | 0.003 0.000 | 0.033 | 287.137 |
| < 5.00> | 1.963 0.006 | 1.759 0.006 | 0.052 0.002 | 0.001 0.001 | 0.002 0.000 | 0.033 | 287.137 |
| < 6.00> | 2.536 0.009 | 2.375 0.008 | 0.070 0.001 | 0.002 0.001 | 0.003 0.000 | 0.033 | 287.137 |
| < 7.00> | 2.248 0.007 | 2.031 0.009 | 0.060 0.002 | 0.002 0.001 | 0.003 0.000 | 0.034 | 287.137 |
| 7.50 | 2.564 0.007 | 2.175 0.007 | 0.067 0.001 | 0.001 0.000 | 0.003 0.000 | 0.034 | 287.137 |

**Measured volumes are x 1E-10 cm3 NTP. All errors are 2 x standard error. Intrim13 28-Mar-02**

**KL-6: MS-32B Bt HP**

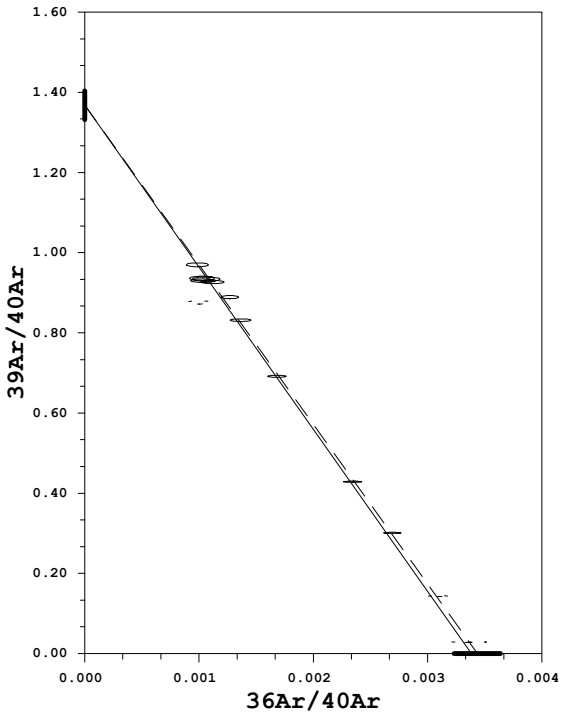


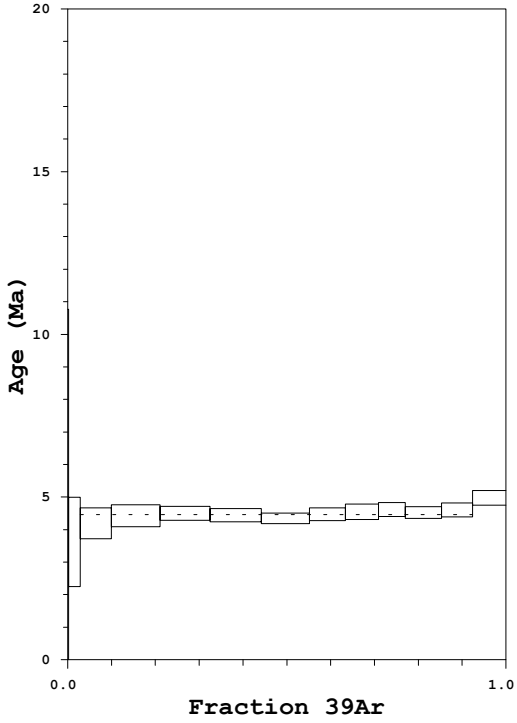


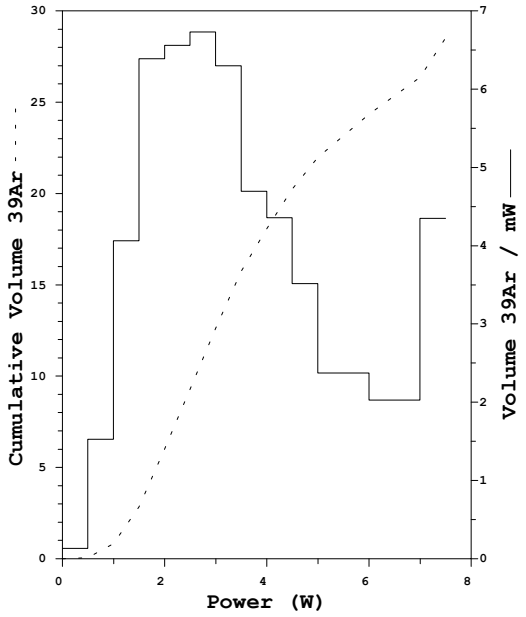


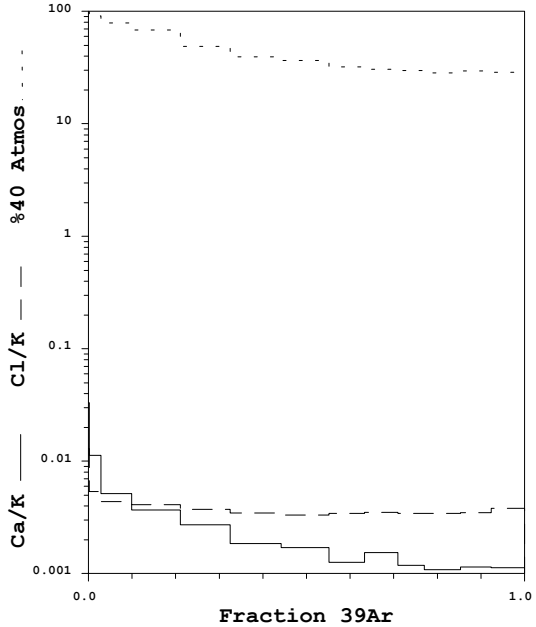


Measured volumes are x 1E-10 cm3 NTP. All errors are 2 x standard error. Intrim13 28-Mar-02

## KL-7: MS-16 Bt HP

**Run date:** 2010/12/19 **Can/Pos:** 208/12 **J Value:** 0.003449
**Printed:** 2008/01/29 **Mass:** 0.0 mg ± 0.000022

**Volume 39K:** 9.34 x 1E-10 cm3 NTP **Approx.** % K
**Integrated Age:** 52.62 ± 0.40 Ma % Ca

**Initial 40/36:** 557.92 ± 384.13 (MSWD = 4.70, isochron between 0.29 and 2.41)
**Correlation Age:** 50.52 ± 4.36 Ma ( 67.4% of 39Ar, steps marked by >) **MSWD** 7.677

**Plateau Age:** 53.89 ± 0.41 Ma ( 67.4% of 39Ar, steps marked by <) **Mod. err.** 0.62

| Power | 36Ar/40Ar | 39Ar/40Ar | r | Ca/K | %40Atm | %39Ar | 40Ar*/39K | Age |
|---|---|---|---|---|---|---|---|---|
| 0.50 | 0.002761±0.000128 | 0.040125±0.000466 | 0.012 | 0.276 | 81.48 | 1.47 | 4.592±0.950 | 28.35±5.82 |
| 1.50 | 0.000579 0.000029 | 0.108706 0.000487 | 0.006 | 0.065 | 17.03 | 23.52 | 7.628 0.087 | 46.85 0.53 |
| < 2.00> | 0.000226 0.000026 | 0.108258 0.000489 | 0.004 | 0.015 | 6.64 | 16.20 | 8.622 0.082 | 52.86 0.50 |
| < 2.50> | 0.000253 0.000026 | 0.104981 0.000572 | 0.004 | 0.014 | 7.42 | 12.60 | 8.816 0.088 | 54.04 0.53 |
| < 3.00> | 0.000274 0.000025 | 0.102972 0.000521 | 0.005 | 0.013 | 8.04 | 15.10 | 8.928 0.086 | 54.72 0.52 |
| < 3.50> | 0.000225 0.000028 | 0.105978 0.000642 | 0.004 | 0.010 | 6.61 | 8.89 | 8.811 0.096 | 54.01 0.58 |
| < 4.00> | 0.000191 0.000033 | 0.108741 0.000592 | 0.004 | 0.009 | 5.59 | 6.81 | 8.681 0.103 | 53.22 0.62 |
| < 5.00> | 0.000158 0.000030 | 0.106970 0.000674 | 0.002 | 0.009 | 4.63 | 7.76 | 8.914 0.100 | 54.63 0.60 |
| 6.00 | 0.000163 0.000041 | 0.103441 0.000691 | 0.001 | 0.009 | 4.78 | 4.67 | 9.204 0.134 | 56.38 0.81 |
| 7.00 | 0.000314 0.000131 | 0.086014 0.001309 | 0.003 | 0.009 | 9.23 | 1.00 | 10.550 0.480 | 64.48 2.88 |
| 7.50 | 0.000228 0.000065 | 0.070457 0.000699 | 0.002 | 0.012 | 6.69 | 1.99 | 13.241 0.305 | 80.56 1.81 |

| Power | 40Ar | 39Ar | 38Ar | 37Ar | 36Ar | Blank 40Ar | Atmos 40/36 |
|---|---|---|---|---|---|---|---|
| 0.50 | 3.456±0.008 | 0.138±0.002 | 0.011±0.001 | 0.007±0.001 | 0.010±0.000 | 0.033 | 287.137 |
| 1.50 | 20.313 0.023 | 2.212 0.009 | 0.172 0.005 | 0.024 0.002 | 0.012 0.001 | 0.033 | 287.137 |
| < 2.00> | 14.059 0.020 | 1.524 0.006 | 0.120 0.003 | 0.005 0.001 | 0.004 0.000 | 0.033 | 287.137 |
| < 2.50> | 11.286 0.016 | 1.186 0.006 | 0.095 0.002 | 0.004 0.001 | 0.003 0.000 | 0.034 | 287.137 |
| < 3.00> | 13.780 0.020 | 1.421 0.007 | 0.115 0.003 | 0.004 0.001 | 0.004 0.000 | 0.033 | 287.137 |
| < 3.50> | 7.896 0.014 | 0.836 0.005 | 0.068 0.002 | 0.002 0.001 | 0.002 0.000 | 0.034 | 287.137 |
| < 4.00> | 5.907 0.012 | 0.641 0.003 | 0.051 0.002 | 0.002 0.000 | 0.001 0.000 | 0.034 | 287.137 |
| < 5.00> | 6.836 0.011 | 0.730 0.004 | 0.058 0.002 | 0.002 0.001 | 0.001 0.000 | 0.033 | 287.137 |
| 6.00 | 4.264 0.008 | 0.439 0.003 | 0.035 0.001 | 0.002 0.001 | 0.001 0.000 | 0.034 | 287.137 |
| 7.00 | 1.119 0.006 | 0.094 0.001 | 0.008 0.001 | 0.001 0.000 | 0.001 0.000 | 0.033 | 287.137 |
| 7.50 | 2.674 0.007 | 0.187 0.002 | 0.015 0.001 | 0.002 0.001 | 0.001 0.000 | 0.033 | 287.137 |

**Measured volumes are x 1E-10 cm3 NTP.** **All errors are 2 x standard error.** **Intrim13 28-Mar-02**

**KL-7: MS-16 Bt HP**

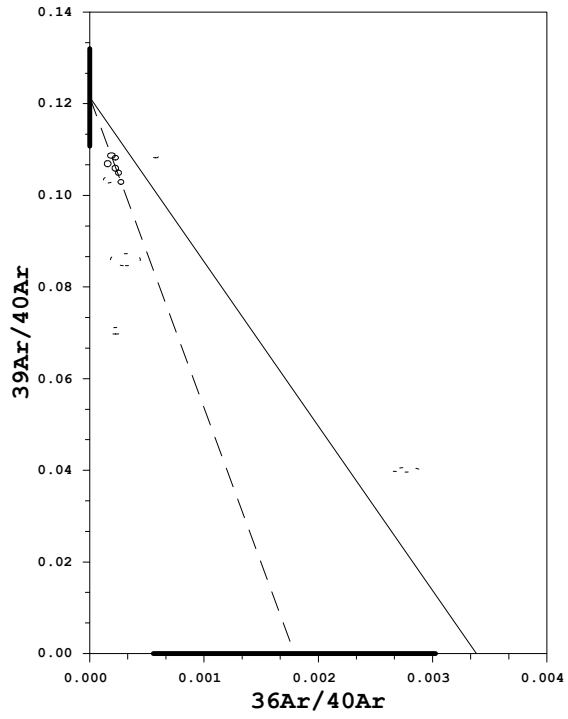


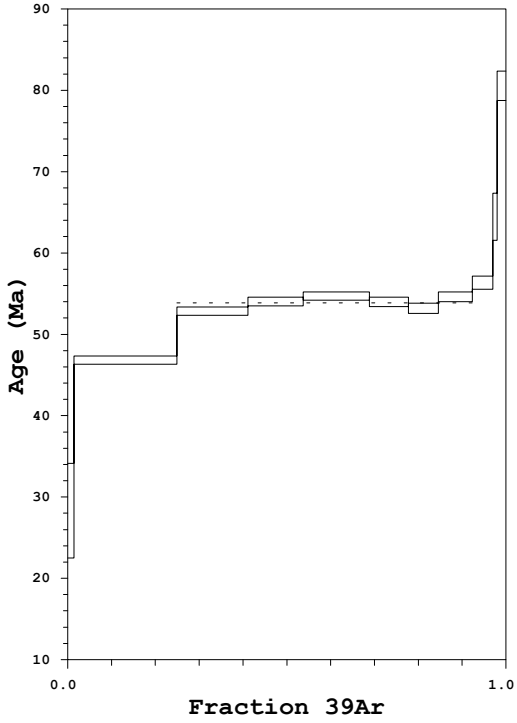


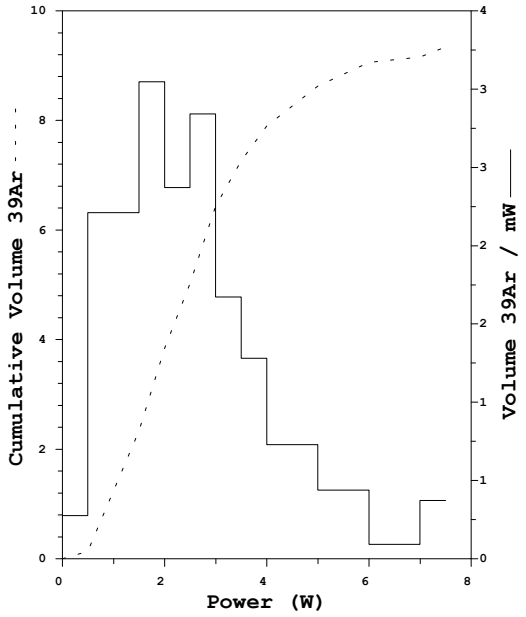


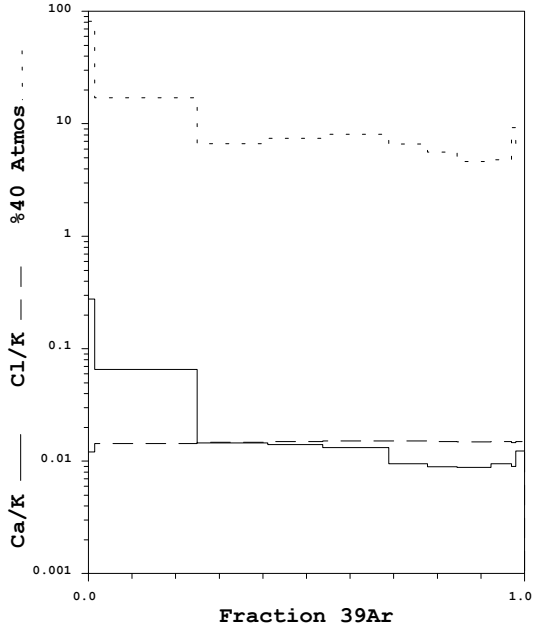


Measured volumes are x 1E-10 cm3 NTP. All errors are 2 x standard error. Intrim13 28-Mar-02

## KL-8: MS-30 Mu HP

**Run date:** 2007/12/20 **Can/Pos:** 208/9 **J Value:** 0.003444
**Printed:** 2008/01/29 **Mass:** 0.0 mg ± 0.000022

**Volume 39K:** 14.52 x 1E-10 cm3 NTP **Approx. % K**
**Integrated Age:** 4.46 ± 0.14 Ma 14.28% Ca

**Initial 40/36:** 288.43 ± 39.40 (MSWD = 0.75, isochron between 0.47 and 2.07)
**Correlation Age:** 4.47 ± 0.31 Ma ( 94.2% of 39Ar, steps marked by >) **MSWD** 0.442

**Plateau Age:** 4.34 ± 0.14 Ma ( 94.2% of 39Ar, steps marked by <) **Mod. err.** 0.19

| Power | 36Ar/40Ar | 39Ar/40Ar | r | Ca/K | %40Atm | %39Ar | 40Ar*/39K | Age |
|---|---|---|---|---|---|---|---|---|
| 0.50 | 0.003056±0.000215 | 0.020060±0.000652 | 0.013 | 0.000 | 90.24 | 0.14 | 4.838±3.171 | 29.81±19.38 |
| < 1.50> | 0.002793 0.000095 | 0.234340 0.001410 | 0.032 | 0.004 | 81.97 | 6.45 | 0.745 0.121 | 4.62 0.75 |
| < 2.00> | 0.002566 0.000077 | 0.360962 0.001493 | 0.027 | 0.001 | 75.01 | 16.01 | 0.670 0.064 | 4.16 0.40 |
| < 2.50> | 0.001933 0.000097 | 0.607302 0.002152 | 0.028 | 0.000 | 56.09 | 19.96 | 0.706 0.047 | 4.38 0.29 |
| < 3.00> | 0.002044 0.000088 | 0.573913 0.002337 | 0.031 | 0.001 | 59.37 | 16.19 | 0.690 0.045 | 4.28 0.28 |
| < 3.50> | 0.001641 0.000119 | 0.738740 0.003819 | 0.026 | 0.001 | 47.44 | 12.16 | 0.697 0.048 | 4.33 0.30 |
| < 4.00> | 0.001435 0.000158 | 0.811994 0.005201 | 0.024 | 0.001 | 41.40 | 7.46 | 0.709 0.058 | 4.40 0.36 |
| < 5.00> | 0.001538 0.000185 | 0.794889 0.005058 | 0.022 | 0.001 | 44.39 | 7.04 | 0.686 0.069 | 4.26 0.43 |
| < 6.00> | 0.001443 0.000207 | 0.809359 0.005465 | 0.019 | 0.001 | 41.63 | 5.99 | 0.709 0.076 | 4.40 0.47 |
| < 7.00> | 0.001178 0.000303 | 0.852563 0.008400 | 0.011 | 0.000 | 33.94 | 2.95 | 0.765 0.105 | 4.74 0.65 |
| 7.50 | 0.000661 0.000188 | 0.872786 0.006438 | 0.008 | 0.001 | 19.04 | 5.64 | 0.922 0.064 | 5.72 0.40 |

| Power | 40Ar | 39Ar | 38Ar | 37Ar | 36Ar | Blank 40Ar | Atmos 40/36 |
|---|---|---|---|---|---|---|---|
| 0.50 | 1.086±0.005 | 0.021±0.001 | 0.001±0.000 | 0.001±0.000 | 0.004±0.000 | 0.038 | 287.137 |
| < 1.50> | 4.062 0.010 | 0.943 0.005 | 0.014 0.001 | 0.001 0.000 | 0.012 0.000 | 0.039 | 287.137 |
| < 2.00> | 6.547 0.012 | 2.340 0.009 | 0.033 0.001 | 0.002 0.000 | 0.017 0.000 | 0.038 | 287.137 |
| < 2.50> | 4.897 0.010 | 2.918 0.008 | 0.038 0.001 | 0.001 0.000 | 0.010 0.000 | 0.038 | 287.137 |
| < 3.00> | 4.206 0.009 | 2.367 0.008 | 0.031 0.001 | 0.001 0.000 | 0.009 0.000 | 0.038 | 287.137 |
| < 3.50> | 2.482 0.007 | 1.778 0.007 | 0.023 0.001 | 0.001 0.000 | 0.004 0.000 | 0.038 | 287.137 |
| < 4.00> | 1.405 0.006 | 1.090 0.005 | 0.014 0.001 | 0.001 0.000 | 0.002 0.000 | 0.039 | 287.137 |
| < 5.00> | 1.356 0.005 | 1.030 0.005 | 0.013 0.001 | 0.001 0.000 | 0.002 0.000 | 0.039 | 287.137 |
| < 6.00> | 1.141 0.005 | 0.876 0.004 | 0.011 0.001 | 0.001 0.000 | 0.002 0.000 | 0.039 | 287.137 |
| < 7.00> | 0.553 0.003 | 0.431 0.003 | 0.006 0.001 | 0.001 0.000 | 0.001 0.000 | 0.038 | 287.137 |
| 7.50 | 1.003 0.005 | 0.825 0.004 | 0.010 0.001 | 0.001 0.000 | 0.001 0.000 | 0.040 | 287.137 |

**Measured volumes are x 1E-10 cm3 NTP.** **All errors are 2 x standard error.** **Intrim13 28-Mar-02**

**KYL-8: MS-30 Mu HP**

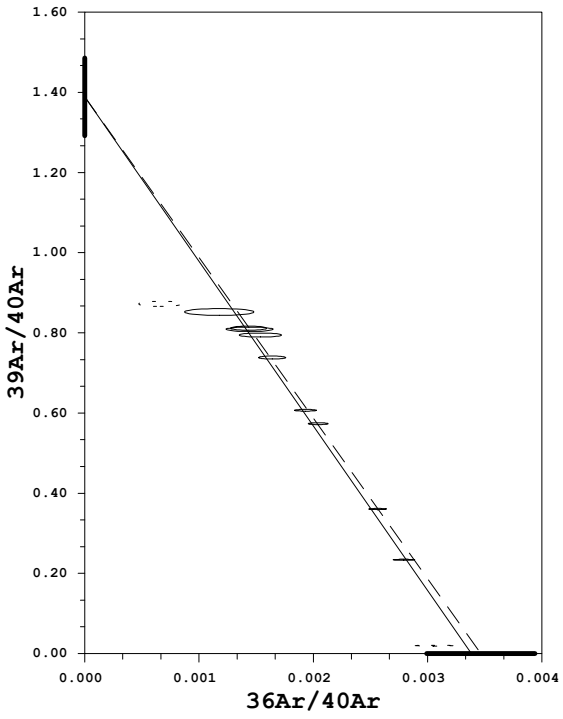


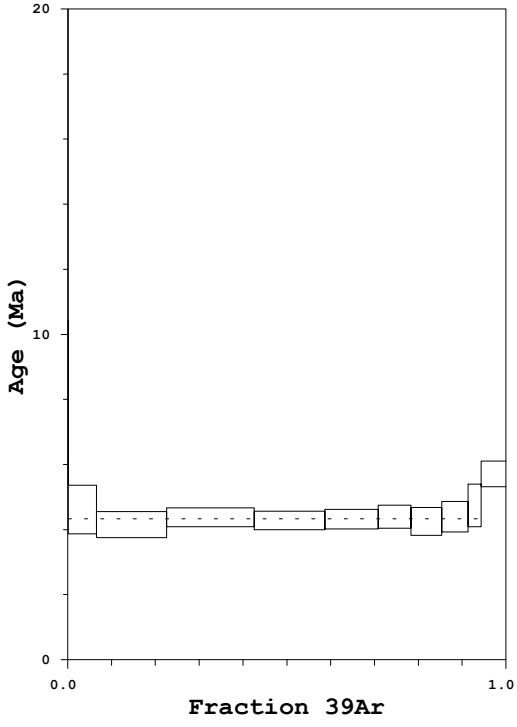


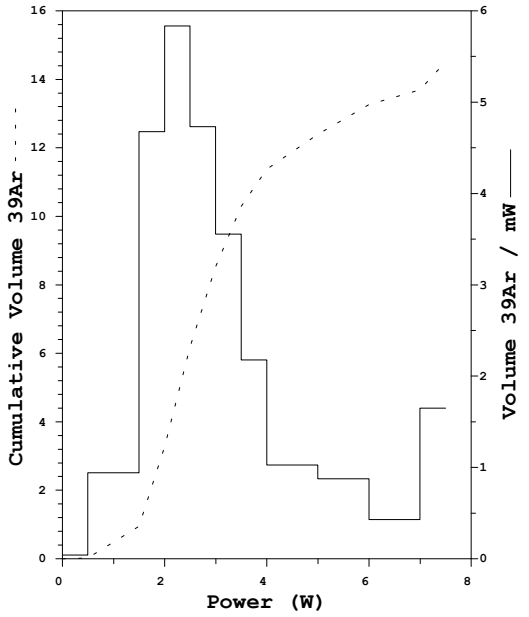


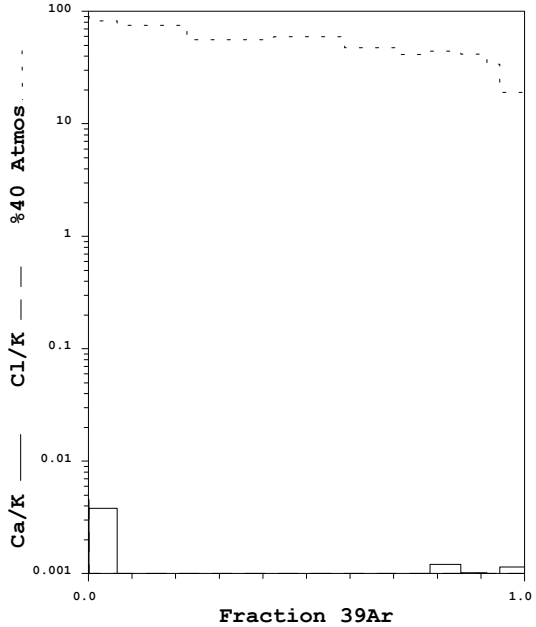


Measured volumes are x 1E-10 cm3 NTP. All errors are 2 x standard error. Intrim13 28-Mar-02

## KL-9: MS-30 Bt HP

**Run date:** 2007/12/20 **Can/Pos:** 208/8 **J Value:** 0.003442
**Printed:** 2008/01/29 **Mass:** 0.0 mg ± 0.000022

**Volume 39K:** 13.33 x 1E-10 cm3 NTP **Approx.** % K
**Integrated Age:** 2.62 ± 0.16 Ma % Ca

**Initial 40/36:** 280.95 ± 123.66 (MSWD = 0.53, isochron between 0.37 and 2.26)
**Correlation Age:** 2.93 ± 0.68 Ma ( 95.1% of 39Ar, steps marked by >) **MSWD** 0.633

**Plateau Age:** 2.60 ± 0.15 Ma ( 95.1% of 39Ar, steps marked by <) **Mod. err.** 0.15

| Power | 36Ar/40Ar | 39Ar/40Ar | r | Ca/K | %40Atm | %39Ar | 40Ar*/39K | Age |
|---|---|---|---|---|---|---|---|---|
| 0.50 | 0.003352±0.000174 | 0.034674±0.000600 | 0.015 | 0.019 | 98.95 | 0.47 | 0.273±1.482 | 1.69±9.19 |
| < 1.50> | 0.003095 0.000080 | 0.241346 0.001134 | 0.038 | 0.002 | 90.78 | 16.70 | 0.355 0.099 | 2.20 0.61 |
| < 2.00> | 0.002426 0.000093 | 0.675092 0.002881 | 0.038 | 0.001 | 70.21 | 17.28 | 0.420 0.041 | 2.61 0.26 |
| < 2.50> | 0.001943 0.000147 | 0.957043 0.005008 | 0.032 | 0.001 | 55.75 | 12.68 | 0.446 0.046 | 2.76 0.28 |
| < 3.00> | 0.001901 0.000153 | 0.983813 0.005480 | 0.036 | 0.001 | 54.50 | 11.75 | 0.446 0.046 | 2.77 0.29 |
| < 3.50> | 0.002138 0.000194 | 0.867661 0.004798 | 0.030 | 0.001 | 61.50 | 10.16 | 0.425 0.066 | 2.64 0.41 |
| < 4.00> | 0.002147 0.000195 | 0.864024 0.004945 | 0.029 | 0.001 | 61.79 | 10.13 | 0.424 0.067 | 2.63 0.41 |
| < 6.00> | 0.002213 0.000114 | 0.785523 0.003322 | 0.033 | 0.000 | 63.84 | 16.40 | 0.441 0.043 | 2.74 0.27 |
| 7.00 | 0.002331 0.000387 | 0.661410 0.006608 | 0.024 | 0.000 | 67.50 | 2.90 | 0.471 0.173 | 2.92 1.07 |
| 7.50 | 0.002241 0.000573 | 0.592100 0.008457 | 0.023 | 0.003 | 65.01 | 1.54 | 0.571 0.286 | 3.54 1.77 |

| Power | 40Ar | 39Ar | 38Ar | 37Ar | 36Ar | Blank 40Ar | Atmos 40/36 |
|---|---|---|---|---|---|---|---|
| 0.50 | 1.844±0.006 | 0.063±0.001 | 0.004±0.000 | 0.001±0.000 | 0.007±0.000 | 0.039 | 287.137 |
| < 1.50> | 9.330 0.020 | 2.241 0.009 | 0.078 0.002 | 0.002 0.000 | 0.030 0.001 | 0.039 | 287.137 |
| < 2.00> | 3.519 0.008 | 2.319 0.008 | 0.072 0.002 | 0.002 0.000 | 0.009 0.000 | 0.039 | 287.137 |
| < 2.50> | 1.856 0.006 | 1.702 0.006 | 0.052 0.001 | 0.001 0.000 | 0.004 0.000 | 0.039 | 287.137 |
| < 3.00> | 1.678 0.006 | 1.577 0.006 | 0.049 0.001 | 0.001 0.000 | 0.003 0.000 | 0.039 | 287.137 |
| < 3.50> | 1.640 0.006 | 1.363 0.005 | 0.042 0.001 | 0.001 0.000 | 0.004 0.000 | 0.039 | 287.137 |
| < 4.00> | 1.642 0.006 | 1.360 0.005 | 0.041 0.001 | 0.001 0.000 | 0.004 0.000 | 0.039 | 287.137 |
| < 6.00> | 2.887 0.007 | 2.200 0.007 | 0.068 0.002 | 0.001 0.000 | 0.007 0.000 | 0.040 | 287.137 |
| 7.00 | 0.634 0.004 | 0.389 0.003 | 0.012 0.001 | 0.001 0.000 | 0.002 0.000 | 0.039 | 287.137 |
| 7.50 | 0.391 0.003 | 0.206 0.002 | 0.006 0.001 | 0.001 0.000 | 0.001 0.000 | 0.039 | 287.137 |

**Measured volumes are x 1E-10 cm3 NTP.** **All errors are 2 x standard error.** **Intrim13 28-Mar-02**

**KL-9: MS-30 Bt HP**

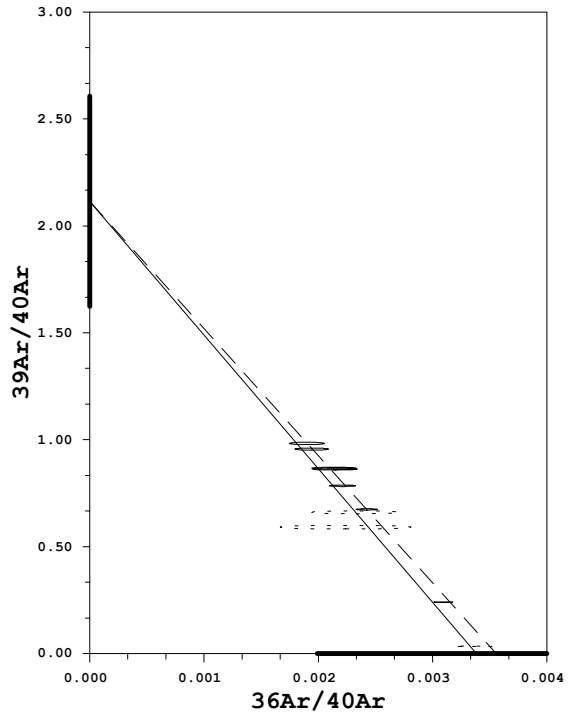


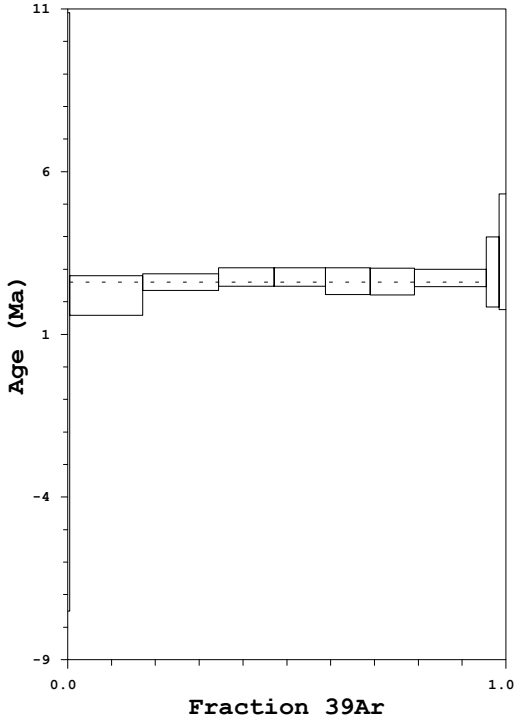


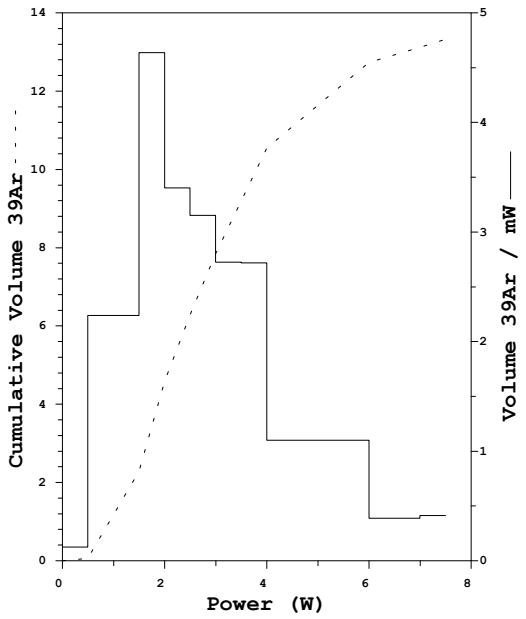


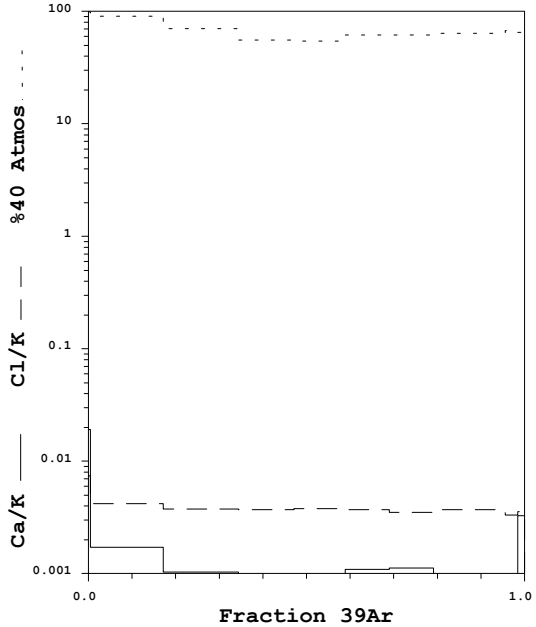


Measured volumes are x 1E-10 cm3 NTP. All errors are 2 x standard error. Intrim13 28-Mar-02

## KL-10: MS-23B Mu HP

**Run date:** 2007/12/21 **Can/Pos:** 208/11 **J Value:** 0.003447
**Printed:** 2008/01/29 **Mass:** 0.0 mg ± 0.000022

**Volume 39K:** 6.45 x 1E-10 cm3 NTP **Approx. % K**
**Integrated Age:** 3.23 ± 0.24 Ma 3.81% Ca

**Initial 40/36:** 302.12 ± 96.13 (MSWD = 0.37, isochron between 0.42 and 2.15)
**Correlation Age:** 2.98 ± 0.56 Ma ( 99.6% of 39Ar, steps marked by >) **MSWD** 0.217

**Plateau Age:** 3.07 ± 0.20 Ma ( 87.1% of 39Ar, steps marked by <) **Mod. err.** 0.41

| Power | 36Ar/40Ar | 39Ar/40Ar | r | Ca/K | %40Atm | %39Ar | 40Ar*/39K | Age |
|---|---|---|---|---|---|---|---|---|
| 0.75 | 0.003246±0.000285 | 0.030188±0.000867 | 0.017 | 0.021 | 95.82 | 0.41 | 1.355±2.785 | 8.40±17.24 |
| 1.50> | 0.003107 0.000210 | 0.097942 0.001288 | 0.015 | 0.004 | 91.53 | 2.12 | 0.837 0.634 | 5.20 3.93 |
| 2.00> | 0.002969 0.000120 | 0.190860 0.001066 | 0.024 | 0.000 | 87.23 | 10.38 | 0.643 0.187 | 3.99 1.16 |
| < 2.50> | 0.002310 0.000102 | 0.654230 0.002869 | 0.038 | 0.000 | 66.95 | 31.77 | 0.485 0.047 | 3.01 0.29 |
| < 3.00> | 0.001933 0.000184 | 0.862418 0.004784 | 0.028 | 0.001 | 55.67 | 22.59 | 0.497 0.063 | 3.09 0.39 |
| < 3.50> | 0.002044 0.000320 | 0.858183 0.007946 | 0.026 | 0.000 | 58.89 | 8.59 | 0.461 0.110 | 2.87 0.68 |
| < 5.00> | 0.002117 0.000338 | 0.721622 0.006124 | 0.022 | 0.002 | 61.23 | 7.95 | 0.519 0.139 | 3.22 0.86 |
| < 7.00> | 0.001783 0.000289 | 0.952934 0.008321 | 0.029 | 0.000 | 51.21 | 8.90 | 0.496 0.090 | 3.08 0.56 |
| < 7.50> | 0.001414 0.000436 | 1.090274 0.011702 | 0.017 | 0.001 | 40.46 | 7.29 | 0.534 0.118 | 3.32 0.74 |

| Power | 40Ar | 39Ar | 38Ar | 37Ar | 36Ar | Blank 40Ar | Atmos 40/36 |
|---|---|---|---|---|---|---|---|
| 0.75 | 0.902±0.005 | 0.026±0.001 | 0.002±0.000 | 0.001±0.000 | 0.003±0.000 | 0.034 | 287.137 |
| 1.50> | 1.432 0.005 | 0.138 0.002 | 0.003 0.000 | 0.001 0.000 | 0.005 0.000 | 0.034 | 287.137 |
| 2.00> | 3.562 0.008 | 0.674 0.003 | 0.011 0.001 | 0.001 0.000 | 0.011 0.000 | 0.034 | 287.137 |
| < 2.50> | 3.228 0.008 | 2.063 0.007 | 0.027 0.001 | 0.001 0.000 | 0.008 0.000 | 0.034 | 287.137 |
| < 3.00> | 1.768 0.006 | 1.467 0.006 | 0.019 0.001 | 0.001 0.000 | 0.004 0.000 | 0.034 | 287.137 |
| < 3.50> | 0.695 0.004 | 0.558 0.004 | 0.007 0.001 | 0.001 0.000 | 0.002 0.000 | 0.033 | 287.137 |
| < 5.00> | 0.760 0.004 | 0.517 0.003 | 0.007 0.001 | 0.001 0.000 | 0.002 0.000 | 0.034 | 287.137 |
| < 7.00> | 0.654 0.004 | 0.578 0.003 | 0.008 0.001 | 0.001 0.000 | 0.001 0.000 | 0.034 | 287.137 |
| < 7.50> | 0.479 0.004 | 0.474 0.003 | 0.006 0.000 | 0.001 0.000 | 0.001 0.000 | 0.033 | 287.137 |

**Measured volumes are x 1E-10 cm3 NTP. All errors are 2 x standard error. Intrim13 28-Mar-02**

**KL-10: MS-23B Mu HP**

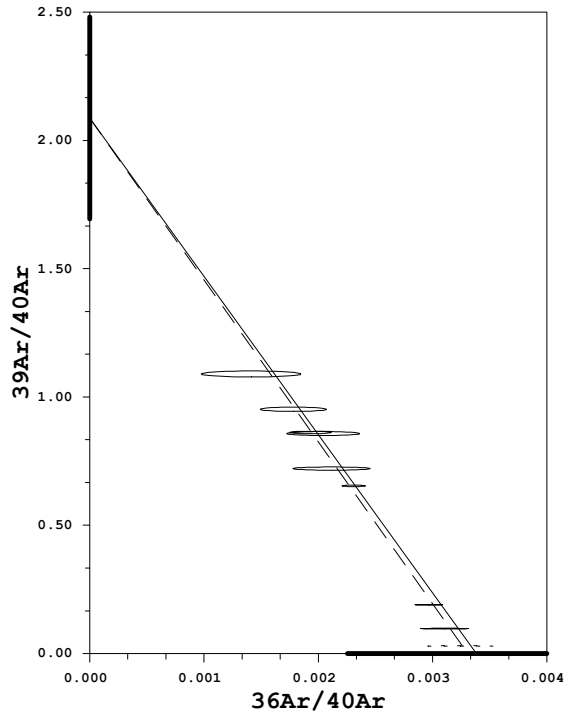


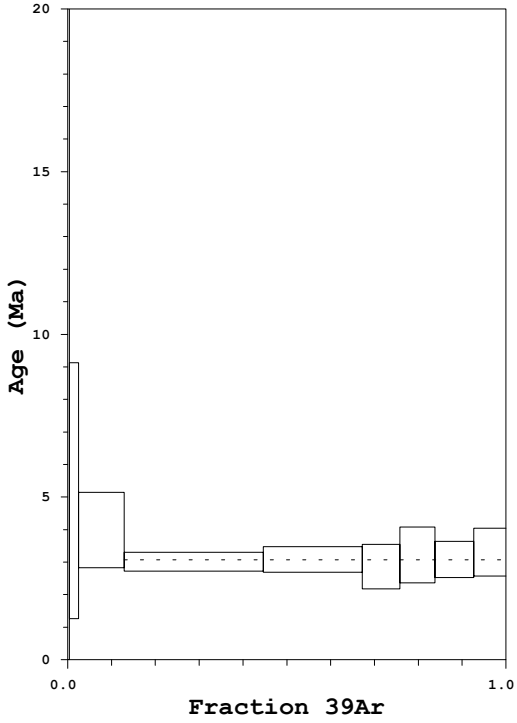


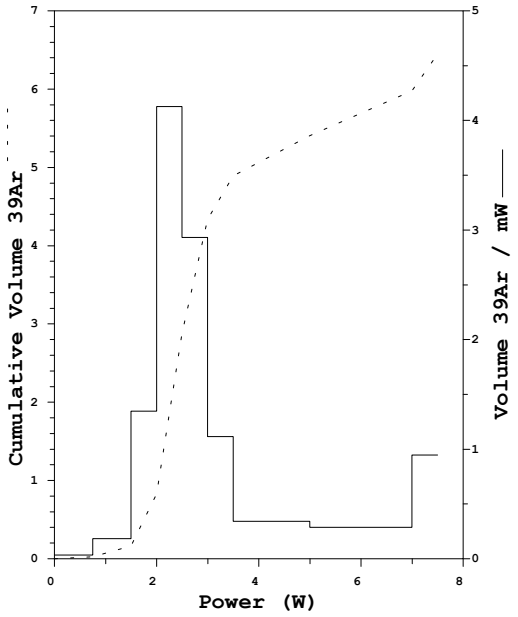


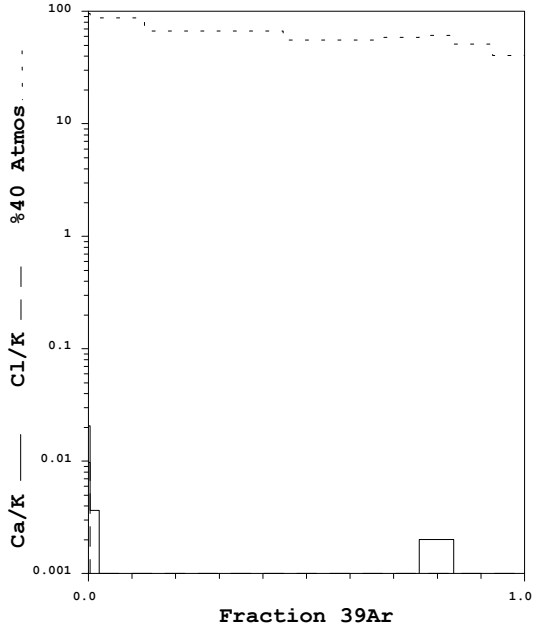


Measured volumes are x 1E-10 cm3 NTP. All errors are 2 x standard error. Intrim13 28-Mar-02

## KL-11: MS-23B Bt HP

**Run date:** 2007/12/21 **Can/Pos:** 208/10 **J Value:** 0.003445
**Printed:** 2008/01/29 **Mass:** 0.0 mg ± 0.000022

**Volume 39K:** 17.22 x 1E-10 cm3 NTP **Approx.** % K
**Integrated Age:** 3.82 ± 0.12 Ma % Ca

**Initial 40/36:** 291.35 ± 80.76 (MSWD = 0.07, isochron between 0.53 and 1.94)
**Correlation Age:** 3.90 ± 0.52 Ma ( 99.8% of 39Ar, steps marked by >) **MSWD** 0.162

**Plateau Age:** 3.83 ± 0.12 Ma ( 99.8% of 39Ar, steps marked by <) **Mod. err.** 0.23

| Power | 36Ar/40Ar | 39Ar/40Ar | r | Ca/K | %40Atm | %39Ar | 40Ar*/39K | Age |
|---|---|---|---|---|---|---|---|---|
| 0.50 | 0.003354±0.000199 | 0.023502±0.000631 | 0.015 | 0.036 | 99.04 | 0.24 | 0.377±2.503 | 2.34±15.54 |
| < 1.00> | 0.003162 0.000132 | 0.124806 0.000928 | 0.017 | 0.010 | 93.08 | 2.38 | 0.526 0.314 | 3.27 1.95 |
| < 1.50> | 0.002817 0.000098 | 0.284839 0.001225 | 0.026 | 0.005 | 82.52 | 8.74 | 0.589 0.102 | 3.66 0.64 |
| < 2.00> | 0.002291 0.000107 | 0.523493 0.002327 | 0.030 | 0.003 | 66.61 | 11.43 | 0.618 0.060 | 3.83 0.38 |
| < 2.50> | 0.001866 0.000121 | 0.736450 0.003756 | 0.027 | 0.003 | 53.92 | 11.42 | 0.609 0.049 | 3.78 0.30 |
| < 3.00> | 0.001648 0.000115 | 0.826528 0.003601 | 0.028 | 0.003 | 47.48 | 11.97 | 0.621 0.041 | 3.86 0.26 |
| < 3.50> | 0.001363 0.000162 | 0.961303 0.004661 | 0.016 | 0.002 | 39.09 | 11.05 | 0.622 0.050 | 3.86 0.31 |
| < 4.00> | 0.001195 0.000151 | 1.024198 0.006797 | 0.028 | 0.001 | 34.21 | 9.13 | 0.632 0.044 | 3.92 0.27 |
| < 5.00> | 0.001148 0.000124 | 1.049195 0.005204 | 0.020 | 0.002 | 32.85 | 11.96 | 0.630 0.035 | 3.91 0.22 |
| < 6.00> | 0.001138 0.000128 | 1.064228 0.005546 | 0.021 | 0.002 | 32.54 | 11.18 | 0.624 0.036 | 3.87 0.22 |
| < 7.00> | 0.001108 0.000165 | 1.095158 0.007602 | 0.023 | 0.001 | 31.66 | 6.86 | 0.614 0.045 | 3.82 0.28 |
| < 7.50> | 0.001304 0.000279 | 0.993557 0.007703 | 0.017 | 0.006 | 37.37 | 3.64 | 0.619 0.083 | 3.84 0.52 |

| Power | 40Ar | 39Ar | 38Ar | 37Ar | 36Ar | Blank 40Ar | Atmos 40/36 |
|---|---|---|---|---|---|---|---|
| 0.50 | 1.802±0.008 | 0.042±0.001 | 0.003±0.000 | 0.001±0.000 | 0.006±0.000 | 0.035 | 287.137 |
| < 1.00> | 3.332 0.008 | 0.413 0.003 | 0.014 0.001 | 0.002 0.000 | 0.011 0.000 | 0.034 | 287.137 |
| < 1.50> | 5.365 0.010 | 1.516 0.006 | 0.042 0.001 | 0.002 0.001 | 0.016 0.001 | 0.034 | 287.137 |
| < 2.00> | 3.855 0.009 | 1.982 0.007 | 0.050 0.001 | 0.002 0.000 | 0.009 0.000 | 0.034 | 287.137 |
| < 2.50> | 2.765 0.008 | 1.981 0.008 | 0.049 0.002 | 0.002 0.000 | 0.005 0.000 | 0.034 | 287.137 |
| < 3.00> | 2.590 0.007 | 2.076 0.006 | 0.051 0.001 | 0.002 0.001 | 0.005 0.000 | 0.034 | 287.137 |
| < 3.50> | 2.071 0.006 | 1.916 0.007 | 0.047 0.001 | 0.002 0.000 | 0.003 0.000 | 0.035 | 287.137 |
| < 4.00> | 1.617 0.008 | 1.583 0.007 | 0.039 0.001 | 0.001 0.000 | 0.002 0.000 | 0.034 | 287.137 |
| < 5.00> | 2.060 0.007 | 2.074 0.007 | 0.051 0.001 | 0.002 0.000 | 0.003 0.000 | 0.034 | 287.137 |
| < 6.00> | 1.901 0.007 | 1.938 0.007 | 0.047 0.001 | 0.002 0.000 | 0.002 0.000 | 0.034 | 287.137 |
| < 7.00> | 1.149 0.005 | 1.190 0.005 | 0.029 0.001 | 0.001 0.000 | 0.002 0.000 | 0.034 | 287.137 |
| < 7.50> | 0.684 0.004 | 0.631 0.003 | 0.015 0.001 | 0.002 0.000 | 0.001 0.000 | 0.035 | 287.137 |

**Measured volumes are x 1E-10 cm3 NTP. All errors are 2 x standard error. Intrim13 28-Mar-02**

**KL-11: MS-23B Bt HP**

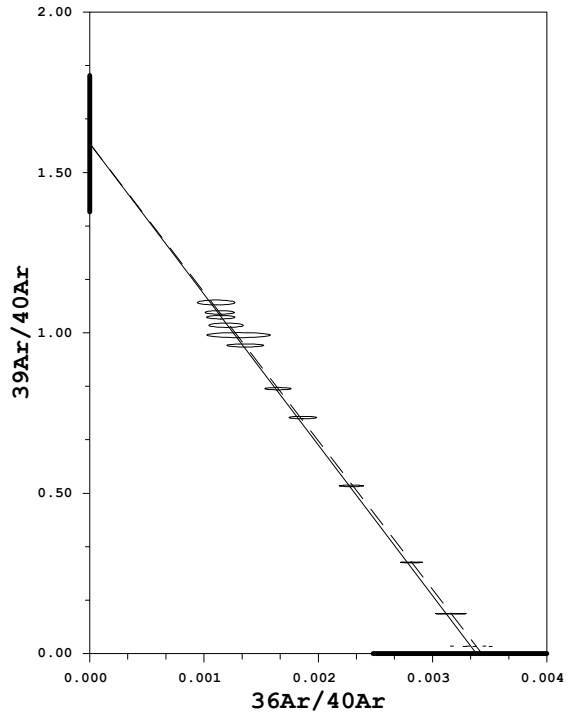


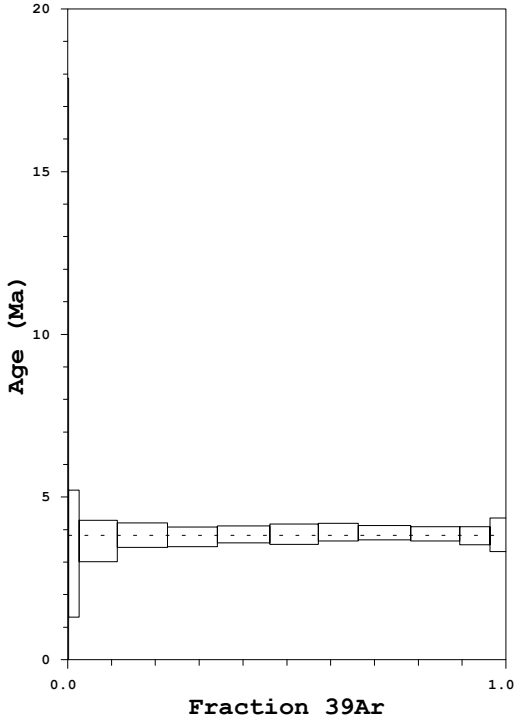


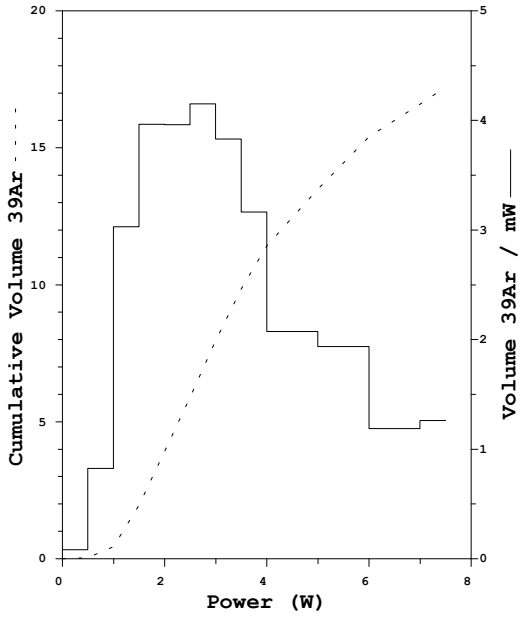


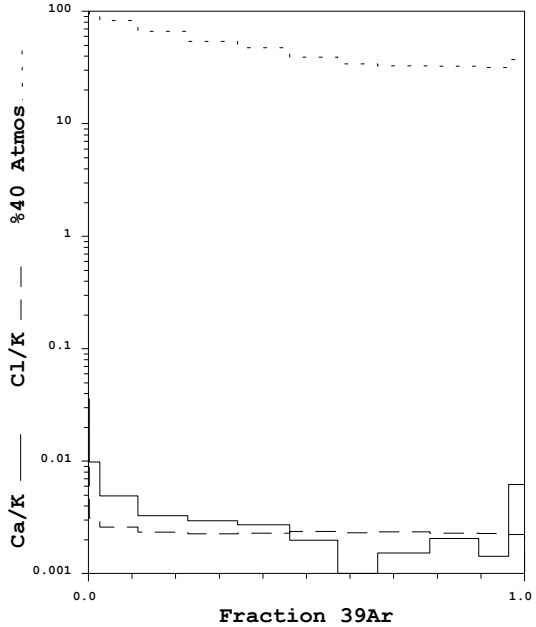


Measured volumes are x 1E-10 cm3 NTP. All errors are 2 x standard error. Intrim13 28-Mar-02

## KL-12: MS-43 Mu HP

**Run date:** 2007/12/22 **Can/Pos:** 208/3 **J Value:** 0.003433
**Printed:** 2008/01/29 **Mass:** 0.0 mg ± 0.000020

**Volume 39K:** 20.16 x 1E-10 cm3 NTP **Approx.** % K
**Integrated Age:** 15.26 ± 0.16 Ma % Ca

**Initial 40/36:** 284.61 ± 18.12 (MSWD = 0.57, isochron between 0.42 and 2.15)
**Correlation Age:** 15.50 ± 0.31 Ma ( 77.0% of 39Ar, steps marked by >) **MSWD** 0.953

**Plateau Age:** 15.19 ± 0.18 Ma ( 77.0% of 39Ar, steps marked by <) **Mod. err.** 0.14

| Power | 36Ar/40Ar | 39Ar/40Ar | r | Ca/K | %40Atm | %39Ar | 40Ar*/39K | Age |
|---|---|---|---|---|---|---|---|---|
| 0.75 | 0.003248±0.000169 | 0.021618±0.000435 | 0.011 | 0.003 | 95.92 | 0.23 | 1.856±2.312 | 11.46±14.23 |
| 1.50 | 0.002747 0.000149 | 0.074871 0.000779 | 0.015 | 0.005 | 81.00 | 0.82 | 2.513 0.591 | 15.50 3.63 |
| < 2.00> | 0.002482 0.000098 | 0.112624 0.000625 | 0.013 | 0.004 | 73.09 | 2.69 | 2.367 0.258 | 14.60 1.58 |
| < 2.50> | 0.001597 0.000051 | 0.216379 0.000839 | 0.019 | 0.001 | 46.88 | 11.85 | 2.441 0.071 | 15.05 0.44 |
| < 3.00> | 0.001196 0.000046 | 0.261415 0.000920 | 0.015 | 0.001 | 35.05 | 19.36 | 2.474 0.053 | 15.26 0.33 |
| < 3.50> | 0.001177 0.000052 | 0.268491 0.000981 | 0.014 | 0.002 | 34.50 | 13.45 | 2.429 0.059 | 14.98 0.36 |
| < 4.00> | 0.000916 0.000048 | 0.295321 0.001062 | 0.014 | 0.002 | 26.82 | 10.35 | 2.470 0.049 | 15.23 0.30 |
| < 4.50> | 0.000633 0.000059 | 0.327621 0.001787 | 0.010 | 0.004 | 18.51 | 7.69 | 2.482 0.055 | 15.31 0.34 |
| < 5.00> | 0.000664 0.000084 | 0.319420 0.001736 | 0.007 | 0.011 | 19.45 | 4.25 | 2.516 0.079 | 15.52 0.48 |
| < 7.00> | 0.000556 0.000058 | 0.333310 0.001553 | 0.007 | 0.030 | 16.28 | 7.40 | 2.507 0.053 | 15.46 0.32 |
| 7.50 | 0.000105 0.000026 | 0.384858 0.001277 | 0.002 | 0.065 | 3.06 | 21.91 | 2.518 0.022 | 15.53 0.13 |

| Power | 40Ar | 39Ar | 38Ar | 37Ar | 36Ar | Blank 40Ar | Atmos 40/36 |
|---|---|---|---|---|---|---|---|
| 0.75 | 2.163±0.006 | 0.046±0.001 | 0.005±0.000 | 0.001±0.000 | 0.007±0.000 | 0.036 | 287.137 |
| 1.50 | 2.243 0.006 | 0.166 0.002 | 0.004 0.000 | 0.001 0.000 | 0.007 0.000 | 0.037 | 287.137 |
| < 2.00> | 4.873 0.008 | 0.547 0.003 | 0.009 0.001 | 0.002 0.000 | 0.013 0.000 | 0.037 | 287.137 |
| < 2.50> | 11.150 0.017 | 2.406 0.008 | 0.034 0.001 | 0.002 0.000 | 0.019 0.001 | 0.036 | 287.137 |
| < 3.00> | 15.090 0.021 | 3.931 0.012 | 0.052 0.002 | 0.002 0.000 | 0.019 0.001 | 0.037 | 287.137 |
| < 3.50> | 10.220 0.015 | 2.731 0.009 | 0.037 0.001 | 0.002 0.000 | 0.013 0.001 | 0.036 | 287.137 |
| < 4.00> | 7.165 0.012 | 2.101 0.007 | 0.028 0.001 | 0.002 0.000 | 0.007 0.000 | 0.037 | 287.137 |
| < 4.50> | 4.817 0.011 | 1.562 0.008 | 0.020 0.001 | 0.002 0.001 | 0.003 0.000 | 0.037 | 287.137 |
| < 5.00> | 2.744 0.006 | 0.862 0.004 | 0.011 0.001 | 0.003 0.001 | 0.002 0.000 | 0.037 | 287.137 |
| < 7.00> | 4.561 0.009 | 1.503 0.006 | 0.020 0.001 | 0.008 0.001 | 0.003 0.000 | 0.037 | 287.137 |
| 7.50 | 11.651 0.017 | 4.449 0.013 | 0.056 0.002 | 0.045 0.002 | 0.002 0.000 | 0.037 | 287.137 |

**Measured volumes are x 1E-10 cm3 NTP. All errors are 2 x standard error. Intrim13 28-Mar-02**

**KL-12: MS-43 Mu HP**

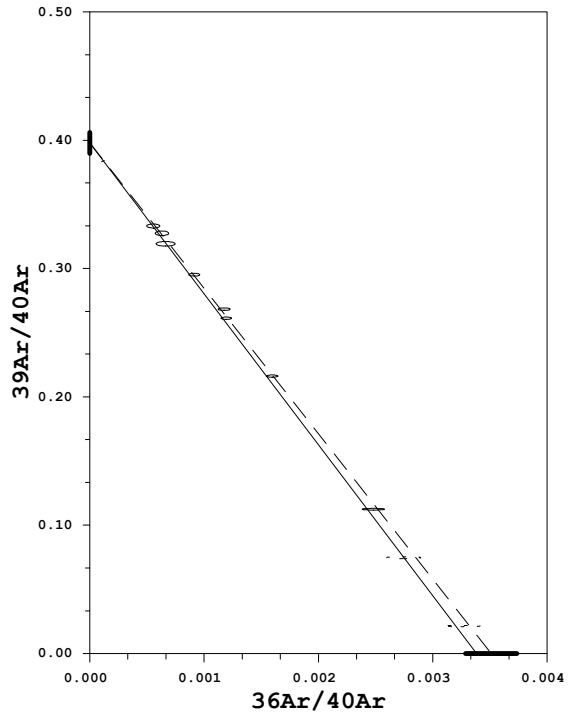


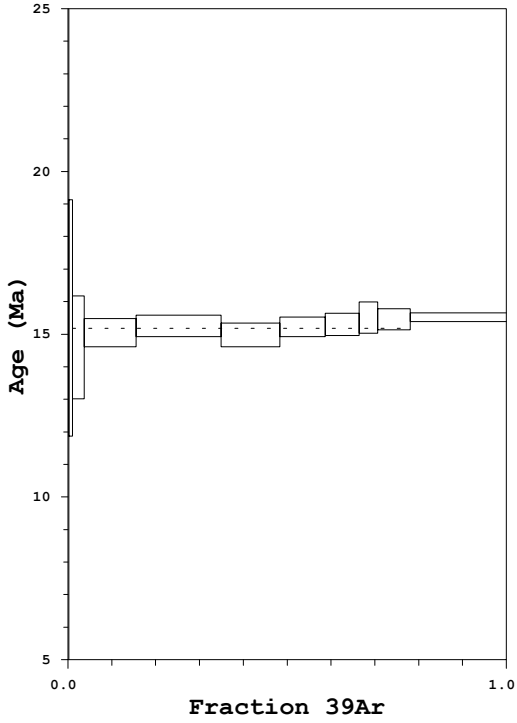


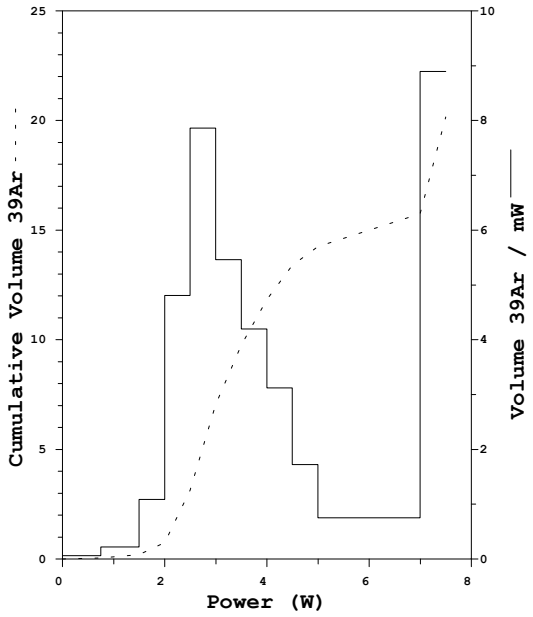


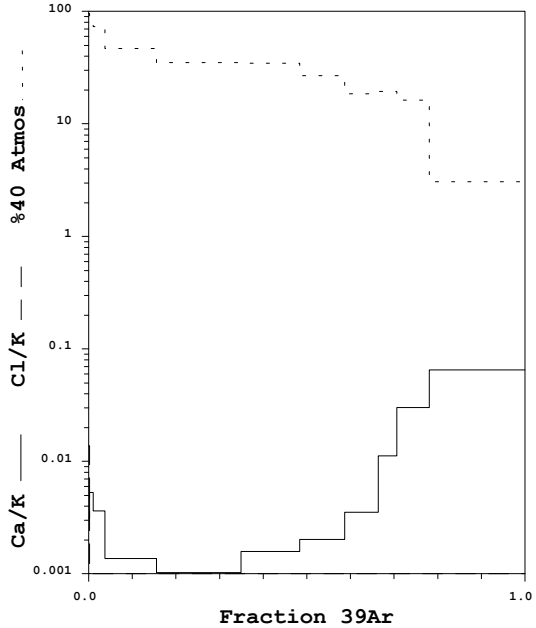


Measured volumes are x 1E-10 cm3 NTP. All errors are 2 x standard error. Intrim13 28-Mar-02

# Appendix D - Manaslu-Himal Chuli Himalaya (Chapter 4) Electron Microprobe Data

Quantitative analyses were made on an automated 4 spectrometer Cameca Camebax MBX electron probe by the wavelength dispersive x-ray analysis method (WDX). Operating conditions were: 15kv accelerating voltage, 20 nan0-amperes beam current . Specimens were analyzed using either a focused electron beam (1 micron diameter) or a rastered electron beam 5 x5 to 10x10 microns in size on beam sensitive minerals such as plagioclase or mica. Counting times were 15-40 seconds or 40,000 accumulated counts. Background positions were carefully selected to avoid instances of peak overlap. Background measurements were made at 50% peak counting time on each side of the analyzed peak. Raw x-ray data were converted to elemental weight % by the Cameca PAP matrix correction program. A suite of well characterized natural and synthetic minerals and compounds were used as calibration standards. Analyses are accurate to 1-2 % relative for major elements (>10 wt %), 3-5 % relative for minor elements ( >0.5<5.0 wt %). As detection limit is approached (<0.1 wt %), relative errors approach 100 %.

Element Line Standard

Si,Ca K-alpha wollastonite

Al K-alpha syn spinel

Ti,Mn K-alpha syn MnTiO3

Cr K-alpha syn Cr2O3

Fe K-alpha syn. fayalite

Mg K-alpha olivine

Ba L-alpha barite

Na K-alpha albite

K K-alpha orthoclase

Cl K-alpha tugtupite

F K-alpha syn LiF

Specimens were also examined with an EDX (energy-dispersive x-ray analysis) system to confirm mineral identifications and determine the presence or absence of major and trace elements prior to quantitative analysis.

Digital BSE ( back-scattered electron ) images were collected at 512 x 512 pixel resolution with an Electron Optic Services digital imaging system consisting of : a 4Pi Analysis Inc. digital imaging and EDX x-ray system and Power Macintosh G3 computer interfaced to at a Lamont 4 element solid state BSE detector and BSE Quad Summing Amplifier, Kevex EDX detector, and Aptec spectroscopy amplifier.

In specimens ms62, ms32B, ms34, ms21, and ms12 analyses of two paired garnet/ biotite phases were measured. The temperature (and pressure if appropriate) of equilibrium was calculated for each pair; the results from the same specimen were invariably well-within error. Rather than choose one estimate over another from one specimen the thermobarometric estimates used in this study represents the average of the two analysis.

*Mineral compositions from schists and gneisses*
*Budhi Gandaki and Darondi valleys, central Nepal*

***Plagioclase rim compositions***

| Sample | ms62-1 | ms62-2 | ms59 | ms31 | ms32B-1 |
|---|---|---|---|---|---|
| XAn | 0.234 | 0.237 | 0.197 | 0.126 | 0.200 |
| XAlb | 0.763 | 0.758 | 0.796 | 0.870 | 0.793 |
| XOr | 0.004 | 0.006 | 0.007 | 0.004 | 0.007 |

| Sample | ms32B-2 | ms34-1 | ms34-2 | ms47 | ms37 |
|---|---|---|---|---|---|
| XAn | 0.199 | 0.231 | 0.210 | 0.239 | 0.226 |
| XAlb | 0.793 | 0.759 | 0.783 | 0.750 | 0.763 |
| XOr | 0.008 | 0.009 | 0.007 | 0.011 | 0.011 |

***Garnet Minimum-Mn compositions***

| Sample | ms76 | ms12-1 | ms12-2 | ms21A-1 | ms21A-2 |
|---|---|---|---|---|---|
| XPrp | 0.122 | 0.097 | 0.093 | 0.106 | 0.095 |
| XAlm | 0.838 | 0.810 | 0.806 | 0.825 | 0.779 |
| XSps | 0.010 | 0.006 | 0.007 | 0.005 | 0.007 |
| XGrs | 0.031 | 0.088 | 0.095 | 0.063 | 0.118 |
| Fe/(Fe+Mg) | 0.873 | 0.893 | 0.897 | 0.886 | 0.891 |

| Sample | ms62-1 | ms62-2 | ms59 | ms31 | ms32B-1 |
|---|---|---|---|---|---|
| XPrp | 0.170 | 0.181 | 0.100 | 0.124 | 0.072 |
| XAlm | 0.682 | 0.671 | 0.799 | 0.734 | 0.752 |
| XSps | 0.080 | 0.080 | 0.061 | 0.112 | 0.144 |
| XGrs | 0.068 | 0.067 | 0.041 | 0.030 | 0.032 |
| Fe/(Fe+Mg) | 0.800 | 0.787 | 0.889 | 0.856 | 0.912 |

*Garnet Minimum-Mn compositions*

| Sample | ms32B-2 | ms34-1 | ms34-2 | ms47 | ms37 |
|---|---|---|---|---|---|
| XPrp | 0.071 | 0.078 | 0.072 | 0.093 | 0.094 |
| XAlm | 0.751 | 0.704 | 0.712 | 0.747 | 0.780 |
| XSps | 0.146 | 0.183 | 0.182 | 0.125 | 0.093 |
| XGrs | 0.033 | 0.036 | 0.033 | 0.034 | 0.033 |
| Fe/(Fe+Mg) | 0.914 | 0.901 | 0.908 | 0.889 | 0.893 |

*MIca compositions (bt, biotite; ms, muscovite)*

| Sample | ms76 bt | ms12-1 bt | ms12-2 bt | ms21A-1 bt | ms21A-2 bt |
|---|---|---|---|---|---|
| Si | 2.946 | 2.997 | 2.975 | 2.945 | 2.974 |
| Al | 1.959 | 1.935 | 1.906 | 1.921 | 1.924 |
| Ti | 0.038 | 0.055 | 0.070 | 0.073 | 0.042 |
| Mg | 1.126 | 1.071 | 1.081 | 0.886 | 1.036 |
| $Fe^{2+}$ | 1.451 | 1.430 | 1.460 | 1.658 | 1.528 |
| Mn | 0.002 | 0.000 | 0.004 | 0.004 | 0.003 |
| Ca | 0.002 | 0.002 | 0.007 | 0.004 | 0.000 |
| Na | 0.021 | 0.034 | 0.057 | 0.053 | 0.050 |
| K | 1.004 | 0.949 | 0.940 | 0.961 | 0.975 |
| Fe/(Fe+Mg) | 0.563 | 0.572 | 0.575 | 0.652 | 0.596 |

| Sample | ms62-1 bt | ms62-2 bt | ms59 bt | ms31 bt | ms32 ms |
|---|---|---|---|---|---|
| Si | 2.969 | 2.995 | 2.964 | 2.961 | 3.353 |
| Al | 1.800 | 1.782 | 1.876 | 1.862 | 3.020 |
| Ti | 0.139 | 0.139 | 0.131 | 0.146 | 0.044 |
| Mg | 1.283 | 1.311 | 0.997 | 1.241 | 0.066 |
| $Fe^{2+}$ | 1.271 | 1.236 | 1.504 | 1.246 | 0.074 |
| Mn | 0.011 | 0.007 | 0.003 | 0.010 | 0.000 |
| Ca | 0.000 | 0.002 | 0.001 | 0.001 | 0.000 |
| Na | 0.057 | 0.064 | 0.035 | 0.049 | 0.225 |
| K | 0.963 | 0.931 | 0.931 | 0.928 | 0.827 |
| Fe/(Fe+Mg) | 0.498 | 0.485 | 0.601 | 0.501 | 0.529 |

| Sample | ms32B-1 bt | ms32B-2 bt | ms34-1 bt | ms34-2 bt | ms47 bt |
|---|---|---|---|---|---|
| Si | 2.968 | 2.968 | 2.909 | 2.904 | 2.926 |
| Al | 1.845 | 1.834 | 1.868 | 1.889 | 1.958 |
| Ti | 0.147 | 0.158 | 0.229 | 0.211 | 0.127 |
| Mg | 0.714 | 0.680 | 0.810 | 0.802 | 0.873 |
| $Fe^{2+}$ | 1.725 | 1.751 | 1.550 | 1.577 | 1.547 |
| Mn | 0.021 | 0.024 | 0.014 | 0.020 | 0.013 |
| Ca | 0.001 | 0.000 | 0.001 | 0.000 | 0.001 |
| Na | 0.016 | 0.015 | 0.026 | 0.021 | 0.021 |
| K | 1.051 | 1.052 | 1.035 | 1.023 | 1.021 |
| Fe/(Fe+Mg) | 0.707 | 0.720 | 0.657 | 0.663 | 0.639 |

Mica compositions continued (bt, biotite; ms, muscovite)

| Sample | ms37 bt |
|---|---|
| Si | 2.924 |
| Al | 2.009 |
| Ti | 0.103 |
| Mg | 0.886 |
| $Fe^{2+}$ | 1.507 |
| Mn | 0.009 |
| Ca | 0.001 |
| Na | 0.025 |
| K | 1.024 |
| Fe/(Fe+Mg) | 0.630 |

# Appendix E - Station Locations and Field Data

*Latitude and Longitude are based on the WGS84 datum

**Manaslu-Himal Chuli Himalaya**

| Station | Latitude | Longitude | Elevation (m) | Structure | Azimuth | Dip/Plunge | Comments |
|---|---|---|---|---|---|---|---|
| MS001 | 28˚01.500 | 084˚40.099 | 964 | crenulation cleavage | 138 | 32 | |
| | | | | foliation (dominant) | 260 | 45 | |
| MS002 | 28˚02.286 | 084˚45.139 | 916 | fault plane | 20 | 32 | |
| | | | | foliation (dominant) | 332 | 32 | |
| | | | | mineral lineation | 35 | 6 | |
| MS003 | 28˚04.429 | 084˚49.494 | 533 | crenulation cleavage | 260 | 68 | |
| | | | | foliation (dominant) | 18 | 19 | |
| | | | | mineral lineation | 244 | 14 | |
| | | | | mineral lineation | 354 | 25 | |
| | | | | s plane | 246 | 25 | |
| | | | | shear band | 45 | 10 | |
| MS004 | 28˚05.961 | 084˚50.124 | 562 | foliation (dominant) | 132 | 25 | |
| | | | | foliation (dominant) | 155 | 28 | |
| MS005 | 28˚06.845 | 084˚50.488 | 599 | fold axial plane | 294 | 64 | |
| | | | | fold axis | 292 | 32 | |
| | | | | foliation (dominant) | 168 | 20 | |
| | | | | foliation (dominant) | 206 | 31 | |
| MS006 | 28˚07.944 | 084˚51.236 | 617 | fault plane | 272 | 55 | |
| | | | | foliation (dominant) | 173 | 25 | |
| | | | | stretching lineation | 38 | 54 | |
| MS007 | 28˚08.525 | 084˚51.630 | 665 | foliation (dominant) | 232 | 22 | |
| | | | | mineral lineation | 12 | 6 | |
| MS008 | 28˚08.961 | 084˚51.679 | 738 | foliation (dominant) | 254 | 14 | |
| | | | | mineral lineation | 18 | 14 | |
| | | | | shear band | 191 | 28 | |
| MS009 | 28˚09.653 | 084˚52.198 | 710 | foliation (dominant) | 265 | 11 | |
| | | | | late fold axis | 266 | 5 | |
| MS010 | 28˚09.789 | 084˚52.337 | 752 | foliation (dominant) | 206 | 13 | |
| | | | | foliation (dominant) | 252 | 38 | |
| | | | | mineral lineation | 36 | 9 | |
| | | | | shear band | 182 | 20 | |
| | | | | shear band | 232 | 38 | |
| MS011 | 28˚10.157 | 084˚52.705 | 756 | fold axial plane | 285 | 56 | |
| | | | | foliation (dominant) | 245 | 13 | |
| | | | | foliation (dominant) | 232 | 11 | |
| | | | | late fold axis | 295 | 16 | |
| | | | | shear band | 178 | 16 | |
| MS012 | 28˚11.418 | 084˚52.528 | 788 | foliation (dominant) | 233 | 52 | |
| | | | | foliation (dominant) | 230 | 56 | in sstone |
| | | | | mineral lineation | 9 | 32 | |
| | | | | s plane | 271 | 46 | |
| | | | | shear band | 217 | 25 | |
| MS013 | 28˚11.791 | 084˚52.535 | 797 | foliation (dominant) | 259 | 24 | |
| | | | | s plane | 297 | 56 | |
| | | | | shear band | 270 | 9 | |
| MS014 | 28˚12.009 | 084˚52.490 | 780 | foliation (dominant) | 287 | 44 | |
| | | | | mineral lineation | 13 | 45 | on s plane |
| | | | | s plane | 286 | 66 | |
| | | | | shear band | 295 | 39 | |
| MS015 | 28˚12.987 | 084˚52.545 | 809 | compositional layering | 223 | 50 | |
| | | | | compositional layering | 227 | 54 | in siliciclastics |
| | | | | fold axial plane | 256 | 84 | |
| | | | | foliation (dominant) | 241 | 50 | |

**Manaslu-Himal Chuli Himalaya continued**

| | | | | | | | |
|---|---|---|---|---|---|---|---|
| | | | | s plane | 243 | 64 | |
| | | | | shear band | 242 | 39 | |
| MS016 | 28°13.352 | 084°52.548 | 842 | foliation (dominant) | 272 | 47 | |
| MS017 | 28°13.529 | 084°52.434 | 824 | foliation (dominant) | 245 | 45 | |
| MS018 | 28°14.388 | 084°52.579 | 830 | foliation (dominant) | 276 | 34 | |
| | | | | mineral lineation | 16 | 29 | |
| MS019 | 28°14.532 | 084°52.613 | 855 | fold axis | 70 | 15 | |
| | | | | foliation (dominant) | 276 | 32 | |
| | | | | mineral lineation | 13 | 31 | |
| MS020 | 28°14.913 | 084°52.832 | 892 | foliation (dominant) | 280 | 31 | |
| MS021 | 28°15.451 | 084°53.188 | 930 | foliation (dominant) | 286 | 40 | |
| | | | | foliation (dominant) | 294 | 33 | 20m down trail |
| | | | | mineral lineation | 28 | 35 | |
| | | | | mineral lineation | 15 | 33 | 20 down trail on foliation |
| | | | | s plane | 284 | 50 | |
| | | | | shear band | 294 | 20 | |
| MS022 | - | - | - | foliation (dominant) | 301 | 52 | no GPS lock |
| | | | | mineral lineation | 18 | 49 | |
| MS023 | 28°16.461 | 084°53.894 | 969 | foliation (dominant) | 278 | 38 | |
| | | | | foliation (dominant) | 299 | 31 | |
| | | | | mineral lineation | 28 | 31 | |
| | | | | s plane | 310 | 43 | |
| | | | | shear band | 270 | 29 | |
| MS024 | - | - | - | foliation (dominant) | 273 | 25 | no GPS lock |
| | | | | mineral lineation | 350 | 25 | |
| MS025 | 28°18.725 | 084°54.185 | 1095 | foliation (dominant) | 138 | 38 | |
| | | | | foliation (late) | 130 | 48 | |
| MS026 | 28°19.776 | 084°54.506 | 1312 | fold axial plane | 312 | 32 | |
| | | | | foliation (dominant) | 320 | 40 | |
| | | | | late fold axis (z) | 319 | 24 | |
| | | | | mineral lineation | 56 | 40 | |
| MS027 | 28°19.874 | 084°54.375 | 1351 | foliation (dominant) | 190 | 32 | |
| MS028 | 28°20.138 | 084°54.183 | 1374 | foliation (dominant) | 274 | 29 | |
| MS029 | 28°21.134 | 084°53.653 | 1410 | foliation (dominant) | 255 | 45 | |
| | | | | mineral lineation | 21 | 39 | |
| MS030 | - | - | - | foliation (dominant) | 250 | 40 | no GPS lock |
| | | | | mineral lineation | 30 | 25 | |
| MS031 | 28°22.276 | 084°53.170 | 1428 | foliation (dominant) | 244 | 41 | |
| | | | | foliation (dominant) | 236 | 45 | |
| | | | | s plane | 260 | 41 | |
| | | | | shear band | 220 | 20 | |
| MS032 | 28°25.048 | 084°53.782 | 1554 | foliation (dominant) | 264 | 36 | |
| | | | | foliation (dominant) | 278 | 25 | |
| | | | | mineral lineation | 2 | 30 | |
| | | | | s plane | 265 | 32 | |
| MS033 | 28°25.333 | 084°53.752 | 1600 | foliation (dominant) | 260 | 46 | |
| | | | | s plane | 274 | 60 | |
| | | | | shear band | 273 | 19 | |
| MS034 | 28°25.903 | 084°53.849 | 1627 | foliation (dominant) | 292 | 38 | more qtz rich |
| | | | | foliation (dominant) | 260 | 43 | less qtz |
| | | | | foliation (dominant) | 245 | 74 | |
| | | | | mineral lineation | 38 | 29 | |
| MS035 | - | - | - | foliation (dominant) | 245 | 61 | no GPS lock |
| MS036 | - | - | - | fold axial plane | 262 | 44 | no GPS lock |
| | | | | fold axial plane | 245 | 74 | |
| | | | | fold axial plane | 230 | 20 | |
| | | | | foliation (dominant) | 250 | 71 | |

## Manaslu-Himal Chuli Himalaya continued

| | | | | | | | |
|---|---|---|---|---|---|---|---|
| | | | | foliation (dominant) | 67 | 74 | other side of the fold |
| | | | | foliation (dominant) | 238 | 72 | one side of fold |
| | | | | foliation (dominant) | 270 | 32 | Further up trail |
| MS037 | 28°28.914 | 084°51.987 | 1918 | foliation (dominant) | 292 | 45 | |
| | | | | foliation (dominant) | 291 | 48 | |
| | | | | other | 0 | 0 | |
| | | | | shear band | 286 | 37 | |
| MS038 | 28°29.857 | 084°52.118 | 1956 | fault plane | 192 | 21 | |
| | | | | fold axis (s) | 75 | 40 | |
| | | | | foliation (dominant) | 269 | 55 | |
| | | | | foliation (dominant) | 251 | 57 | |
| | | | | foliation (dominant) | 258 | 59 | with c' at 250/54 |
| | | | | foliation (dominant) | 255 | 70 | w shear band at 210/55 |
| | | | | shear band | 261 | 61 | |
| | | | | shear band | 258 | 69 | possibly top-to-the-north |
| | | | | shear band | 250 | 54 | |
| | | | | shear band | 210 | 55 | |
| MS039 | 28°30.721 | 084°51.359 | 2040 | foliation (dominant) | 234 | 38 | |
| | | | | foliation (dominant) | 252 | 49 | |
| | | | | foliation (dominant) | 278 | 49 | |
| | | | | s plane | 224 | 60 | |
| | | | | shear band | 224 | 57 | |
| | | | | shear band | 220 | 59 | |
| MS040 | 28°31.000 | 084°50.981 | 2008 | foliation (dominant) | 273 | 60 | |
| | | | | shear band | 239 | 45 | top t-t- north |
| MS041 | 28°31.700 | 084°50.377 | 2157 | foliation (dominant) | 270 | 60 | |
| | | | | shear band | 333 | 30 | |
| | | | | shear band | 281 | 45 | |
| MS042 | 28°32.046 | 084°48.254 | 2204 | dike | 242 | 57 | |
| | | | | foliation (dominant) | 297 | 34 | |
| | | | | foliation (dominant) | 270 | 44 | |
| | | | | s plane | 302 | 10 | |
| | | | | shear band | 268 | 61 | |
| MS043 | 28°32.977 | 084°45.570 | 2714 | foliation (dominant) | 294 | 44 | |
| | | | | mineral lineation | 69 | 31 | |
| MS044 | 28°33.764 | 084°43.865 | 2779 | foliation (dominant) | 275 | 56 | |
| | | | | foliation (dominant) | 276 | 56 | |
| | | | | s plane | 262 | 32 | |
| | | | | shear band | 288 | 70 | |
| MS045 | 28°34.240 | 084°42.586 | 3068 | foliation (dominant) | 289 | 34 | |
| MS046 | 28°27.471 | 084°53.147 | 1968 | foliation (dominant) | 252 | 57 | |
| MS047 | 28°27.250 | 084°53.386 | 2177 | foliation (dominant) | 247 | 69 | |
| | | | | foliation (dominant) | 245 | 75 | |
| | | | | mineral lineation | 62 | 12 | on 245/75 |
| MS048 | 28°26.699 | 084°52.269 | 2750 | foliation (dominant) | 55 | 90 | variable |
| | | | | mineral lineation | 65 | 16 | sillimanite |
| MS049 | 28°26.755 | 084°51.841 | 2773 | fold axial plane | 244 | 75 | |
| | | | | fold axis | 56 | 34 | + sill lineation |
| | | | | foliation (dominant) | 262 | 85 | |
| MS050 | 28°25.711 | 084°44.791 | 3365 | foliation (dominant) | 312 | 25 | |
| MS051 | 28°22.102 | 084°42.042 | 4332 | foliation (dominant) | 330 | 25 | |
| | | | | s plane | 307 | 53 | |
| | | | | shear band | 332 | 16 | |
| MS052 | 28°21.517 | 084°43.615 | 4716 | foliation (dominant) | 282 | 20 | |
| | | | | s plane | 265 | 24 | |
| | | | | shear band | 260 | 22 | |
| MS053 | 28°21.248 | 084°43.701 | 4557 | foliation (dominant) | 236 | 23 | may be slumped |

## Manaslu-Himal Chuli Himalaya continued

| | | | | | | | |
|---|---|---|---|---|---|---|---|
| MS054 | 28°21.144 | 084°43.756 | 4438 | | | | |
| MS055 | 28°21.067 | 084°43.821 | 4369 | foliation (dominant) | 209 | 35 | |
| | | | | foliation (dominant) | 3 | 79 | folded foliation |
| MS056 | 28°20.835 | 084°44.020 | 3949 | fold axis | 250 | 3 | parallel to sillimanite lin |
| | | | | foliation (dominant) | 65 | 28 | |
| | | | | foliation (dominant) | 259 | 68 | |
| | | | | foliation (dominant) | 65 | 48 | folded |
| MS057 | 28°20.195 | 084°44.110 | 3584 | foliation (dominant) | 279 | 43 | |
| | | | | s plane | 285 | 46 | |
| | | | | shear band | 255 | 29 | |
| MS058 | 28°20.047 | 084°44.027 | 3536 | foliation (dominant) | 249 | 26 | |
| MS059 | 28°18.858 | 084°44.020 | 3544 | foliation (dominant) | 259 | 54 | |
| MS060 | 28'18.326 | 084'44.257 | 3246 | foliation (dominant) | 237 | 57 | |
| | | | | foliation (dominant) | 221 | 44 | |
| MS061 | | | | foliation (dominant) | 227 | 56 | |
| MS062 | 28'16.244 | 084'44.474 | 2651 | foliation (dominant) | 206 | 57 | |
| | | | | shear band | 185 | 65 | |
| MS063 | 28'15.851 | 084'44.761 | 2573 | foliation (dominant) | 210 | 43 | |
| MS064 | 28'15.797 | 084'44.754 | 2499 | foliation (dominant) | 227 | 32 | |
| | | | | foliation (dominant) | 241 | 33 | |
| | | | | shear band | 265 | 20 | |
| MS065 | 28'14.984 | 084'44.914 | 2049 | foliation (dominant) | 230 | 24 | |
| | | | | foliation (dominant) | 358 | 76 | fold limb |
| | | | | foliation (dominant) | 254 | 25 | fold limb |
| | | | | shear band | 220 | 34 | |
| MS066 | 28'14.900 | 084'45.131 | 2085 | foliation (dominant) | 220 | 31 | |
| | | | | shear band | 207 | 32 | |
| MS067 | 28'14.443 | 084'45.030 | 2009 | foliation (dominant) | 236 | 35 | |
| MS068 | 28'14.288 | 084'45.021 | 1977 | foliation (dominant) | 235 | 35 | |
| | | | | s plane | 227 | 45 | |
| | | | | shear band | 276 | 32 | |
| MS069 | 28'13.706 | 084'45.324 | 2052 | foliation (dominant) | 251 | 23 | |
| MS070 | 28'13.302 | 084'45.245 | 1992 | foliation (dominant) | 273 | 44 | |
| MS071 | 28'12.892 | 084'45.354 | 1913 | foliation (dominant) | 282 | 26 | |
| MS072 | 28'11.713 | 084'43.738 | 1473 | foliation (dominant) | 261 | 28 | |
| | | | | mineral lineation | 24 | 9 | |
| MS073 | 28'11.284 | 084'43.138 | 893 | foliation (dominant) | 338 | 20 | |
| MS074 | 28'10.916 | 084'42.790 | 816 | mineral lineation | 36 | 10 | |
| MS075 | 28'10.275 | 084'42.428 | 787 | foliation (dominant) | 29 | 26 | seems odd |
| MS076 | 28'07.421 | 084'40.478 | 606 | foliation (dominant) | 244 | 42 | |
| | | | | s plane | 240 | 54 | |
| | | | | shear band | 236 | 35 | |
| MS077 | 28'07.092 | 084'40.354 | 633 | foliation (dominant) | 305 | 45 | |
| | | | | mineral lineation | 11 | 44 | |
| MS078 | 28'05.706 | 084'39.537 | 570 | fault plane | 245 | 50 | |
| | | | | foliation (dominant) | 305 | 49 | |
| | | | | mineral lineation | 2 | 45 | |
| | | | | s plane | 264 | 87 | |
| MS079 | 28'04.888 | 084'39.543 | 559 | fold axial plane | 135 | 18 | kink |
| | | | | foliation (dominant) | 282 | 64 | |
| | | | | foliation (dominant) | 292 | 44 | |
| | | | | late fold axis | 115 | 6 | kink |
| | | | | mineral lineation | 21 | 44 | |
| | | | | s plane | 295 | 84 | |
| | | | | shear band | 286 | 48 | |
| MS080 | 28'03.563 | 084'39.109 | 543 | crenulation lineation | 351 | 29 | |
| | | | | foliation (dominant) | 309 | 46 | |

## Manaslu-Himal Chuli Himalaya continued

| | | | | | | | |
|---|---|---|---|---|---|---|---|
| | | | | foliation (dominant) | 294 | 55 | muddier rock |
| MS081 | 28'01.998 | 084'36.356 | 600 | foliation (dominant) | 92 | 25 | |
| MS082 | 28'01.514 | 084'37.817 | 1022 | foliation (dominant) | 30 | 15 | |
| MS083 | 28'00.676 | 084'38.066 | 1186 | foliation (dominant) | 192 | 43 | |
| MS084 | 27'59.183 | 084'37.916 | 954 | fold axial plane | 325 | 25 | late? |
| | | | | foliation (dominant) | 176 | 20 | |
| | | | | late fold axis | 344 | 14 | |
| MS085 | 27'58.952 | 084'38.014 | 965 | | | | |
| MS086 | 27'58.101 | 084'36.283 | 767 | crenulation lineation | 3 | 7 | |
| | | | | foliation (dominant) | 310 | 6 | |
| | | | | foliation (dominant) | 285 | 25 | |
| | | | | intersection lineation (m) | 11 | 20 | |
| MS087 | 27'58.447 | 084'34.542 | 618 | fold axial plane | 263 | 33 | |
| | | | | foliation (late) | 270 | 31 | axial planar cleavage |
| | | | | late fold axis | 0 | 37 | |
| MS088 | 27'59.111 | 084'38.026 | 938 | crenulation lineation | 5 | 10 | |
| | | | | foliation (dominant) | 137 | 14 | |

## Changgo Area

| Station | Latitude | Longitude | Elevation (m) | Structure | Azimuth | Dip/Plunge |
|---|---|---|---|---|---|---|
| **Changgo culmination** | | | | | | |
| CH-01 | 29'10.689 | 084'47.001 | 4809 | compositional layering | 253 | 23 |
| | | | | foliation (S2) | 250 | 35 |
| | | | | foliation (unkown) | 24 | 87 |
| | | | | foliation (S5) | 156 | 85 |
| CH-02 | 29'10.600 | 084'47.061 | 4833 | | | |
| CH-03 | 29'10.404 | 084'47.135 | 4907 | compositional layering | 298 | 20 |
| | | | | foliation (S2) | 305 | 35 |
| CH-04 | 29'10.244 | 084'47.218 | 4969 | compositional layering | 250 | 30 |
| | | | | foliation (S5) | 181 | 85 |
| CH-05 | 29'10.174 | 084'47.282 | 4981 | calcite vein | 255 | 49 |
| | | | | shear band | 309 | 33 |
| | | | | shear band | 338 | 29 |
| | | | | compositional layering | 258 | 50 |
| | | | | fold axis (F2: isoclinal) | 56 | 37 |
| CH-06 | 29'09.933 | 084'47.481 | 5147 | foliation (S2) | 288 | 44 |
| | | | | mineral lineation | 303 | 24 |
| CH-07 | 29'10.063 | 084'47.832 | 5029 | | | |
| CH-08 | 29'10.164 | 084'47.873 | 5012 | foliation (S2?) | 274 | 36 |
| CH-09 | 29'10.389 | 084'48.310 | 4863 | compositional layering | 322 | 60 |
| CH-10 | 29'10.142 | 084'48.578 | 4948 | compositional layering | 323 | 69 |
| CH-11 | 29'10.032 | 084'48.714 | 4969 | compositional layering | 292 | 52 |
| CH-12 | 29'09.905 | 084'48.612 | 5036 | compositional layering | 297 | 37 |
| | | | | compositional layering | 69 | 1 |
| CH-13 | 29'09.224 | 084'48.383 | 5140 | quartz vein | 39 | 49 |
| | | | | quartz vein | 159 | 70 |
| | | | | foliation (S2) | 320 | 59 |
| CH-14 | 29'08.548 | 084'48.496 | 5108 | foliation (S?; mylonitic) | 298 | 37 |
| | | | | granite dyke | 23 | 78 |
| CH-100 | 29'11.282 | 084'50.101 | 4684 | fold axial plane (F2) | 294 | 18 |
| | | | | compositional layering | 259 | 24 |
| | | | | compositional layering | 274 | 11 |
| | | | | compositional layering | 252 | 18 |
| | | | | fold axis (F2; isoclinal) | 324 | 7 |
| CH-101 | 29'11.063 | 084'50.133 | 4724 | compositional layering | 304 | 10 |
| | | | | foliation (S2) | 279 | 52 |
| | | | | foliation (S5) | 156 | 89 |
| CH-102 | 29'10.979 | 084'50.151 | 4754 | compositional layering | 20 | 16 |
| | | | | foliation (S2) | 306 | 38 |
| | | | | foliation (S2) | 302 | 19 |
| | | | | intersection lineation | 237 | 9 |
| | | | | foliation (S2?) | 35 | 12 |
| | | | | mineral lineation | 130 | 4 |
| CH-103 | 29'10.813 | 084'50.143 | 4833 | foliation (S2) | 201 | 2 |
| | | | | fold axial plane (F3) | 307 | 45 |
| | | | | intersection lineation | 310 | 4 |
| | | | | foliation (S2) | 126 | 58 |
| | | | | foliation (S2) | 144 | 12 |
| | | | | mineral lineation | 288 | 10 |
| CH-104 | 29'10.774 | 084'50.164 | 4851 | | | |
| CH-105 | 29'12.024 | 084'50.180 | 4792 | foliation (S2) | 280 | 35 |
| | | | | foliation (S2) | 259 | 31 |
| | | | | foliation (S2) | 264 | 36 |

**Changgo Area continued**

| | | | | | | |
|---|---|---|---|---|---|---|
| | | | | axial planar cleavage | 245 | 68 |
| | | | | foliation (S5) | 9 | 70 |
| | | | | vein | 41 | 46 |
| | | | | vein | 228 | 86 |
| | | | | vein | 6 | 54 |
| CH-106 | 29'11.968 | 084'50.254 | 4832 | compositional layering | 160 | 15 |
| | | | | axial planar cleavage (S1) | 213 | 23 |
| | | | | intersection lineation | 274 | 15 |
| CH-107 | 29'12.021 | 084'50.366 | 4951 | compositional layering | 298 | 55 |
| | | | | compositional layering | 149 | 32 |
| | | | | quartz vein | 302 | 36 |
| | | | | minor reverse fault | 149 | 32 |
| | | | | fold axis (F1) | 293 | 34 |
| | | | | compositional layering | 126 | 30 |
| CH-108 | 29'12.044 | 084'50.503 | 5064 | compositional layering | 134 | 29 |
| | | | | compositional layering | 315 | 84 |
| | | | | fold axis (F1) | 302 | 14 |
| CH-109 | 29'12.029 | 084'50.572 | 5130 | foliation (S5) | 164 | 75 |
| | | | | compositional layering | 326 | 21 |
| | | | | compositional layering | 279 | 75 |
| | | | | axial planar cleavage (S1) | 267 | 23 |
| | | | | axial planar cleavage (S1) | 237 | 20 |
| | | | | fold axis (F1) | 292 | 24 |
| CH-110 | 29'12.072 | 084'50.649 | 5215 | compositional layering | 188 | 31 |
| | | | | compositional layering | 304 | 78 |
| | | | | axial planar cleavage (S1) | 256 | 31 |
| | | | | fold axis (F1) | 314 | 31 |
| | | | | compositional layering | 224 | 27 |
| | | | | axial planar cleavage (S1) | 314 | 54 |
| | | | | minor fault | 344 | 24 |
| CH-111 | 29'11.921 | 084'50.806 | 5171 | compositional layering | 105 | 88 |
| | | | | compositional layering | 227 | 13 |
| | | | | joint | 333 | 65 |
| | | | | joint | 55 | 84 |
| CH-112 | 29'11.762 | 084'50.865 | 5136 | over-turned bedding | 294 | 54 |
| | | | | axial planar cleavage (S1) | 291 | 21 |
| | | | | minor fault | 281 | 50 |
| CH-113 | 29'11.525 | 084'50.881 | 5116 | foliation (S5) | 341 | 86 |
| | | | | compositional layering | 332 | 15 |
| CH-114 | 29'11.363 | 084'50.855 | 5108 | compositional layering? | 40 | 14 |
| CH-115 | 29'11.169 | 084'50.684 | 5096 | foliation (S5) | 29 | 65 |
| | | | | foliation (S5) | 344 | 90 |
| | | | | compositional layering | 45 | 2 |
| | | | | axial planar cleavage (S1) | 342 | 28 |
| CH-116 | 29'11.237 | 084'50.410 | 4989 | compositional layering | 341 | 3 |
| | | | | foliation (S5) | 310 | 88 |
| CH-117 | 29'11.379 | 084'50.372 | 4920 | compositional layering | 275 | 29 |
| CH-118 | 29'11.497 | 084'50.243 | 4811 | compositional layering | 168 | 21 |
| | | | | fold axial plane (F1) | 196 | 15 |
| | | | | fold axis (F1) | 284 | 14 |
| CH-119 | 29'08.879 | 084'50.053 | 5314 | | | |
| CH-120 | 29'08.838 | 084'50.376 | 5392 | quartz vein | 174 | 52 |
| CH-121 | 29'08.603 | 084'50.357 | 5519 | | | |
| CH-122 | 29'08.448 | 084'50.279 | 5591 | foliation (S3; mylonititic) | 332 | 26 |
| | | | | mineral lineation | 146 | 1 |
| | | | | foliation (S3; mylonititic) | 319 | 20 |
| CH-123 | 29'07.687 | 084'50.097 | 5792 | quartz vein | 68 | 46 |

**Changgo Area continued**

| | | | | | | |
|---|---|---|---|---|---|---|
| | | | | foliation (S2) | 64 | 10 |
| CH-124 | 29'08.507 | 084'50.289 | 5563 | foliation (S3; mylonititic) | 329 | 25 |
| | | | | boudin neck (lineation) | 115 | 15 |
| CH-125 | 29'09.078 | 084'50.792 | 5234 | foliation (S2) | 296 | 59 |
| | | | | foliation (S2) | 80 | 69 |
| | | | | foliation (S2) | 311 | 30 |
| | | | | foliation (S2) | 32 | 35 |
| | | | | foliation (S2) | 45 | 11 |
| | | | | mineral lineation | 69 | 3 |
| CH-126 | 29'09.152 | 084'50.798 | 5219 | foliation (S2) | 330 | 32 |
| | | | | joint | 137 | 43 |
| CH-127 | 29'09.221 | 084'50.791 | 5210 | compositional layering | 155 | 27 |
| | | | | compositional layering | 143 | 34 |
| | | | | foliation (S2) | 311 | 59 |
| | | | | compositional layering | 146 | 30 |
| | | | | foliation (S2) | 321 | 35 |
| | | | | foliation (S2) | 302 | 66 |
| | | | | compositional layering | 144 | 45 |
| CH-128 | 29'09.271 | 084'50.791 | 5196 | foliation (dominant)? | 248 | 32 |
| | | | | foliation (dominant)? | 285 | 34 |
| CH-129 | 29'09.346 | 084'50.841 | 5186 | foliation (dominant)? | 302 | 43 |
| | | | | fold axial plane (F3?) | 300 | 18 |
| | | | | fold axis (F3?) | 82 | 18 |
| | | | | foliation (dominant)? | 310 | 8 |
| | | | | joint set (dominant) | 117 | 90 |
| CH-130 | 29'09.535 | 084'50.838 | 5116 | foliation (S2) | 269 | 42 |
| | | | | foliation (S2) | 285 | 33 |
| | | | | joint set (dominant) | 156 | 90 |
| | | | | fold axial plane (F2) | 280 | 46 |
| | | | | fold axis (F2; isoclinal) | 68 | 11 |
| | | | | foliation (S2) | 260 | 40 |
| CH-131 | 29'09.642 | 084'50.754 | 5080 | foliation (S2) | 295 | 45 |
| | | | | vein | 296 | 42 |
| | | | | boudin neck axis | 33 | 52 |
| **Kung Tang culmination** | | | | | | |
| CH-132 | 29'03.269 | 085'06.807 | 4738 | compositional layering | 280 | 42 |
| | | | | compositional layering | 275 | 35 |
| CH-133 | 29'01.855 | 085'05.265 | 5530 | minor fault | 215 | 49 |
| | | | | foliation (S2) | 280 | 36 |
| CH-134 | 29'02.080 | 085'05.789 | 5198 | foliation (S2) | 288 | 44 |
| | | | | joint set (dominant) | 20 | 67 |
| | | | | fold axis (F2; isoclinal) | 235 | 25 |
| | | | | fold axial plane (F2) | 255 | 60 |
| | | | | reverse fault | 262 | 39 |
| CH-135 | 29'02.171 | 085'05.806 | 5161 | foliation (S2) | 305 | 52 |
| | | | | compositional layering | 92 | 46 |
| | | | | foliation (S2) | 283 | 52 |
| | | | | compositional layering | 314 | 35 |
| CH-136 | 29'02.231 | 085'05.831 | 5131 | foliation (S2) | 295 | 25 |
| | | | | joint set (dominant) | 82 | 90 |
| CH-137 | 29'02.317 | 085'05.843 | 5172 | foliation (S2) | 296 | 34 |
| CH-138 | 29'02.353 | 085'05.846 | 5184 | minor normal fault | 287 | 45 |
| CH-139 | 29'02.463 | 085'05.808 | 5271 | foliation (S2) | 255 | 44 |
| | | | | foliation (unknown) | 354 | 71 |

**Changgo Area continued**

| | | | | | | |
|---|---|---|---|---|---|---|
| | | | | foliation (unknown) | 290 | 88 |
| | | | | joint set (dominant) | 62 | 73 |
| CH-140 | 29'04.126 | 085'07.083 | 4600 | compositional layering | 287 | 74 |
| | | | | compositional layering | 288 | 59 |
| | | | | compositional layering | 258 | 48 |
| | | | | comp. layering (overturned) | 114 | 78 |
| | | | | comp. layering (overturned) | 124 | 72 |
| | | | | comp. layering (overturned) | 119 | 55 |

## Dhaulagiri Himalaya

| Station | Latitude | Longitude | Elevation (m) | Structure | Azimuth | Dip/Plunge |
|---|---|---|---|---|---|---|
| 1 | 28° 40' 23.0'' | 083° 35'49.2'' | 2577 | foliation (dominant) | 319 | 14 |
| | | | | crenulation lineation | 83 | 19 |
| 2 | 28°38'48.5'' | 083°35'39.1'' | 2503 | foliation (dominant) | 290 | 31 |
| 3 | 28°38'37.1'' | 083°35'43.9'' | 2543 | foliation (dominant) | 338 | 28 |
| | | | | foliation (dominant) | 338 | 34 |
| 4 | 28°37'32.1'' | 083°37'21.1'' | 2372 | foliation (dominant) | 293 | 40 |
| | | | | foliation (dominant) | 288 | 46 |
| | | | | foliation (dominant) | 264 | 30 |
| | | | | mineral lineation | 348 | 32 |
| 5 | 28°37'30.4'' | 083°'37'32.5'' | 2308 | foliation (dominant) | 284 | 41 |
| 6 | 28°36'57.6'' | 083°38'19.6'' | 2174 | foliation (dominant) | 284 | 27 |
| | | | | foliation (dominant) | 265 | 27 |
| 7 | 28°36'48.1'' | 083°38'24.2'' | 2202 | foliation (dominant) | 287 | 38 |
| | | | | mineral lineation | 5 | 26 |
| | | | | crenulation lineation | 80 | 12 |
| 8 | 28°35'21.7'' | 083°38'54.2'' | 1914 | foliation (dominant) | 286 | 32 |
| 9 | 28°34'58.0'' | 083°38'52.4'' | 1929 | foliation (dominant) | 272 | 36 |
| 10 | 28°34'49.6'' | 083°38'54.1 | 1952 | foliation (dominant) | 315 | 38 |
| 11 | 28°34'09.9'' | 083°38'29.9'' | - | foliation (dominant) | 292 | 30 |
| 12 | 28°33'49.4'' | 083°38'20.7'' | 1833 | foliation (dominant) | 289 | 60 |
| 13 | 28°33'12.4'' | 083°38'30.5'' | 1559 | foliation (dominant) | 279 | 45 |
| 14 | 28°32'47.8'' | 083°38'42.6'' | 1492 | foliation (dominant) | 294 | 61 |
| 15 | 28°32'41.4'' | 083°38'43.4'' | 1452 | foliation (dominant) | 300 | 42 |
| 16 | 28°32'33.2'' | 083°38'53.7'' | 1445 | foliation (dominant) | 295 | 53 |
| 17 | 28°33'12.0'' | 083°39'39.2'' | 2441 | foliation (dominant) | 287 | 49 |
| 18 | 28°33'13.0'' | 083°39'43.5'' | 2577 | foliation (dominant) | 266 | 48 |
| | | | | foliation (dominant) | 282 | 65 |
| 19 | 28°33'59.1'' | 083°39'49.2'' | 3377 | - | - | - |
| 20 | 28°34'25.8'' | 083°40'03.1'' | 3640 | foliation (dominant) | 270 | 37 |
| | | | | foliation (dominant) | 257 | 44 |
| | | | | mineral lineation | 26 | 41 |
| 21 | 28°34'12.8'' | 083°39'53.0'' | 3384 | foliation (dominant) | 308 | 29 |
| | | | | foliation (dominant) | 282 | 30 |
| 22 | 28°33'49.9'' | 083°39'53.4'' | 3374 | foliation (dominant) | 282 | 30 |
| 23 | 28°33'37.0'' | 083°39'54.4'' | 3147 | foliation (dominant) | 302 | 18 |
| 24 | 28°33'29.5'' | 083°39'54.6'' | 3027 | foliation (dominant) | 296 | 30 |
| 25 | 28°33'19.1'' | 083°39'48.7'' | 2730 | foliation (dominant) | 282 | 44 |
| 26 | 28°32'57.3'' | 083°39'34.7'' | 2222 | foliation (dominant) | 296 | 54 |
| 27 | 28°32'50.7'' | 083°39'36.2'' | 2108 | foliation (dominant) | 296 | 54 |
| | | | | foliation (secondary) | 240 | 61 |
| 28 | 28°32'42.4'' | 083°39'32.3'' | 2015 | foliation (dominant) | 331 | 60 |
| | | | | foliation (dominant) | 288 | 81 |
| | | | | foliation (dominant) | 321 | 59 |
| | | | | fold axis | 94 | 58 |
| | | | | axial planar cleavage? | 305 | 88 |
| 29 | 28°31'42.1'' | 083°39'06.6'' | 1452 | foliation (dominant) | 285 | 54 |
| 30 | 28°31'37.1'' | 083°39'20.8'' | 1387 | foliation (dominant) | 268 | 48 |
| | | | | fold axis | 11 | 39 |
| 31 | 28°31'33.9'' | 083°39'22.8'' | 1401 | foliation (dominant) | 312 | 45 |
| 32 | 28°31'30.0'' | 083°39'27.2'' | 1394 | foliation (dominant) | 275 | 46 |
| | | | | axial planar cleavage? | 108 | 54 |
| | | | | fold axis | 330 | 58 |
| 33 | 28°31'15.2'' | 083°39'30.8'' | 1424 | foliation (dominant) | 310 | 39 |

**Dhaulagiri Himalaya continued**

| | | | | | | |
|---|---|---|---|---|---|---|
| 34 | 28°31’13.8’’ | 083°39’31.6’’ | 1391 | foliation (dominant) | 334 | 39 |
| | | | | foliation (secondary) | 139 | 37 |
| | | | | crenulation lineation | 303 | 9 |
| 35 | 28°31’08.3’’ | 083°39’32.1’’ | 1350 | foliation (dominant) | 310 | 54 |
| | | | | crenulation lineation | 141 | 6 |
| | | | | crenulation lineation | 135 | 8 |
| 36 | 28°431’03.1’’ | 083°39’31.1’’ | 1338 | foliation (dominant) | 261 | 64 |
| 37 | 28°30’40.2’’ | 083°39’23.6’’ | 1353 | foliation (dominant) | 308 | 61 |
| 38 | 28°30’37.3’’ | 083°39’23.7’’ | 1362 | foliation (dominant) | 310 | 56 |
| | | | | mineral lineation | 20 | 50 |
| | | | | foliation (dominant) | 309 | 60 |
| | | | | mineral lineation | 24 | 51 |
| | | | | foliation (dominant) | 329 | 60 |
| 39 | 28°30’22.2’’ | 083°39’29.0’’ | 1287 | foliation (dominant) | 301 | 44 |
| | | | | crenulation lineation | 7 | 53 |
| | | | | foliation (dominant) | 293 | 71 |
| | | | | foliation (secondary) | 295 | 13 |
| | | | | foliation (secondary) | 334 | 68 |
| | | | | boudin neck axis | 6 | 40 |
| | | | | mineral lineation | 19 | 45 |
| 40 | 28°30’11.3’’ | 083°39’23.1’’ | 1263 | foliation (dominant) | 295 | 48 |
| | | | | fold axial plane | 154 | 54 |
| 41 | 28°30’09.9’’ | 083°39’23.2’’ | - | foliation (dominant) | 315 | 43 |
| | | | | mineral lineation | 51 | 43 |
| | | | | mineral lineation | 54 | 43 |
| | | | | fold axis (isoclinal) | 55 | 35 |
| | | | | foliation (dominant) | 293 | 53 |
| | | | | foliation (secondary) | 279 | 35 |
| 42 | | no GPS lock | | foliation (dominant) | 297 | 48 |
| | | | | foliation (dominant) | 302 | 45 |
| | | | | mineral lineation | 32 | 43 |
| | | | | foliation (dominant) | 305 | 39 |
| | | | | foliation (secondary) | 334 | 64 |
| | | | | mineral lineation | 37 | 40 |
| 43 | 28°29’10.9’’ | 083°38’53.3’’ | 1209 | foliation (dominant) | 294 | 53 |
| 44 | 28°28’44.4' | 083°38’34.0’’ | 1140 | foliation (dominant) | 303 | 43 |
| | | | | mineral lineation | 40 | 43 |
| | | | | boudin neck axis | 78 | 36 |
| | | | | foliation (secondary) | 281 | 56 |
| | | | | mineral lineation | 81 | 45 |
| | | | | fold axial plane | 272 | 64 |
| | | | | fold axis | 91 | 17 |
| 45 | 28°28’35.9’’ | 083°38’20.3’’ | 1153 | foliation (dominant) | 348 | 47 |
| | | | | foliation (dominant) | 316 | 44 |
| | | | | axial planar cleavage? | 124 | 54 |
| | | | | foliation (secondary) | 323 | 32 |
| 46 | 28°28’18.3’’ | 083°38’03.6’’ | 1193 | foliation (dominant) | 319 | 36 |
| | | | | mineral lineation | 34 | 39 |
| 47 | 28°27’54.7’’ | 083°37’50.7’’ | 1150 | foliation (dominant) | 317 | 34 |
| 48 | 28°28’45.6’’ | 083°38’33.7’’ | 1185 | foliation (dominant) | 284 | 23 |
| | | | | mineral lineation | 10 | 34 |
| 49 | 28°29’27.4’’ | 083°38’57.7’’ | 1234 | foliation (dominant) | 315 | 45 |
| | | | | mineral lineation | 37 | 54 |
| 50 | 28°28’58.1’’ | 083°38’57.9’’ | 1293 | foliation (dominant) | 275 | 44 |
| | | | | foliation (secondary) | 294 | 64 |
| 51 | 28°28’49.2’’ | 083°39’03.5’’ | 1274 | foliation (dominant) | 297 | 42 |
| 52 | 28°28’35.4’’ | 083°39’09.2’’ | 1352 | foliation (dominant) | 301 | 33 |

**Dhaulagiri Himalaya continued**

| | | | | | | |
|---|---|---|---|---|---|---|
| 53 | 28°28’26.8’’ | 083°39’12.9’’ | 1509 | foliation (dominant) | 328 | 42 |
| | | | | mineral lineation | 51 | 45 |
| | | | | foliation (dominant) | 319 | 27 |
| 54 | 28°27’44.8’’ | 083°39’16.8’’ | 1634 | foliation (dominant) | 263 | 48 |
| 55 | 28°27’05.3’’ | 083°39’34.8’’ | 1790 | foliation (dominant) | 344 | 59 |
| 56 | 28°26’43.5’’ | 083°40’01.2’’ | 1915 | foliation (dominant) | 350 | 47 |
| 57 | 28°26’12.8’’ | 083°40’27.8’’ | 2006 | foliation (dominant) | 230 | 20 |
| 58 | 28°25’51.5’’ | 083°40’42.5’’ | 2222 | foliation (dominant) | 35 | 51 |
| | | | | mineral lineation | 256 | 21 |
| 59 | 28°25’42.4’’ | 083°40’56.6’’ | 2227 | foliation (dominant) | 0 | 37 |
| | | | | mineral lineation | 63 | 30 |
| 60 | 28°25’25.5’’ | 083°41’27.9’’ | 2337 | foliation (dominant) | 275 | 22 |
| 61 | 28°25’17.4’’ | 083°41’45.8’’ | 2425 | foliation (dominant) | 242 | 21 |
| | | | | foliation (secondary) | 245 | 58 |
| 62 | 28°25’07.4’’ | 083°41’52.7’’ | 2479 | foliation (dominant) | 300 | 44 |
| 63 | 28°24’57.9’’ | 083°41’57.9’’ | 2535 | foliation (dominant) | 332 | 23 |
| 64 | 28°24’43.6’’ | 083°41’57.3’’ | 2626 | foliation (dominant) | 306 | 24 |
| | | | | mineral lineation | 18 | 24 |
| 65 | 28°24’33.8’’ | 083°41’53.7’’ | 2703 | foliation (dominant) | 281 | 33 |
| 66 | 28°24’01.5’’ | 083°41’57.7’’ | 2851 | foliation (dominant) | 281 | 69 |
| | | | | mineral lineation | 23 | 10 |
| 67 | 28°23’19.1’’ | 083°42’23.4’’ | 2631 | foliation (dominant) | 314 | 10 |
| | | | | foliation (dominant) | 6 | 24 |
| | | | | crenulation lineation | 20 | 2 |
| | | | | foliation (dominant) | 303 | 22 |
| 68 | 28°23’07.7’’ | 083°42’27.8’’ | 2650 | foliation (dominant) | 318 | 7 |
| | | | | foliation (dominant) | 270 | 18 |
| | | | | crenulation lineation | 224 | 13 |
| 69 | 28°23’04.2’’ | 083°42’39.9’’ | 2638 | foliation (dominant) | 58 | 21 |
| | | | | crenulation lineation | 244 | 12 |
| | | | | foliation (dominant) | 27 | 10 |
| | | | | foliation (secondary) | 312 | 58 |
| | | | | foliation (dominant) | 293 | 20 |
| 70 | 28°22’46.3’’ | 083°42’52.9’’ | 2404 | foliation (dominant) | 283 | 19 |
| | | | | crenulation lineation | 305 | 15 |
| 71 | 28°22’41.6’’ | 083°42’59.0’’ | 2404 | foliation (dominant) | 317 | 8 |
| | | | | crenulation lineation | 312 | 4 |
| 72 | 28°22’22.7 | 083°43’32.6’’ | 2282 | foliation (dominant) | 292 | 7 |
| 73 | 28°21’16.4’’ | 083°44’10.0’’ | 1946 | foliation (dominant) | 292 | 15 |
| 74 | 28°21’01.3’’ | 083°44’34.4’’ | 1499 | foliation (dominant) | 293 | 36 |
| 75 | 28°20’24.6’’ | 083°44’25.5’’ | 1437 | foliation (dominant) | 2 | 42 |
| | | | | foliation (secondary) | 193 | 68 |
| 76 | 28°20’18.0’’ | 083°44’25.0’’ | 1404 | foliation (dominant) | 346 | 28 |
| 77 | 28°19’42.6’’ | 083°44’48.6’’ | 1224 | foliation (dominant) | 286 | 36 |
| 78 | 28°19’15.2’’ | 083°45’32.8’’ | 1243 | foliation (dominant) | 265 | 49 |
| 79 | 28°18’55.0’’ | 083°45’51.4’’ | 1248 | foliation (dominant) | 281 | 49 |
| | | | | crenulation lineation | 6 | 39 |

# Appendix D - Quartz Textures

## Dhaulagiri Himalaya - Chapter 2 (arranged by structural position)

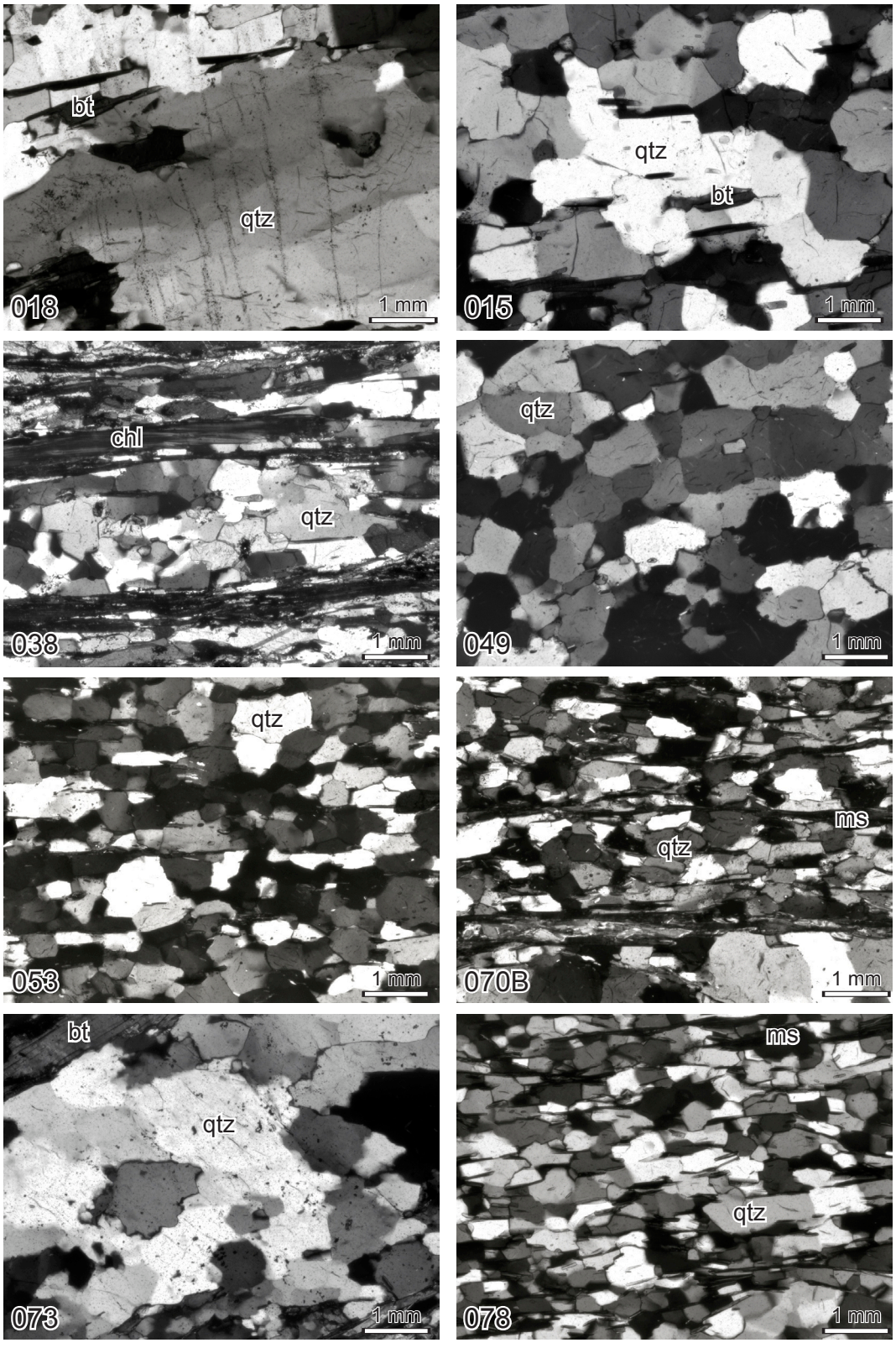


qtz, quartz; bt, biotite; ms, muscovite; chl, chlorite

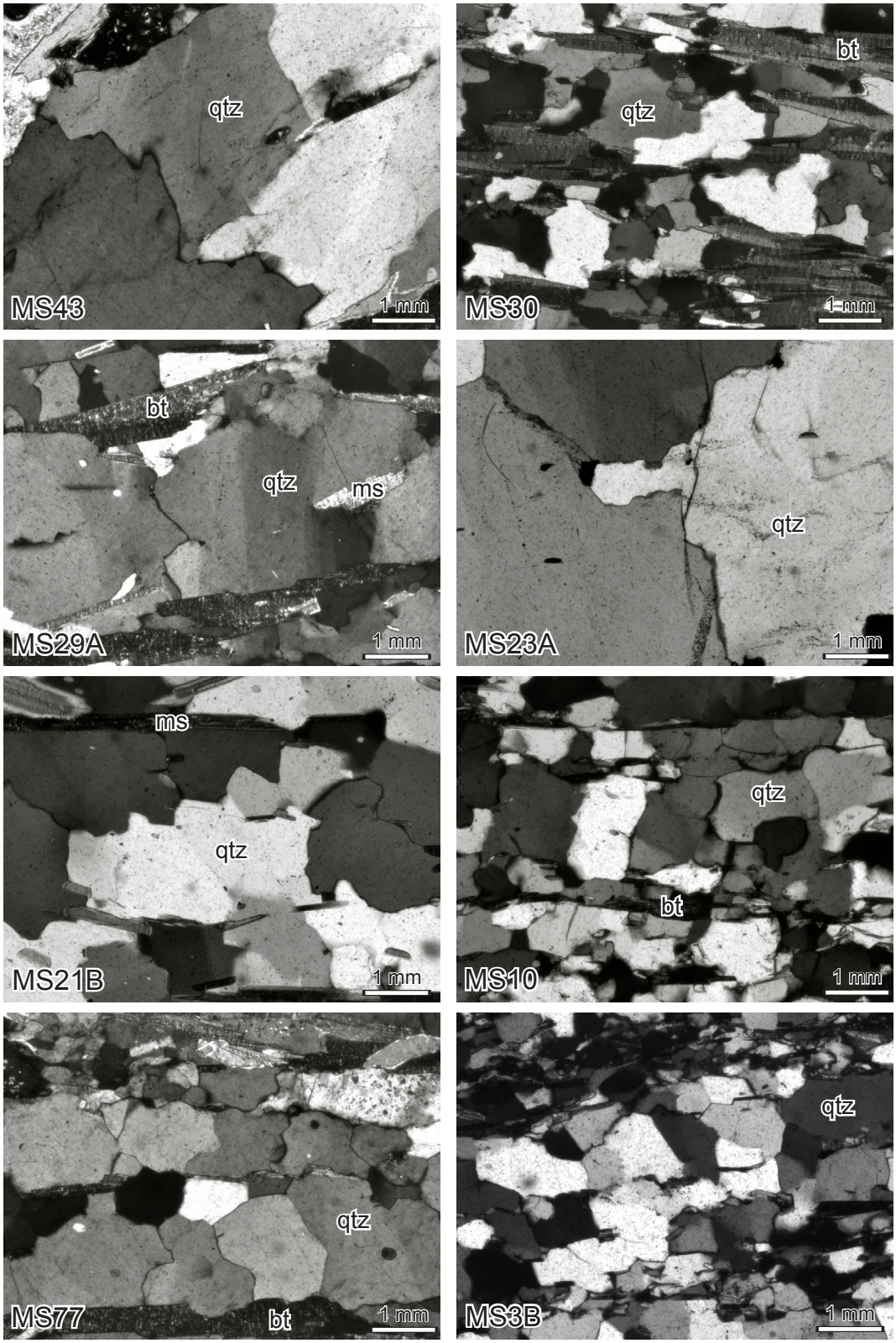


qtz, quartz; bt, biotite; ms, muscovite